ISSN 1880-8468

Technical Report of
International Development Engineering

国際開発工学報告

TRIDE-2016-03 May 9, 2016

Abstracts of Master Theses
Presented in February 2016

Department of International Development Engineering,
Graduate School of Science and Engineering,
Tokyo Institute of Technology
http://www.ide.titech.ac.jp/TR

Preface

Master theses of Department of International Development Engineering, Tokyo Institute of Technology were presented successfully on August 4, 2015 and February 12, 2016, respectively. This technical report consists of the abstracts of those theses.

TECHNICAL REPORT OF INTERNATIONAL DEVELOPMENT ENGINEERING
TRIDE-2016-03

TABLE OF CONTENTS

A NEW COMPOSTING OPERATION REDUCING ODOR EMISSION AND ELIMINATING PATHOGEN

Student Number: 13M51520 Name: Wonkyung CHOI Supervisor: Kiyohiko NAKASAKI

アンモニアガス発生の抑制と病原菌殺菌のための新規なコンポスト化操作

崔源景

In this study, a new composting method which reduces odorous ammonia gas emission and removes pathogen from the composting process is suggested. 40 °C was the optimum composting temperature with the lowest ammonia gas emission, and it was found that high heat treatment at 80 °C in the early stage of composting could eliminate pathogenic bacteria. Also, good quality of the final compost product was achieved. Thus, preliminary heat treatment followed by composting at 40 °C was proposed as the innovative composting operation reducing ammonia gas emission and removing pathogen.

1 Introduction

Due to its eco-compatibility and relatively easy operational procedures [1], composting is a sustainable way in which large amounts of organic waste can be converted into useful products [2]. It is an environmental friendly method for recycling organic wastes such as food wastes, animal manure, or sewage sludge as the substrates to produce compost products which may further be used as organic fertilizers. Compost made from animal waste and other organic refuse can serve as a valuable nutrient resource to the agricultural fields, and decrease environmental load if they are treated properly [3].

Although composting has many benefits, there are some significant problems in composting process. A major problem in composting is the odor caused by the release of ammonia [4] which may also cause atmospheric pollution [5]. Conversion of nitrogen from protein of composting material is converted into microbial cell mass or the ammonia gas. Furthermore, it is possible that pathogenic bacteria are not completely destroyed and survived in the compost [3] in that they were not exposed to high temperature of heat. In this study, it was aimed to suggest a new composting operation reducing odorous ammonia gas and eliminating pathogen.

2 Material & Methods

2. 1. Composting with temperature control for reduction of ammonia gas emission

Rabbit food, sawdust, and seeding material (Alles-G) were mixed in a ratio of 10:9:1 on dry weight basis, followed by mixing with sterilized water to set the initial moisture content of 50 % for the compost raw material. The initial pH was set at 7.5 by adding slaked lime.

Schematic diagram of the composting system is shown in Fig. 1. The raw composting mixture of 15 g was placed into each mini-reactor in the incubator. The air flow was adjusted to the rate of 5.5 mL/min with flow meter, and was flown into NaOH flaks to trap external carbon dioxide gas, and then into distilled water in the flasks to be moisturized. The air was then moved to the mini-reactors in the incubators, and then to the Tedlar bags. The ammonia gas and carbon dioxide gas emitted from composting were collected in the Tedlar bags for daily measurement of the concentrations and calculation of the cumulative emission for each gas.

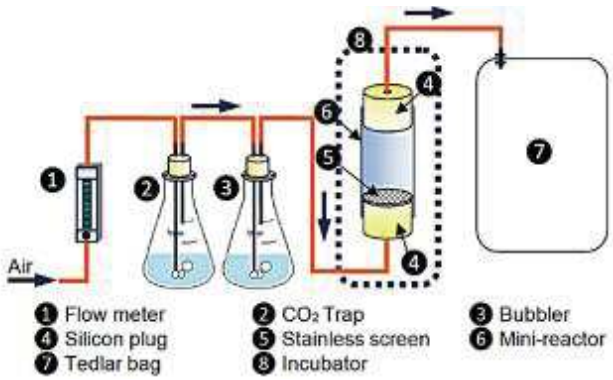

Fig. 1 Schematic diagram of the composting system.

Three different composting Run A, Run B, and Run C, of which temperature were at 30, 40 and 60 °C

were conducted. Low composting temperatures were more focused as low ammonia gas emission was expected due to large microbial cell mass in compost. All of the composting processes were run for 10 days with constant temperature. The samples of day 0, 1, 2, 3, 5, 7, and 10 were collected to monitor the moisture content and pH. The total cell density of bacteria from the final compost products of Run A (30 °C), Run B (40 °C), and Run C (60 °C) was compared by real-time PCR.

2. 2. Effect of heat pre-treatment in composting operation for elimination of pathogen

Rabbit food, sawdust, and seeding material (Alles-G) in a ratio of 10:9:1 on dry weight basis was used in this chapter. The moisture content was adjusted to 50 %. In addition, as a model of pathogenic bacteria, inoculum of *Escherichia coli* was prepared by culturing *E. coli* K12 on Luria Bertani (LB) agar plate at 37 °C for 24 hours followed by transferring the colonies into LB liquid medium in a flask which is shaken in 120 rpm for the next 24 hours. The prepared inoculum of *E. coli* was supplied to the raw composting mixture at the start of composting.

Two types of composting experiments, Run D and Run E were performed. Run D was conducted at 40 °C for 10 days, and Run E was carried out with heat pre-treatment at 80 °C for 2 days prior to 10-day composting at 40 °C. Carbon dioxide and ammonia gas concentration was measured daily and cumulative emission of those was calculated. Also, composting samples of day 0, 1, 2, 3, 5, 7, and 10 were collected in Run D, and those on day 0, 1, 2, 3, 4, 5, 7, 9, and 12 were collected in Run E for analysis of cell density of mesophilic bacteria, thermophilic bacteria, and *E. coli*. The experimental apparatus of these experiments was the same with those described above.

2. 3. Composting operation with pH control and inoculation of seeding material after heat pre-treatment

The integration of 2-day preliminary heat treatment at 80 °C and 10-day composting at 40 °C was applied in Run F. Run F was conducted with the control and the inoculation of the seeding material after the heat pre-treatment to accelerate organic matter degradation.

In Run F, raw composting mixture of rabbit food, sawdust, and seeding material (Alles-G) in a ratio of 10:9:1 on dry weight basis was used. *E. coli* was inoculated for as well. After heat pre-treatment for 2 days, the pH of composting mixture was increased to 7.5 with addition of slaked lime. At this point, Alles-G was also added to the composting mixture as the seeding material.

Carbon dioxide and ammonia gas concentration was measured daily for further analysis. For this run, compost samples on day 0, 1, 2, 3, 4, 5, 7, 9, and 12 were collected to measure the moisture content, pH, and cell density of mesophilic bacteria, thermophilic bacteria and *E. coli*. In addition, germination index was conducted to test the phytotoxicity of the final compost product.

3 Results & Discussion

3. 1. Composting with temperature control for reduction of ammonia gas emission

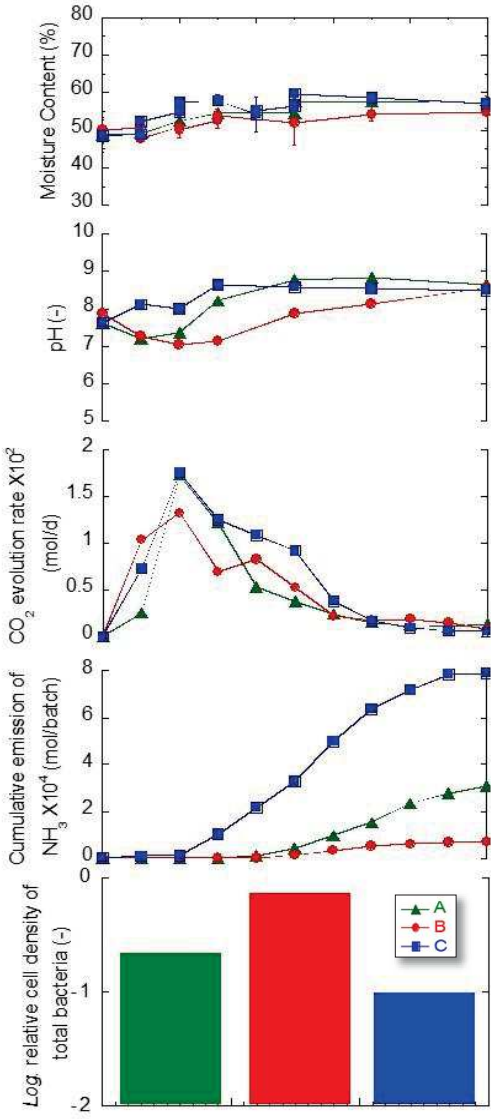

Fig. 2 The courses of temperature, pH, evolution rate of CO_2, cumulative emission of NH_3, and *log.* relative cell density of total bacteria for Run A, Run B, and Run C.

The courses of temperature, pH, evolution rate of CO_2 (carbon dioxide), cumulative emission of NH_3 (ammonia), and *log.* relative cell density of total bacteria for Run A, Run B, and Run C are shown in Fig. 2. The moisture content of all runs were maintained within the optimum range of 40 – 60 %. The pH of all runs increased to approximate value of 8.5 on the last day of composting. Carbon dioxide evolution rate peaked on day 2 for all runs as there was vigorous organic matter degradation by microbial activity in the early stage of composting. The cumulative emission of ammonia gas was the highest for Run C, of which composting temperature was 60 °C. Unexpectedly, the lowest emission of ammonia was observed in Run B which was conducted at 40 °C.

Although it is recently generalized that more ammonia gas is emitted at higher composting temperature, ammonia gas was emitted even less at Run B (40 °C) than at Run A (30 °C) in this research. In fact, the relative cell density of total bacteria in compost products of Run B determined by real-time PCR was the highest among three runs. It is considered that specific bacteria of which optimum temperature are 40 °C propagated. More bacteria existing in compost products of Run B was considered assimilate more ammonia, resulting in the least cumulative ammonia emission.

3. 2. Effect of heat pre-treatment in composting operation for elimination of pathogen

In Fig. 3, the courses of temperature, pH, evolution rate of CO_2, cumulative emission of NH_3, and *log.* cell density of *E. coli* for Run D and Run E are demonstrated. The moisture content of both runs was retained within 40 – 60 %. The pH decreased only in the early stage of composting and increased along with the composting.

Carbon dioxide evolution rate peaked on day 2 of Run D, which is similar to CO_2 evolution in Run A – C. Organic matter was decomposed during this early stage of composting. On the other hand, carbon dioxide barely increased in Run E as the microorganisms in the composting mixture were inactive due to high heat process. Thus, distinct microbial activity was not observed until the latter phase of Run E as carbon dioxide evolution rate peaked on day 9 of Run E. This indicates that organic matter degradation was delayed in Run E.

Cumulative emission of ammonia gas of Run E was the lowest among Run A – E. That of Run D was higher than that of Run B (40 °C), but it was still lower than that of Run A (30 °C). Lastly, *E. coli* was still observed until the last day of compost product in Run D while it was totally eliminated in Run E. Therefore, Run E showed high efficiency in removal of pathogenic bacteria and reducing ammonia gas in spite of low cumulative emission of carbon dioxide.

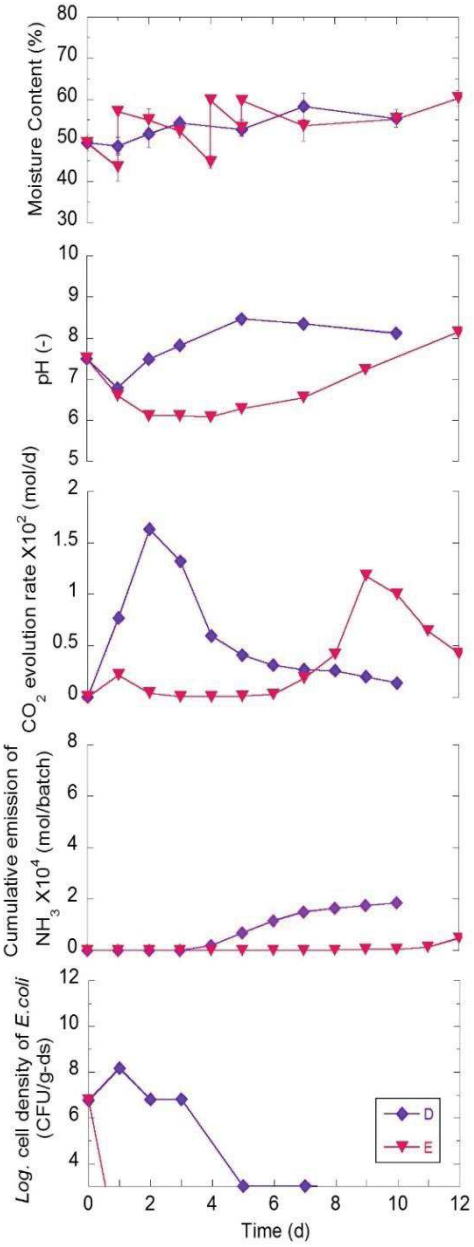

Fig. 3 The courses of temperature, pH, evolution rate of CO_2, cumulative emission of NH_3, and *log.* cell density of *E.coli* for Run D and Run E.

3. 3. Composting operation with pH control and inoculation of seeding material after heat pre-treatment

Fig. 4 presents the courses of temperature, pH, evolution rate of CO_2, cumulative emission of NH_3, and *log.* cell density of *E.coli* for Run F. Optimum range of moisture content of 40 – 60 % was attained. The pH decreased during heat pre-treatment, but was successfully adjusted to 7.5 at the beginning of 40 ℃ composting.

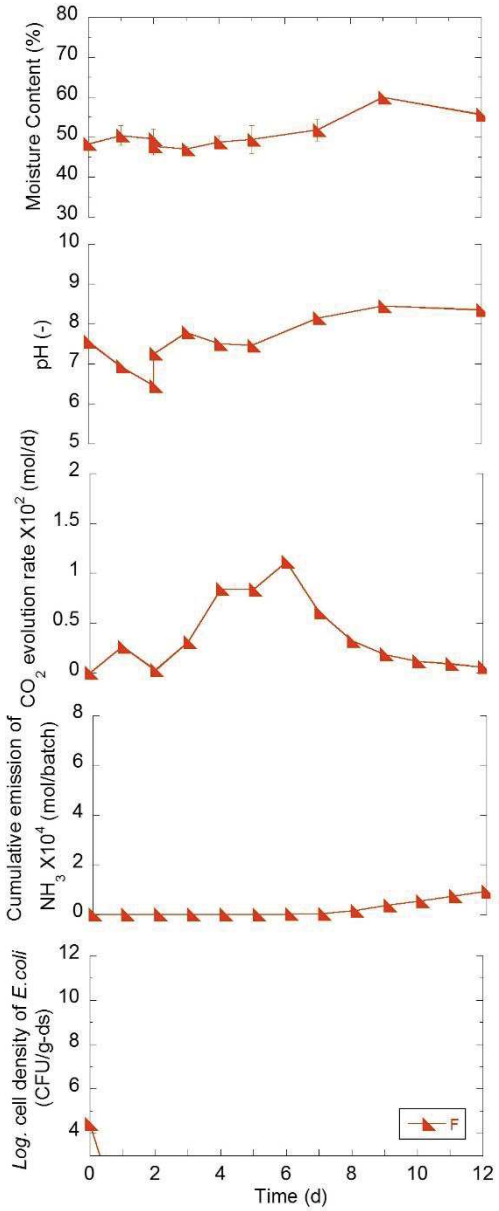

Fig. 4 The courses of temperature, pH, evolution rate of CO_2, cumulative emission of NH_3, and *log.* cell density of *E.coli* for Run F.

There was a very small peak of CO_2 evolution rate on day 1, but it was almost 0 after completion of heat process. After inoculation of heat treated seeding material (Alles-G), the carbon dioxide emission increased for Run F to 0.01 mol/day. The peak appeared earlier than Run E, revealing that the lag time of organic matter degradation was shortened. There was no significant change in cumulative emission of CO_2 between Run E and Run F. Cumulative emission of NH_3 was still very low. Lastly, no appearance of *E. coli* was observed since heat pre-treatment. The germination index of the final compost product of Run F was 86.4 %, indicating that heat pre-treatment at 80 ℃ followed by composting at 40 ℃ results in good compost quality as well.

4 Conclusions

Among composting temperatures of 30, 40, and 60 ℃, 40 ℃ is the optimum composting temperature for suppression of odor emission as NH_3 was reduced the most by conversion of nitrogen into microbial cell mass. Since complete elimination of *E. coli* was impracticable in composting at 40 ℃, the heat pre-treatment step was added. In fact, the heat process at 80 ℃ was effective in eliminating *E.coli* K12, which was selected as the representative bacteria for pathogen. Also, germination index of the compost product was over 50 % and good compost quality was confirmed in that it can be used in the farmland.

In conclusion, heat pre-treatment at 80 ℃ followed by composting at 40 ℃ is suggested as the innovative composting operation for reducing odor emission and eliminating pathogen.

References

[1] Sullivan, D.M., Bary, A.I., Thomas, D.R., Fransen, S.C., Cogger, C.G., 2002. Food waste compost effects on fertilizer nitrogen efficiency, available nitrogen, and tall fescue yield. Soil Sci. Soc. Am., J. 66, 154-161.

[2] Raut, M.P., Prince William, S.P.M., Bhatttacharyya, J.K., Chakrabarti, T., Devotta, S., 2008. Microbial dynamics and enzyme activites during rapid composting of municipal solid waste – a compost maturity analysis perspective. Bioresour. Technol. 99, 6512-1118.

[3] Gong, C.M., 2007. Microbial safety control of compost material with cow dung by heat treatment. J. Environ. Sci. (China) 19, 1014-1019

[4] Hong, J.H., Park, K.J., 2005. Compost biofiltration of ammonia gas from bin composting. Bioresour. Technol. 96, 741-745.

[5] Pagans, E., Barrena, R., Font, X., Sanchez, A., 2006. Ammonia emissions from the composting of different organic wastes. Dependency on process temperature. Chemosphere 62, 1534-1542.

Treatment of Acid Mine Drainage Using Indonesian Natural Zeolites

Student Number: 13M51537 Name: Fernando Supervisor: Ryuichi EGASHIRA

This study focuses on the removal of the heavy metals and control of the *p*H in the model and real acid mine drainage (AMD) by natural zeolites. The zeolites obtained from Sukabumi and Bogor deposits, whose base components were clinoptilolite-Ca and mordenite, were chemically stable even in relatively low *p*H range (*p*H<5). In the batch equilibrium adsorptions, the samples could adsorb heavy metals contained in the solution; the sample from Bogor adsorbed the heavy metals, removed all of Fe, Cu, Zn and about 0.87 of Mn, and restored the *p*H from low range to higher than 7 in the real AMD.

1. Introduction

The rapid growth of coal mining industry in the last twenty years in Indonesia contributes an important role in the economic growth; however it has also resulted in environmental impacts such as water contamination caused by acid mine drainage (AMD). The high concentration of dissolved heavy metals and high acidity (*p*H<5) are the main characteristics of AMD. AMD is formed naturally when pyrite and sulfide minerals with the rock of coal seams are exposed to atmospheric conditions and are oxidized. The acid generation and the discharge may continue to occur even after mines are closed and abandoned. There are various techniques exist for treatment of AMD, and mainly divided into active and passive treatments. Lime neutralization have been studied extensively and mainly employed in both treatments. However, some treatment methods generate unrecovered sludge in huge amount.

The deposits of Indonesian natural zeolite were found abundantly in West Java Province and widespread in Java, Sumatera, Sulawesi, Lombok and Flores. The base components of the zeolites are mainly clinoptilolite and mordenite. Presently, they have been utilized mostly in agriculture and aquaculture industries; therefore further developments of these useful and abundant resources are highly expected. Zeolites are microporous materials that are capa ble of cation exchange and are used to adsorb and remove heavy metal cations from solution[2].

The removal of heavy metal ions from mine waste waters using natural zeolite has been great interest among researchers. Egashira *et al.* (2013), Li *et al.* (2007), and Motsi *et al.* (2009) studied on the treatment of mine waste water using natural zeolite from Mongolia, Canada, and Turkey respectively, and revealed that the zeolite could adsorb and remove heavy metals from the solution. There have been no previous studies conducted addressing the possibility of utilizing Indonesian natural zeolite in treating real AMD from coal mine in Indonesia.

This study focuses on the removal of heavy metals and control of the *p*H in the model and real AMD. A number of experiments such as characterization of the zeolites, batch equilibrium adsorptions, and precipitation studies using lime in model and real AMDs under various conditions were performed.

2. Materials and Methods

2.1. Characterization of the zeolites

The natural zeolites were obtained from Sukabumi (SKB) and Bogor (BGR) deposits, West Java. The zeolites samples were crushed, ground and sieved to adjust the particle size smaller than 150 $\times 10^{-6}$ m. The comminuted samples were washed to remove any water soluble impurities such as soil and were then dried. The prepared samples were kept in desiccators with a saturated ammonium chloride solution at room temperature to control the moisture of the zeolites samples, and were then provided for the following characterization and adsorption runs.

The base components of the zeolites samples were analyzed using X-ray diffraction (XRD). The specific surface areas of the particles in the samples were measured from their nitrogen–gas-adsorption isotherms and the Brunauer–Emmett–Teller (BET) method.

The hydrofluoric acid (HF) dissolution method was employed in the analysis of element composition of the zeolites samples. The cation exchange capacity (CEC) of the zeolites samples was measured using Method 9081 of the US Environmental Protection Agency (EPA) [1]. Those liquid phases were then analyzed using ICP-AES (SPS7800 Series, Seiko Instruments Inc.) in order to determine the concentrations of the metals present in them. The standard solutions used for chemical analyses were prepared from standard metal solutions from Wako Pure Chemical Ind., Ltd.

The experimental conditions of the structural stability studies of the zeolites are summarized in **Table 1**. Aqueous sulphuric acid solutions (H_2SO_4) with the *p*H range from 2 to 5 covering the range of environment for AMD were mixed with the zeolites samples in 100×10^{-6} m^3 Erlenmeyer flask with screw cap. The mixtures were shaken using thermostatic shaking water bath machine at 300 K for 240 hours to obtain the equilibrium. The acid-treated zeolites samples were then characterized by XRD and HF dissolution.

2.2. Batch equilibrium adsorption studies

The experimental conditions of batch equilibrium adsorption studies are presented in **Table 1**. A single component aqueous solutions of analytical grade reagents of $Fe_2(SO4)_3$.nH2O, $CuSO_4.5H_2O$, $MnSO_4.5H_2O$ and $ZnSO4._7H_2O$ respectively (Wako Pure Chemical Ind., Ltd) were used as the model AMDs as the feed solution for the batch equilibrium adsorption studies using the natural zeolites and precipitation studies using lime. The mixtures of the zeolites samples and model AMD solutions in 100×10^{-6} m^3 Erlenmeyer flask with screw cap were shaken using thermostatic shaking water bath machine at 300 K for 240 hours to obtain the equilibrium. The liquid phases were then analyzed by *p*H meter and ICP-AES to determine the *p*H of the solutions and metal concentrations in the equilibrium solutions.

2.3. Precipitation studies using lime

The lime sample obtained from Bogor deposit was prepared as same as the preparation of the zeolites and was characterized in term of elemental contents prior to the precipitation runs. The experimental conditions of

Table 1 Principal conditions of experimental run for structural stability, batch adsorption, precipitation and treatment of AMD

Feed solutions for structural stability studies of natural zeolites	Aqueous sulphuric acid solution (H_2SO_4)
Feed solutions for batch equilibrium adsorption studies and precipitation studies	Aqueous solutions of $Fe_2(SO_4)_3.nH_2O$,$CuSO_4.5H_2O$, $MnSO_4.5H_2O$ and $ZnSO4._7H_2O$
Feed solutions for the treatment of AMD	Real AMD from coal mining in Indonesia
Volume of feed solution, V_0 [m^3]	20×10^{-6}
Initial metals concentration, $C_{i,0}$ [kmol m^{-3}]	$0 - 2.7 \times 10^{-2}$
Initial *p*H of feed solution, pH_0	2 – 5 (adjusted by H_2SO_4 solution)
Adsorbent for batch adsorption studies and treatment of AMD	Natural zeolites from Sukabumi and Bogor deposits
Mass of zeolite, *S* [kg]	1×10^{-3}
Lime for precipitation studies and treatment of AMD	Natural lime from Bogor deposit
Mass of lime [kg]	$0 - 1 \times 10^{-3}$
Contacting time [hours]	240
Temperature [K]	300

precipitation studies are summarized in **Table 1.** The mixtures of lime and model AMD solutions were shaken using thermostatic shaking water bath machine at 300 K for 240 hours. The liquid phases were then analyzed by *p*H meter and ICP-AES to determine the *p*H of the solutions and metal concentrations in the solutions.

2.4. Treatment of real AMD

The samples of AMDs were obtained from 2 different locations in coal mining site in Indonesia. The samples were analyzed by *p*H meter and ICP-AES to determine the *p*Hs and metal concentrations in the solutions.

In this study, the treatment of AMD by adsorption using the natural zeolites was preliminarily compared with the precipitation method using lime. The experimental conditions of treatment of AMD are summarized in **Table 1.** The standing (STD) and shaking (SHK) tests were employed in this study. The samples of zeolites or lime were mixed with 20×10^{-6} m^3 of real AMD. The mixtures were contacted for 240 hours in thermostatic shaking water bath machine at 300 K. The liquid phases were then also analyzed by *p*H meter and ICP-AES to determine the *p*H of the solutions and metal concentrations in the solutions.

3. Results and Discussion

3.1. Characterization of the zeolites

Based on the XRD analysis result, the base components of the zeolites were clinoptilolite-Ca and mordenite; the zeolites also contained with small quantity of impurities such as albite ($NaAlSi_3O_8$) and cristobalite (SiO_2). In the case of BGR, the sample also contained with calcite ($CaCO_3$). The element compositions of the zeolites are presented in **Table 2**. It was confirmed that the zeolites contained with exchangeable cations such as Ca^{2+}, Na^+, K^+ and Mg^{2+}. The principal characteristics of the zeolites are summarized in **Table 3**. There was a relationship between Si/Al ratio and CEC in term of the amount of negative charge in the zeolite balanced by the exchangeable cations.

Figure 1 shows the XRD results of untreated and treated zeolites. The result showed that no radical change in crystallinity of the zeolites even treated at pH_0=2 during 240 hours. Nevertheless, the peak intensities of the treated zeolites have been reduced slightly. This might be due to the leaching of major elements in the structure of zeolite and dissolution of amorphous materials. However, the decreased of the volume of some elements in the zeolites such as Al, Fe, Ca, Na, K, and Mg was insignificant to the disruption of zeolites structure and framework due to the high ratio of Si in the framework[4].

3.2. Batch equilibrium adsorption studies

Figure 2 shows the estimated solubility curve of metal hydroxides described as a solid line and the relation between the equilibrium *p*H values and the concentrations of the metals as determined from the adsorption runs. This figure clarifies that the precipitation of metal hydroxides occurred on the removal of Fe^{3+} by SKB and BGR, and removal of Cu^{2+} and Zn^{2+} in model AMD by BGR. **Figure 4** shows the change of *p*H by adsorption. The greater values of equilibrium *p*H than the initial *p*H, pH_0 indicate that the zeolites could also adsorb the H^+ ions in solution; however, the difference between equilibrium *p*H and pH_0 demonstrated a descending tendency with the increment in metal concentration of the equilibrium solutions. It was clarified that the zeolites preferred to adsorb metal ions than H^+ ions.

The amount of metal adsorbed ion on the zeolite, q_i, was calculated by material balance relationship with the concentrations in liquid phases. Since the change in the

Table 2 The element composition of the zeolites

Elements	%-weight	
	Sukabumi	Bogor
SiO_2	79.6	80.9
Al_2O_3	13.3	10.2
MnO	0.004	0.02
TiO_2	0.3	0.2
ZnO	0.01	0.01
Fe_2O_3	1.3	1.1
MgO	1.9	1.9
CaO	1	1.4
Na_2O	0.4	2.3
K_2O	2.2	1.8

Table 3 Principal characteristics of the zeolites

Deposit	Sukabumi	Bogor
Surface area $\times 10^3$ [m^2 kg-zeo^{-1}]	38.4	100.6
CEC $\times 10^{-4}$ [kmol kg-zeo^{-1}]	11.3~14.3	6.7~7.5
Si/Al ratio [-]	5.3	7

Table 5 Principal characteristics of real AMD and the quality standard of treated AMD in Indonesia

	Concentration [mg l^{-1}]				*p*H
	Fe	Mn	Cu	Zn	
Real AMD I	34.11	3.87	0.04	0.53	2.72
Real AMD II	28.45	3.7	0.13	1.14	2.66
The quality standard of treated AMD	< 7	< 4	< 2	< 5	6–9

Table 4 The element composition of lime

Elements	%-weight
CaO	93.9
SiO_2	2.4
Al_2O_3	1.6
CuO	0.02
MnO	0.05
TiO_2	0.1
ZnO	0.2
Fe_2O_3	1
MgO	0.6
Na_2O	0.2
NiO	0.01

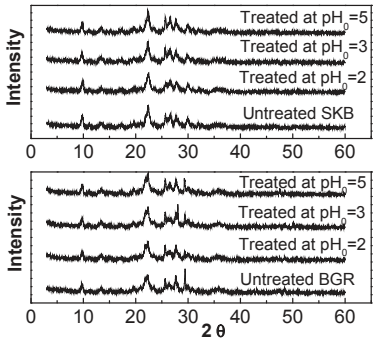

Figure 1 XRD patterns of the zeolites at different pH_0 treated conditions

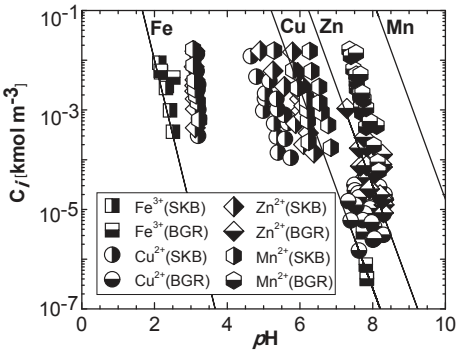

Figure 2 Estimated solubility curves of the heavy metal hydroxides and the relation between the solution pH values and the concentrations of the metals as determined from the adsorption runs

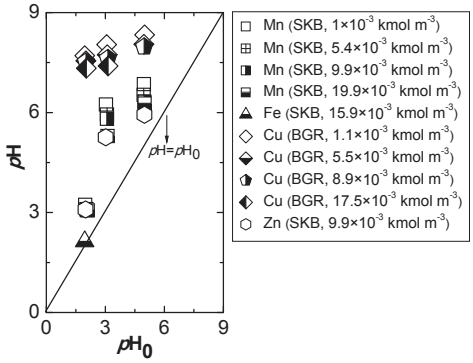

Figure 3 Changing pH in equilibrium solutions

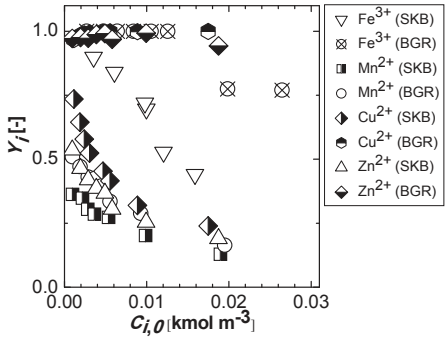

Figure 4 Fractional removals of metals on the respective zeolites at pH_0 =2

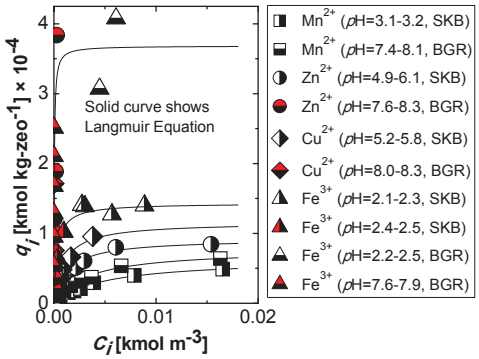

Figure 5 Comparisons of the adsorption isotherms for various heavy metal–zeolite combinations

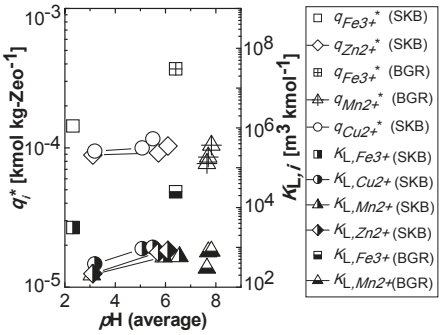

Figure 6 Effect of the equilibrium pH of solutions on the saturated adsorption amount, q_i*, and adsorption coefficient, $K_{L,i}$, in Langmuir equation for various heavy metal–zeolite combinations

volume of the feed solution after adsorption was negligible, the material balance relationship for the metals could be expressed by,

$$V_0 C_{i,0} = V_0 C_i + S q_i \quad (1)$$

and the fractional removal of metal i, Y_i, was defined as,

$$Y_i = (C_{i,0} - C_i) / C_{i,0} \quad (2)$$

This fractional removal of metals, Y_i, is shown in **Figure 4**. In general, the Y_i decreased with the increment of initial metal concentration, $C_{i,0}$. The Y_i of Cu^{2+} and Zn^{2+} by BGR in model AMD was almost 1 due to the precipitation of the metals.

Figure 5 shows the adsorption isotherms of the metals. The isotherms were examined using Langmuir equation:

$$q_i = q_i^* K_{L,i} C_i / (1 + K_{L,i} C_i) \quad (3)$$

Generally, the amount of adsorbed metal, q_i, increased as the increment in metal concentration of the equilibrium solution until the tendency become constant. It means that the maximum adsorbent sites on the zeolites surface have been attained. The q_i increased as the increment in pH of the equilibrium solutions. The red colored results refer to the occurrence of precipitation of metal hydroxides. The saturated adsorbed amounts, q_i^*, and the Langmuir constants, $K_{L,i}$, in the equation estimated by fitting with the experimental results are summarized in **Figure 6**. $K_{L,i}$ increased with pH, but the q_{Mn2+}^* was almost constant. The q_{Fe3+}^* and $K_{L,Fe3+}$ were higher than those of metals at any different pH. According to the Langmuir parameters, the adsorbability of the heavy metal ions on the zeolites were Fe^{3+}>Cu^{2+}>Zn^{2+}>Mn^{2+}. This tendency was same as in the previous study[2]. The difference in the adsorbability might attribute to the hydration diameters and solubility of the metals. The hydration radii of the cations are: r_HCu^{2+}=4.19Å, r_HZn^{2+}=4.30Å, r_HMn^{2+}=4.38Å and r_HFe^{3+}=4.57Å[6]. The smaller particles should be adsorbed faster and much more quantities compared to the larger

particles. However, in the case of the Fe^{3+}, it is confirmed that the precipitation of iron hydroxide was the main mechanism in the removal of iron in model AMD by the zeolites. In addition, ion exchange was also responsible on its removal particularly on high concentration of iron with low *p*H in equilibrium solution. **Figure 7** shows the comparison of the total amount of leached exchangeable cations and the amount of adsorbed mangan by the zeolites. An enhanced amount of the exchangeable cations at equilibrium solution clarified that ion exchange was taken place. **Figure 8** shows the relationships between q_i* and CEC on the adsorption of mangan by SKB and BGR. The $q_{Mn}{}^*$ by BGR was greater than the $q_{Mn}{}^*$ by SKB. In addition, the $q_{Mn}{}^*$ by both zeolites were much lower than those predicted from the cation exchange capacity. It was because some of these exchangeable cations are located at inaccessible sites of the zeolite structure and the exchangeable cations might be components of impurities, and accordingly not possible to take part in ion exchange[3].

Compare to the previous study[2], the efficiency of Indonesian natural zeolites to adsorb and remove heavy metal cations from solution was lower than Mongolian natural zeolites. However, the utilization of Mongolian natural zeolites in Indonesia is not applicable due to the cost of material and transportation.

3.3. Precipitation studies using lime

The chemical composition of Indonesian lime is presented in **Table 4**. **Figure 9** shows the result of the precipitation studies such as the fractional removal of mangan and the changing *p*H at various initial mangan concentrations, $C_{Mn2+,0}$. The lime sample could adjust the *p*H to alkaline conditions (*p*H >12), thus removed all of the metals completely by precipitated them out.

3.4. Treatment of real AMD

Table 5 shows the characteristics of real AMDs and the standard of treated AMD in Indonesia. The *p*H values and iron concentration in real AMDs were over than the regulation. **Table 6** shows the fractional removal of metal and *p*H of treated AMD. The quality of the treated AMD using the zeolite from Bogor was complied with the level of quality standard in Indonesia by removed all of Fe^{3+}, Cu^{2+}, Zn^{2+} and about 0.87 of Mn^{2+}, and restored the *p*H from low range to higher than 7 either by standing or shaking test.

4. Conclusions

The base components of Indonesian natural zeolites were clinoptilolite-Ca and mordenite. They were chemically stable in AMDs treatment. The zeolites could adsorb and remove the heavy metals, and restore the *p*H to the appropriate level in AMD. Removal of the heavy metal ions was due to the adsorption, ion exchange, and precipitation of metal hydroxides. The removal of Fe^{3+} was larger than Cu^{2+}, Zn^{2+}, and Mn^{2+}. The efficiency of Indonesian natural zeolite in the adsorption of the heavy metals from AMDs would increase as the increment of initial *p*H. Based on the treatment of real AMD studies, the Indonesian natural zeolite has a great promising alternative adsorbent for the treatment of AMD.

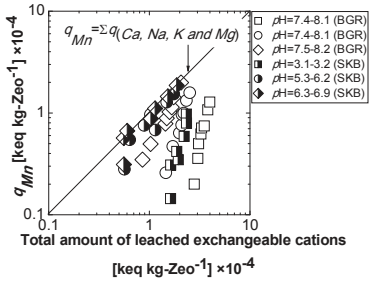

Figure 7 Relationship between the amount of total leached cations and adsorbed mangan at different *p*H and C_i,

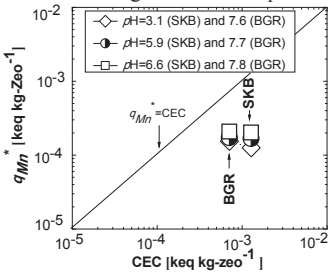

Figure 8 The relationships between q_i* and CEC on the adsorption of mangan on respective zeolites

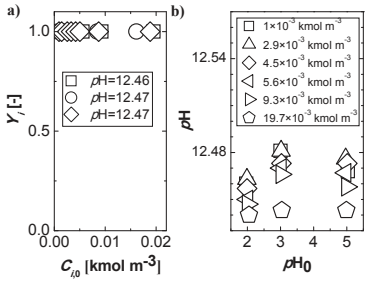

Figure 9 The result of precipitation studies: a) fractional removal of Mn, b) changing *p*H at various $C_{Mn2+,0}$

Table 6 The Y_i [-] and *p*H of treated AMD

Y_i [-]		SKB		BGR		Lime	
		AMD I	AMD II	AMD I	AMD II	AMD I	AMD II
Fe	STD	1	0.99	1	1	1	1
	SHK	1	1	1	1	1	1
Mn	STD	0.66	0.27	0.87	0.54	1	1
	SHK	0.66	0.27	0.87	0.54	1	1
Cu	STD	1	0.62	1	1	1	1
	SHK	1	1	1	1	1	1
Zn	STD	1	0.99	1	1	1	1
	SHK	1	1	1	1	1	1
***p*H**	STD	4.46	4.11	7.9	7.8	12.5	12.49
	SHK	5.12	4.25	8.27	8.06	12.53	12.52

Nomenclature

C_i: concentration of metal *i* in liquid at equilibrium [kmol m^{-3}], $C_{i,0}$: concentration of metal *i* in liquid at initial [kmol m^{-3}], $K_{L,i}$: Langmuir constant [m^3 kmol^{-1}] $q_i{}^*$: saturated adsorbed amount of metal *i* [kmol kg-zeo^{-1}], V_0: volume of liquid [m^3], Y_i: fractional removal of metal *i* [–], pH_0: initial *p*H of solution, *p*H: equilibrium *p*H, S: mass of zeolite [kg], SKB: natural zeolite from Sukabumi, BGR: natural zeolite from Bogor, STD: standing test, SHK: shaking test

References

1) Chapman, H. D.; Chemical and Microbiological Properties, C. A. Black ed., pp. 891–900, U.S.A. (1965)
2) Egashira, R. *et al.*, *JCEJ*, **46**, 50-55 (2013)
3) Inglezakis, V.*et al*., *Water Research*, **36**, 2784-2792 (2002)
4) Li, L.Y. *et al.*,*Applied Clay Science*, **39**, 1-9 (2007)
5) Motsi, T. *et al.*, *Int. J. Miner. Process.*, **92**, 42–48 (2009)
6) Nightingale,E.R.J., *J. Phys. Chem.*, **63**, 1381–1387 (1959)

Understanding factors affecting primary school teachers' use of ICT for student-centered education in Mongolia

Student Number: 13M51550 Name: Shengru LI
Supervisors: Shinobu YAMAGUCHI and Jun-ichi TAKADA

In recent years, Mongolian education policies focus on student-centered education (SCE) and the use of information and communication technology (ICT) in teaching and learning. This study aims to understand the factors affecting teachers' perceptions on use of ICT for SCE as there lacks its study in Mongolian context. Both quantitative and qualitative analysis were conducted. The study found: 1) teachers' professional competency and perception of benefits on use of ICT are significant factors affecting the use of ICT tool for SCE; 2) teacher cooperation is affecting their perceptions on use of digital contents for SCE; and 3) endogenous teacher level factors such as teacher's job satisfaction and self-confidence are affecting their perception on the use of ICT for SCE.

1 Introduction

The Mongolian education system experienced decentralization since early 1990s. It resulted in increased roles and responsibilities of local governments and schools.

During such transitional period, Mongolian primary education faced decreases in the school enrollment rate and school completion rate [1]. Given this situation, Mongolian government implemented educational reforms with new policies to assist the changes in education sector. Specifically, the Ministry of Education, Culture and Science (MECS) issued "New Education Standard" in 2003 to promote the concept of student-centered education in school curriculum. In 2015, "Core Curriculum" was introduced for the teachers to apply student-centered education.

Further, "Master Plan to Develop Education of Mongolia in 2006 - 2015" formulated policies to implement ICT in education. This Master Plan emphasized the utilization of ICT for teacher training programs to promote ICT integration into classroom teaching. With this policy guidance, there is a growing interest among teachers to integrate ICT into teaching.

However, there are limited number of studies conducted in Mongolia to understand primary school teachers' perception on use of ICT for student-centered education. In particular, it is important to discuss what is influencing teachers to motivate and experiment effective use of ICT for their teaching and other educational activities with quantitative and qualitative approaches.

2 Literature Review

2.1 Educational change

Educational change has been discussed widely in supporting educational reforms, educational technology innovations and any other changes associated with transformation in educational policies. Fullan has established the comprehensive theory for school administrators, teachers and other stakeholders to understand and practice educational change successfully [2].

Practicing educational change can arise on different levels, for instance, teachers, school administrators, and district administrators. Educational change on teacher level is discussed here because teachers are core stakeholders in practicing educational change since they are the closest to instruction and learning. The major aspect of practicing new programs and policies in a classroom is not unidimensional, but instead, it contains at least three following dimensions: 1) the possible use of new instructional materials, curriculum materials or technologies; 2) the possible use of new pedagogies (teaching strategies and activities); and 3) the possible alteration of beliefs (pedagogical assumptions and theories underlying particular new policies or programs) (Fullan, 2007, p.30). Among these three dimensions, the third dimension for teacher's educational belief is considered fundamental to realize sustainable educational change.

There are multiple studies both in developed and developing countries illustrating the dimensionality of educational change. They also examined the importance of the dimension concerning teachers' educational belief. For example, Bussis et al. showed a case where teachers provide substantial materials to the classrooms with the faith that they will promote certain learning priorities [3]. In this study, teachers developed new instructional materials based on the belief that new materials would promote learning outcomes. For another example, Johns et al. examined three dimensions of educational change among secondary school teachers in the context of physical education in Hong Kong [4]. His study showed that the situational and personal-social factors prevented untested ideas to be transformed into firm beliefs and values. These studies indicate the importance of teachers' educational belief in introducing new programs and policies into schools.

2.2 Factors affecting teacher's educational use of ICT

There exist multiple studies focusing on factors affecting ICT implementation in school in general, with the assumption that the use of ICT in education will lead to change in learning arrangement and pedagogies. However, the factors influencing ICT use for student-centered

education are not specifically addressed [5][6]. Drent established a framework for identifying and categorizing factors affecting innovative use of ICT from teacher's perspective [7].

Under Drent's framework, factors can be categorized into exogenous and endogenous, school and teacher level factors. Exogenous conditions refer to the non-manipulative conditions while endogenous conditions involve conditions that can be changed. Specifically, four categories of factors are endogenous teacher level, exogenous teacher level, endogenous school level and exogenous school level. For example, endogenous teacher level factors are teachers' professional competency, perception on digital teaching materials and job satisfaction. For exogenous teacher level, age and gender are included. As for endogenous school level, ICT infrastructure and support from school management are the examples. At last, exogenous school level has school location and type of school as example factors.

2.3 Importance of endogenous level factors in Mongolian context

The survey was conducted in 2014 to find out the category of factors that teachers believe is affecting on their use of ICT for SCE. The questionnaire was developed containing 47 potential factors based on literature review and related documents of education in Mongolia. Four demographic questions were added. The survey utilizes 5-point Likert scale to enquire to what extent teachers agree that each factor affect their perception on the use of ICT.

Respondents of the survey (N=153) were located in two provinces and the capital city in Mongolia. The collected survey data were analyzed and interpreted together with interviews and observations.

The analysis shows that endogenous teacher level factors are affecting teachers' perception on use of ICT for SCE. Such examples include teacher's professional competency, basic ICT skills, and perception on effectiveness in use of digital materials.

3 Methodology

3.1 Research objective

The study aims to understand factors that affect teachers' perception on use of ICT for SCE in Mongolia context. Based on the survey result and the research question, the following hypothesis was formulated.

Hypothesis: Endogenous teacher level factors are affecting teachers' perception on use of ICT tools and digital contents for SCE in primary schools in Mongolia.

3.2 Data source

The study utilized the data from the survey conducted in JICA funded project "Quality improvement of primary education teachers through development of training materials using ICT." This survey was to review school and teacher condition on the use of ICT in primary education during 2012 - 2013 [8]. There are three justifications to use this baseline survey data: 1) the data cover four provinces and the capital city representing local characteristics of five regions in Mongolia with 838 respondents; 2) the data contain multiple aspects of information with regards to teachers' use of ICT in education; and 3) the data were collected in 2102 - 2013, reflecting current perception of primary school teachers in Mongolia.

3.3 Data analysis procedure

Based on research objective, dependent and independent variables were identified from baseline survey instrument. Two dependent and seven categories of independent variables were determined. Table 1 shows the details of dependent variables. Seven potential categories of affecting factors were selected based on literature review of general factors affecting teachers' use of ICT. 36 survey items were fitted into the potential seven categories based on the understanding of each category. The seven categories of independent variables are: 1) teacher's quality; 2) technical support; 3) access to ICT resources; 4) time; 5) teacher's educational beliefs; 6) location and demographic factors; and 7) school management and leadership.

Table 1: List of dependent variables

Dependent Variable	Measurement Item from Baseline Survey
Perception on use of ICT tool for SCE	I think the use of ICT tool makes a progress towards student-centered education
Perception on use of digital contents for SCE	I think the use digital contents makes a progress towards student-centered education

Note. Measurement is recoded in 4-point Likert scale (1=completely disagree to 4=completely agree)
Source: developed by author based on baseline survey, 2015

After dependent and independent variables were identified, the following steps were proceeded. Four steps were involved in data analysis procedure. First, the selected items for dependent and independent variables went through descriptive analysis to detect any irregular missing patterns and outliers. Second, after data cleaning, the original 5-point Likert scale questions were recoded into 4-point Likert scale. The "I don't know" option was recoded into system missing according to current literatures and discussions with baseline survey designer [9] [10]. As for the location categorical variable, it was recoded into two dummy variables using dummy coding. Third, after the data treatment, exploratory factor analysis was conducted on items identified under seven potential categories of factors. Specifically, principal component analysis with Varimax rotation method was utilized to detect highly correlated items and the result justified the categorization of factors into latent variables. Fourth, linear multiple regression analysis was utilized to analyze the relationships between potential affecting factor with teachers'

perception on use of ICT tools and digital contents towards SCE.

4 Data analysis

4.1 Demographics

Most of the teacher respondents to the baseline survey were female (95.6%). The respondents' age were distributed in four ranges, with more than a third aged between 31 to 40 years old (39.5%). Teaching years were also distributed in four ranges, with the biggest portion of respondents having 1 to 10 years of experience (36.9%). Finally, it can be seen that the respondents belong to schools in Ulaanbaatar (41.1%), province center (31.7%), and village center (27.2%), relatively equally.

4.2 Exploratory factor analysis

The exploratory factors analysis was conducted on 30 potential items towards teachers' use of ICT for SCE. There were 6 items exempted from the factor analysis for two reasons either due to high missing rate or due to demographical and categorical nature. The item measuring technical support from school was excluded from the factor and regression analysis due to high missing rate (66%). Demographical and categorical items were carried directly into multiple regression analysis, namely, computer ownership, age, gender, years of service and location of school (recoded into two dummy variables).

Through principal component analysis and Varimax rotation, items with component loadings greater than 0.6 were considered significant. As a result, 23 items out of 30 potential items were categorized into seven latent variables. The naming for these latent variables were decided upon the consultation with educational experts, namely, 1) professional competency (PC), 2) Supportive school environment for ICT integration (SE), 3) quality of school computers (QSC), 4) teacher cooperation (TC), 5) benefits on use of ICT (BICT), 6) available time for use of ICT in education (T), and 7) resistance to change (RC). Each latent variable was constructed by averaging its constructing items.

4.3 Multiple regression analysis

Multiple regression analysis was applied to find out what are the factors affecting teachers' belief on use of ICT for SCE. Twelve independent variables which include seven latent variables and six demographic variables were included in the analysis. Two regression models were established using two dependent variables. The results of regression models are summarized below.

Equation (1) below shows that two factors, namely, professional competency (PC) and benefits on use of ICT (BICT) have statistical significance as independent variables to explain teachers' perception on use of ICT tool for SCE. The model explains that teachers perceive higher professional competencies of themselves by 1 scale score, their perceptions on use of ICT tool for SCE increases by 0.394 scale score. Furthermore, if teachers perceive higher benefits on use of ICT by 1 scale score, their perceptions on use of ICT tool for SCE increases by 0.281 scale score. This model explains 27% of the variance in perception on use of ICT tool for SCE by two factors, namely, professional competency and benefits on use of ICT.

$$PTSCE = 0.976 + 0.394(PC) + 0.281(BICT) \quad (1)$$

Equation (2) below shows that three factors, namely, professional competency, teacher cooperation and benefits on use of ICT have statistical significance as independent variables to explain teachers' perception on use of digital contents for SCE. The model explains that if teachers perceive higher professional competencies of themselves by 1 scale score, their perception on use of digital contents for SCE will change positively by 0.421 scale score. Furthermore, if teachers perceive higher benefits on use of ICT by 1 scale score, their perception on use of digital contents for SCE will increase by 0.234 scale score. In addition, if teachers perceive better teacher cooperation by 1 scale score, their perception on use of digital contents will increase by 0.147 scale score. This model explains that 29% of the variance in perception on use of digital contents for SCE by three factors, namely, professional competency, teacher cooperation and benefits on use of ICT.

$$PDCSCE = 0.766 + 0.421(PC) + 0.234(BICT) + 0.147(TC) \quad (2)$$

5 Discussion

This section summarizes the major findings based on both quantitative and qualitative analysis.

First, professional competency of teachers was found to be a factor influencing both teachers' perception on use of ICT tool for SCE and teachers' perception on use of digital contents for SCE. This finding agrees with current literatures on teacher's use of ICT in education. Existing studies and literatures emphasize the importance of teacher's professional competency in successfully utilizing ICT in educational contexts [11]. In Mongolian context, under the government policy support, multiple teacher training programs are implemented at central and local levels, reaching out teachers with hand-on experiences of using ICT into their classroom teaching. This finding can be interpreted that such efforts are influencing teachers to believe the importance of professional competency.

Second, the study found that teachers' perception of benefits on use of ICT also affects both teachers' perception on use of ICT tool for SCE and teachers' perception on use of digital contents for SCE. The finding supports multiple literatures indicating that teachers are more likely to make use of ICT if they are aware of the advantages of using technology in their teaching [12]. During fieldwork, specific benefits of integrating ICT into teaching were observed in both rural and urban schools. For example, teachers in Ulaanbaatar utilized animations to explain solar system in the galaxy, illustrating the existence of Earth relative to the other planets in the space.

Teachers in Bayankhongor province found videos containing recordings of local instrument useful for students' understanding of music theory. These qualitative data collected in schools indicate that teachers recognized the usefulness and benefit of ICT as a part of their lessons. This implies that future teacher training programs need to emphasize clear objectives of use of ICT in school settings.

Third, the study finding supports that teacher cooperation affects teachers' perceptions on use of digital contents for SCE. Existing literatures report that teachers view technology as a constant area of change where teachers have shared need to learn it for creating new classroom teaching contents [13]. During the local teacher training session in rural Mongolia, it was observed that teachers from different schools cooperated when they presented, discussed and shared opinions to improve their digital teacher training materials. This finding may suggest school administrators that building an environment for teachers to create, share and exchange ideas for digital teaching materials could potentially promote teachers' perception on use of ICT for SCE.

Fourth, in this study, school location did not influence teachers' perception on use of ICT tools and digital contents for SCE. A study in South Africa found that the teachers from rural and urban areas differ in the perception on adopting ICT in education due to the difference in teachers' exposure to opportunities [14]. Further, a previous study in Mongolia discovered the different conditions in rural and urban areas could affect teachers' frequency in use of ICT for communications [15]. With Mongolian government policy to introduce ICT in schools, infrastructure and human resources have been developed rapidly, especially in rural areas. While the different level of development in schools of different locations may affect the utilization of ICT, the finding of this study explains the importance of policies and its implementation regardless of the location.

Fifth, in this study, ICT infrastructure was not found to be a factor affecting teachers' perception on use of ICT for SCE. Current literatures support that basic ICT infrastructure is needed for teachers to utilize ICT for administrative tasks, but teachers' use of ICT for educational purposes may also depend on teachers' pedagogy and educational philosophy [16]. While computer infrastructure is important for teachers to use ICT in education, this finding contributes to the literature arguing that whether teachers can effectively integrate ICT into classroom teaching and other educational activities requires more than infrastructure itself [16].

6 Conclusion

During the recent educational reforms in Mongolia, use of ICT in primary education has been identified as means to raise quality of education. The study aimed to answer the question on "what are the factors affecting teachers' perception on use of ICT for student-centered education?" Both quantitative and qualitative analysis were utilized, covering 838 responses of primary school teachers of four provinces and Ulaanbaatar. The study found that professional competency and benefit on use of ICT are factors affecting on both teachers' perception on use of ICT tools and digital contents promoting student-centered education. Teacher cooperation was found to be the factor affecting teachers' perception on use of digital contents for student-centered education.

Three factors identified to affect teachers' perception on use of ICT for student-centered education are all endogenous teacher level factors. This confirms the hypothesis of this study. This implied while investing resources in infrastructure development, policy makers could also consider designing training programs to improve teacher's professional competency, by conveying the benefits of using ICT tools and digital contents in education. It is also very important to create learning environment for teachers to promote their cooperation through collaborative tasks on use of ICT.

References

[1] J. Engel, A. Prizzon, and G. Amgaabazar, "From decline to recovery: post-primary education in Mongolia," 2014.

[2] M. Fullan, The New Meaning of Educational Change. New York: Teacher College Press, 2007.

[3] A. M. Bussis, E. A. Chittenden, and M. Amarel, Beyond surface curriculum: an interview study of teachers' understandings. 1976.

[4] D. P. Johns, A. S. C. Ha, and D. J. Macfarlane, "Raising Activity Levels: A Multidimensional Analysis of Curriculum Change," Sport. Educ. Soc., Aug. 2010.

[5] H. J. Becker, "Findings from the teaching, learning and computing survey: is Larry Cuban correct?" Irvine, US, 2000.

[6] W. J. Pelgrum, "Obstacles to the integration of ICT in education : results from a worldwide educational assessment," Comput. Educ., vol. 37, no. 2, pp. 163–178, 2001.

[7] M. Drent and M. Meelissen, "Which factors obstruct or stimulate teacher educators to use ICT innovatively?" Comput. Educ., vol. 51, no. 1, pp. 187–199, Aug. 2008.

[8] Mon Educ LLC., "Report of the baseline survey of 'Quality improvement of primary education teachers through development of training materials using ICT' project funded by JICA, Japan," Ulaanbaatar, 2013.

[9] K. K. Tsang, "The use of midpoint on Likert scale: the implications for educational research," Hong Kong Teach. Cent. J., vol. 11, pp. 121–130, 2012.

[10] J. Sukhbaatar, "Personal communications on understanding measurement instrument in baseline survey," 2015.

[11] K. A. Bingimlas, "Barriers to the Successful Integration of ICT in Teaching and Learning Environments: A Review of the Literature." EURASIA J. Math. Sci. Technol. Educ., vol. 5, no. 3, pp. 235–245, Nov. 2008.

[12] BECTA, "A review of the research literature on barriers to the uptake of ICT by teachers." 2004.

[13] S. Dexter, K. R. Seashore, and R. E. Anderson, "Contributions of professional community to exemplary use of ICT," J. Comput. Assist. Learn., vol. 18, no. 4, pp. 489–497, Dec. 2002.

[14] K. Cassim and S. Obono, "On the factors affecting the adoption of ICT for the teaching of word problems," Proceedings of World Congress on Engineering and Computer Science, 2011.

[15] O. Tsogtsaikhan, "Factors Affecting Information Communication Technology (ICT) Integration of Primary School Teachers in Mongolia," Tokyo Institute of Technology, 2014.

[16] D. Watson, "Pedagogy before technology: Re-thinking the relationship between ICT and teaching," Educ. Inf. Technol., 2001.

WAREHOUSE LOCATION DETERMINATION FOR HUMANITARIAN RELIEF DISTRIBUTION IN NEPAL

Student Number: 13M51566 Name: Rajali MAHARJAN Supervisor: Shinya HANAOKA

Warehouse for storing emergency relief items has been proven to improve overall efficiency and effectiveness of disaster response while also decreasing the cost incurred in process. Apart from that, warehouses also reduce response/delivery time, problems arising in field due to unsolicited goods while overcoming failures due to uncertainty in transport modes. The ultimate goal is to build resilience and achieve better outreach of relief aid. Due to high vulnerability to disasters in Nepal, there is an alarming need for improving national resilience. Thus in an effort to suggest improvement in preparedness, this study determined appropriate number and location for placing warehouses. The results can be implemented in real life with some modifications to adjust resource availability and organizational capacity.

1 Introduction

Disasters destroy the very infrastructure of the country, affecting the social, financial, economic and physical structure of the society and can be triggered by natural, political and economic events (Whybark 2007), also evident from Nepal Earthquake 2015. The least developed countries are the ones most vulnerable to disasters (Kovacs and Spens 2007). The overarching aim of the humanitarian sector is to save lives, meet the basic needs of people and alleviate suffering (Van Wassenhove 2006), which is partly contingent on the speed of humanitarian response (Campbell et al 2008).

Over 90 percent of international relief aid is still dedicated to disaster response meaning much attention and investment has been made for immediate response with less investment for preparedness in advance. However the success and failure of disaster response activities highly depends upon the level of preparedness beforehand. Hence, focus on preparedness as emergency planning, construction of emergency operation centers, prepositioning of emergency supplies can translate to better outreach of aid and a better level of service to beneficiaries.

Among several activities which can be done to improve preparedness, this study focuses on warehousing for inventory prepositioning. In addition to merits mentioned above, warehousing also encourages cooperation and collaboration between large numbers of governmental, non-governmental, national and international organizations working in the field of disaster management in Nepal while making them wary of important factors in advance. The figure below shows details of disaster operation and role of warehouses.

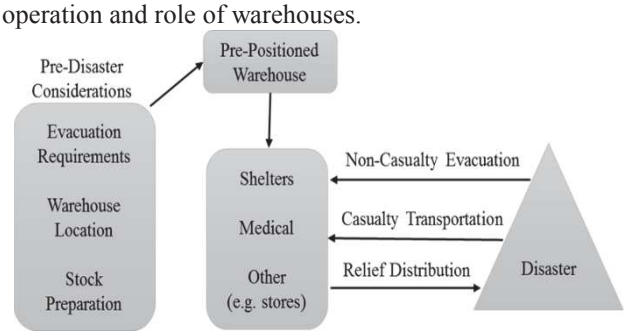

Figure 1-1: Disaster operation and role of warehouse prepositioning

Despite the importance of preparedness less has been done in Nepal in terms of inventory prepositioning. Located in the central of the Himalaya range, Nepal is prone to various types of natural disasters due to its fragile geophysical structure, very high peaks, complex geology, variable climatic condition, active tectonic processes, unplanned settlement, and weak economic and political condition.

Based upon an assumption that predetermination of optimal locations for warehousing by the concerned authorities will encourage inventory preposition, this study aims to determine the location for constructing warehouses for storage of humanitarian relief. This study has following specific objectives:

1. Determine the optimal number of warehouses for desired coverage.
2. Determine the optimal location of warehouses.
3. Perform sensitivity analysis using number of warehouses and constraints.

2. Methodology

The problem of determining optimal location and optimal number of warehouses for disaster relief distribution during immediate aftermath of disaster can be modeled as Maximum covering location problem (MCLP) with additional constraints. The model includes candidate points which can serve as a potential location for placing warehouse and the demand point which needs to be covered. In addition to coverage distance, the selection of warehouse location is also influenced by transportation accessibility, level of development and disaster safety of the respective candidate points. In facility location covering models, a source of demand is defined covered if it is located within a specified response distance or time from a facility. User accessibility in terms of response distance or time are two criterion that determines the selection of warehouse location. This study uses the notion of response distance.

Demand point selection is based on disaster mapping which is essentially the districts highly vulnerable to earthquake, flood, and landslide. Disaster mapping has been done considering return periods of 100, 50 and 25 years for earthquake, greater than and equal to ten

kilometers of land area expected to be inundated for flood, and rainfall induced and earthquake induced landslide scenarios. Union of the districts susceptible to all three disaster scenarios has been considered as demand points which counts for 55 out of 75 total districts of Nepal. Whereas all the 75 districts are eligible for candidate points, however due to lack of data only 71 districts has been considered as candidate points and 54 as demand nodes.

The study uses development index to interpret level of development, transportation accessibility index for ease of access, and disaster safety index for safety of candidate points. Human development index has been used as a proxy to represent level of development, which is essentially a measure of life expectancy, education, and per capita income indicators. Transportation accessibility index has been derived from road density data which represents abundancy of road network in each district. Three disaster scenarios; Earthquake, Landslide, and Flood has been used to come up with disaster safety index. Higher values in case of development index and transportation index means higher level of development and better ease of access and higher value for disaster safety index reflect safer locations. The selection of higher values of development index is preferred in the candidate points assuming that higher values ensures better availability of labor force and technological support which is one of the key factors for warehousing requirement. Distances between candidate points and demand nodes has been calculated using shortest path method made available by Department of Roads, Nepal. Figure 1-1, below shows the framework of methodology used in this study.

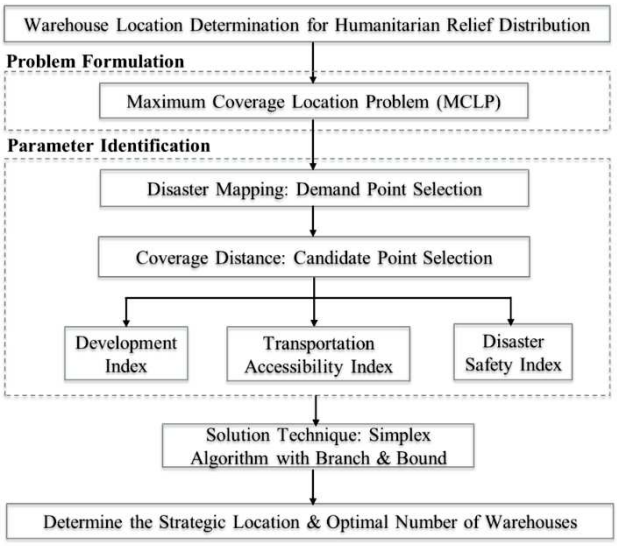

Figure 1-1: Methodology framework

Traditional MCLP formulation has been adapted to reflect the situation of Nepal by adding additional constraints (4), (5), and (6). These constraints stipulate that the individual values of transportation accessibility, development and disaster safety index of candidate points should be greater than or equal to the average minimum value to be selected as warehouse location. The mathematical formulation of MCLP is shown as:

$$\text{Maximize,} \quad Z = \sum a_i y_i \qquad (1)$$

$$\text{S.T.} \quad \sum_j x_j \geq y_i \qquad \forall i \in I \; j \in N_i \qquad (2)$$

$$\sum_j X_j \leq P \qquad j \in J \qquad (3)$$

$$\sum T_j x_j \geq N_T \sum x_j \qquad j \in J \qquad (4)$$

$$\sum V_j x_j \geq N_V \sum x_j \qquad j \in J \qquad (5)$$

$$\sum R_j x_j \geq N_R \sum x_j \qquad j \in J \qquad (6)$$

$$x_j \in \{0,1\} \qquad \forall j \in J \qquad (7)$$

$$y_i \in \{0,1\} \qquad \forall i \in I \qquad (8)$$

Where,

I = *denotes the set of demand nodes*

J = *denotes the set of warehouse locations*

a_i = *demand at a node* $i \in I$

P = *number of warehouses to locate*

$$x_j = \begin{cases} 1 & \text{if a warehouse is located at candidate site } j \in J \\ o & \text{otherwise} \end{cases}$$

$$y_i = \begin{cases} 1 & \text{if demand node } i \in I \text{ is covered} \\ o & \text{otherwise} \end{cases}$$

N_T = *the minimum value for transportation accessibility index*

N_V = *the minimum value for development index*

N_R = *the minimum value for disaster safety index*

T_j = *the individual value for transportation accessibilityfor site* j

V_j = *the individual value for development for site* j

R_j = *the minimum value for disaster safety for site* j

The following figure shows the solution approach used for calculation:

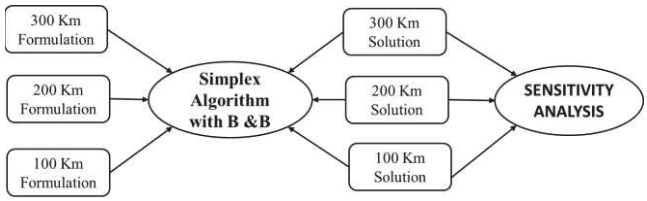

Figure 1-2: Solution approach

3. Calculation Result and Analysis

Calculations were done for three different scenarios with different coverage distances of 100 Km, 200 Km and 300 Km. Each scenario determines the maximum coverage obtained with minimum number of warehouses. In each of the scenarios, the demand points are treated as binary variables. Binary solution seeks to cover each of the

demand point at least once, multiple coverage does not improve the quality of the solution.

3.1 100 Km Scenario

The objective here is to find minimum number of warehouses for maximum coverage for 100 Km coverage distance. From the graph below we can see the coverage rates provided by varying number of warehouses. A total of 26 warehouses will be required to cover 100 percent demand. Redundant coverage will be obtained by further increasing the number of warehouses above 26. However our objective does not seek for redundant coverage. Figure 3-1, below shows the coverage rates for all three scenarios.

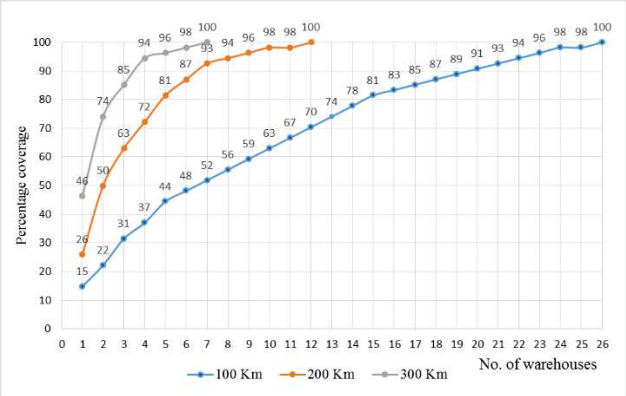

Figure 3-1: Combined coverage for 100 Km, 200 Km & 300 Km scenario

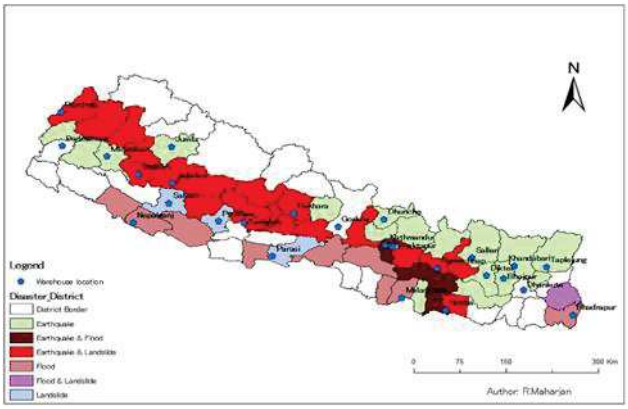

Figure 3-2: Warehouse locations for 100 Km coverage distance

3.2 200 Km Scenario

Upon increasing the coverage distance, the minimum number of warehouses required to cover all of the demand points decreases while also decreasing the service level. A minimum of 12 warehouse will be required to obtain 100 percent demand coverage when the coverage distance is 200 Km. Redundant coverage is not considered in this scenario too. Figure 3-3, shows the location of warehouses.

3.3 300 Km Scenario

When the coverage distance was further increased to 300 Km, only seven warehouses were sufficient to cover 54 demand nodes. The graph below shows the coverage rates and map shows the spatial distribution of warehouse locations.

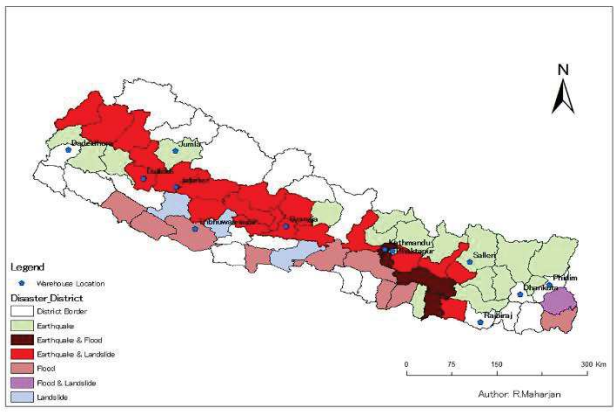

Figure 3-3: Warehouse locations for 200 Km coverage distance

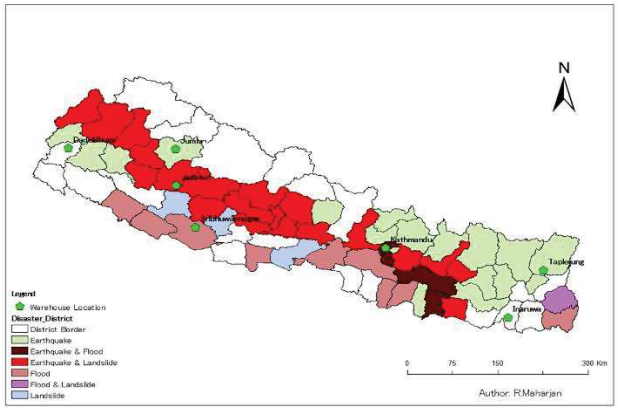

Figure 3-4: Warehouse locations for 300 Km coverage distance

3.4 Demand distribution

This section shows the details of demand allocation of different districts to warehouses for 300 Km scenario. As the warehouse are considered incapacitated, demand distribution is non-uniform, hence some warehouses are subjected to large number of demand points whereas others to very few. The figures below shows the details of demand nodes allocated to each warehouse.

Location	Dadheldh	Dang	Jajarkot	Jumla	Kathmandu	Sunsari	Taplejung
Numbers	7	11	1	2	15	15	3
Demand Nodes	Achham	Chitwan	Jajarkot	Dailekh	Baglung	Bajhang	Illam
	Baitadi	Dang		Jumla	Bhaktapur	Bhojpur	Jhapa
	Bajura	Gulmi			Dhading	Dhanusa	Taplejung
	Banke	Nawalparasi			Dolakha	Khotang	
	Bardiya	Parbat			Kaski	Mahottari	
	Darchula	Pyuthan			Kathmandu	Makwanpur	
	Doti	Rolpa			Kavrepalanchok	Okhaldhunga	
		Rukum			Lalitpur	Rautahat	
		Rupandehi			Lamjung	Sankhuwasabha	
		Salyan			Myagdi	Sarlahi	
		Syangja			Nuwakot	Sindhuli	
					Ramechhap	Siraha	
					Rasuwa	Solukhumbu	
					Sindhupalchok	Tarhathum	
					Tanahu	Udayapur	

Figure 3-5: Demand node allocation for 300 Km scenario

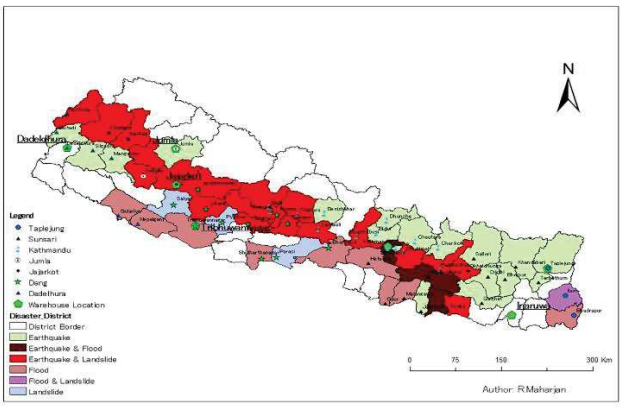

Figure 3-6: Spatial diagram for demand allocation to warehouses for 300 Km scenario

3.5 Sensitivity Analysis

Sensitivity analysis has been done to understand how the change in number of warehouses and values of constraints will affect overall coverage provided by combination of facilities. Figure 3-7, below shows the impact of changing number of warehouses to four and to one. Demand point coverage decreases drastically for 200 Km and 100 Km scenario when the warehouse numbers were decreased, apparently due to smaller coverage distance. Warehouse location in Bhaktapur was found to be important when the number of warehouse was limited to one in all three scenarios, as it was common to all three solutions.

Sensitivity analysis was also done to see the impact of each values, however there was no significant decrease in coverage until these values were raised as high as 60 percent. Thus only the output of three constraint value change has been included which is shown in figure 3-8. Coverage rates seemed to decrease with increase in minimum required values of constraints.

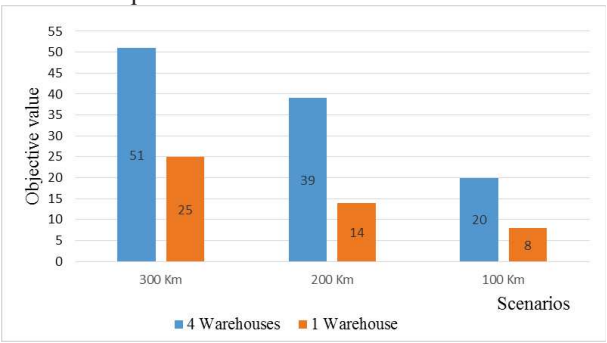

Figure 3-7: Impact of changing no. of warehouses for 300 Km

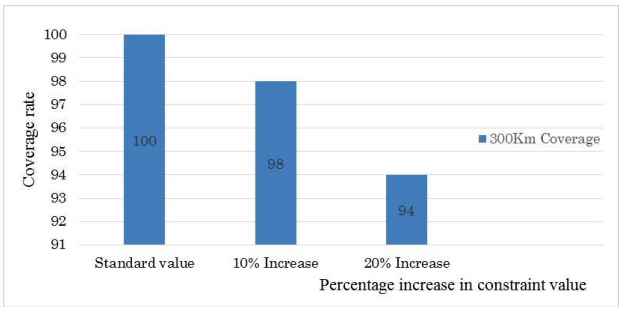

Figure 3-8: Change in coverage due to change in constraints for 300 Km

3.6 Discussion

The importance of warehousing in Nepal can be explained in relation to recent Earthquake in April 2015. 15 out of 75 districts suffered huge damages due to this disaster and to my surprise these districts were already known to be susceptible to disasters from the studies conducted earlier. 14 of these districts are among the 54 demand nodes which have been considered for this study. Warehouses were established in the form of Mobile Storage Units in various locations to provide relief items to victims. However less had been done to prepare for immediate response causing delay in response which could have been avoided while increasing its efficiency and effectiveness with earlier warehousing efforts.

Nepal is also home to hundreds of NGOs and INGOs working in the field of disaster management. These organizations have their own warehousing and stock prepositioning strategies. Nevertheless, lack of coordination and cooperation between government and aid organization has been identified as one of the major bottleneck. Government of Nepal can make use of their abundant presence and willingness to help by determining appropriate locations for placing warehouses and encouraging consolidation of their efforts. This study provides several alternative options to choose from for selecting appropriate location. Thus we believe implementation of this kind of study with some modifications to meet and reflect the needs on ground will definitely improve national resilience against future disasters.

4. Conclusion

This study determined various combination of warehouse numbers coverage provided by each and their respective location taking into consideration geographical features, level of development and disaster safety which is very unique to Nepal. Three different scenarios were considered to take into account appropriate response distance and also to weigh the pros and cons of having larger number of warehouses versus larger coverage distance. The overarching aim is to reduce overall response time and associated uncertainty arising due to disaster therefore alleviating impacts of disasters to affected people.

References

Balcik, B. and Beamon, B.M. (2008) "Facility location in humanitarian relief", *International Journal of Logistics: Research and Application,* Vol. 126, no. 2, pp. 101-121.

Basdemir, M.M. (2004) "Locating search and rescue stations in the Aegean and western Mediterranean regions of Turkey", *Journal of Aeronautics and Space Technologies,* vol. 1 no. 3 (63-76)

Church, R. and Revelle, C. (1974) "The maximal covering location problem", *Papers of the Regional Science Association, Vol.32, pp 101-118.*

Rawls, C.G. and Turnquist, M.A. (2010) "Prepositioning emergency supplies for disaster response", *Transportation Research Part B: Methodological,* vol. 44, no. 4, pp. 521-534.

Klose, A. and Drexl, A. (2005) "Facility location models for distribution system design", *European Journal of Operational Research,* vol. 162, no. 1, pp. 4-29.

DEVELOPMENT OF CHANNEL SOUNDER PROTOTYPE FOR OUTDOOR DISTRIBUTED WIRELESS NETWORKS

Student Number: 13M51572 Name: Tossaporn Srisooksai Supervisor: Jun-ichi Takada

Abstract

Although, the traditional channel sounders were successfully utilized by existing works to measure and develop the correlation model for indoor distributed channels in distributed wireless networks (DWNs), it is difficult to implement such a system in large scale of outdoor distributed measurement which requires the numerous transmitter and receiver nodes. Therefore, the well-suited channel sounder prototype for the outdoor DWNs is developed by adopting the standalone system of the open source USRP hardware. The time-grid acquisition of received signal is implemented in order to overcome the drawback of the limited data rate within USRP in this work. By this solution, the data rate can be successfully reduced to 1/8 without sacrificing the accuracy of the channel characteristics. To extend the developed system for distributed measurement, the framework of the synchronization and the protocol of communication among nodes for obtaining the correlation in the distributed channels in large scale of outdoor distributed measurement is pointed out and proposed.

1 Introduction

Recently, distributed wireless networks (DWNs) are considered as an alternative for the next generation wireless networks. While each communication in the centralized wireless networks, e.g. mobile network, is controlled by the base station, the devices are able to communicate each other independently in DWNs. This improves the robustness of the network, since each device has more than a communication link. Especially, in an emerging wireless application such as disaster network, it strongly requires the robustness operation during earthquake, tsunami or fire.

To maximize the robustness of such DWNs, the cooperative distributed algorithms are essential in which knowing the correlation model of the distributed channels is required. Without such information, the algorithms can only be investigated using the model-based mathematical assumptions which can not be guaranteed in some real scenarios. The example of such a issue is pointed out in [1], in which the probability of path failure in multi-hop wireless network, which is one of DWN scenarios, is considered. Although, in such case, independent and identically distributed (i.i.d.) log-normal shadowing is typically assumed as a simple and mathematically tractable model for evaluation, they found that it is not the suitable model for such scenario when comparing with the correlated shadowing model extracted from the real measurement. This raises the importance of the correlation channel model and the measurement approach in DWNs. However, the existing testbeds for DWNs, e.g. in [2], aim to measure the network performance, e.g. bits/second, rather than the wireless channel parameters which are necessary in developing the accurate complex correlation model. In addition, the existing testbeds depend on the commercial devices and drivers of IEEE802.11 (WLAN). This causes the difficulty in customizing such testbeds for measuring the correlation behavior of DWNs. In contrast to those testbeds, the channel sounder is more flexible. The study in [3] showed that the channel sounder could be utilized to measure and develop the correlation model for indoor distributed channels. However, to measure the wireless channels in large scale of outdoor DWNs, it requires the numerous transmitter (Tx) and receiver (Rx) nodes. In such condition, it is difficult to implement the traditional channel sounder because it lacks of portability and also requires big amount of cost.

Therefore, the objective of this research is to develop the channel sounder prototype which is able to capture the correlation behavior of the distributed wireless channels and to be customized flexibly for different kinds of the outdoor DWN measurements which commonly require the small and portable channel sounders and the scalable deployment in large scale area. Although, the wireless sensor devices were developed for the outdoor distributed measurement in [1], such devices are able to measure only the received signal strength (RSS) which cannot be used to determine the small scale fading or multipath fading of the distributed channels. The authors in [4] pointed out that knowing the exact model of small scale fading is essential when considering the partner selection algorithm of cooperative wireless sensor networks since each small scale fading model has the different effect to the evaluation of the error probability over the wireless channel. This error probability significant impacts to the efficiency of the partner assignment algorithms. Therefore, our proposed channel sounder which is able to measure the small scale fading, can be implemented to eliminate such a limitation.

1.1 Design consideration

1.1.1 Channel estimation by channel sounder

To estimate the channel parameters, the transmitter (Tx) part of channel sounder sends the signal through the environment which consists of several scatterers to the receiver (Rx) part. Then, the channel characteristics can be estimated by performing the signal processing on the received and transmitted signal. The trans-

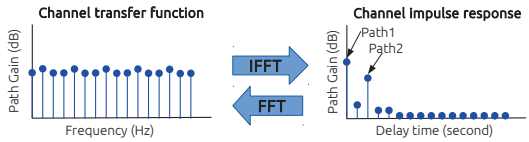

Figure 1: Channel parameters for the example of two path channel

mitted signal in this work is the unmodulated complex Newman phase multitone (NPM) signal same as [5]. This NPM signal is periodic for every t_p which is referred as *a symbol duration*.

Fig. 1 illustrates two channel characteristics which are channel transfer function (TF) and channel impulse response (CIR) corresponding to the simple environment which consists only a scatterer and two paths of signal. The path gain fluctuation due to multipath interference which is usually called small scale fading can be observed in this figure. Please note that CIR can be obtained by taking inverse fast fourier transform (IFFT) on TF. In real environments, the multipath is not the only source of fading. If there are any objects such as buildings or trees along the path of the signal, some part of the transmitted signal is lost through absorption, reflection, scattering, and diffraction. This effect is called shadowing fading. These channel transfer function and impulse response can be analyzed further by varying the distance between Tx and Rx. It is simply called distance-path loss relation. Furthermore, in distributed channels, each of these major effects may not be independent. The measurement results in [1] reveal that there exists the correlation between shadowing fading of the various communication links over distributed space. The correlation among these major effects are also possible, e.g. the correlation between path loss and small scale fading observed in [3].

1.1.2 Proposed channel sounder and design issue

In this study, the large scale of outdoor distributed measurement as shown in Fig. 2 is considered. A channel sounder is represented as a single node which consists a Tx and a Rx. Each node is be able to communicate with other nodes located in its coverage area. The proposed channel sounder is designed based on the software defined radio (SDR) platform. The open source SDR called universal software radio peripheral (USRP) is selected as the main tool because of the flexibility in customization.

With the characteristic of DWNs, each sounder or node has to be a portable and compact one. The E1x0 model which is the embedded series of USRP produced by Ettus Research Inc is suitable. The block diagram of each node based on such a device is shown in Fig. 3. In Tx flow, the transmitted signals is generated in embedded computer board or host and is sent from host to field-programmable gate array (FPGA) though 4 MS/s data bus. The interpolation unit (Interp) is responsible for interpolating the signal to the sample rate of 32 MS/s which is further interpolated by digital up con-

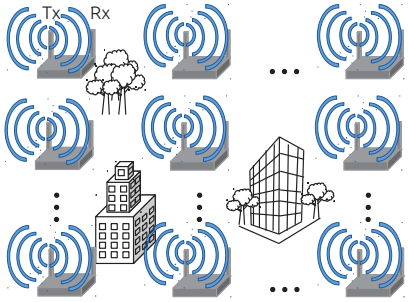

Figure 2: Outdoor distributed measurement in large scale

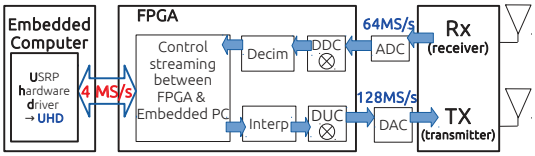

Figure 3: Block diagram of each node of proposed channel sounder

verter (DUC) unit by a factor of four to the digital to analog converter (DAC) rate of 128MS/s. Please note that the Interp unit is realized by FPGA implementation, however the DUC unit is realized by AD9862 mixed-signal front-end processor. Then, the signal is transmitted over wireless channel by radio frequency (RF) daughter board. In Rx flow, the digital down converter (DDC) and decimation unit (Decim) are responsible for decimating the signal obtained from analog to digital converter (ADC) from the rate of 64 MS/s to the rate which is lower than or equal 4 MS/s in order to be able to sent it to the host.

Regarding the proposed architecture, it is obvious that the measurement bandwidth is limited by the data transfer rate from the host to FPGA (4 MS/s) and vise versa. According to the sampling theorem, this channel sounder would have only 2 MHz bandwidth which is small comparing to 22 MHz bandwidth of IEEE802.11a/b/g. The solutions for this hardware limitation and its validation result are presented in Sect. 2. While the hardware issue is considered for individual channel sounder, the synchronization and protocol of communication among nodes for obtaining the possible correlation in the distributed channels are considered and proposed for extending this proposed system for the distributed measurement in Sect. 3.

2 Hardware implementation and validation

2.1 Hardware implementation

By considering the specification of Tx and Rx in this system at center frequency (f_c) 2.45 GHz, it is able to capture CIR's maximum signal delay duration (τ_{max}) at 5.8 μs. Thus, in this work, t_p of the NPM signal is

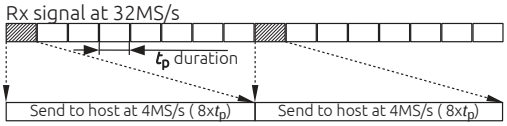

Figure 4: Time-grid of received signal acquisition

designed at 8 μs which is greater than $\tau_{\max}$ in order to capture all the delay paths. The simple way to solve the limitation of data rate in Tx flow is to store one period with length of t_{p} of NPM signal into FPGA and transmit it out repeatedly. In such case, based on the fixed interpolation rate which is four of the AD9862 chip, the maximum sampling rate of transmitted signal is 32 MS/s or maximum 16 MHz bandwidth when considering the sampling theorem. In Rx flow, since the sampling rate of transmitted signal is 32 MS/s, the sampling of received signal is also 32 MS/s, consequentially. Sending such a sample rate to the host through 4 MS/s data bus, time-grid of received signal acquisition concept is applied as depicted in Fig. 4. This acquisition concept is introduced for solving the storage issue of received signal in developing the MIMO channel sounder for 11 GHz [5], while in this work, this scheme is modified for solving the data rate limitation. As shown in the figure, only one t_{p} period in every $8 \times t_{\mathrm{p}}$ of the full received signal at 32 MHz sampling rate is transfered to host. This does not sacrifice the accuracy of the channel characteristics, since $8 \times t_{\mathrm{p}} = 64\,\mu$s is lower than $\frac{1}{2f_{\mathrm{d}}} = 5\ m$s, where f_{d} is maximum doppler frequency and the doppler shift when scattering objects are in motion is considered as static in such a period. Then, the solutions for both transmitter and receiver paths are realized by modifying the FPGA of E1x0 device.

2.2 System validation

To verify the system validation after implementing the concept presented in Sect. 2.1 and after applying several calibrations, the measurement results of the proposed system in real wireless channel of indoor environment are compared with the results of commercial vector network analyzer (VNA). The measurement is conducted in the experiment room of Takada laboratory in Tokyo Institution of Technology, where several tables, laboratory equipments, computers and metallic shelves exist. The distance between Tx and Rx is 3 m. Radio wave absorber is placed between Tx and Rx to avoid clear line of sight (LOS) path. The antennas used in this measurement are omni-directional vertical antennas at 3dBi Gain. The height of both Tx and Rx antennas is 0.34 m. The center frequency and bandwidth are set at 2.45 GHz and 16 MHz, respectively. In the case of channel sounder measurement, the first E1x0 is set as Tx and the second one is set as Rx. The result is shown in Fig. 5. There is the good agreement between VNA and the proposed channel sounder.

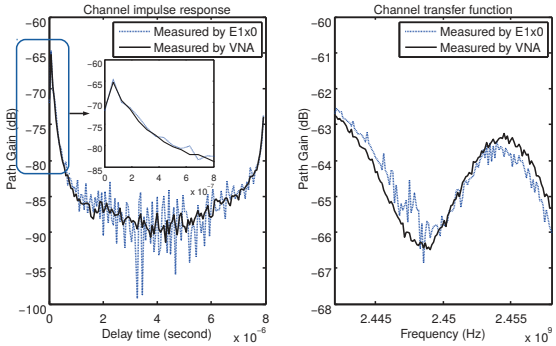

Figure 5: Indoor measurement result

Table 1: Comparison of the reference clocks

Reference Clock	OCXO	Rubidium	Cesium	GPSDO
Short-term stability (Avg. time = 1 s.)	1×10^{-11}	2×10^{-11}	5×10^{-12}	1×10^{-11}
Accuracy	5×10^{-8}	5×10^{-11}	5×10^{-13}	1×10^{-12}
Size (cm^3)	1.5×2.8×1	9×21×33	13×42×52	2×4×1
Weight (kg.)	0.09	4	30	0.1
Cost (JPY)	lowest	330k	highest	96k

3 Extending the System for distributed measurement

In this section, the framework of extending the proposed channel sounder for DWNs are constructed.

3.1 Distributed synchronization

All the system clocks in the proposed channel sounder are generated from 10 MHz signal of the reference clock. To obtain the accurate estimation of the absolute signal delay and the channel transfer function, it requires the precise time and frequency synchronization. This can be simply realized by using a highly stable atomic oscillator as reference clock and sharing it by wired connection. Since, this system is designed for large scale measurement, it is obvious that the wireless sharing is essential. Considering the existing references in Table 1, the easiest way to synchronize the start time (t_0) to obtain the accurate absolute signal delay without wired connection is to utilize the global positioning system disciplined oscillator (GPSDO) which can provide the global time and pulse-per-second signal to each channel sounder. Although, the main drawback of GPSDO is that the GPS signal is easily shadowed by the obstacles, other advantages of GPSDO which are the low cost device, low weight and portable size make it is feasible to implement in large scale (Table 1).

Another important point, frequency accuracy of each reference type is related to the frequency offset between Tx and Rx which causes the long-term phase drift, thus limiting the estimation accuracy of absolute signal delay. In case of GPSDO, the frequency accuracy f_{a} is in order of 10^{-12}. If the carrier frequency f_{c} of proposed channel sounder is 2.45 GHz, the maximum phase drift in a second is $2\pi f_{\mathrm{c}} f_{\mathrm{a}} = 0.015$ radian which can be negligible as analyzed in [6].

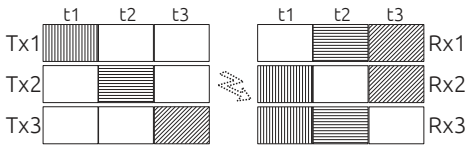

(a) Mode 1

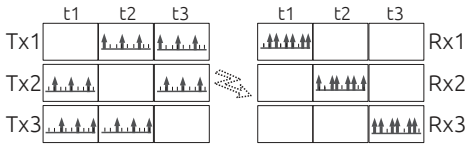

(b) Mode 2

Figure 6: Distributed measurement protocol

3.2 Distributed correlation measurement protocol

The main objective of the proposed channel sounder is to capture the correlation behavior of the distributed wireless channels. Therefore, it needs the protocol of communication among nodes for obtaining the possible correlation in the distributed channels. There are two importance insights which should be taken into account when considering such a protocol. The existing works in [1, 3] reveal the first insight that any links between the nodes which have either a common Tx or common Rx or both shows the high value of correlation coefficients. The second insight, as pointed out in [7], is that the multi-link propagation issues in some scenarios arise because they suffer from both distributed correlation propagation channels and interference among various links.

Therefore, the measurement protocol in this work consists of two modes. It is able to measure all common Tx/Rx link pairs regarding the first insight and aims to identify the impact of interference to the correlation level in the propagation channels regarding the second insight. The first mode can be realized by utilizing the time-division multiplexing (TDM) scheme as shown in Fig. 6(a) which is the example of conducting the distributed measurement by using three channel sounders, each has a Tx and a Rx. The link pairs which have a common Tx in this mode can be measured simultaneously. For instance, the Tx1-Rx2 link and Tx1-Rx3 link are measured at the time slot t_1. In contrast, the link pairs which have a common Rx cannot be measured simultaneously, e.g. Tx2-Rx1 link at t_2 and Tx3-Rx1 at t_3. However, the good point of this mode is that the interference impact can be eliminated. The second mode shows as Fig. 6(b) is done by implementing the the multi-tone frequency-division multiplexing (MTFDM) [8] in TDM manner. In this mode, the link pairs which have a common Rx can be now measured simultaneously, e.g. Tx2-Rx1 link and Tx3-Rx1 at t_1. With relying on FDM, the interference may impact the propagation channel in the second mode. However, by comparing the correlation result between the first and second modes may give some insights for identifying the difference mechanisms between the interference and correlation impact.

4 Conclusion

This research proposes the channel sounder system which is able to solve the limitations of the existing distributed measurement systems for large scale of outdoor environment. The validation in laboratory environment in term of hardware implementation is already evaluated. However, it still needs more validation in terms of wireless synchronization and measurement protocol in outdoor environments. Once all the processes are completed, this proposed system will be one of the facilitators in identifying and modeling the correlation mechanisms of outdoor distributed channels in future work in order to enhance the robustness of the distributed wireless application.

References

[1] P. Agrawal and N. Patwari, "Correlated Link Shadow Fading in Multihop Wireless Networks," *IEEE Transactions on Wireless Communications*, vol. 8, no. 8, pp. 4024–4036, August 2009.

[2] J. Lee, S.-J. Lee, W. Kim, D. Jo, T. Kwon, and Y. Choi, "Understanding Interference and Carrier Sensing in Wireless Mesh Networks," *IEEE Communications Magazine*, vol. 47, no. 7, pp. 102–109, July 2009.

[3] C. Oestges, N. Czink, B. Bandemer, P. Castiglione, F. Kaltenberger, and A. Paulraj, "Experimental Characterization and Modeling of Outdoor-to-Indoor and Indoor-to-Indoor Distributed Channels," *IEEE Transactions onVehicular Technology*, vol. 59, no. 5, pp. 2253–2265, Jun 2010.

[4] P. Castiglione, S. Savazzi, M. Nicoli, and T. Zemen, "Impact of Fading Statistics on Partner Selection in Indoor-to-Outdoor Cooperative Networks," in *IEEE ICC proceeding*, May 2010.

[5] Y. Konishi, Y. Chang, M. Kim, and J. Takada, "Versatile Radio Channel Sounder for Double Directional and Multi-link MIMO Channel Measurements at 11 GHz," *IEICE TRANSACTIONS on Electronics*, vol. E97-C, no. 10, pp. 994–1004, 2014.

[6] M. Lin and I. Wassel, "Impact of Channel Sounder Frequency Offset on the Estimation of Channel Parameters," in *Proc. IEEE 64th Vehicular Tech. Conf. (VTC-2006 Fall)*, September 2006.

[7] C. Oestges, "Multi-Link Propagation Modeling for Beyond Next Generation Wireless," in *Loughborough Antennas and Propagation Conference (LAPC)*, November 2011.

[8] K. Sakaguchi, J. Takada, and K. Araki, "A Novel Architecture for MIMO Spatio-Temporal Channel Sounder," *IEICE TRANSACTIONS on Electronics*, vol. E85-C, no. 3, pp. 435–441, 2002.

11 GHz Urban Microcell Radio Channel Estimation Using SAGE Algorithm

Student ID: 13M51589 Name: Xu Chao Supervisor: Jun-ichi TAKADA

With the growing demand for higher data rate of radio channel, higher frequency spectrum and MIMO system are preferred to be utilized since they can improve the capacity and data rate of system. However, the performance of MIMO system depends on radio channel conditions. Therefore, considering about system design and antenna selection, we must characterize radio channel to get the best performance of MIMO system. Here we estimate channel behavior of 11 GHz urban microcell radio channel by parametric modeling of wide-band double-directional measurement data which was measured by building an 11 GHz 24x24 MIMO channel sounder with 400 MHz, and conducting massive outdoor measurement campaigns.

1. Introduction

In 21st century, wireless communication has attracted more and more attention because it plays an important role in providing services for both social and personal requirement. In next decade, It is a trend that the number of users connected into networks is increasing, and the demand for high data rate for cellular networks is growing. Since the frequencies in the lower microwave range (below 5GHz) has been used for current mobile communication while higher frequencies remain unused. Therefore, the utilization of high frequency spectrum in microcell has a large potential in increasing data rate since wider bandwidth can be guaranteed. In addition, a method called multiple-input and multiple-output (MIMO) for multiplying the capacity of a radio link using multiple transmit and receive antennas to exploit multi-path propagation has become an essential element of wireless communication standards including IEEE 802.11n (Wi-Fi), IEEE 802.11ac (Wi-Fi), HSPA+ (3G), WiMAX (4G), and Long Term Evolution (4G).

However, these spectral efficiency gain often requires an accurate knowledge of the channel at the receiver or at the transmitter, sometimes at both side. Our challenge is that the channel properties at low frequency has been studied, but for high frequency (especially in the outdoor environment), they are not clear in the current studies. Therefore, it is necessary to characterize radio channel at higher frequency spectrum.

To characterize radio channel, 11 GHz 24x24 MIMO channel sounder with 400 MHz bandwidth has been built, and massive indoor and outdoor measurement campaigns are conducted[1]. And a kind of high resolution parameter estimation technique known as space alternating generalized expectation maximization (SAGE) has been applied to the process of these measurement data. And after getting the results parameters from SAGE, utilize some factors and estimation method to process these results in order to characterize wide-band double-directional channels. these parameters can be utilized to reconstruct transfer function (TF), and the method of antenna selection based of TF has been introduced in [2]. And from the characteristics of delay, direction, power, etc., some behavior in outdoor scenario at higher frequency can be studied by comparing channel conditions at high frequency and channel conditions at lower frequency studied in [3][4]. Further more, these results can give some advices for system design.

2. Extraction of Propagation Channel Parameters

Measurement data is utilized to analyze radio channel conditions. And channel model is based on the measurement data. Before discussing the method of processing measurement data, firstly, channel model should be introduced.

Double directional channel model can be described by:

$$H_{\mathrm{MIMO}}(f)=\sum_{l=1}^{L}\mathbf{a}_{\mathrm{R},l}(\varphi_{\mathrm{R},l},\theta_{\mathrm{R},l},f)\cdot\Gamma_{l}\cdot\mathbf{a}_{\mathrm{T},l}(\varphi_{\mathrm{T},l},\theta_{\mathrm{T},l},f)e^{-j2\pi f\tau_{l}} \quad (1)$$

where L is the number of paths, f is frequency, $\mathbf{a}_{\mathrm{T}}$ and $\mathbf{a}_{\mathrm{R}}$ is antenna array of transmitter and receiver respectively, $\varphi_{\mathrm{T}},\theta_{\mathrm{T}},\varphi_{\mathrm{R}},\theta_{\mathrm{R}}$ denote the azimuth and co-elevation at transmitter side called Direction of Departure (DoD) and receiver side called Direction of Arrival (DoA), τ is time delay, and Γ includes four kinds of polarization complex path gain. A propagation channel can be character-

ized by nine parameters, i.e. DoD, DoA, time delay, and polarization complex path gain.

SAGE[5] is a kind of channel parameter estimation algorithm. It is based on Maximum Likelihood Estimation (MLE). The basic idea of MLE is to find parameters that maximum the likelihood function. Basing on MLE, SAGE is divided into two steps to achieve lower complexity: Expectation step (E-step) which is to decompose data into different signal components and Maximization step (M-step) which is to search for parameters.

3. Verification of SAGE with Indoor Measurement data

Our main task is to analyze microcell radio channel measurement data. Firstly, to verify SAGE algorithm, we would like to process measurement data measured in indoor scenario where all of the snapshots are Line of Sight (LoS) and the moving directions of Mobile Station are not changeable.

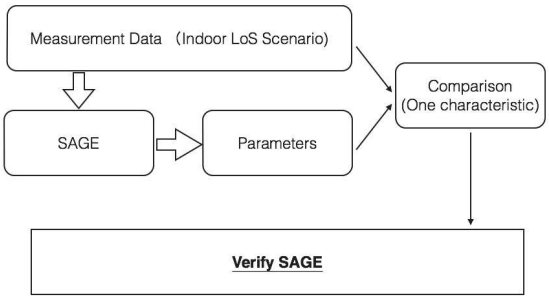

Figure1. The concept of SAGE verification

3.1 Measurement campaign

The measurement was conducted in collaboration room of West-9 Hall of Tokyo Tech. Tx which can also be seen as MS (Mobile Station) is moving while Rx which can also be seen as BS (Base Station) is fixed. It is 24×24 MIMO system, and both transmitter and receiver are Uniform Circular Array with height of 170cm. Some system parameters can be seen as the following table.

Center frequency	11 GHz
Signal bandwidth	400 MHz
Tx power per antenna	10 mW
No. of multitones	2048
Tone separation	195 kHz

Table 1. System parameters

After getting the transfer function of each individual frequency by measurement, we can input the measurement data with initial parameters into SAGE, and get parameters for every path.

3.2 Path loss characteristics comparison

Here we choose path loss characteristic to test the results of SAGE, because it is a fundamental channel characteristic which explains how the average power level changes when the distance between transmitter and receiver is increased. It is of most importance in any wireless communication systems as it determines the coverage of the radio signal in the given environment with assigned transmitted power and signal-to-noise ratio (SNR) requirement at the receiver.

To make comparison, we must calculate path loss from measurement and SAGE results respectively. And the following figures are the results.

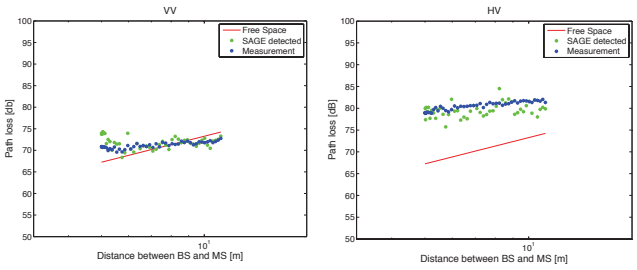

Figure 2 Path loss comparison

We choose VV-polarization as the example for co-polarization case and HV-polarization as the example for cross-polarization case. Form the results, we can see that co-polarization contributes most of the path weight of one snapshot, and the path loss calculated from measurement data directly and that from SAGE results of both cases match well, especially for co-polarization case. Therefore, SAGE algorithm is believed to be applicable.

4. Analysis of Urban Radio Channel Measurement

After verifying SAGE, we can analyze propagation channel conditions based on measurement data conducted by channel sounder in outdoor scenario.

4.1 Measurement campaign

The measurement was conducted along the streets of Ishigaki city. Figure 3 shows the map of measurement. Tx which can also be seen as MS (Mobile Station) is moving along the Tx route with red color, while Rx which can also be seen as BS

(Base Station) is fixed on the Rx position with blue color.

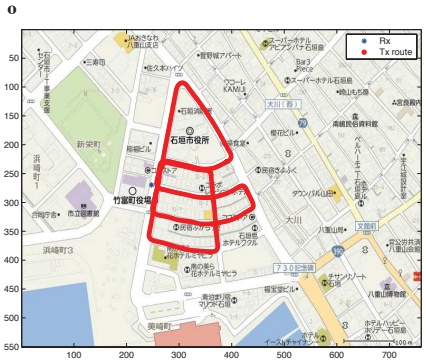

Figure 3. Transmitter route of measurement

Tx is located on a moving car. and the maximum speed is 10km/h. The height of Tx is 3m and the definition of 0° at transmitter side is the moving direction, while the height of Rx is 2.5m and the definition of 0° at receiver side is 75° North by East. Both array response of transmitter and receiver are UCA. But one of the AD board is broken, so it is 12V12H×12V10H MIMIO system. System parameters are same with table 1, and measurement parameters are shown as the following table.

Antenna gain	7 dbi
Delay resolution	2.5 ns
No. of Snapshots	800

Table 2. Measurement parameters

By checking residual power combined with average path gain of each snapshots. there are four parts of snapshots that can be analyzed by applying their data into SAGE. Based on the transmitter route and their positions, we can divide all of these snapshots into two course which are shown in the following figures.

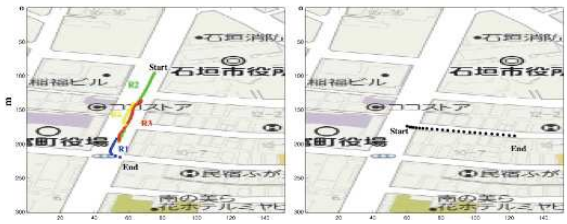

Figure 4. Two transmitter courses

The residual power of all snapshots is under 30% and the total number is 111, and all are LoS snapshots.

4.2 Data Analysis

By utilizing SAGE, we can get direction, delay, and path weight parameters of each path. To make these parameters meaningful for channel estimation, our next step is to analyze them by some factors.

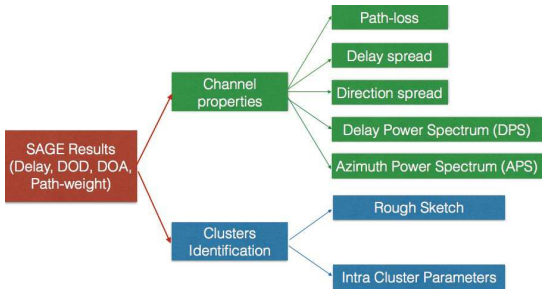

Figure 5. Data analysis process

Here the process has been divided into two parts as shown in figure 5. One is some characteristics that can be calculated by results directly, the other one is clusters identification that must be analyzed combining with other proper methods.

4.2.1 Characteristics of Radio Channel

1. Path loss and polarization characteristics:

Path loss has been mentioned above. And the path loss model we will use in this analysis is distance dependence with linear fitting in dB scale.

And an important parameter that characterizes the channel polarization is the cross-polarization power ratio (XPR) which indicates the power ratios of co-polarization to cross-polarization for vertical and horizontal polarization. Similarly, the co-polarization power ratio (CPR) which indicates the power ratio of the vertical polarization (VV) to the horizontal polarization (HH).

Results: By comparing the results with those in lower frequency, linear fitting path loss results are lager. In case of XPR, it is smaller comparing with a typical factor of 10~30 dB. One of the reasons may be the some small errors of SAGE, On the other hand, the high frequency spectrum require large polarization diversity of antennas.

2. Delay spread:

Delay spread is one indicator of the multi-path richness of the radio channel. It can present the spread of paths in terms of time domain.

Results: Delay spread is 4~33ns which is smaller comparing with 38/50 ns in case of 2GHz and 22~88 ns in case of 5.3 GHz. And The largest delay spread appear around the snapshot which obtains the longest distance from BS.

3. Direction spread:

We describe a direction as a unit vector Ω (calculation coordinate) which the initial point at O and the terminal point is located on a sphere and only consider azimuth.

Results: The direction at MS is more distributed than that of BS. The reason is that the azimuth of departure ranges among all directions while the azimuth of arrival is limited by the measurement courses. In addition, we can also find that direction spread is quite large, so we need further analysis by power spectrum.

4. Delay power spectrum and azimuth power spectrum

The delay power spectrum (DPS) and azimuth power spectrum (APS) can be calculated based on azimuth-beam forming.

Results: From the results of DPS, We can find that SAGE detected most of dominant paths successfully. And by plotting APS, we can find the direction of LoS component. For other NLoS components, so we detect them by clustering.

4.2.1 Identification of clusters

Visual clustering has been used for a long time, but visual identification of clusters contains a certain level of uncertainly and interpretation, also very difficult to deal with huge amount of data. So the clustering algorithm will be used here is K-Power Means (KPM) clustering.

The basic concept of K-Means clustering is "*Clusters are chosen such that they minimize the total distance from their centroids*". Different from K-Means algorithm, KPM also includes the influence of power to make clustering result more reliable.

We also we analyzed the delay spread and direction spread intra clusters.

Results: From the clustering results, here we can choose some of the main clusters of one snapshots to draw a rough sketch of clusters combining with map.

Intra-cluster delay spread is from 0 to 18 ns and more that 90% are under 4 ns which means that the delay has been well detected by clustering. Intra-cluster direction spreads of AoA and AoD are almost same. It reduces a lot compared with the direction spread among all the individual paths but still a little bit large. The reason may be that The effects of the scattering of rays from the rough surface of building walls and small objects are more dominant in the higher frequency.

5. Conclusion

Finally, the comparison results can be seen as the following table.

	Low Frequency (2 GHz)[3]	Low Frequency (5.3 GHz)[4]	High Frequency (11 GHz)	Comparison (for higher frequency)
Microcell radius	150 m	200 m	150 m	×
Path loss	a=2.2 b=34.0 ※Based on model in [6]	a=2.2 b=42.5 ※Based on model in [6]	a=2.42 b=48.9/53.2	Larger
Delay spread	38/50ns	22-88 ns	4-33 ns	Smaller
Direction spread	Angular ranges within 40°	Angular ranges within 40°	Angular ranges within 60°-70°	larger

Table 3. Comparison Results

The most important contributions of this thesis can be summarized below:

- At high frequency spectrum, radio channel parameters can be extracted by SAGE algorithm from data measured by channel sounder, and we can estimate these parameters by comparing characteristics of path loss, delay spread and direction spread with those of lower frequency spectrum.
- For path loss, it is larger than the path loss at lower frequency.
- For delay spread, it is smaller than the delay spread at lower frequency. This results can be used for designing the guard intervals of OFDM based system.
- For direction spread, it is quite larger than the direction spread at lower frequency. This results can be used for designing the antenna pattern in the system.
- The main scatters are building walls in this scenario, and for all snapshots, there are 11~17 main clusters can be detected by KPM clustering algorithm.

References

[1] M. Kim, J. Takada, and Y. Konishi, "Novel Scalable MIMO Channel Sounding Technique and Measurement Accuracy Evaluation with Transceiver Impairments," IEEE Trans. Instrum. Meas., vol. 61, no. 12, Dec. 2012.

[2] Molisch, Andreas E. "MIMO systems with antenna selection-an overview." *Radio and Wireless Conference, 2003. RAWCON'03. Proceedings*. IEEE, 2003.

[3] Saito, Kazuyuki, Tetsuro Imai, and Yukihiko Okumura. "2 GHz Band MIMO Channel Properties in Urban Small Cell Scenario in Crowded Area." *Vehicular Technology Conference (VTC Fall), 2014 IEEE 80th*. IEEE, 2014.

[4] Zhao, Xiongwen, et al. "Propagation characteristics for wideband outdoor mobile communications at 5.3 GHz." *Selected Areas in Communications, IEEE Journal on* 20.3 (2002): 507-514.

[5] Pham Van Hue, Radio Channel Parameters Estimation Using SAGE Algorithm, Master thesis, International Development Engineering, Tokyo Institute of Technology, Mar, 2014

[6] Series, M. "Guidelines for evaluation of radio interface technologies for IMT-Advanced." *Report ITU* (2009): 2135-1.

Factors influencing time series electricity consumption trend at TokyoTech campus

Student Number: 13M51514 Name: Yuji HIRAI Supervisor: Naoya ABE

東工大における時系列電力消費量の変動要因

平井雄之

本論文では東工大における電力消費量変動を過去５年間の時系列データを分析し、変動の生じた時期、変動の大きさ、継続性を建物毎での電力消費量変動の寄与に着目し実態把握を行った。その結果、電力消費量変動傾向は主に大量の電力を消費している情報棟、本館、南９号館の寄与により生じており、その変動要因は気温変動と高効率機器の導入によったものであると推察された。

1. Introduction

1.1 Electricity consumption and universities

Realizing higher level of energy saving is one of the most important challenges for achieving sustainable society. In Japan energy consumption in commercial sector is increasing markedly and account for 32.5%. Approximately 70% of energy consumed in commercial sector is caused by electricity consumption. Therefore electricity saving in commercial sector is one of urgent issues.

Tokyo Tech, which electricity consumption is regarded as a part of commercial sector consumption, is a research university that consumes the electricity as much as 17,000 households do every year, meaning that its consumption patterns and quantity could draw more public attentions. Indeed both central government and Tokyo metropolitan government enacted various laws to regulate companies, offices and organizations to reduce electricity consumption for the sake of environmental conservation. In this regard, Tokyo Tech is obligated to reduce 1% of electricity consumption every year in accordance of the laws, the Energy Conservation Act by the central government and the Tokyo Metropolitan Environmental Security Ordinance. According to the regulations, Tokyo Tech was required to propose its electricity saving policy. In the policy, Tokyo Tech committed to conduct effective electricity saving practices as long as Tokyo Tech can keep its quality of education and research activities. Under this policy, Tokyo Tech focuses on peak-cut and base-cut by monitoring and controlling electricity consumption and real-time electricity consumption visualization system or alarming system. For example they shift a part of machine operation schedule to midnight (peak-cut) and take a second look at machine operation to improve electricity use (base-cut). As a result, by the end of 2014, Tokyo Tech successfully reduced 2.2% in average in the last 8 years by promoting those electricity saving actions and installing high electricity efficient equipment [1].

However detailed electricity consumption trend over time at university setting have not been investigated well while cross-sectional consumption pattern are well reported in each university's environmental reports or alike. In order to come up with sustainable and effective actions for electricity saving over time, it is important to clarify how electricity consumption has change over time and what factors could influence the time series electricity consumption trend at university settings.

1.2 Current understandings of university electricity consumption

Electricity consumption in university is divers because of their different functions, majors, staffs, and students. In this context, each university in Japan reports their contribution to electricity saving. For example, University of Tokyo and Osaka University insists their roles as research universities to lead sustainable society through their electricity saving actions [2][3]. Kyusyu University focused on understanding current electricity consumption situation [4]. The University of Electro-Communications considers contribution to environment and reports to society is responsibility to establish reliance and openness [5]. Tokyo University of Agriculture and Technology mentions importance to reduce cost for electricity consumption to maintain quality of its academic activities toward rising electricity prices [6]. According to those reports, investigating electricity consumption data is meaningful for understanding current consumption structure to specify energy saving policy and evaluate policies in order to contribute to sustainable society and fulfill their responsibility as research institute.

Oohashi et al.(2013)[7] and So(2010)[8] investigated electricity consumption pattern at university and distinguished electricity use related to human activities and others to specify electricity use to cut. Yamahane et al.(2012)[9] and W.P.Wong[10] evaluated electricity saving actions and estimated future electricity consumption pattern and by creating the model. The review of those reports and previous articles, however, do not provide enough insights about how electricity consumption pattern change over time and what factors could influence the trend.

2. Objectives and Contribution

2.1 Objectives

Tokyo Tech also has unique electricity consumption pattern caused by different electricity consumption patterns at different size, function and facilities. In this

research, the pattern was investigated especially focused on when and how the trend of electricity consumption pattern changed and which building contributed to the pattern change.

The objective of this study is to identify factors influencing time series electricity consumption trend at Tokyo Tech campus under following three perspectives:

- To clarify the point when the electricity consumption pattern changed based on rate of electricity consumption trend change.
- To identify the buildings contribute to the electricity consumption trend change.
- To clarify the factors affecting the trend change.

2.2 Significance of the study

From the result of this study, the cause of electricity consumption trend change is clarified and different electricity consumption patterns in different buildings are confirmed, therefore This research will contribute to propose effective and sustainable electricity consumption reduce policy and actions in the future.

3. Data collection and methodology

3.1 Data collection

In this research electricity consumption time series data from June 2011 to Oct 2015 is investigated, those data are measured, collected and maintained by Tokyo Institute of Technology Energy Conservation office.

Table 1: Summary of electricity consumption data collected

	Area	Frequency	Duration
Data	Whole campus	Monthly	2011 Jun ~ 2015 Oct
	51 Buildings	Monthly	2011 Jun ~ 2015 Oct
Administrator	Tokyo Institute of Technology Energy Conservation Promotion Office		

3.2 Methodology

3.2.1 Seasonal effect modification

As original time series has seasonal effect fluctuation, the original pattern can be understood as containing Trend series ($T_{(t)}$), cycle series($C_{(t)}$), seasonal series($S_{(t)}$), and irregular series ($I_{(t)}$). (equation (1)) In this study seasonal effects are eliminated by moving-average method in order to define trend change. Figure 1 shows the result of seasonal effect modification for electricity consumption at Tokyo Tech campus in 5years by using R program.

Figure 1 shows original electricity consumption time series, and Figure 2 shows seasonal effect modified electricity consumption time series.

$$Y_{(t)} = TC_{(t)} + S_{(t)} + I_{(t)} \cdots (eq.1)$$

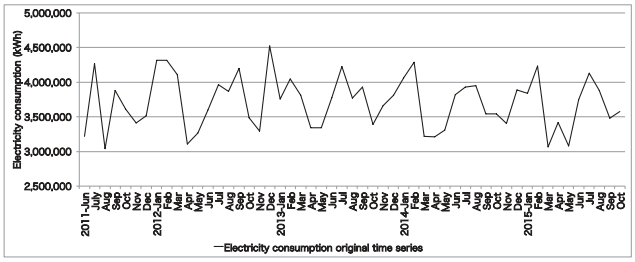

Figure 1: Original electricity consumption time series at Tokyo Tech campus

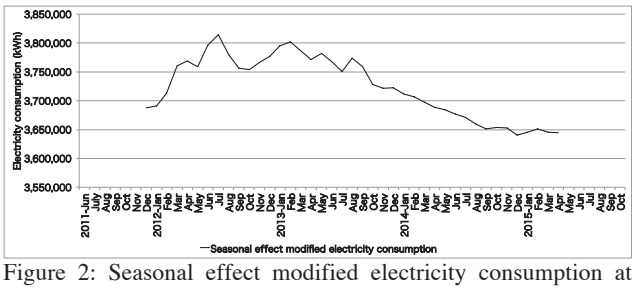

Figure 2: Seasonal effect modified electricity consumption at Tokyo Tech campus

3.2.2 Contribution to percentage change

To measure how each building's electricity consumption trend change contributes to the university-wide overall electricity consumption trend change, contribution to percentage change is calculated. Equation (2) shows the formula of the calculation. Difference of electricity consumption in one building from last month is divided by electricity consumption as whole campus in last month. The total amount of contribution to percentage change by each building is equal to the rate of electricity consumption change at the whole campus's electricity consumption.

$$\Lambda_t = \frac{(X_t - X_{t-1})}{Y_{t-1}} \quad \cdots (eq.2)$$

t : $Month$ (Dec 2011 – Apr 2015)
Λ_t : $Contribution\ to\ percentage\ change$
X_t : $Electricity\ consumption\ at\ the\ building$
X_{t-1} : $Electricity\ consumption\ at\ the\ building\ in\ last\ month$
Y_{t-1} : $Electriciti\ consumption\ at\ whole\ campus\ in\ last\ month$

4. Electricity consumption at Tokyo Tech campus

4.1 Change of electricity consumption trend

Figure 3 shows the rate of electricity consumption trend change. According to the result, electricity consumption trend can be classified into 3 terms; Term1: from December 2011 to September 2012, Term2: from August 2012 to December 2013, Term3: from January 2014 to April 2015. In term 1, the electricity consumption trend increased continuously. In Term 2, the trend fluctuated drastically. In term 3, the trend kept small change until Oct 2014, then gradually shifted to balanced situation.

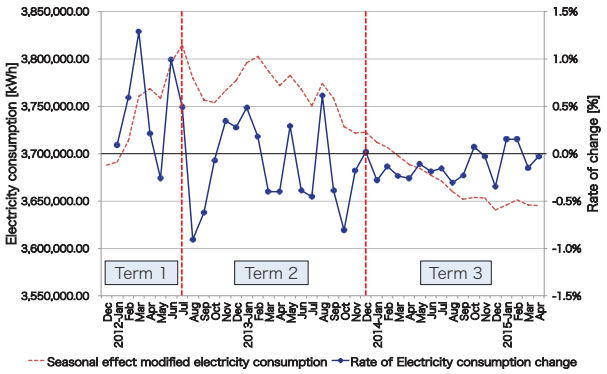

Figure 3: Rate of electricity consumption trend change

4.2 Contribution of electricity consumption trend change in each building

Figure 4 shows the number of buildings contributing electricity consumption increase or decrease in each month. The result shows the number of buildings that contribute to increase or decrease of electricity consumption has been changing as rate of electricity consumption change. It means that electricity consumption change in each month was common phenomenon for each building.

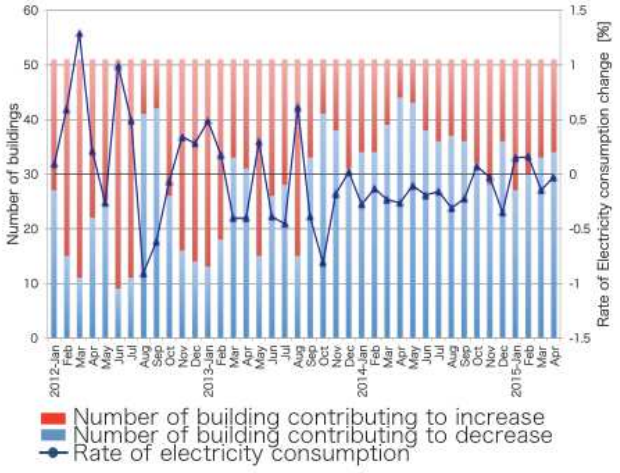

Figure 4: Number of buildings contributing electricity consumption increase/decrease in each month

On the other hand, in Tokyo Tech, electricity was not consumed equally by each building. For example the computing center accounted for 25%, the main building accounted for 10% and top 10 buildings accounted for 60% of all electricity consumption. Gini index of electricity consumption among buildings were also calculated, confirming that the electricity consumption distribution on the campus is indeed quite uneven the Gini index is about 0.63 consistently in those 5 years. According to the fact, next question is whether contribution by each building was even or not.

In Term 1 (from December 2011 to September 2012) the computing center and the main building accounted for 28% of contribution to electricity consumption increase. In Term 2 (from August 2012 to December 2013) only 3 buildings accounted for 25% of each trend change. Especially after May 2013 the main building and the south 9th building accounted for 20% of contribution to electricity consumption increase and the computing center accounted for 50% of contribution to electricity consumption decrease. In Term 3 until September 2014, the computing center and the main building accounted for 20% of contribution to electricity consumption decrease. After October 2014, the computing center accounted for 29% of contribution to electricity consumption increase and the main building accounted for 28% of contribution to electricity consumption.

It can be said that indeed the electricity consumption trend change was common phenomena among each buildings, but buildings that consume much electricity such as the computing center or the main building mainly contributed to trend change.

Through analysis of contribution to percentage change by buildings, the buildings that mainly contribute to electricity consumption trend change were clarified, however each building has its own trend. Therefore in order to figure out how those trends affected electricity consumption trend change, each building is divided into 5 groups by using cluster analysis based on its electricity consumption trend. And contribution to percentage change by each groups were calculated.

Figure 5 shows contribution to percentage change of each electricity consumption pattern group and Table 2 shows name of buildings that belong to each groups. The numbers beside the name indicate the ranking of electricity consumption among buildings.

Result shows that consumption increase in the Term1 was caused by increase in the Group 3 and the Group 4, in the Term 2 the Group 2 shifted from decrease to increase, the Group 3 shifted increase to decrease and the Group 4 kept increase trend, consumption decrease in the Term 3 was caused by decrease in the Group 3 and the Group 4 but Group 3 was gradually shifting to increase trend.

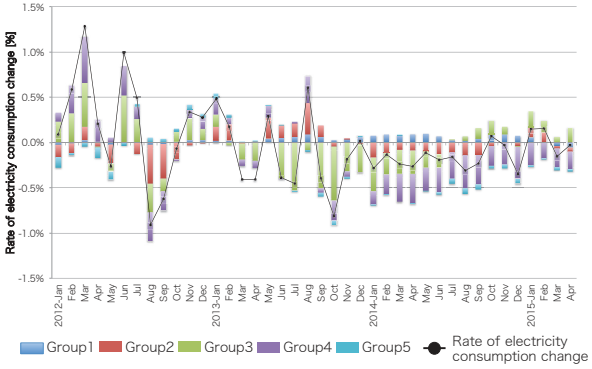

Figure 5: Contribution to percentage change by each electricity consumption pattern group

Table 2: Electricity consumption trend group

Group 1	Group 2	Group 3	Group 4	Group 5
Ishikawadai Bldg. 5 (12)	South Bldg. 9 (3)	Computing center (1)	Main Bldg. (2)	Midorigaoka Bldg. 1 (17)
Venture Business (30)	East Bldg.1 (10)	South Bldg. 8 (4)	West Bldg.8W (5)	North lab. Bldg.3b (32)
South Bldg. 5 (51)	South Bldg. 3 (11)	South Bldg. 7 (6)	West Bldg.9 (7)	Van de Graaff Lab. (34)
	Ishikawadai Bldg.1st (13)	South Bldg. 1 (8)	West Bldg.8E (14)	Midorigaoka Bldg.5 (39)
	West Bldg. 4 (15)	Institute Library (9)	Ishikawadai Bldg. 6 (18)	North lab. Bldg.5 (49)
	East Bldg. 2 (16)	Ishikawadai Bldg.2 (20)	Cafeteria (19)	Radioisotope Lab. (50)
	South Bldg. 6 (23)	Ishikawadai Bldg.3 (21)	Administration Bureau (26)	
	South Bldgs. 4 (24)	Tokyo Tech Front (22)	West Bldg.3 (28)	
	Research center for low temperature Phsics (25)	The Centennal Hall (33)	North Bldg.1 (29)	
	Ishikawadai Bldg. 4 (27)	North Bldg. 2 (35)	West Bldg.7 (31)	
	North Lab. Bldg. 1 (43)	International House (36)	Global Bldg. (38)	
	West Bldg. 1 (44)	North lab. Bldg 2b (37)	Midorigaoka Bldg. 3 (40)	
	Environmental safety management Bldg. (45)	The 70th Anniversary Auditorium (41)	The 80th Anniversary Hall (48)	
		North lab. Bldg. 4-1 (42)		
		Health Service Center (46)		
		North lab. Bldg. 6 (47)		

(Number in parenthesis: Electricity consumption ranking)

5. Influencing factors

Based on the electricity consumption situation in last 5 years, influencing factors are examined. First, correlation between electricity consumption trend and temperature trend are considered. Figure 6 shows electricity consumption trend change and temperature trend change. A correlation coefficient of electricity and temperature in the Term1, the Term 2, and the Term3 is -0.032, -0.151 and 0.985 respectively. From the result, continuous reduction in the Term 3 could be caused by temperature change.

The correlation coefficients in Group 1, Group 2, Group 3, Group 4 and Group 5 are -0.265, 0.073, 0.203, 0.640 and 0.765 respectively. Electricity consumption trend change at Group 4 and Group 5 could be caused by temperature change.

The introduction of high efficient equipment could cause electricity consumption trend change. Five buildings among ten that introduced high efficient equipment in 2014 belong to Group 4 that caused reduction trend in the Term 3.

Figure 7 shows Electricity consumption trend and Electricity charge trend. Rising electricity charge is big incentive for Tokyo Tech to reduce electricity consumption. However electricity consumption reduction was not enough to reduce electricity charge. From January 2013 electricity consumption reduced but payment to electricity bill increased. To make up the cost caused by rising electricity price from 2011, 9,547,406 kWh must be cut. That is 21.5% of electricity consumption in 2015.

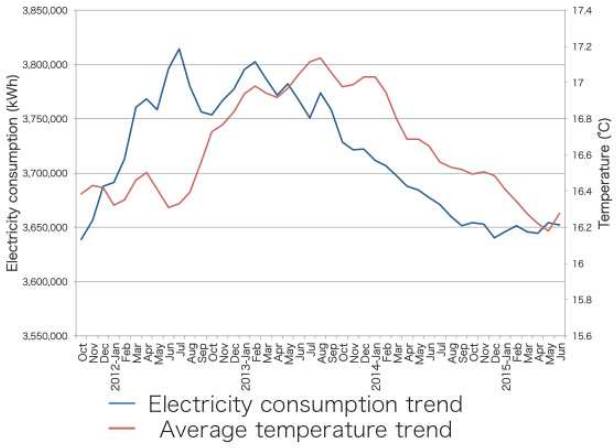

Figure 6: Electricity consumption trend and temperature trend

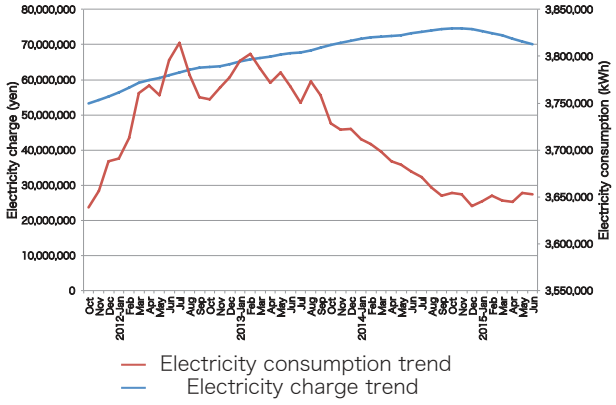

Figure 7: Electricity consumption trend and Electricity charge trend

6.Conclusion

Regarding current electricity consumption situation in the last 5 years, electricity consumption trend at Tokyo Tech is divided into 3 terms based on the rate of electricity consumption change. Electricity consumption trend changes in both Term 1 and Term 2 were relatively large and short-term change. On the other hand, electricity consumption trend change in Term 3 was small and long-term change.

The increase in electricity consumption from December 2011 to September 2012 was mainly caused by increase trend at the computing center and the main building (Term 1). Drastic trend change from August 2012 to December 2013 was mainly caused by the transition from continuous decreasing trend to increasing trend at the south 9th building and by the transition from continuous increasing to continuous decreasing in the computing center (Term 2). Continuous decreasing from January 2014 to April 2015 was mainly caused by the decrease trend at main building and the computing center (Term 3).

Based on current electricity consumption situation, influencing factors were investigated. Especially in Term3, two factors such as temperature trend change and installation of high efficient equipment are explored as influencing factors. Those factors could affect the electricity consumption reduction at the buildings belong to Group 4 such as the main building that caused electricity consumption reduction at Tokyo Tech campus.

For the future effective and continuous electricity consumption reduction, the most important thing is to maintain drastically lower electricity consumption at the buildings, which consume much electricity such as the computing center, the main building and the south 9th building. However, considering the fact that those buildings are also quite important on the campus for research and educational activities, other approach and countermeasures for the further reduction of electricity consumption needs to be also seriously considered. For that end, further study is necessary to investigate empirically how the people on the Tokyo Tech campus are actually using the electricity and how the change of their electricity consumption-related behaviors could actually contribute to the campus-wide consumption reduction. It is also important to clarify in-what-form and how the necessary information and incentives could be provided to the people for the electricity saving behaviors, as the simple provision of electricity consumption information would not contribute to the actual reduction of electricity consumption.

Reference

[1] 国立大学法人東京工業大学 (2015) 東京工業大学環境報告書 2015
[2] 国立大学法人東京大学 (2015) 東京大学環境報告書 2015
[3] 国立大学法人大阪大学 (2015) 大阪大学環境報告書 2015
[4] 国立大学法人九州大学 (2015) 九州大学環境報告書 2015
[5] 国立大学法人電気通信大学 (2015) 電気通信大学環境報告書 2015
[6] 国立大学法人 東京農工大学 (2015) 東京農工大学環境報告書 2015
[7] 大橋巧・宮崎正幸・下田吉之(2013)「大規模総合大学施設のエネルギー消費実態に関する研究電力日負荷曲線の実測データを用いた大阪大学のエネルギー消費特性分析」『日本建築学会環境系論文集』第 78 巻第 684 号,193-201.
[8] 宗城基(2010)「多様な空調システムが混在する大学キャンパスのエネルギー消費実態調査研究」『空気調和・衛生工学会論文集』No.156.
[9] 山羽基・伊藤佑介・加藤大貴・田中俊一 (2012)「レトロコミッショニングを用いた中部大キャンパスのエネルギー消費量の分析」『総合工学』第 24 巻 47-54.
[10] W.P. Wong R.F. Fellows A.M.M. Liu, (2006),"Use of electrical energy in university buildings: a Hong Kong case study", Facilities, Vol. 24 Iss 1/2 pp. 5 - 17

Effects of self-discharge on charge-discharge efficiency of electric double-layer capacitor

Student number: 14M18052 Name: Kenta KOH Supervisor : Kunio TAKAHASHI

電気二重層キャパシタにおける自己放電が充放電効率に及ぼす影響

高　健太

本研究では電気二重層キャパシタの充電過程、溜めた電荷を使用するまでの待機時間中に発生しているエネルギーロスをイオン拡散と内部抵抗によるものと分類し、解析することにより自己放電が充放電効率に及ぼす影響を調べた。これにより電気二重層キャパシタを蓄電デバイスとして利用する際に待機時間に応じてどのように充電を行えば充放電効率良く使えるか提案する。

1. Introduction

Electric double-layer capacitors (EDLC), forming double-layer which is several nanometers are currently discussed as a storage device. They are used cases of changing storage device is difficult, maintenance free and so on.

Because of their small internal resistance and long cycle life, they have less volumetric and gravimetric energy density to compared with rechargeable battery.

Storage devices have self-discharge that is the decrease of its open circuit voltage as shown Fig1. The self-discharge of EDLC is much higher than that of rechargeable batteries.

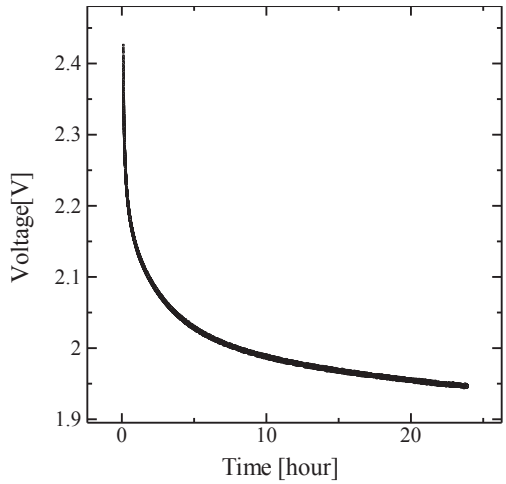

Fig1 Voltage drop by self-discharge

In research[1-3], the self-discharge consists of a relatively fast ion diffusion process and a slower leakage current. They estimate voltage drop of capacitor under condition that capacitance is constant.

This estimation doesn't contain effect of charge current. In addition, capacitance is changed by internal state of capacitor. So we cannot estimate energy of capacitor from open circuit voltage. Charge-discharge efficiency is significant parameter for storage devices to design for energy harvesting and so on.

Therefor purpose of my research is investigating effects of self-discharge on charge discharge efficiency and suggest how to charge with high charge discharge efficiency.

2. Energy loss in charge-discharge process

We consider energy loss in charge discharge process classify into ion diffusion and internal resistance[1] Ion diffusion, accumulation of an excess ionic concentration occur in charging process.

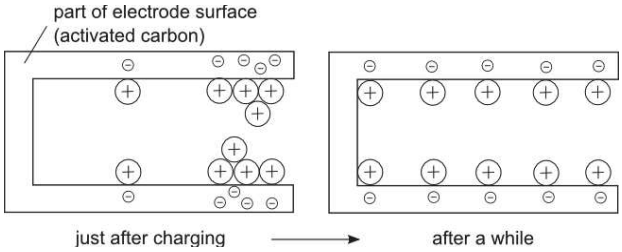

Fig2 schematic ion distribution model

When the capacitor is disconnected from the charging circuit, the charge of double-layer will stay in place but the excess ionic concentration near the carbon surface will diffuse to an equilibrium state as shown in Fig2. So the area increase, the capacitance C also increase. And the open-circuit voltage of the capacitor decrease. In this paper, to determine C, we use output charge of discharge capacitor. Precisely, we should use stored charge in capacitor, but it is enough as a first approach. So we use C_t which is the ratio of output charge and voltage of capacitor as capacitance. The case ion diffusion is over, $C_t = C_\infty$ is constant. Energy loss by ion diffusion is difficult to make model. So we investigate energy loss by ion diffusion with experiment.

Energy loss by internal resistance, the model as shown in Fig3.

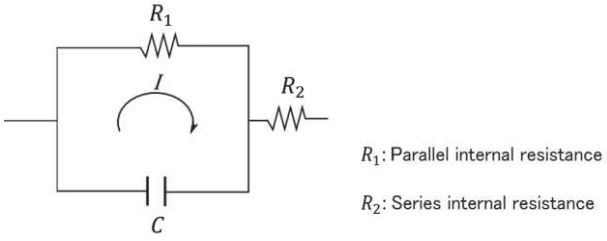

Fig3 model of internal resistance

Leak current is occurred by disappearing a part of charges between double-layer and flowing charge on surface of capacitor. Energy loss occur by parallel internal resistance R_1 in charge process and open circuit process. R_1 is changed by ion diffusion and internal state of capacitor [4]. However after enough

time pass, the circuit consist of ideal capacitor and ideal resistance because capacitance is constant. In this state, voltage of capacitor in open circuit process obtained as

$$V_{\mathrm{w}} = \mathrm{A} * \exp\left(-\frac{t}{R_1 C_{\infty}}\right) \quad (1)$$

So the Energy loss by parallel internal resistance, in range of capacitance is constant, obtained

$$E_{\mathrm{Ploss}} = \int \frac{{V_{\mathrm{w}}}^2}{R_1}\,\mathrm{dt} \quad (2)$$

Energy loss by series internal resistance occur when charging process and discharge process. Constant current charging is desirable charging method typically, we use constant current charging in this paper. So we use I_{c} as charge current, the energy loss is obtained

$$E_{\mathrm{Sloss}} = R_2 I_{\mathrm{c}}^2 \quad (3)$$

On the other hand, discharge process, the energy loss is dependent on load. The smaller the load is, the higher the energy loss. In this paper, the load which is connected in discharge process is bigger than series internal resistance. So we ignore this energy loss.

Using input energy E_{in}, output energy E_{out}, energy loss by ion diffusion and internal resistance before enough time passed E_{Dloss}, total energy loss E_{Tloss} defined as

$$E_{\mathrm{in}} - E_{\mathrm{out}} = E_{\mathrm{Tloss}} = E_{\mathrm{Dloss}} + E_{\mathrm{Ploss}} + E_{\mathrm{Sloss}} \quad (4)$$

We have to estimation R_1 and R_2 and E_{Tloss} to know effect of E_{Dloss} on charge discharge efficiency by experiment.

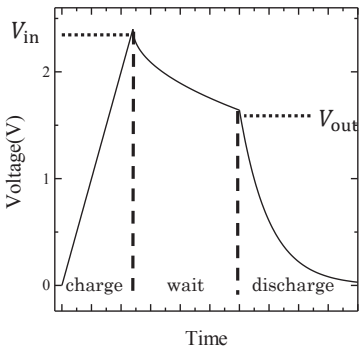

I_{c} : charge current
T_{w} : wait time
Q_{in} : input charge
Q_{out} : output charge
V_{in} :initial voltage
V_{out} : output voltage
C_{t} $(= \frac{Q_{\mathrm{out}}}{V_{\mathrm{out}}})$:capacitance

Fig4 Experiment process and parameters

To estimate R_1 enough time passed, we use fitting method with equation (1) and C_{∞}. So we do experiment changing T_{w}, we obtain C_{t} and equation of voltage drop.

To estimate R_2, we use voltage drop ΔV just after charging. In charging process, the voltage drop is

$$\Delta V = R_2 I_{\mathrm{c}} \quad (5)$$

It is unknown that which series internal resistance change or not by charge current, initial voltage and so on.

3. Experiment and result

3.1 Equipument

We determine each parameter in experiment. The circuit and equipment are shown in Fig5 and Table1.

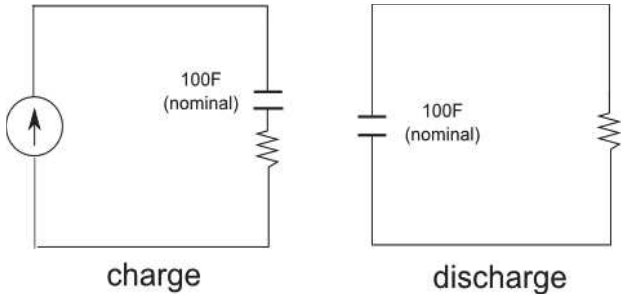

Fig5 charge-discharge circuit

Capacitor	Elna DYNACAP DZ
Voltage measure	GRAPHTEC GL900
Power source	Matsusada ECD5-5

Table1 equipment

We choose EDLC which has capacitance of 100F (nominal) and voltage logger which has impedance of 1MΩ, that is several ten times bigger than R_1.
In this experiment, the parameter we can determine are I_{c}, T_{w}, Q_{in}, V_{in}. And the parameter we can measure are Q_{out},V_{out}. So we can calculate C_{t}.

3.2Result

Experiment is done with $I_{\mathrm{c}} = 0.1$[A], $V_{\mathrm{in}} = 2.4$[V] because we can observe ion diffusion and leak current. Fig6 shows whole process. We calculated capacitance with output charge of discharge and output voltage. The capacitance is constant from 12h from Fig7.

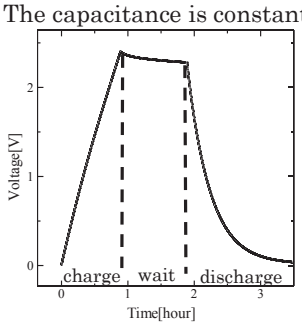

Fig6 charge-discharge process

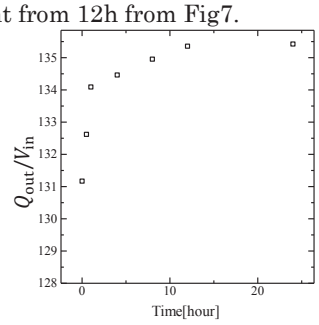

Fig7 Capacitance change

So fitting wait time to equation(1) from 12h to24h, we obtained

$$R_1 C_{\infty} = 2.951 * 10^6$$
$$C_{\infty} = 135.4$$
$$R_1 = 22024[\Omega]$$

In the same way, voltage drop on condition that initial voltage are 0.6V, 1.5V, 2.4V. Fig8 shows the initial voltage is higher, effect of ion diffusion is the bigger and diffusion time is the shorter.

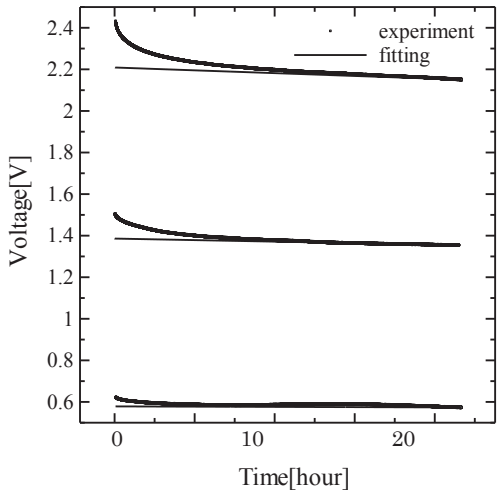

Fig8 Deference voltage drop each initial voltage

Fig9 shows change of R_1 by initial voltage. From this graph, R_1 is depend on initial voltage. And initial voltage is small, leak current is also small.

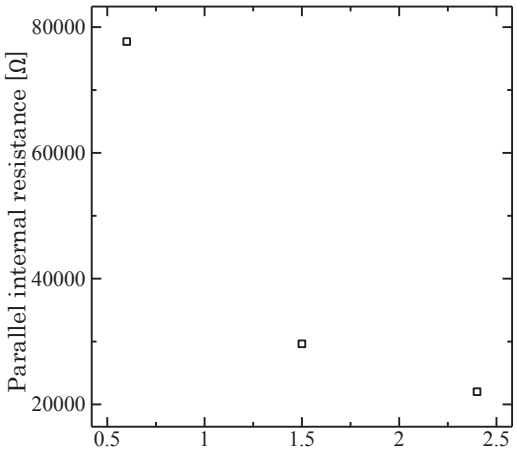

Fig9 dependence of internal resistance on initial voltage

Table2 shows that ΔV and calculate R_2 each current And Table 3 shows that ΔV and calculate R_2 each initial voltage with charge current is 2A. From this result, series internal resistance is independent on charge current and initial voltage. So we use average voltage drop and determine

$$R_2 = 33.5[\mathrm{m\Omega}]$$

I_c[A]	ΔV[V]	R_2[Ω]
1	0.034	0.034
2	0.063	0.0315
3	0.093	0.031

Table2 Dependence of R_2on charge current

V_{in}[V]	ΔV[V]	R_2[Ω]
0.2	0.066	0.033
0.6	0.060	0.03
1.2	0.069	0.0345
1.8	0.066	0.033
2.1	0.074	0.037
2.4	0.067	0.0335

Table3 Dependence of R_2on initial voltage

4. Discussion of charge discharge efficiency

We divided discussion of charge-discharge efficiency with wait time because there is large difference of internal state of capacitor.

4.1 Case of $T_{\mathrm{w}} = 0$

If you want to use energy just after charging,

$$E_{\mathrm{Ploss}} = 0$$

From equation(4)

$$E_{\mathrm{Dloss}} = E_{\mathrm{Tloss}} - E_{\mathrm{Sloss}}$$

E_{Tloss} is measured value and E_{Sloss} is calculated from equation(3).

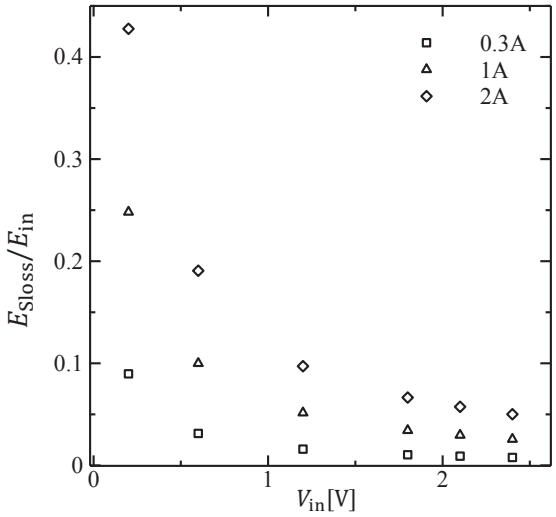

Fig10 Effect of E_{Sloss} on charge discharge efficiency

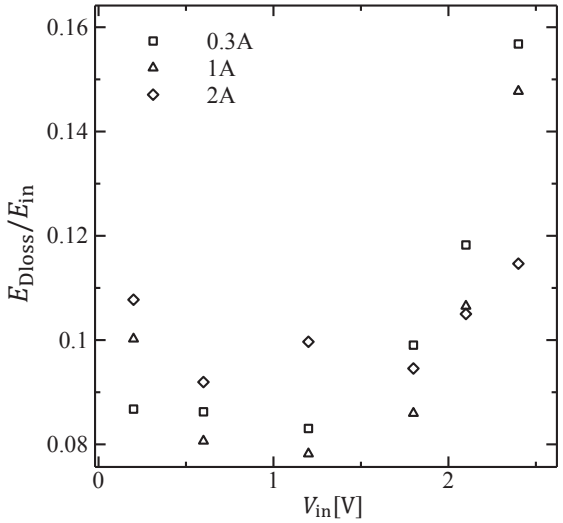

Fig11 Effect of ion diffusion and leak current before enough time passed on charge discharge efficiency

Fig10 shows series internal resistance big effect on charge discharge efficiency when initial voltage is low. Fig11 shows ion diffusion and leak current big effect on charge discharge efficiency when initial voltage is high. So there is the highest efficiency point between 0V to 2.5V as Fig12. From this graph, charge current is the bigger, highest efficiency point is also bigger.

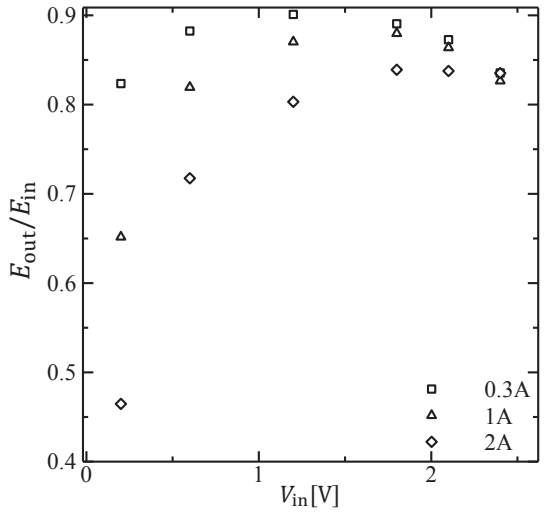

Fig12 Charge discharge efficiency

4.2 Case of T_{w} is enough long time

Case of storage energy long time, effect of E_{Ploss} is big when wait time is long. E_{Dloss} can be represented

$$E_{\mathrm{Dloss}} = E_{\mathrm{Tloss}} - E_{\mathrm{Sloss}} - E_{\mathrm{Ploss}}$$

E_{Tloss} is measured value and E_{Dloss} is calculated from equation(3) and R_2., equation(2) and R_1.
From Fig13 and Fig14, capacitor can be used high charge discharge efficiency with small charge current and small initial voltage

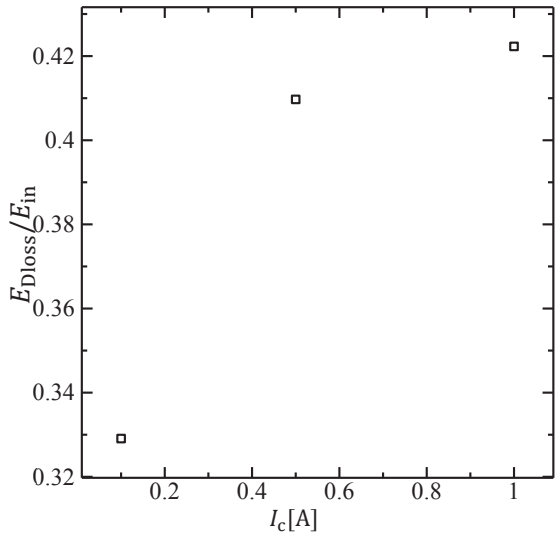

Fig13 Effect of charge current on $E_{\mathrm{Dloss}}(V_{\mathrm{in}} = 2.4[\mathrm{V}])$

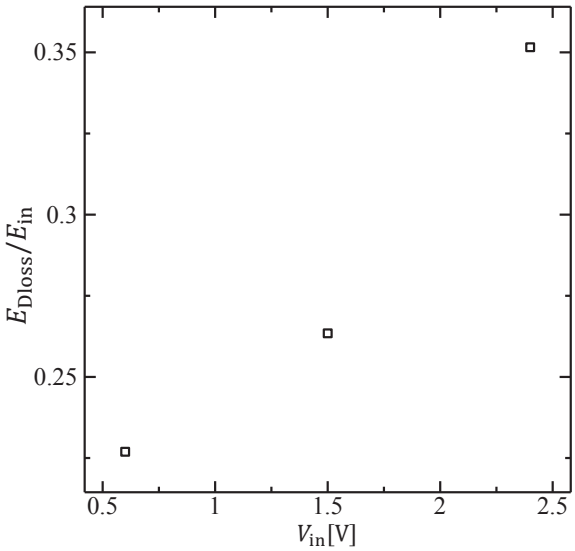

Fig14 Effect of initial voltage on $E_{\mathrm{Dloss}}(I_{\mathrm{c}} = 0.1[\mathrm{A}])$

5. Conclusion

We cleared Effect of ion diffusion and internal resistance depend on initial voltage, wait time and charge current.
Ion diffusion depend on initial voltage and charge current. Series internal resistance do not depend on initial voltage or charge current. Parallel internal resistance depend on initial voltage.
So charge-discharge efficiency depend on initial voltage and charge current. We suggest that how to charge high charge-discharge efficiency each wait time.

Reference

[1] B.W. Ricketts, C. Ton-That, 2000," Self-discharge of carbon-based supercapacitors with organic electrolytes",Journal of Power Sources 89. 64–69
[2] Hengzhao Yang, Ying Zhang, 2011, "Self-discharge analysis and characterization of supercapacitors for environmentally powered wireless sensor network applications", Journal of Power Sources, v 196, n 20, p 8866-8873
[3] Li Zhongxue, Wu Fu, 2011, "Diagnostic Identification of Self-Discharge Mechanisms for Carbon-Based Supercapacitors with High Energy Density" ,Power and Energy Engineering Conference (APPEEC), 2011 Asia-Pacific, 25-28
[4] Julia Kowal, Esin Avaroglu, 2011, "Detailed analysis of the self-discharge of supercapacitors", Journal of Power Sources v196, Issue 1, 1 p573–579

EXPERIMENTAL STUDY ON APPLICATION OF ANODE ELECTRODES IN ELECTRO-CHEMICAL REPAIR WITH WATER SUPPLY CURING METHOD

Student ID: 14M18187 Name: Shu YAMAMOTO Supervisor: Nobuaki OTSUKI

給水養生方法を用いた電気化学的補修工法における各種陽極材の適用に関する実験的検討

山本　周

本研究では，給水養生方法を用いた電気化学的補修工法の陽極材として，従来よりも経済的な各種陽極材の適用可能性を検討した．その結果，その補修効果と価格から，各工法に最適な陽極材として，電着工法にはアルミ，脱塩工法には導電性シート，再アルカリ化工法にはスチールメッシュ，電着工法後に剥落防止工を行う場合には炭素繊維シートを提案することができた．

1. Introduction

Nowadays the deterioration of reinforced concrete structures is widely reported all over the world. It is necessary to maintain these structures to use for long time. Electro-chemical repair [1] is one of repair methods to RC deterioration related to steel corrosion. In this case, it is necessary to provide the external solution on concrete surface in the case of applying electro-chemical repair to RC. Water Supply Curing Method [2] can be applied as one of the reliable solution providing methods.

However, problems remain in practice of electro-chemical repair. The major problem is high construction cost. And titanium mesh which is used as anode electrode accounts for large part of the cost.

In this study, the application of economical anode electrodes to electro-chemical repairs and improvement of the repair effect by replacement of anode electrode is investigated. Therefore the objective of this study is to suggest optimal anode electrode for electrodeposition, desalination, re-alkalization, and strengthening after electrodeposition.

2. Overview of anode electrodes and specimens

(1) Anode electrodes

In this study, target anode electrodes can be roughly divided into three kinds except titanium mesh for comparison. Their resistances and unit prices are shown in Table 1. The unit prices are lower than titanium mesh.

The first anode is metal. Metal is thought to be inappropriate because it is eluted by electrification. And eluted metal has a possibility to affect the repair effect.

The second one is conductive sheet which consists of carbon black and plastic. It is not clear whether the resistance of this sheet is low enough or not because it is not so much low as titanium mesh.

The third one is carbon fiber sheet. If this sheet can be used for strengthening even after usage as anode electrode of electro-chemical repair, the combination repair is efficient and waste material can be reduced.

Table 1: Anode electrodes

Kind of anode electrodes		Resistance (Ω・cm)	Unit price (yen/m^2)
Titanium mesh		4.92E-05	15,000
Metal	Aluminum	2.65E-06	448
	Steel	1.00E-07	160
	Copper	1.68E-08	2,400
	Zinc	6.02E-08	2,000
Conductive sheet		9.45	1,000
Carbon fiber sheet		1.87E-02	6,000

(2) Specimens

In this study, two types of specimens and one existing structure are used.

One specimen is a prism mortar specimen. The size is 40*40*160mm and rebar is embedded in the center. It is used for investigation in which many cases are needed. Specimens having several conditions are shown in Table 2. Repairing system is shown in Fig 1.

Table 2: Parameters of mortar specimens

Chapter	Crack	Initial Cl$^-$	Covering depth
3	Crack	0kg/m^3	10mm
4	Non	8.0 kg/m^3	15mm
6	Non	0kg/m^3	15mm

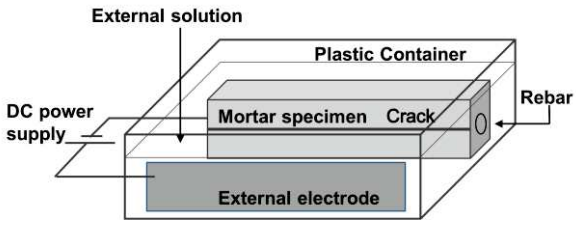

Fig 1 : Repairing system

The other specimen is a RC beam deteriorated under marine environment for 40 years (150*300*1800mm). It is used for investigation of simulation of field practice with Water Supply Curing Method. The rebar arrangements are shown in Fig 2 and repairing with Water Supply Curing Method is shown in Fig 3.

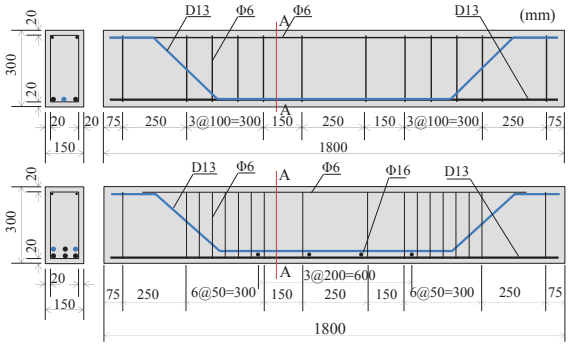

Fig 2 : Rebar arrangement
(upper : chapter.3,4, lower : chapter.6)

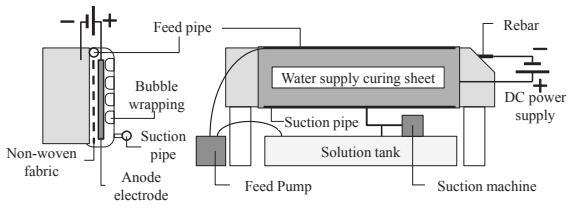

Fig 3 : Repairing system with Water Supply Curing Method

The existing structure is an interior wall deteriorated by carbonation. It is used in chapter.5 to investigate the applicability of steel mesh to field practice of re-alkalization method. The repair area is 1.7m*30m.

3. Electrodeposition

Aluminum, steel, copper, and zinc are easily-available metals. These metals are thought to be eluted with electrification and affect the property of electrodeposit. In this chapter, resistivity against Cl^- permeation is investigated with mortar specimens. And aluminum is applied as anode electrode to electrodeposition method with Water Supply Curing Method.

(1) Resistivity against Cl^- penetration

After repairing (shown in Fig 1), specimens had been immersed 10% NaCl water for 7 days. Then Cl^- penetration depth is measured in silver nitrate spray test. And Cl^- on rebar is measured in test shown in Fig 4. The results are shown in Fig 5 and Fig 6. From the results, electrodeposition method with aluminum and copper have higher or equivalent repair effect to improve resistivity against Cl^- penetration compared with that with titanium mesh.

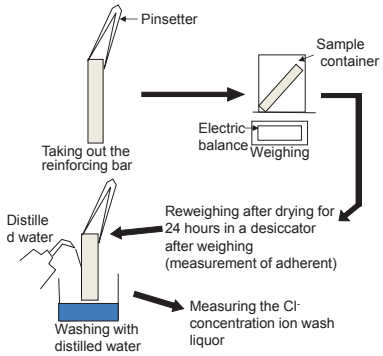

Fig 4 : Measuring method of Cl^- on rebar

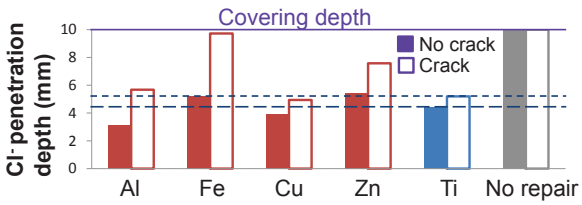

Fig 5 : Cl^- penetration depth

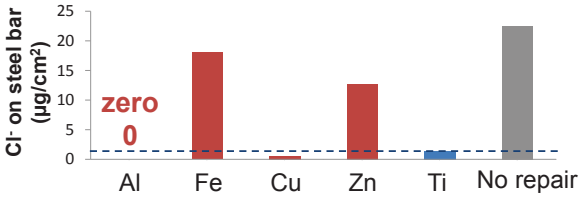

Fig 6 : Cl^- amount on rebar

(2) Visual investigation

In electrodeposition method, electrodeposits cover the concrete surface. Fig 7 shows RC beam specimen after repairing (shown in Fig 3) with aluminum or titanium mesh. From the pictures, electrodeposition method with aluminum has higher surface covering effect than that with titanium mesh.

Fig 7 : Appearance after repair

4. Desalination

In this chapter, desalination effect is investigated with mortar specimens. And effective range of conductive sheet is investigated from current broadening.

(1) Desalination effect

Desalination effect of each anode electrode is evaluated from Cl^- content in external solution during repairing (like Fig 1). The results are shown in Fig 8. From the result, conductive sheet and carbon fiber sheet have equivalent desalination effect as titanium mesh. And aluminum and steel have lower desalination effect than titanium mesh.

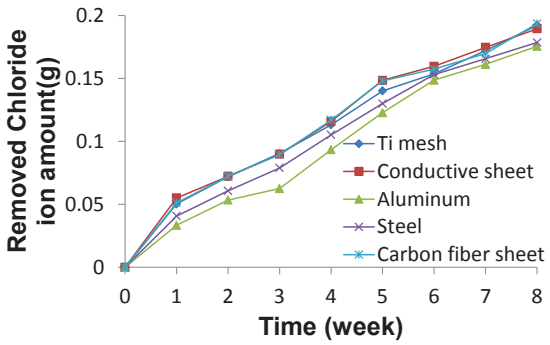

Fig 8 : Desalination effect of each anode electrode

(2) Effective range of conductive sheet

In order to evaluate resistance of conductive sheet, current broadening is investigated. Current which flows in each specimen is measured when repairing system is like Fig 9. And the lowest integrated current density of titanium mesh case is estimated as minimum standard. Fig 10 shows the integrated current density. From the result in case of conductive sheet, the length in which current can flow appropriately is thought to be the distance to third specimen, 48cm at maximum.

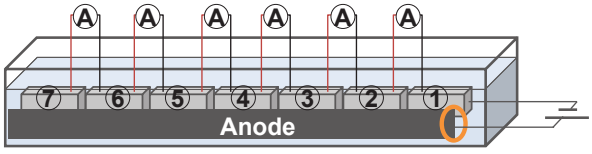

Fig 9 : Repairing system

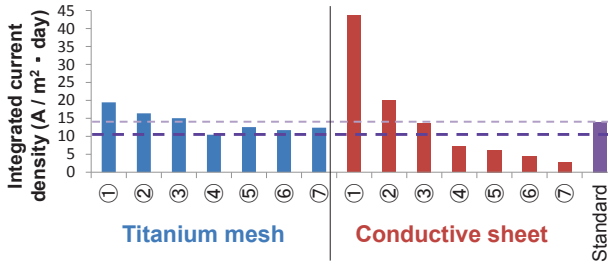

Fig 10 : Integrated current density

And Fig 11 shows the Cl^- on rebar after repairing. Measuring method is same as in chapter.3. The highest Cl^- on rebar of titanium mesh case is estimated as maximum standard. From the result in case of conductive sheet, the length in which desalination effect can be obtained appropriately is thought to be the distance to third specimen, 48cm at maximum. This length is same as that in which current can flow appropriately.

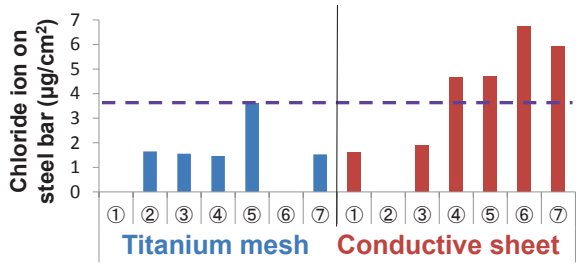

Fig 11 : Cl^- amount on rebar

These results are confirmed in investigation of simulation of field practice with Water Supply Curing Method. Fig 13 shows desalination rate of each point indicated in Fig 12. Desalination rate is calculated from chloride content in concrete before and after repairing. From the result, there is little deference between the desalination effects of two points. Therefore, it can be said that conductive sheet can be applied within about 45cm in this experiment.

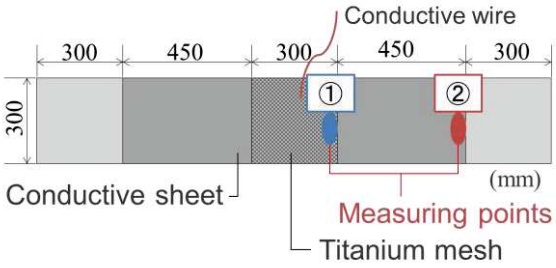

Fig 12 : Measuring points

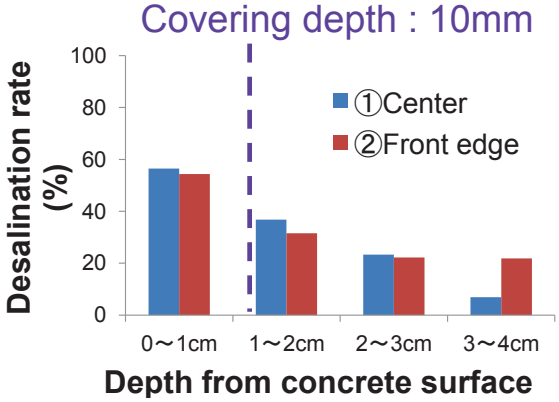

5. Re-alkalization

In conventional field practice of re-alkalization method, steel mesh can be applied because the period of this method is shorter. In this chapter, the applicability of steel mesh to field practice of re-alkalization method with Water Supply Curing Method is investigated. The repair area is 1.7m*30m in total.

(1) Current density

Design current density is 1.0 A/m^2 and maximum limit of voltage is 40V. The appearance of interior wall during repairing is shown in Fig 14. Fig 15 shows the current density and voltage. From the result, design current in case of steel mesh can flow in appropriate voltage except first several days like as titanium mesh case.

Fig 14 : Appearance during repairing

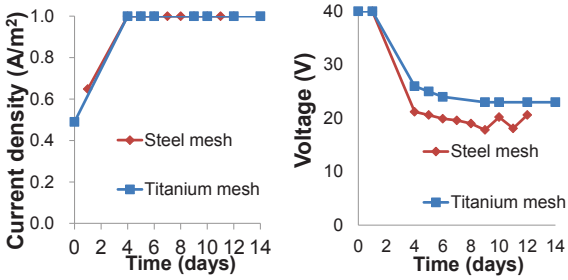

Fig 15 : current density and voltage

(2) Re-alkalization effect

Re-alkalization effect is evaluated from carbonated depth before and after repairing. Fig 16 shows the core discolored by phenolphthalein reaction. From the result, re-alkalization method with steel mesh is completed like as that with titanium mesh.

Fig 16 : Corbonated depth

6. Strengthening after electrodeposition

Carbon fiber sheet has been used for strengthening the concrete. It has high conductivity and it can be applied to anode electrode in electro-chemical repair. It is thought that this sheet can be easily pasted on concrete by pouring low-viscosity epoxy resin into space between concrete and water supply curing sheet after electro-chemical repair. In this chapter, the strengthening effect by carbon fiber sheet is investigated with mortar specimens and RC beam. And the applicability to prevent concrete falling is investigated by bond strength test.

(1) Strengthening effect

The maximum loading capacity of mortar specimens after repairing and pasting carbon fiber sheet is measured in loading test shown in Fig 17. The size of carbon fiber sheet is 40mm*90mm and it is pasted on under surface and side surface. Table 3 shows the condition and result. From the result, the strengthening effect is obtained.

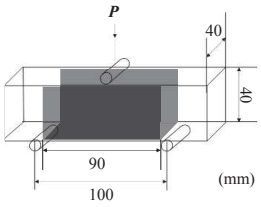

Fig 17 : Loading test of mortar specimens

Table 3: Parameters and loading capacity

Electrodeposition	Pasting carbon fiber sheet	Loading Capacity (N)
Conducted	Conducted	13,125
Conducted	Non-conducted	7,475
Non-conducted	Non-conducted	7,250

In case of investigation with RC beam, strengthening effect is evaluated by load-deflection relation. At first, electrodeposition method is applied to 3 RC beams (like Fig 3). Anode electrodes are titanium mesh, aluminum foil, and carbon fiber sheet. Then, carbon fiber sheet is pasted by low-viscosity epoxy resin on the carbon fiber sheet anode case. Finally, loading test is conducted. The way to set the equipment and load is shown in Fig 18. Fig 19 shows the result of load-deflection relation of each case. From the result, there is little deference among 4 patterns. This result conflicts the result of mortar test. The reason is thought to cause from deference of cross-section ratio of (cross-section area of carbon fiber sheet in tensile side) / (cross-section area of RC beam). The cross-section ration of mortar specimen is 0.28% and that of RC beam is 0.06%. The smaller this value is, the smaller strengthening effect is. Therefore, it is thought that strengthening effect cannot be obtained in case of RC beam.

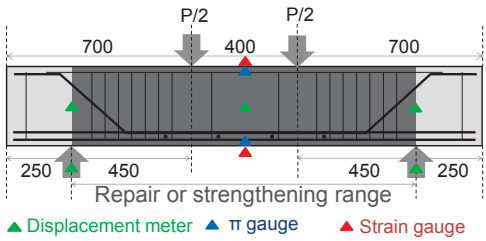

Fig 18 : Equipments and loading and support position

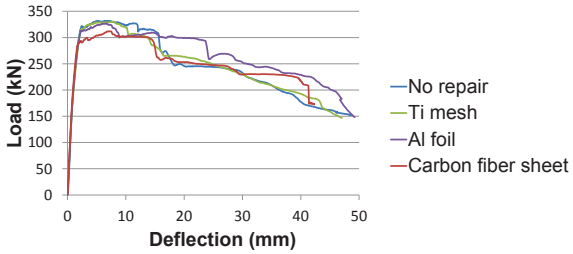

Fig 19 : Load-deflection relation of RC beams

(2) Bond strength

Bond strength is criterial parameter for prevention concrete falling. It is evaluated after loading test of RC beam like Fig 20. Table 4 shows the result. From the result, although the bond strength cannot be accurately measured in almost points (①), at least measured bond strength is over 1.5N/mm^2 which is standard in Procedure of Design and Construction of bridge structures (Shutoko Engineering Company) [3].

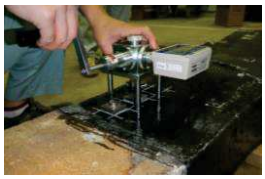

Fig 20 : Bond strength test

Table 4 : Bond strength

Number of measured points	12
①Disbonded between attachment and carbon	11
②Disbonded between carbon and concrete	1
Average bond strength of ①(N/mm^2)	3.05
Average bond strength of ②(N/mm^2)	1.86

7. Conclusions

The following conclusions are derived from the investigations of this study:

1) Aluminum showed higher repair effect as anode electrode than conventional anode electrode (titanium mesh) for electrodeposition method.
2) Conductive sheet can be applied to desalination method in the appropriate length (in this study: about 45cm).
3) Steel mesh can be applied to re-alkalization method with Water Supply Curing Method and the repair effect can be obtained.
4) It was suggested that carbon fiber sheet can be used to prevent concrete falling after electrodeposition. If cross-section ratio of (cross-section area of carbon fiber sheet in tensile side) / (cross-section area of RC beam) is large, carbon fiber sheet can be used also for strengthening.

Considering from the results and the price of each anode electrode, optimal anode electrode for electrodeposition, desalination, re-alkalization, and strengthening after electrodeposition can be suggested as Table 5.

Table 5: Optimal anode electrodes

Electrodeposition	Aluminum
Desalination	Conductive sheet
Re-alkalization	Steel mesh
Strengthening after electrodeposition	Carbon fiber sheet

8. Reference

[1] Japan Society of Civil Engineers: Recommendation for Design and Construction of Electrochemical Corrosion Control Method; 2001.11

[2] Hazama Ando Corporation: Water Supply Curing System of Concrete Structure, “Aqua Curtain”;2013.4

[3] Shutoko Engineering Company: Procedure of Design and Construction of bridge structures; 2008

Comparison of Transportation Equipment Companies in terms of Environmental and Management efficiency

Student Number: 14M18023 Name: Masataka Kashiwa Supervisor: Naoya Abe

環境効率性と経営効率性からみた輸送用機器企業間の比較

柏 雅貴

本研究では、2014 年度に環境報告書を発行した輸送用機器企業 9 社を対象とし、各企業が公表している定量的環境データと財務関連データを用いて、DEA（Data Envelopment Analysis）により、環境効率性と経営効率性を算出した。またこれらの算出された効率性情報に加え、民間調査機関による環境経営度調査による環境経営に関するデータを用いて、経営活動と環境活動の関係性について考察した。

1 Introduction

1.1 Background and literature review

Corporate activities, which are assumed as to maximize profit, have caused some environmental issues in Japan from 1890s. Because of enacted environmental law and regulations on and after late 1960's and general citizen`s request for better living conditions, corporations including manufacturing enterprises, had to comply with legal requirements. These correspondences have changed to do pollution prevention, competitive strategy and sustainable management [1]. Accomplishing the improvement of management activity and profitability and the reduction of environmental burden by incorporating an environmental consideration into every corporate activity independently is called "Environmental Management".

There are many arguments about the relationship between Environmental activity and Management activity. Levy(1995) and Kagata(2006) argued that environmental management don`t always generate profit for the company and even become additional cost, depending on the situations. [2,3]. Kaneko (2015) argued that there is no significant correlation between Environmental efficiency (Sales/CO2) and Management efficiency (ROA)[4].

This research focused on the transportation equipment industry which is assumed as a major industry in Japan and is related to several industries from material procurement to production, sale and maintenance. The value of shipments of manufactured goods of this industry occupies 20.1% of whole manufacturing industry. Many numerical parts approximately 20,000-30,000 points per one and many affiliates are involved in car manufacturing. The emission from this industry was assumed as one of the main air and water pollutants sources and this manufacturing activities have been regulated by various environmental law such as Revised Energy Conservation Act, PRTR raw and End-of-life Vehicle Recycling Law. Thus it is significant to focus on this sector in this study.

1.2 Objective of the study

This research will do inter-enterprise comparison to grasp the actual state of environmental management of the transportation equipment industry. This research will clarify the relationship between an environmental activity and a management activity with efficiency that was calculated by corporate quantitative data and the relationship between an efficiency and another data such as corporate information, Environmental Management survey ranking.

2 Analytical method & Data

2-1 DEA (Data Envelopment Analysis)

In this research selected Data Envelopment Analysis (DEA) that Charnes, Cooper and Rhodes proposed in 1978. This is a non-parametric method for evaluating Decision Making Units (DMUs) can be such as company and people with the efficiency. CCR and BCC model are two basic DEA models, where the former is under constant return to scale technology and the latter is under variable return to scale technology. The difference of CCR and BCC model in DEA was showed in Figure 1. DEA can deal with multiple inputs, outputs

and different unit data for the evaluation. The source of inefficiency and the reference for DMU can be clarified.

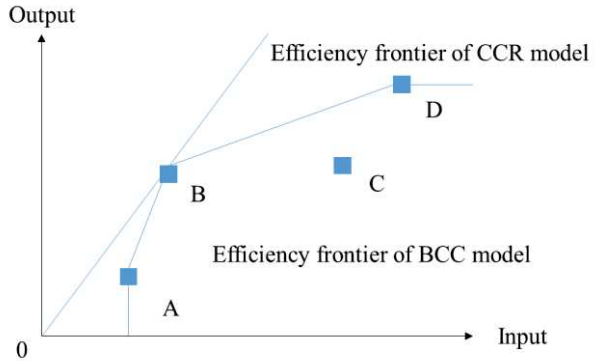

Figure 1: The difference of CCR and BCC model in DEA

At first, assuming that four DMUs (A, B, C, D) spend some fortunes and produce some fortunes. The incline of the straight line to link the origin of DMU B is the biggest. In other words, the maximum ratio of output / input represents most efficient DMU. All DMUs except B are wrapped up under this efficient frontier and are recognized inefficient.

$$< FP_o > \quad max\theta_o = \frac{\sum_s u_r y_{ro}}{\sum_m v_i x_{io}} \ (i = 1,\cdots,m\,; r = 1,\cdots,s) \quad (1.1)$$

$$\frac{\sum_s u_r y_{rj}}{\sum_m v_i x_{ij}} \leq 1 \ (j = 1,\cdots,n) \quad (1.2)$$

$$v_1, v_2, \cdots v_m \geq 0 \quad (1.3)$$

$$u_1, u_2, \cdots u_s \geq 0 \quad (1.4)$$

$$< LP_o > \quad max \ \ \theta_o = \sum_{r=1}^{s} u_r y_{ro} \quad (1.5)$$

$$\sum_{i=1}^{m} v_i x_{io} = 1 \quad (1.6)$$

$$\sum_s u_i y_{ij} < \sum_m v_i x_{ij} \quad (1.7)$$

$$v_1, v_2, \cdots v_m \geq 0 \quad (1.8)$$

$$u_1, u_2, \cdots u_s \geq 0 \quad (1.9)$$

In this approach, n *DMUs* and m inputs variable, s outputs variables are assumed and DMU_o is defined as target *DMU* and x_{1o}, x_{2o}, $\cdots$ x_{mo} as input data of DMU_o, y_{1o}, y_{2o}, $\cdots$, y_{so} as output data of DMU_o and v_1, v_2, $\cdots$, v_m as weights of input, u_1, u_2, $\cdots$, u_s as weights of output. The efficiency ratio is represented in the formula (1.1). The formula (1.2) represents that the efficiency shall not exceed 1.0. Because it`s difficult to find optimum solution with fractional programming model, this model can be converted into a Linear programming model in (1.5) under constraint conditions (1.6). Linear programming model gives several variables the best weights and calculates the efficiency under optimal weight. These are repeated for every DMUs.

2-2 Target companies and Usage data

This research selected target companies which published environmental report in 2014 and whose sales are over 1 trillion yen and divided 9 target companies into 2 groups by accounting method as Table1. The scope of consolidated accounting included a subsidiary and an affiliate around the world against only one`s company of unconsolidated accounting in this research.

Table 1: Group validation

Consolidated accounting group	Unconsolidated accounting group
Nissan motors	Mitsubishi motors
Denso	Kawasaki heavy industry
Komastu	Yamaha motors
Kubota	Isuzu motors
	Hino motors
Total 4 companies	Total 5 companies
Total 9 companies	

Table 2: Input variables and Output variables

Efficiency	Input	Output
Management	Employees	Sale
	Capital investment	Net profit
	Research and development expenses	
Environmental	Amount of energy	CO2 emmision
	Amount of raw material	Waste amount
	Amount of water	Wastewater
Environmental Management	Environmental preservation cost	Sale
	Amount of energy	Net profit
	Amount of raw material	
	Amount of water	
	Environmental preservation cost	
	CO2 emmision	
	Waste amount	
	Wastewater	

Management efficiency was defined as the degree of how to produce maximum for constant resource input. Environmental efficiency means the degree of how to reduce environmental burden maximum for constant environmental resource input. Environmental management efficiency means the degree of how to produce maximum and reduce environmental burden for constant environmental resource input. Because there are great scale differences of the data which was used to calculate the management efficiency within unconsolidated accounts group, BCC model was applied only to these against CCR model.

3 Results

3-1 Inter-enterprise comparison

Using two efficiencies, we conducted Inter-enterprise comparison and proposed points of improvement and a company to be referred.

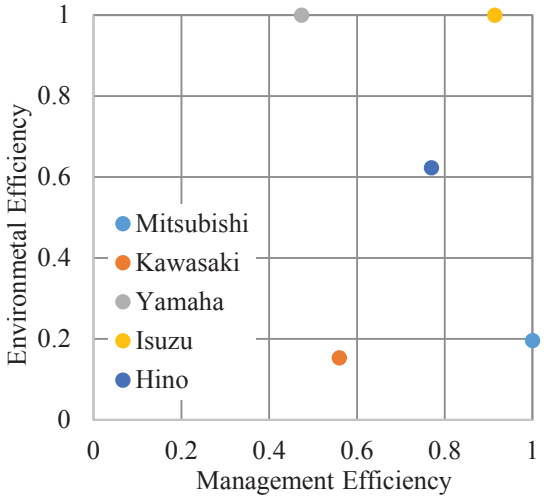

Figure2: The efficiency of unconsolidated accounts group

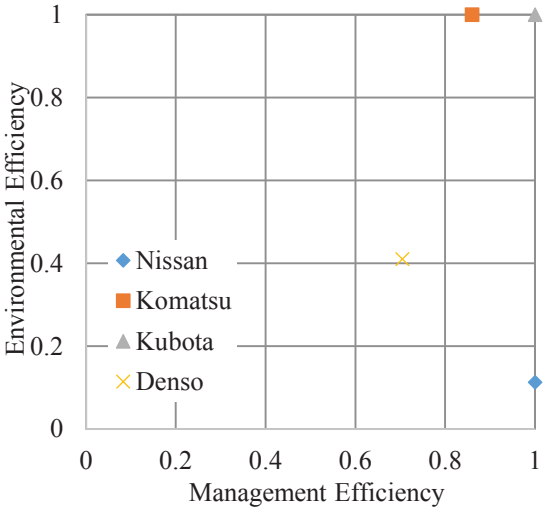

Figure3: The efficiency of consolidated accounts group

About 5 unconsolidated accounting companies, Isuzu was the most efficient company in terms of both activities. On the contrary to this, Kawasaki was the most inefficient company. As for environment activity, Kawasaki and Mitsubishi were proposed the improvement of all input variables and Mitsubishi and Hino were proposed large improvement of waste amounts and CO2 emissions. As for management activity, the reason why there are differences of management efficiency between Mitsubishi and Kawasaki, Yamaha is there are differences of the profit for constant resource input.

About 4 unconsolidated accounting companies, Kubota was the most efficient company in terms of both activities. On the contrary to this, Denso was the most inefficient company. As for environment activity, Nissan was proposed the improvement of all input variables and large improvement of CO2 emissions and waste water. Denso was proposed large improvement of amounts of energy and water. As for management activity, the reason why there are differences of management efficiency between Kubota and Nissan and Denso is Kubota made a moderate profit by a few inputs and Nissan made a large profit by a large inputs and Denso made a moderate profit by a large inputs.

3-2 The relationship between environmental activity and management activity

This section revealed the relationship between two efficiencies and corporate informations, the environmental management degree.

The company which is high in sales and the number of employees was lower in environmental efficiency. Several trends were revealed that management efficiency improved with a rise in net profit and sales except Nissan, Denso which theirs were by far high from others and the statistical significant difference of management efficiency among three groups which were distributed by net profit. The number of employees was the factor which decrease both efficiencies. There were positive correlations between Environmental efficiency, Management efficiency and Environmental management efficiency. These results were same in unconsolidated and consolidated accounting group. Contrary to expectation, environmental efficiency of the company which spend a large amount of the cost on Environmental preservation was low as figure4.

Using the environmental management degree which was evaluated by Nihon Keizai Shimbun, Inc, the relationship between the efficiency and synthesis score of five indexes (full marks 500 points) was verified in this sector. The company which is high in net profit is higher in the environmental management degree. About the relationship between the number of employee and the degree of environmental management, there were different tendencies between high and low degree groups. So this research focused individually.

The difference of the environmental management degree corresponds with the difference of account

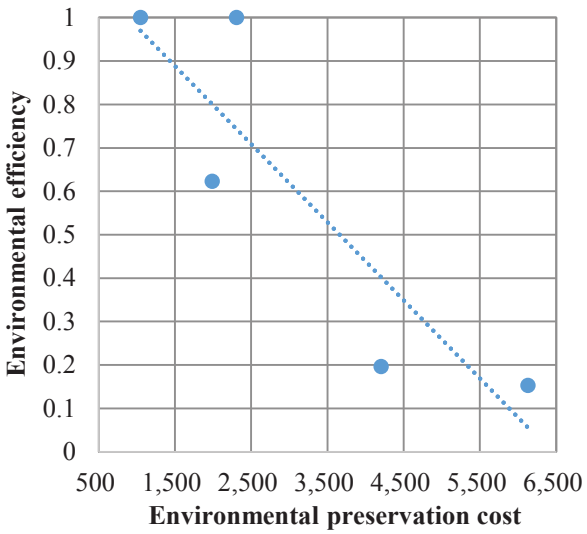

Figure4: Environmental efficiency and preservation cost

procedure and the degree of all consolidated accounting companies was larger than that of all unconsolidated accounts companies. Among consolidated accounts group, a company with large number of employees was higher in environmental management degree. On the contrary this, among unconsolidated accounting group, a company with small number of employees was higher in degree.

Although there are different efficiencies of Nissan, Denso and Komatsu in the consolidated accounts group, the environmental management degree was similar. The degree of Kubota is low although environmental and management efficiency is 1.0.

4 Conclusions

About the efficiency, if management efficiency increase, sales and net profit increase, but even if environmental efficiency increase, sales and net profit doesn`t increase, rather decrease. As an example, the environmental efficiency of the company which made a high profit was low in Nissan, Denso.

An inconsistency between efficiency and the environmental management degree was appeared a lot. Especially the efficiency of Nissan and Denso was very low although their degree was very high. The reason for this can be considered that there is difference between what this research wants to clarify with using efficiency which was defined and the meaning of evaluating with the environmental management degree. The environmental efficiency expressed whether the company can effectively treat input which affects environment and can reduce environmental burden as output in this research.

About a target company, there are different firm sizes, so it was difficult to handle as same group. Especially Nissan, Denso, there are different characteristics from another companies. There were few comparable data in target companies, and a count range was different in consolidated and unconsolidated accounting group. So this research had to analyze with very few samples.

This research found that a large cost on Environmental preservation doesn`t contribute the improvement of environmental efficiency from the relationship between these two.

There was different tendency within 2 accounting groups in the relationship between the environmental management degree and the employee number. It is conceivable that consolidated accounts companies can afford to carry out environment management and a large extent of environmental consideration have been evaluated high than unconsolidated accounting companies from the result that the degree of environmental management of all consolidated accounts companies was larger than that of all unconsolidated accounting companies.

Further study

This research should consider how improvement of efficiency contributes to environmental management and focus on production volume and should concern about the selection of company and variable with considering the tradeoff of these. This research evaluated company activity with using the quantitative data, but comparing the evaluation of this research with actual environment activity is expected in the future.

Reference

[1]Richard Welford(1995) Environmental Strategy and Sustainable Development: The Corporate Challenge for the Twenty-first Century, Routledge

[2] Marc A.Levy (1995) “Is the Environment a National Security Issue?” International Security Vol.20 pp.35-62

[3] Kagata(2006) “An Empirical Study of the Relationship between Environmental Performance and Financial Performance” Journal of Policy Studies No.21 pp.121-142 (in Japanese)

[4] Kaneko, Nishitani, Fujii, Komatsu(2015) “Study on environmental policies and corporate behavior in the epoch of proactive corporate environmental management” Environmental Economics・Policy Research Vol.8, No1, 61-73(in Japanese)

CORRIDOR CHOICE OF TRANSIT CARGO TRANSORT IN LANDLOCKED COUNTRIES OF EAST AFRICA

Student Number: 14M18098 Name: Masashi SOTA Supervisor: Shinya HANAOKA

東アフリカ内陸国のトランジット貨物輸送における回廊選択

祖田　真志

本研究では、経済回廊の交通インフラ整備に関与するステークホルダーの役割と活動目的を特定し、エージェントベースモデルを用いてステークホルダー間の相互作用をモデル化した。東アフリカを対象とし、ケニアからウガンダに接続する北部回廊に標準軌の新規鉄道敷設を想定するシナリオ、地域共同体が東アフリカ地域内のインフラ整備を意思決定するシナリオ、外的変化を想定しないベースシナリオの比較により各回廊の輸送状況の変化を考察した。その結果、新規鉄道の敷設により他方の回廊の整備が促進されること、また地域共同体の整備計画策定によりステークホルダーの総収益と荷主の消費者余剰の合計である社会的便益が最大となることが実証された。

1. Introduction

Landlocked Developing countries (LLDCs) heavily depend on transport infrastructures in Transit Countries (TCs) to access to ports, since LLDCs are entirely enclosed by land. Transporting cargos to LLDCs requires multiple clearances and transloading from one mode of freight. These circumstances force LLDCs to face higher transportation cost and longer transport time than TCs. As a result, it negatively influences on LLDC's economic growth.

LLDCs face various complicated problems, such as poor interconnections due to inconsistency in technical standards of transport infrastructure, lack of interoperability caused by complicated custom procedures for international transport, and insufficient transport infrastructure (Arvis et al, 2011). Nevertheless, there is no fully functional transit regime to improve the situation LLDCs face, in spite of lots of measures implemented by various regional authorities. What is worse, LLDC's right to infrastructure development in transit countries are limited, even if LLDC attempts to develop it by themselves (United Nations, 2003). Consequently, LLDCs are placed at a competitively disadvantage to change the situation they are facing.

However, there is possibility of taking advantage of being LLDCs. Being surrounded by several countries, LLDCs have multiple route choices to the seaport. TCs can expect transit cargos from LLDCs can bring economic benefits for the market growth of the relevant industry. Taking this into consideration, TCs compete with each other for transit cargos. Utilizing the circumstances enables LLDCs to induce TCs to improve the situation of LLDCs transporting cargo to the seaport. This study thus clarifies whether LLDCs can take advantage of possessing multiple routes by developing the model to simulate stakeholders' interactions corresponding to corridor choice of transit cargo transport in LLDC under the competitive circumstances between TCs.

The objectives of this research are the following: (1) To identify the most influential factors for shippers' and forwarders' route choice, (2) To determine main stakeholders who can affect the performance of a corridor and clarify how each stakeholder affect it, (3) To develop model: each stakeholder's decision-making process and understand how transport network dynamically changes corresponding to stakeholders' decisions by Agent-Based Model (ABM). This research finally focuses on East Africa as a case study.

2. Methodology

2.1. Shippers' and forwarders' preference for route choice

Literature review enables to identify factors on which shippers put significance for route choice. Factors influencing route choice to seaport is split into two parts, ones related to port choice and hinterland transport to ports. The most influential factors relevant to port choice are quality of terminal operation, adequacy of infrastructure and frequency of shipping visits. As for the factors related to inland transport, the total logistic cost, transport time, time reliability and safety are regarded as important factors in the past studies.

Notwithstanding that a great number of factors related to port choice and inland transport identified in past studies, most of the factors have connections with transport time and transport cost. These two attributes are utilized for the estimation of cargo distribution on each corridor.

2.2. Stakeholder's interest and their relationship

Various kinds of stakeholders get involved in the development and maintenance of corridors. In case of corridor management, the willingness of each stakeholder to support the enhancement of corridor performance largely depends on the benefits they can obtain. In addition, each category of stakeholders focuses on different factors for the performance of corridors. Therefore, it is necessary to figure out each stakeholder's objective and roles in order to examine the transit

Table 1: Main stakeholders' primary interests

Stakeholders	Main interests
Shipper	- Consignment moved from origin to destination in the shortest possible time and at minimum cost - Safe transportation and handling
Forwarders	- Reduction in operating cost - Increase volume of cargo handled - Fast clearance process, Harmonization of documents
Port Authority	- Improve cargo throughput - Increase port utilization - Enhancing port competitiveness
Road Authority	- Asset preservation through axle load control. - Infrastructure cost recovery.
Railway Authority	- Recover the initial cost and ensure maintenance cost sustainably. - Enhance competitiveness to transport more cargo.

corridor development. Shippers, forwarders, port authorities, road authorities and railway authorities are selected as the main stakeholders for the reason that these stakeholders have strong influence on the important factors for shippers' and forwarders' route choice. The primary objectives and expectations of each category of stakeholders are summarized in the Table 1.

2.3. Agent-Based Model

This study adopts ABM on purpose of simulating stakeholders' interactions. ABM simulates actions and interactions among autonomous intelligent agents that can be seen as a system of capable of interacting independently within the environment. Utilizing ABM to this study enables to predict the stakeholders' reactions against other stakeholders' action and estimate shipper's route choice decided based on changed corridor's performance, which represent competitive situation between multiple corridors connecting LLDCs to ports in TCs.

2.3.1. Flow chart of the model

An overview of the model components and interconnections are shown in Figure 1, following recent studies. Trip distribution can be calculated with the stochastic model utilizing the concept of generalized cost. Generalized cost is composed of monetary and non-monetary unit, which is transport time in case of this study. On the basis of the trip distribution, traffic flow on each link can be calculated to estimate each transport authority's revenue and cost. Based on the revenues, each stakeholder make decisions on investment for capacity expansion and pricing to maximize their profit, providing an update network. These decisions are done once in a year. The modeling process iterates annually for 20 years. Economic growth is taken as exogenous variables because economic growth cannot be completely explained only by the corridor development. The transition of corridor performance is observed in terms of shippers' surplus, revenue of each agent, generalized cost and capacity of hinterland network and port facility.

2.3.2. Trip distribution

A multinomial logit model is used to estimate route choice of shippers. Travel disutility of OD i and path p is represented as Generalized travel cost (GC_{ip}) (Equation (1)).

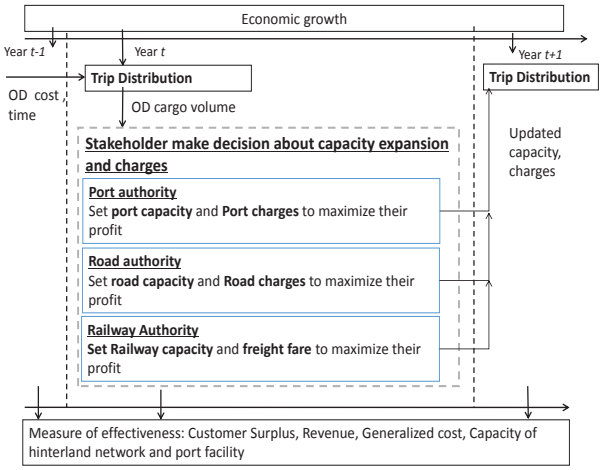

Figure 1: Flow chart of the model

The components of that defines travel disutility include port charge (PC_x), cost for hinterland transportation (C_{ip}), cost for crossing border (BC_x), Road Charge in RCs (RC_x) and monetary units of trip duration from ports to destination (D_{ip}). Let β_m and l_j denote fare per kilometer per TEU and the distance of link j, respectably. Cost for hinterland transportation (C_{ip}) can be expressed in Equation (2). Travel duration for a path p (D_{ip}) is defined as the dwell time of port x (t_x) and the sum of travel time for all links (Equation (3)). The dwell time of port (t_x) is represented by 'free flow travel time' ($t_{ff,x}$) and port throughput (Q_x) / the capacity (Kp_x) ratio. 'Free flow travel time' expresses ideal service time without port congestion. In second term of right hand side of Equation (3), the transport duration of link (t_j) is also similarly represented with 'free flow travel time' of links (t_j), cargo flow on each link (q_j) and capacity of each link (Kh_j)

The hinterland transportation paths are aggregated into a single link to avoid biased results because of different number of hinterland transportation paths per port. A formulation of the generalized cost for port n is shown in Equation (4). In this equation, θ represents the spreading parameter. Cargo distribution from TCs and LCs are represented in Equation (5). Let Q_n be trade volume of country n. From Equation (5), (6), cargo flow on each link (q_j) as well as volume of cargo (Q_x) each port handle can be obtained.

$$GC_{ip} = \sum_x (PC_x + BC_x + TC_x)\delta_{xp} + C_{ip} + \alpha_{vot} \cdot D_{ip} \quad (1)$$

$$C_{ip} = \sum_j \sum_m \beta_m l_j \delta_{mj} \delta_{jp} \quad (2)$$

$$D_{ip} = t_x + \sum_{jj} t_j \delta_{jp}$$

$$= t_{ff,x}\left(1 + \sigma_1 \left(\frac{Q_x}{KP_x}\right)^{\sigma_2}\right) + \sum_j t_{ff,j}\left(1 + \sigma_1 \left(\frac{q_j}{Kh_j}\delta_{jp}\right)^{\sigma_2}\right) \quad (3)$$

$$GC_i = \sum_p^{\Pi_{i,p}} \frac{GC_{ip} \cdot exp(-\theta \cdot GC_{ip})}{\sum_p^{\Pi_{i,p}} exp(-\theta \cdot GC_{ip})} \quad (4)$$

$$q_{ip} = Q_n \cdot \frac{exp(-\theta \cdot GC_{ip})}{\sum_p^{\Pi_{i,p}} exp(-\theta \cdot GC_i)} \quad (5)$$

$$q_j = \sum_i \sum_p q_{ip} \delta_{jp} \delta_{pi} \quad (6)$$

$$Q_x = \sum_j \sum_p^{\Pi_{p,i}} q_{ip} \delta_{xp} \quad (7)$$

2.3.3. Stakeholder's objective function

A) Port Authority's profit

The profits generated by Port Authority is calculated based on total revenue from port charge (PC_x^y) minus operating cost and capacity expansion cost of port. The total cost for the operation and maintenance cost is represented with port capacity (Kp_{xy}) and marginal capacity cost (M_{port}) representing marginal production cost to increase one unit of capacity.

$$MAX \quad \pi_x(PC_x^y, Kp_x^y) = PC_x^y \cdot Q_x - M_{port} \cdot Kp_x^y \quad (8)$$

Subject to: $0 \le PC_x^y \le 2PC_x^0$ (9)

$$Kp_x^{y-1} \le Kp_x^y \quad (10)$$

B) Road Authority's profit

The profits of Road Authority is calculated based on total revenue from collecting road charge (TC_n^y) minus operating cost and capacity expansion cost of road. Let M_{road} and $Kh_j{}^y$ denote marginal capacity cost and capacity of link j,

respectively.

$$MAX\ \ \phi_n\left(RC_n^y, Kh_j^y\right) = RC_x^y \cdot q_j - \sum_j^{\Pi_{j,n}} M_{road} \cdot Kh_j^y \delta_{mj} \quad (11)$$

Subject to: $0 \le RC_n^y \le 2RC_n^0$ (12)

$$Kh_j^{y-1} \le Kh_j^y \quad (13)$$

C) Railway Authority's profit

The profits of railway are calculated based on the revenue composed of freight fare ($\beta_m{}^y$) minus operating cost and capacity expansion cost of railway. The first term of right hand side denotes revenue from freight fare. Let M_{road} and $Kh_j{}^y$ denote the marginal capacity cost of railway and capacity of link j, respectively.

$$MAX\ \psi_n\left(\beta_m^y, Kh_j^y\right) = \sum_j^{\Pi_{j,n}} \beta_m^y \cdot l_j q_j \delta_{mj} - \sum_j^{\Pi_{j,n}} M_{rail} \cdot Kh_j^y \delta_{mj} \quad (14)$$

Subject to: $0 \le \beta_n^y \le 2\beta_n^0$ (15)

$$Kh_j^{y-1} \le Kh_j^y \quad (16)$$

2.3.4. Solution algorithm

This study develops the heuristic approach for each transport authority to identify the optimal pricing and capacity. It is assumed that the capacity and charges of other transport authorities will remain unchanged at the point optimal pricing and capacity are calculated for each authority. Constrained maximization problem in Equations (8)-(10), (11)-(13) and (14)-(16) are transformed into an unconstrained maximization with penalty functions as follows:

$$\Pi_x(PC_x^y, Kp_x^y) = \pi_x(PC_x^y, Kp_x^y) - c_x\left(max^2\{0, PC_x^y - 2\,PC_x^0\} + max^2\{0, Kp_x^{y-1} - Kp_x^y\}\right) \quad (17)$$

$$\Phi_n\left(RC_n^y, Kh_j^y\right) = \phi_x\left(RC_n^y, Kh_j^y\right) - c_n\left(max^2\{0, RC_n^y - 2\,RC_n^0\} + max^2\{0, Kh_j^{y-1} - Kh_j^y\}\right) \quad (18)$$

$$\Psi\left(\beta_m^y, Kh_j^y\right) = \psi_n\left(\beta_m^y, Kh_j^y\right) - c\left(max^2\{0, \beta_m^y - 2\,\beta_m^0\} + max^2\{0, Kh_j^{y-1} - Kh_j^y\}\right) \quad (19)$$

c_x, c_n and c are a penalty parameter. Variables that are not satisfied with constraints influence variables through a penalty that equals to the square of the violation. If the value of penalty parameter is appropriately large, the augmented objective function avoids a penalty and produces optimal value following constraints.

In order to solve this augmented objective function, Hooke – Jeeves pattern search, one of the pattern search methods, is utilized into this study (Hooke *et al*, 1961). The algorithm for each transport authority's profit can be shown in Figure 2. As initial step, select initial charges/freight fares and capacity. Initial value for penalty parameter is set. As iterative step, the Hooke-Jeeves pattern search technique is used to find the equilibrium solutions for each transport authority's profit. For every movement of variables, cargo flows and profits of transport authority are calculated to get closed to the optimal value. If the constraints are not satisfied, increase the value of penalty parameter by γ (γ = 5 in this research) and back to the iterative step.

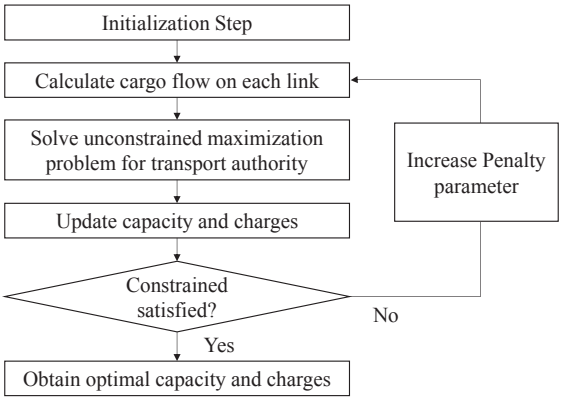

Figure 2: Solution Algorithm for each transport authority

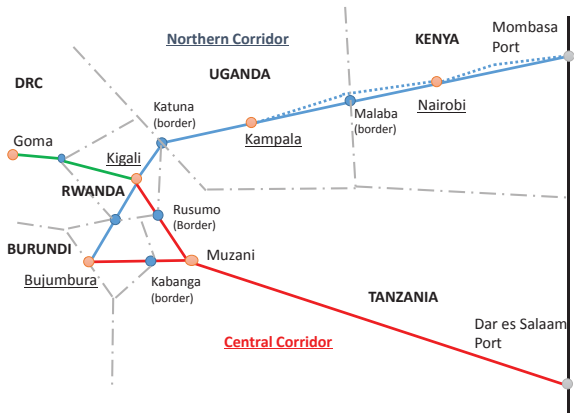

Figure 3: Simplified network in East Africa

3. Case Study

3.1. Inputs for the simulation

This study applies the developed model to East Africa as case study. In order to make the network reflects the current situation simply without compromising, the network in Figure 3 is assumed in this study. Blue and Red Solid line represent the road network of the Northern Corridor and Central Corridor, respectively. Blue dot line shows railway network. Blue dots represents national border and red dots are capital city of countries. In case of DRC and Tanzania, Goma and Muzani are recognized as representative city.

This simulation sets assumptions as follows;

- Representative city of each country except borders in Figure 3 are origin of export and destination of import.
- Import cargos of each country come from one of the ports and export cargos of each country go to one of the ports.
- Cargo volume of each country will increase as shown in Table 2.

Table 2: Average annual trade growth 2015-2030

	Import (%)	Export (%)
Kenya	7	5
Tanzania	7	7
Uganda	4	6
Rwanda	6	12
Burundi	3	9
Eastern DRC	7	13

3.2. Scenario building

A) Base case scenario

There is no exogenous change other than trade growth.

B) Railway expansion scenario in Northern Corridor

This scenario assumes project scheduled to be implemented. This project is planning to construct a standard gauge railway network connecting their countries from the Port of Mombasa. Corresponding to actual plan, this study expects the capacity of the line between Mombasa and Nairobi will be 12.95 million ton per year at 2017, and the capacity between Nairobi and Kampala will increase to 1.66 million ton per year at 2019. In addition, this scenario assumes free flow transport speed of each railway link will be half when this project is finished.

C) Organization restructuring

This scenario assumes that there is one regional organization authorized to operate the complete system of ports and hinterland networks, controlling capacity expansions and pricing of all transport modes. Pricing and investments decision for ports and hinterland networks are decided based on the objective function of the regional organization, Equation (20). The left hand side of the Equation is the social benefit as the sum of total profits from ports, roads and railway, and shippers' surplus. The first three terms of the right hand side are the profits from ports, roads and railway, respectably. The fourth term of the Equation is consumers' surplus between year 1 and year *t*, which is approximated by the rule of half.

$$\text{Max } SW = \sum_x \pi_x + \sum_n \phi + \varphi + \sum_i \sum_p \frac{(Q_{ip}^0 + Q_{ip}^t)(GC_{ip}^0 - GC_{ip}^t)}{2} \quad (20)$$

In case of organization restructuring, two scenarios are assumed depending on maximum annual capacity growth.

C-1) Regular investment scenario

Maximum annual capacity growth is less than 10%

C-2) Progressive investment scenario

Maximum annual capacity growth is less than 20%.

3.3. Results

The results of scenario are compared herein. Table 3 shows the capacity change on each scenario In case of "Railway expansion scenario", more capacity expansion occurs in both of the ports and roads except roads connecting cities in TCs and ports. In addition, transport facilities in Central Corridor are improved. Considering this phenomena, railway expansion has an influence on the development of Central Corridor. Stakeholders relevant to Central corridors take actions to enlarge the capacity, in order to prevent cargo in LLDCs from choosing Northern Corridors. In both scenarios of "Organization restructuring", all transport infrastructure's capacities will be expanded than "Base case". However, investment allocation is different in scenarios of "Organization restructuring". While investment is focused on road expansion in "Regular investment scenario", railway capacity expansion is done in "Progressive investment case.

Table 4 summarizes authority's benefit and shippers' surplus at the end of simulation. Comparing "Base case scenario" with "Railway expansion scenario", railway authority's benefit dramatically increases owing to increased volume of cargo. The situation for shippers is also improved as shown in the decrease of shippers' surplus. Regarding both scenarios of "Organization restructuring", shippers' surplus is remarkably improved. Especially, the circumstances for shippers in LLDCs become better off. As a result, social benefit is higher than other two scenarios, despite its low revenue.

Table 3: Capacity change on each scenario at 2035

(mil.TEU/year)	Initial inputs	Scenario A	B	C-1	C-2
Port					
Mombasa	20.03	35.21	38.43	111.36	128.07
Dar es Salaam[1]	10.14	36.57	40.01	56.38	63.81
Road					
Mombasa-Nairobi	22.05	34.96	23.98	72.78	44.74
Nairobi-Malaba	7.89	7.89	8.64	21.16	16.31
DES-Muzani	6.64	13.50	24.83	29.17	28.61
Muzani-Kabanga	0.31	0.32	8.64	0.38	0.44
Muzani-Rusumo	2.21	3.67	12.64	4.82	4.99
Railway					
Mombasa-Nairobi	1.00	1.34	44.13	6.12	25.92
Nairobi–Kampala	0.13	0.27	4.04	0.70	3.24

Table 4: Authority's benefit and shippers' surplus at 2035

(mil. $/year)	Scenario A	B	C-1	C-2
Authority's Benefit				
Mombasa Port	1,317	1,379	855	824
DSM Port	798	726	432	439
Kenya Road	1,131	393	-188	-91
Tanzania Road	562	500	-60	-28
Railway	343	4,865	232	1,256
Shippers' Surplus				
TCs	-13,594	-69	3,667	6,843
LLDCs	-6,027	-2,904	9,835	11,331
Social benefit	-15,468	4,892	14,744	20,575

4. Conclusion

The transition of corridor performance is observed from the results of the simulation. Firstly, in "Base case scenario", the corridor performance 20 years later gets worse than current situation. Management structure where each transport authority only cares about their benefits isn't efficient management structure in this case. The results of Railway expansion scenario show that the development of one corridor can induce the other corridor's development. Even though the expansion of railway on the Northern Corridor does not directly influence the Central Corridor, transport authorities that belong to the Central Corridor take actions to expand capacity more than Base Case Scenario. The results of "Organization restructuring" indicate this management structure can be more effective than railway expansion in terms of social benefit. The removal of inconsistency in each stakeholder's actions contributes to the efficient development of the corridors. Given the situation where stakeholder's motivation are interacted each other, organization restructuring itself is unrealistic. However, the results show that organization restructuring can lead to better circumstances than inconsistent investment done by each stakeholder.

References

[1] Arvis, J., Carruthers, R., Smith, G., and Willoughby, C., 2011. Connecting Landlocked Developing Countries to Markets, The World Bank, Washington, D.C.

[2] United Nations, (2003). Transit transport issues in landlocked and transit developing countries, Economic and Social commission for Asia and the Pacific Landlocked developing counter series, No.1

[3] Hooke, R., Jeeves, T. A., 1961. Direct search solution of numerical and statistical problems, Journal of the ACM, 8, 212–229

STUDY ON THE SUSTAINABLE MANAGEMENT AND USE OF PARTICIPATORY EDUCATION DATABASE: CASE OF NATIONAL EDUCATION SYSTEMS AND POLICIES IN ASIA-PACIFIC (NESPAP) OF UNESCO

Student Number: 13M51508 Name: Takero INOUE Supervisor: Shinobu YAMAGUCHI and Jun-ichi TAKADA

参加型教育データベースの持続的運用及び利用に関する研究: UNESCO の National Education Systems and Policies in Asia-Pacific の事例を用いて

井上毅郎

情報通信技術の活用による情報共有の一環として、ユネスコは参加型教育政策データベース NESPAP を開発した。本研究は NESPAP の持続的な運用およびユーザーのより積極的なコンテンツの提供を目的とし、運用体制の設計およびユーザーの利用動機の調査を行った。分析の結果、運用は役割毎に個別のスタッフが担当することが効果的であり、ユーザーは NESPAP へのコンテンツ提供を重要かつ知識向上に役立つと考えていることが明らかになった。

1 Introduction

UNESCO has a policy to promote universal access to information [1]. Following this policy, UNESCO Regional Bureau for Education in Asia and the Pacific (UNESCO Bangkok) has developed a participatory, National Education Systems and Policies in Asia-Pacific (NESPAP), to promote discussion on education development in UNESCO's networks in the Asia-Pacific region and beyond.

Tokyo Institute of Technology (Tokyo Tech) has been collaborating with UNESCO Bangkok in the development and management of NESPAP since 2013. The joint team identified three problems: 1) the originally developed platform was not suitable for the sustainable management and maintenance; 2) the usability of the website was low; and 3) the software architecture was too complex.

Further, there are two challenges in establishing a sustainable mechanism to manage and maintain NESPAP. First, limited resources were available. Second, there is a need for defining workflows for staff members of UNESCO Bangkok can constantly engage in managing and maintaining the database.

It is also necessary to update the content of NESPAP reflecting users' motivations. It is because users' motivation should be a key driver to make them contribute their knowledge and skills for no monetary rewards. However, little is known about why education experts contribute their expertise to the content of participatory databases.

Given this background, the research objectives are to focus on two aspects related to NESPAP. First, this study identifies factors of sustainable management and maintenance of NESPAP. Second, this study investigates users' motivations to participate in the education database.

2 Literature review

2.1 Web content management

With the Web changing into large and rapidly changing sites, there is a growing need to understand content management of a website. McKeever (2003) provided a framework of the web content management lifecycle [2]. The framework defines two iterative stages of web content lifecycle, namely, the collection of content and the delivery or publishing of that content. NESPAP is a combination of different functions, and users can contribute different types of content. In order to develop workflows that are effective in the management of such complex content, the analysis of NESPAP needs to consider frameworks for web content management. McKeever's web content management lifecycle is suitable in the research context because the framework considers simultaneous processes of multiple content collection and delivery.

2.2 Evaluation of websites

Nakagawa et al. (2001) proposed the Web Usability Scale (WUS) to obtain quantitative information of users' perceptions on the usability a website [3]. The evaluation is developed based on multiple existing survey methods. WUS covers seven factors of the usability: familiarity, usefulness, reliability, operability, configuration, readability and responsiveness. WUS is suitable for evaluating NESPAP because it covers a broad range of the usability of a website, and thus, can be used to perform a comprehensive analysis of the website of the database.

2.3 Volunteer Functions Inventory

There is a growing attention on why people participate in user-generated content (UGC) outlets such as YouTube and Wikipedia since UGC is created by users' voluntary contribution [4][5]. Clary et al. (1998) created Volunteer Functions Inventory (VFI) to understand volunteers' motivation [6]. The VFI defines six motivations to

volunteer, namely Values, Understanding, Social, Career, Protective and Enhancement. The VFI has been widely adopted to study people's voluntary behaviors, including participation in UGC outlets [7][8].

Houle et al. (2005) applied this framework to examine the relationship between people's volunteer motivations and specific volunteer tasks [9]. Two major findings are emphasized: 1) different tasks can be characterized by different motivations; and 2) people choose tasks that serve their specific motivations. The framework is a good reference to explore the relationship between the use of NESPAP functions and users motivations.

3 Methodology

3.1 Research objectives and questions

This study focuses on two aspects related to NESPAP. First, this study identifies factors of sustainable management and maintenance of NESPAP. Second, it investigates users' motivations to participate in the education database. To achieve these objectives, this research aims to answer specific research questions as follows:

1) What are the factors that affect the sustainable management of online education research database?
2) What motivations drive people to participate in online education research databases?

3.2 Research framework

Regarding the management and maintenance of NESPAP, this study adopts McKeever (2003)'s web content management lifecycle to develop workflows to be followed by UNESCO staff members. In addition, this study conducts a questionnaire survey, based on Web Usability Scale, to capture users' perception toward the database. Regarding research objective two, for users' participation, this study incorporates Clary's Volunteer Functions Inventory (VFI) to explore the relationship between users' specific motivations and functions of NESPAP.

3.3 Research process

3.3.1. General framework

The research process is composed of three phases. Phase I focuses on data collection. This phase includes four steps: 1) discussion on roles for the management and maintenance; 2) development of the software system of NESPAP; 3) survey on the usability of the database, based on WUS; and 4) survey based on people's participation motivations, based on VFI.

Phase II focus on the analysis of data. This phase includes three steps: 1) analysis on the management and maintenance of NESPAP; 2) analysis on people's motivation to participate in NESPAP; and 3) interpretation of the results.

Phase III related to the application to UNESCO activities consists of three steps: 1) discussion on the promotion of NESPAP at UNESCO Bangkok; 2) development of manuals; and 3) training of staff members of UNESCO Bangkok.

3.3.2. Survey based on Web Usability Scale

Two questionnaires are conducted to analyze users' perception toward NESPAP, covering seven factors defined in WUS: familiarity, usefulness, reliability, operability, configuration, readability and responsiveness. The questionnaires employ a 5-point symmetric Likert scale, ranging from "Strongly agree" to "Strongly disagree". Respondents also indicate other web services that they use, and provide comments for NESPAP improvement. Mean value and frequency are calculated in the analysis.

3.3.3. Survey based on Volunteer Functions Inventory

A questionnaire is conducted to analyze users' motivation to participate in the database. The questionnaire employs the six motivations of VFI: Values, Understanding, Social, Career, Protective and Enhancement (Table 1).

The questionnaire is composed of three parts. First, respondents indicate how likely they plan to use seven functions of NESPAP. Second, participants indicate how much each motivation drives their use of each function. A 5-point Likert scale is used, ranging from "Very much" to "Not at all". Third, they provide demographic information.

For analyzing data, demographics are examined by frequency. Mean value analysis is conducted for likelihood to use specific functions of NESPAP, and motivations in the use of functions.

Table 1 Six motivations of VFI (Source: Clary et al., 1998, pp. 1517-1518 [6])

Motivation	Description
Values	Expressing or acting on important values
Understanding	Learning more about the world and/or exercise skills that are often unused
Social	Strengthening one's social relationship
Career	Gaining career-related experience
Protective	Reducing negative feelings, such as guilt, or for addressing personal problems
Enhancement	Growing and developing psychologically

4 Analysis and interpretation

4.1 Analysis and interpretation on sustainable software system

4.1.1. The roles for the management and maintenance

Multiple discussions identified four roles and their specific tasks in managing and maintaining NESPAP, IT administrators, content moderators, users and visitors. IT administrators are responsible for maintaining the software system, and content moderators are in charge of maintaining the quality of the contents and activities in the education database. The users are expected to contribute to the contents in addition to participating in site activities, and the visitors do not have site account and thus can only view the site contents.

Specific tasks for each roles are as follows. IT administrators update software (the system core, plug-ins,

and theme), make back-ups, and restore the system. Content moderators validate user-contributed contents and update site contents. Some content moderators are also in charge of assigning and designing other content moderators. Users view and add contents, and participate in other site activities such as discussion with other users. Finally, visitors view contents.

4.1.2. Development of the software system of NESPAP

In developing and improving NESPAP, two basic principles were agreed: 1) to explore system platforms which require a minimum amount of maintenance effort; and 2) to consider two approaches, namely WordPress (CMS) and mashup (web application hybrid) as potential solutions.

These two solutions were compared from the perspective of regular maintenance, bug fixing, quality of service, simplicity of software and compliance with organization policy. WordPress was selected as the solution because bug fixing was easy and software was simple. It also allows storing the site data at UNESCO, which complied with the organization's policy about the location of data storage.

The implementation took two steps for developing the database. First, eMap, eForum and eResources were implemented. Second, ESP and two new components, namely eJob (job board) and eConf (event management system) were implemented.

4.1.3. Survey based on Web Usability Scale (WUS)

The first survey was conducted with members of a UNESCO's regional education network in November 2014. Respondents included education experts from 14 countries and regions in the Asia-Pacific. A total of 43 questionnaires were distributed, and 26 were returned, yielding a response rate of 60.5%. The second survey was conducted between October and November 2015. Email with a link to the survey was sent to those who have experience of using NESPAP. Questionnaires were distributed to 65 education experts, including 25 staff members of UNESCO Offices. A total of 24 were returned, yielding a response rate of 37.5%.

Analyzing two questionnaires, there are five major findings. First, the participants had a good impression on the website, especially its design and contents. Second, the website's configuration (site structure) and responsiveness were the points of improvement. Third, among six components, ESP, eForum and eResources were identified popular components. Fourth, the participants found most NESPAP functions useful. Fifth, functions for recruitment (eJob) were found less attractive among users.

4.2 Analysis and interpretation on users' participation motivations

4.2.1. General outline

The VFI survey was conducted with 36 education experts in November 2014 and 42 staff members of UNESCO Bangkok in February 2015. A total of 78 questionnaires were distributed, and 50 were returned, yielding a response rate of 64.1%.

Summarizing demographics, most respondents identified themselves as researcher, followed by professor. Gender, age, years of experience in the education field were diverse. Fifty-eight percent of them had experience of exchanging and sharing knowledge online. Seventy-nine percent of the participants spend five or more hours on computer and other devices per day.

4.2.2. Likelihood to use seven functions of NESPAP

There were four major findings from the mean value analysis. First, participants gave relatively higher ratings to four functions, namely sharing documents, creating online group, sharing news and discussing specific topics. Second, a function for sharing documents showed the highest score, indicating that users are most interested in utilizing NESPAP to share their documents and information. Third, respondents are interested (mean score over four) in three functions for creating user groups, sharing news and discussing specific topics. This can be interpreted that users are interested in activities about specific events, projects and topics. Fourth, a function for recruitment showed the lowest score, implying that participants were less interested in using NESPAP for recruitment purposes.

4.2.3. Motivations in the use of functions

There were three findings from the result (Table 2). First, the motivation related to "Understanding" and "Values" had highest mean values, 3.90 and 3.84, respectively. This implies that these are the most important motivations of the respondents. Second, scores related to "Social" and "Career" motivations were relatively high, 3.49 and 3.44, respectively. Third, scores related to "Protective" and "Enhancement" were relatively low, 2.42 and 2.65, respectively.

Table 2 Mean scores on motivations in the use of functions

Function\ Motivation	Val-ues	Under-standing	So-cial	Ca-reer	Pro-tec-tive	En-hance-ment
Discussion (general)	3.91	4.10	3.47	3.52	2.26	2.63
Discussion (specific)	3.73	4.02	3.51	3.53	2.47	2.70
Online group	3.89	4.02	3.60	3.44	2.36	2.73
Sharing documents	4.09	4.02	3.38	3.33	2.36	2.73
Self-archiving documents	3.59	3.80	3.25	3.18	2.45	2.51
Sharing news	4.07	3.95	3.66	3.41	2.50	2.66
Recruitment	3.59	3.39	3.57	3.64	2.52	2.57
Mean	3.84	3.90	3.49	3.44	2.42	2.65

4.2.4. Relationship between the likelihood to use functions and motivations in the use of functions

Correlations were computed between the two sets of items: mean scores on participants' likelihood to use functions, and average mean scores for each motivation regarding the use of functions. The result showed that

"Values", "Understanding" and "Social" were significantly correlated with all functions at the 0.01 level (Table 3). The motivation of "Career" were significantly correlated with all functions except "discussion (specific)" (.390). "Protective" was significantly correlated with "discussion (general)" (.409), "discussion (specific)" (.464) and "self-archiving documents" (.420). "Enhancement" was significantly correlated with "discussion (general)" (.478), "discussion (specific)" (.425), "self-archiving documents" (.564), "sharing news" (.522) and "recruitment" (.415)

There were two findings. First, the motivations of "Values", "Understanding", "Social" and "Career" were significant in relation with people's likelihood to use functions of NESPAP. Second, the motivations of "Protective" and "Enhancement" were only partially significant in the use of functions.

Table 3 Relationship between likelihood to use functions and motivations in the use of functions

	Values	Under-standing	So-cial	Ca-reer	Pro-tective	Enhance-ment
Discussion (general)	.700**	.657**	.517**	.434**	.409**	.478**
Discussion (specific)	.648**	.603**	.516**	.390*	.464**	.425**
Online group	.608**	.685**	.627**	.595**	.383*	.384*
Sharing documents	.628**	.689**	.632**	.547**	0.187	0.289
Self-archiving documents	.549**	.582**	.653**	.764**	.420**	.564**
Sharing news	.659**	.679**	.743**	.733**	.380*	.522**
Recruit-ment	.526**	.541**	.696**	.668**	.350*	.415**

**. Correlation is significant at the 0.01 level (2-tailed).
*. Correlation is significant at the 0.05 level (2-tailed).

4.2.5. Interpretation

Analysis on the likelihood of using different NESPAP functions suggests that functions oriented for specific topics, events and projects are more likely to be used.

Analysis on participants' motivations in the use of functions indicated that people participate in NESPAP because it is valuable and it is knowledgeable. Relationship between likelihood to use functions and motivations in the use of functions indicates that people with the "Values", "Understanding", "Social" and "Career" motivations are more likely to use NESPAP.

5 Discussion and conclusion

This study focused on two aspects of a participatory education database, namely, sustainable management and maintenance, and users' motivation to participate in online education database.

Study on the sustainable management and maintenance of NESPAP identified that McKeever's web content management lifecycle as a useful reference when developing the workflows. This study also demonstrated that WUS can be applied to evaluate a website which has been just launched. The study utilized Clary's VFI to analyze influence of users' motivation to participate. VFI was found to be a valuable reference when exploring the motivation of a group of users of educational database.

Future studies is suggested to increase the sample size including different group of respondents such as school teachers and principals to achieve a more comprehensive coverage.

The result is expected to contribute to the literature on utilizing UGC in international development as well as to the practitioner involved in participatory education database.

References

[1] UNESCO. (2005). UNESCO World Report: Towards Knowledge Societies. Retrieved from http://unesdoc.unesco.org/images/0014/001418/141843e.pdf

[2] McKeever, S. (2003). Understanding web content management systems: evolution, lifecycle and market. Industrial Management & Data Systems, 103(9), 686-692.

[3] Nakagawa, K., Suda, T., Zempo, H. & Matsumoto, K. (2001). The Development of Questionnaire for Evaluating Web Usability. Human Interface Society, 421, 424.

[4] Jenkins, H. (2009). What Happened Before YouTube. Retrieved from http://web.mit.edu/uricchio/Public/television/jenkins%20before%20youtube.pdf

[5] Ransbotham, S., & Kane, G. C. (2011). Membership turnover and collaboration success in online communities: Explaining rises and falls from grace in Wikipedia. MIS Quarterly-Management Information Systems, 35(3), 613.

[6] Clary, E. G., Snyder, M., Ridge, R. D., Copeland, J., Stukas, A. A., Haugen, J., & Miene, P. (1998). Understanding and assessing the motivations of volunteers: a functional approach. Journal of personality and social psychology, 74(6), 1516.

[7] Nov, B. O. (2007). What Motivates Wikipedians? Communication of the ACM, 50(11), 60–64.

[8] Fugelstad, P., Dwyer, P., Filson Moses, J., Kim, J., Mannino, C. A., Terveen, L., & Snyder, M. (2012, February). What makes users rate (share, tag, edit...)?: predicting patterns of participation in online communities. In Proceedings of the ACM 2012 conference on Computer Supported Cooperative Work (pp. 969-978). ACM.

[9] Houle, B. J., Sagarin, B. J., & Kaplan, M. F. (2005). A functional approach to volunteerism: Do volunteer motives predict task preference?. *Basic and applied social psychology*, *27*(4), 337-344.

ANALYZING THE IDEAL PROPERTIES OF DATA VISUALIZATION IN THE WORLD DEVELOPMENT REPORT

Student Number: 13M51543 Name: Ma. Sayori D. KARAKAMA Supervisor: Prof. Naoya ABE

Data visualizations (datavis) are used to transform raw data into something readable and understandable. Existing literatures show that evaluating datavis does not guarantee that readers are able to correctly comprehend its contents. This research aims to identify the ideal properties of datavis in the World Development Report (WDR) and recommend evaluation criteria for future authors, readers, and researchers. The Analysis of WDR figures, compilation of relevant literature findings, and trend analysis were performed to identify three properties. Those are color, size, and data sources, which are considered as some of the general ideal properties of datavis, color usage being the most important to portray the message of datavis to the readers. This understanding may contribute to the further enhancements of the World Development Report and other development related materials.

1 Introduction

1.1 Research overview

The World Development Report is an annual publication and considered as one of the major analytical publication of the World Bank where it focuses on a particular and important aspects of international development over the years (The World Bank, 2015). Other than WDR, there are more organizations who publish developmental reports such as the Human Development Report and Inclusive Wealth Report. The increase of developmental reports portrays that the world is facing more and more issues. The role of such reports is to provide updates or a message about what is happening to our world whether there is an improvement or none. There had been various means to address the message not only to the experts, but to the general audience as well. Other than reading the context of the reports, another way of delivering such messages is by the use of data visualization. Data visualization (datavis) can be briefly defined as the "visual representation of data or information using graphical techniques" aimed to communicate its message in any field and support people to amplifying cognition through visual means. Studies show that using visuals provide more insights and impact to the readers (Cukier, 2010).

The WDR contains information about statistical data represented by either tables or visualized data through figures or graphs. This study aims to identify the trends of data visualization and its ideal properties in the WDRs by analyzing the figures present in the report. By tracing the development of data visualization in the report, on how the report represents its data, and how it changed over the years, future reports might be able to follow or refer to how WDR used its datavis to deliver a message to its readers. Although, it can be argued that the visualized data in the report may have flaws such as the figures might be difficult to understand especially for the general audience. Earlier releases of WDR did show such problems in their use of data visualization. Later releases, on the other hand, showed improvements especially with the use of colors. Some existing development-related reports might be facing the same problems as WDR used to have. Therefore, it is important to learn the development of datavis in the WDR so that current or future reports may refer to it and have insights on how to improve their use of data visualization. This research aims to contribute to the authors or organizations of developmental reports and to the researchers of data visualization itself.

2 Literature Review

2.1 History of Data Visualization

The birth of data visualization can be traced back before the 16th century where there was a trend for geometric diagrams and maps to aid in navigation and exploration (Friendly, 2007). Data in this context refers to facts, numbers, or records. Over the years, visualization had evolved to a more complex yet useful form supporting demographic statistics, decision-making, and communication.

2.2 Data Visualization Properties and Evaluation Criteria

Data visualization studies show that there is scare information on how to evaluate data visualization (Plaisant, 2004). Kelleher and Wagener (2011), however, provided ten proposed guidelines for effective data visualization to reduce common pitfalls in the pursuit to effective convey information in the context of scientific publications and presentations:

1. Create the simplest graph that conveys the information you want to convey.
2. Consider the type of encoding object and attribute used to create a plot.
3. Focus on visualizing patterns or on visualizing details, depending on the purpose of the plot.
4. Select meaningful axis ranges.
5. Data transformations and carefully chosen graph aspect ratios can be used to emphasize rates of change for time-series data.
6. Plot overlapping points in a way that density differences become apparent in scatter plots.
7. Use lines when connecting sequential data in time-series plots.
8. Aggregate larger datasets in meaningful ways.
9. Keep axis ranges as similar as possible to compare variables.
10. Select an appropriate color scheme based on the type of data.

Arslan and Toy (2014) specified colors, fonts, formats, layouts and icons play an important role in visualization and analyzed the visual problems on infographics where the common challenges are layout mistakes, irrelevant colors, wrong choice of formats, overuse of pictographic icons, and off topic visual elements. Steele and Illinsky (2010) say, "color is one of the more abused and neglected tools in data visualization" implying that every used

color in any graphic should serve a purpose of clarifying the meaning of the content. Sperandei (2014) and Finan (2015) stressed that graphic presentations are powerful instruments for the communication of research results and are also prone to misunderstanding and manipulation. Every aspects of graphic design such as scales, color, and shapes can influence how results are interpreted (Sperandei, 2014).

This study applied the proposed ten guidelines as reference and modified it accordingly to match the datavis characteristics of the WDR. Thus, leading to the formulation of data visualization evaluation criteria that can be applied in the WDR and other development related materials.

3 Research Methodology

3.1 Overview

The WDR annual publications from 1978 to 2015 were purposively selected as the main source of data as it features a long history of international development reports catering several examples of data visualization (datavis) showing how it evolved through time. There are a total of 37 WDRs. Report from 1999 was not included as some releases included report from two years (1998-1999, 1999-2000, and 2000-2001) and was therefore represented by 1998, 2000, and 2001 respectively.

Table 1: Summary of dataset in WDR figures

<table>
<tr><td>Observations</td><td>1,370 figures</td></tr>
<tr><td>Source</td><td>WDR 1978 – 2015</td></tr>
<tr><td>Dataset</td><td>
Figure Color data
· Number of colors used per report
· Mean and Mode of color usage
· Maximum and Minimum number of colors
· Meaning of each color per report
<table>
<tr><th>Mean</th><th>Mode</th><th>Min</th><th>Max</th><th>Med</th></tr>
<tr><td>7</td><td>8</td><td>2</td><td>11</td><td>9</td></tr>
</table>
Figure Size data (in pixels)
* zoom size was set to 75% relative to letter size (215.9 mm × 279.4 mm) paper*
· Average figure height and width per report
· Minimum and Maximum height and width per report
For height (in pixels):
<table>
<tr><th>Mean</th><th>Mode</th><th>Min</th><th>Max</th><th>Med</th></tr>
<tr><td>410</td><td>N/A</td><td>279</td><td>603</td><td>324</td></tr>
</table>
For width (in pixels):
<table>
<tr><th>Mean</th><th>Mode</th><th>Min</th><th>Max</th><th>Med</th></tr>
<tr><td>366</td><td>333</td><td>192</td><td>508</td><td>374</td></tr>
</table>
Other data
· Data source inclusion in figures status (boolean)
</td></tr>
</table>

(Source: by the author)

The data collection involved collecting that figure and text data from the WDRs to analyze and identify the trends of data visualization and to determine the ideal properties of datavis as one of the objectives of this research. WDR contains several numerical data represented by either tables or visualized data through figures or graphs. Since the focus of this research is about data visualization, by definition is the "visual or graphical representation of data or information" from authors of several academic literatures, figures were selected as the datavis data. Data regarding the figure and table usage frequency were also collected for analysis to learn more about the usage of datavis in the WDR. A total of 1,370 figures listed on the table of contents of WDRs were collected. Table 1 shows a summary of what kind of data were extracted from the figures. Performing a thorough analysis of the all those figures required a huge amount of time. To overcome that ordeal, specific topics were selected based on the extracted frequency of keywords from the contents of the reports programmed in Ruby.

3.2 Keyword selection process

Keyword selection was a necessary part of this research to identify important topics in terms of international development to trace the trends on how data visualization evolved in the WDR and how were its properties different or similar over time. A keyword extraction tool was programmed to filter and extract the keywords from the text version of the reports. The program was iterated until the top results return distinguishable words, nouns, verbs, or adjectives. Results by the program were not fully accurate and would therefore be considered as an estimate. The estimated frequency of each unique keyword per report was then computed together with its accumulated occurrence in all the reports and was compared. The focus on women, health, and poor were the results of computing the frequency or occurrence of those terms in each report (see Figure 1) and comparing it to the general occurrence of those keywords in all the reports (see Figure 2).

It can be assumed that most keywords in the report can be regarded as important, but there are some which are exceptionally more significant than others. In the case of this research, it was measured by how frequently it was mentioned in the reports. For example, in the term "women", it appeared the most in the year 2012 where the topic was about "Gender Equality and Development", which was an obvious result since that was the focus of the report. However, it does not necessarily signify that the topic "women" is highly regarded in the WDR from 1978 to 2015. But in the case of the "women" keyword, it appeared on both Figure 2 and Figure 3, so we can conclude that the term was indeed highly regarded in the WDR in general. Another example was the keyword "climate". The term "climate" appeared the most in 2010 as the topic is about Climate Change. That was understandable. However, computing for its overall occurrence in the reports, it did not appear that much in the other WDRs. Although it was ranked 3rd in the keyword occurrence per report, it was barely mentioned in other reports. Whereas in comparison to the keyword "health", it appeared the most in year 1993, but also had frequent mentions in other years which means that it is one of the important topics in the WDR. Comparing the similar keywords on both tables, topics related to "women", "health", "jobs", "economic", and "poor" appeared on both. To further narrow it down further, the remaining 5 keywords were correlated to the MDGs to select the final 3 keywords to be used in this

study. MDGs indeed came to life in year 2000, but it covers several topics in development through its 8 goals. Topics regarding "women" were related to MDG goal 3: promote gender equality and empower women, and goal 5: improve maternal health. Topic about "health" was related to MDG 4, 5, 6. For keyword "jobs", it was not implicitly shown in the MDGs and was therefore screened out. The same case with the keyword "economic". Lastly, keyword "poor" was related to the MDG goal 1: eradicate extreme poverty and hunger. Therefore, "women", "health", and "poor" were selected as the final keywords to be used in this research to analyze the trend of datavis in those specific topics.

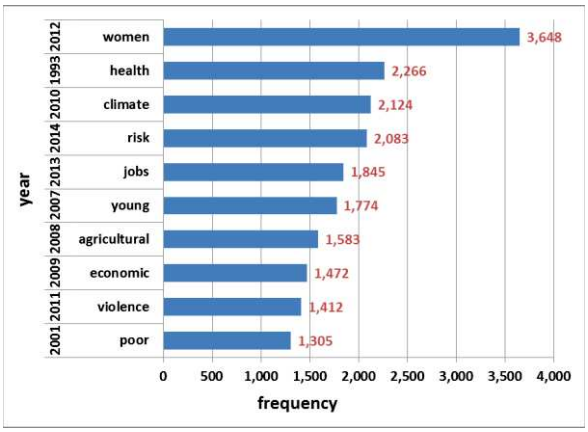

Figure 1: Results of estimated keyword occurrence per report (Top 10 results)

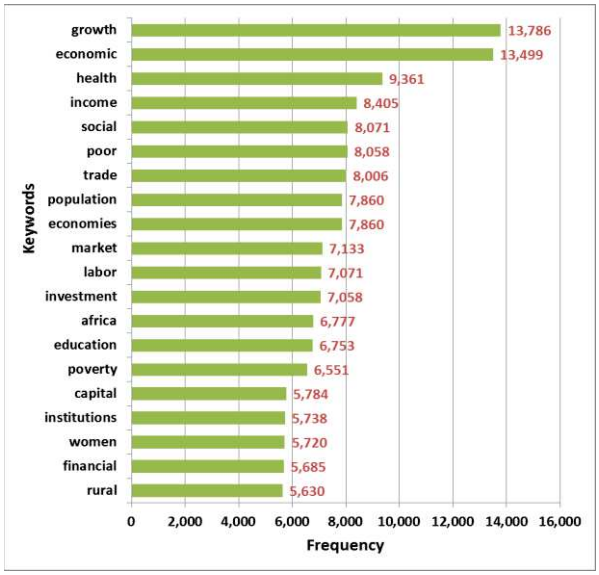

Figure 2: Results of accumulated keyword occurrence from all reports (top 20 results)
(Source: by the author)

3.2 Datavis Evaluation Criteria Formulation

Analyzed datavis trends in the World Development Report revealed its ideal properties and were used to create evaluation criteria applicable for the report. The 10 proposed guidelines for effective data visualization by Kelleher and Wagener (2011) from the literature review were also used as a reference to develop some evaluation criteria for the data visualization in the World Development report. Some of the proposed guidelines from Kelleher and Wagener (2011) were not applicable in the World Development Report and were therefore modified in accordance to its datavis properties.

4 Results and Discussion

4.1 Trends of data visualization in the WDR

There were three parts in the trend analysis in this research. Table 2 shows a summary of the different type of analyses performed in this research and the respective data used for each analysis.

Table 2: Data visualization analysis data usage

ANALYSIS	DATA USED
General Datavis Analysis	• Figure count • Table count
Figure Properties Analysis	• Color frequency • Figure size (height and width)
Specific Topic Analysis	• Keyword frequency • Color, Size, Data source

(Source: by the author)

In the general analysis, data in the WDR was represented with either tables or data visualization through figures that was why a comparison was made between the two (see Figure 3). Although WDR is a well-known report, it was possible that it was not making use of data visualization. By learning this trend, it can be known if the use of data visualization is a necessity or not for developmental reports, at least for the WDR.

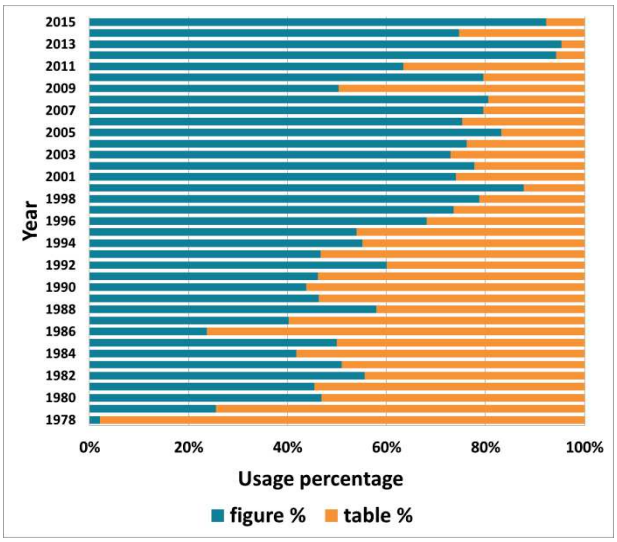

Figure 3: Comparison of figures and tables in the WDR (Source: by the author)

In case the result showed that the use of tables were more prominent even in the recent years, it might say that the use of tables might be more appropriate in such reports rather than data visualization through figures. But since it showed that the use of figures did increase and overtook the use of tables, it means that the World Bank sees that it was necessary or appropriate to use data visualization in the WDR, that tables alone are not enough to express the message of the data. Tables were used as frequently as figures in the earlier years. Changes started to occur from mid-1990s where data visualizations became more frequently used over the tables. The increase of data visualization usage can indicate that the topics in the World Development Report in the later years started to require more attention from its readers wherein tables alone were not sufficient to deliver the message.

The second part of the analysis was the actual observation of all figures per report. Data visualization properties were observed as to how it changed over the years. At first, all known datavis properties based from related literatures were taken into consideration such as dimension, color, size, fonts, graph scale, data source, and data labels. By observing the figures from each year, the most distinguishable changes in the datavis properties can be observed in the figure color usage, size, and data source availability. Trends can be observed from those datavis properties as to how the WDR changed over the years in terms of data visualization.

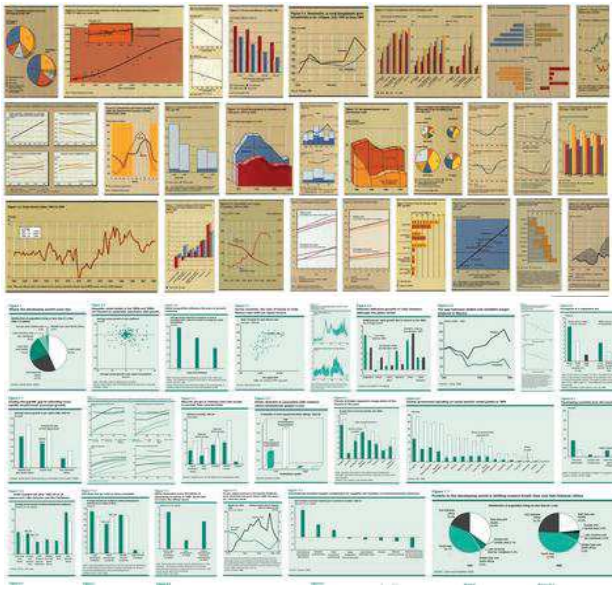

Figure 4: Sample compiled figures from year 1990 – Poverty (top) and 2001 - Attacking Poverty (bottom)
(Figures compiled by the author)

The third part of the trend analysis is to analyze the trends of data visualization regarding some important specific topics. Figure 4 shows an example of how the data visualization for the topic "poor" changed in year 1990 (Poverty) and year 2001 (Attacking Poverty). Both topics of those years were focused on poverty. It was evident that there was an improvement in the color usage. According to Steele and Iliinsky (2010), every used color in a graphic should serve a purpose of clarifying the meaning of the content. In the case of the datavis for keyword poor, the earlier year used around 8 different colors, but its usage was not clear as to what kind of message it wants to deliver to the readers. On the other hand, year 2001 used fewer colors that made the figures easier to read. However, the message of the colors was rather vague as well. There were some similarities observed on both sets. Although the uses of colors were not clearly defined, some certain colors were used to represent countries experiencing poverty that can be found consistent in all figures. In terms of figure size, both years used relatively large figures that occupies around half of a page in max that may imply that the larger the size, the more emphasis the authors wanted to make.

Overall observation of figures per WDR revealed data visualization properties applicable to the report. Three (3) datavis properties were deemed necessary to develop recommendable data visualization evaluation criteria for WDR. Those were color usage, size, and data sources. The color property showed the most pattern of usage in the figures of the reports by analyzing topics about women, health, and poverty. Answering the first objective of this study and identifying the properties of data visualization in the WDR lead to the development of datavis evaluation criteria (see Table 2) adequate for WDR.

Table 2: Proposed evaluation criteria based on the research results and findings

Criteria	Definition and properties	Guidelines
READABILITY	Focuses on the simplicity of the visualized figures composing of "size" and "color" properties.	- Create the simplest graph that conveys the information you want to convey. - Consider the size objects and attribute used to create a figure.
MEANINGFULNESS	Refers to the ability of the figure "colors" to portray the message of the report.	- Select an appropriate color scheme based on the type of data or information. - Focus on visualizing patterns or on visualizing details, depending on the purpose of the figure.
RELIABILITY	Refers to the validity of the visualized figures.	- Consider the validity and source of the data in the figure.

(Source: by the author)

5 Conclusions and Recommendations

Tables were commonly used in the earlier WDR to represent data and changed from mid-1990s where figures were more frequently used over tables which may imply that the World Bank sees that it was necessary or appropriate to use data visualization in the WDR where tables alone were not enough to express the message of the data. Analyzing the trends of datavis in terms of specific keywords such as "women", "health", and "poor" revealed some specific findings about the how datavis properties such as color, size, and data source availability were different or similar over the years. The mentioned datavis properties were some of which that showed the most patterns in its evolution in the WDRs. Based on the findings of the trend analysis, datavis properties, and guidelines proposed by Kelleher and Wagener (2011), "Readability", "Meaningfulness", and "Reliability" were concluded as datavis evaluation criteria adequate in the WDR.

This research can be further improved by testing the recommended evaluation criteria results by conducting a proper survey, advisable for its continuous development and analyzing the trends for other significant keywords. This research may be used as a reference or model in a larger scale such as comparing different developmental reports from other organizations that could expose more interesting findings regarding data visualization in developmental reports that may result to the progress of a more standardized data visualization evaluation criteria and method applicable to most reports not limited to developmental ones.

References

[1] Friendly, M. (2007). A brief history of data visualization. Handbook of Computational Statistics: Data Visualization, Vol. 3, 1-34. Heidelberg: Springer-Verlag.

[2] Kelleher, C. & Wagener, T. (2011). Ten guidelines for effective data visualization in scientific publications. Environmental Modelling & Software. pp.1-6

[3] The World Bank, (2015). World Development Report. Retrieved from https://openknowledge.worldbank.org/handle/10986/2124

[4] Steele, J., & Iliinsky, N. (2010). Beautiful visualization: looking at data through the eyes of experts. Sebastopol, CA: O'Reilly.

COMPETITION BETWEEN LAND CORRIDOR AND MARITIME TRANSPORT IN CROSS-BORDER FREIGHT TRANSPORT

Student Number: 14M18069 Name: Wataru Saito Supervisor: Shinya Hanaoka

クロスボーダー輸送における回廊と海運の競争

齋藤 亘

クロスボーダー輸送では低費用の海運輸送が用いられることが多い。しかし、近年、陸路輸送である回廊が整備され利用されている。本研究は、世界各国間のクロスボーダー輸送を対象に、回廊利用分担率を被説明変数としてロジスティック回帰分析を行い、回廊を利用する要因を明らかにする。また、残差分析により地域個別の要因も明らかにする。分析の結果、内陸国ダミー、輸出国の品目価値、2国間距離、隣国ダミー、陸路インフラレベル、カントリーリスク、港湾アクセス、海運輸送頻度が有意な変数であり、中でも陸路インフラレベル改善が回廊の分担率を大きく上昇させる事を示した。また、東アジアの海運輸送頻度の多さ、国の主要産業が貿易品目に与える影響、地形、テロなどのカントリーリスクが、地域固有の要因であることを明らかにした。

1. Introduction

A cross-border land corridor is the bundle of infrastructure such as highways, railways and border facility that links 2 or more urban areas in different countries. To facilitate the trade by cross-border land corridor, many projects have been carried out by international donor and various countries in the world. "New Silk Road" concept connecting the EU and China proposed by the Chinese government in 2015 is good example of cross-border land corridor project. Land corridor and maritime transport compete each other because maritime transport costs less than land corridor while maritime transport is much slower. Cross-border transport is relatively longer distance and more complex due to border procedure than domestic transport, so that maritime transport can easily be superior to land corridor. Additionally, in developing countries, since the value of commodities is not as high as in developed countries, forwarders tend to choose the maritime transport over land corridor. Therefore, in competition with maritime transport, how much land corridor will be used for cross-border freight transport has not been revealed yet even though there are many cross-border land corridor projects in the world.

The main objectives of this study is to identify the significant factors to select cross-border land corridor by inductive approach and this can be broken down into 2 sub objectives as follows.

1) To develop the model that estimates the land ratio by logistic regression analysis using country Origin-Destination (OD) pairs.

2) To investigate the specific OD pairs situation by residual analysis.

2. Methodology

2.1 OD pair selection

To examine the competition between land corridor and maritime transport, data of the OD pairs both modes have share in 2014 are drawn by the database [1]. 280 samples are selected by the following 2 principal criteria.

1) Origin and destination locate in same or near region (following Global Insight classification).

2) Both overland nominal value/total trade nominal value and seaborne trade nominal value/total trade nominal value are more than 1%.

2.2 Logistic regression analysis

In this study, to identify the significant factors to determine the land ratio of selected OD pairs, logistic regression analysis is applied. Logistic regression aims to find the best fitting model to describe the relationship between explained variable and a set of explanatory variable with generating the coefficient and its significant levels of formula. Logistic regression analysis is modeled as follows.

$$y = \frac{e^{\alpha+\beta_1 x_1+\beta_2 x_2+\cdots+\beta_p x_p}}{1+e^{\alpha+\beta_1 x_1+\beta_2 x_2+\cdots+\beta_p x_p}} \quad (1)$$

y : Explained variable
x_i : Explanatory Variable
α : Constant
β_i : Coefficient

2.3 Explained variable

To focus a competition between land corridor and maritime transport, airborne trade nominal value is subtracted from total trade nominal value ($Thousands) to calculate the land ratio as follows.

y : Land ratio

$$= \frac{\text{Overland・Other Trade Nominal Value}}{\text{Total Trade Nominal Value} - \text{Airborne Trade Nominal Value}} \quad (2)$$

2.4 Explanatory variables

In this study, 11 explanatory variables classified into 4 groups are prepared as follows. The average value of the OD are taken for A1, D9, D10 and D11 while the average value of the OD and passing countries are taken for C7 and C8. The overall information of variables is shown in Table 1.

A1: GDP/capita and A2: Landlocked country dummy are set up to represent the characteristics of country. GDP/capita is used to represent the economic power of shippers or forwarders to take charge of higher land transport cost than maritime. Additionally, landlocked countries are in specific situation since there is no port in their territory. Land corridor should be superior to maritime when either OD is landlocked country. Dummy variable equals to 1 if either OD is landlocked

Table 1: Overall information of the variables

Group	Variables	Max	Min	Average	Standard deviation	Expected sign	Unit	Source
	Land ratio	98.96%	1.07%	42.80%	37.39%		%	Global Insight
A:Characteristic of Country	A1:GDP/capita	73,669.5	819.7	16024.7	15,487.4	+	dollar	World Bank
	A2:Landlocked country dummy	1	0	0.1	0.32	+	-	-
B:Characteristic of Freight	B3:Export (manufacturing)	94.0	0.1	44.8	30.9	+	%	World Bank
C:Characteristic of Mode [Land]	C4:Distance	7,728	81	2496	1,651	—	km	-
	C5:Neighboring dummy	1	0	0.33	0.47	+	-	-
	C6:Number of border	12	1	2.98	2.25	—	-	-
	C7:Infrastructure level	2.0333	-1.3722	-0.1895	0.8909	+	-	World Bank
	C8:Country risk	84.64	29.80	53.23	11.18	+	index	Euromoney
D:Characteristic of Mode [Maritime]	D9:Port access	16.0	2.0	5.4	2.6	+	days	World Bank
	D10:Port infrastructure level	6.7	2.7	4.3	0.7	—	index	World Bank
	D11:Frequency of maritime	139.1	4.7	40.7	23.2	—	index	World Bank

country, 0 otherwise.

A value of freight itself also affects the mode choice. The commodity with higher value should be transported by land corridor. In this study, the ratio of manufactures exports in total merchandise exports (B3) is used to represent the average value of commodity exported by the origin. Data is derived from World Development Indicator [2].

C4-C8 are the variables to express a situation of each OD pairs' land corridor. C4: Distance measured in kilometers between the main city in origin and destination connecting the passing countries represents transport time by land corridor. In land corridor, border crossing is one of the bottlenecks since freight has to follow the procedures such as customs, immigration and quarantine. Dummy variable equals to 1 if OD share land border, 0 otherwise (C5). This study also includes the number of border crossing (C6) when freight is transported from origin to destination by land corridor. Furthermore, land infrastructure level (C7) are measured by composite variables constructed from three variables (total road length/land area size, paved road length/total road length, total railway length/ land area size) by principle component analysis. Finally, the values of country risk (C8) is derived from Euromoney[3] evaluated by consensus survey of the expert opinion. The scores express social network of economic, political country risk. Country risk affects land transport, especially in border area since many ethnical conflicts and corruption such as a bribe often happen. The score ranges from 0 to 100 and higher score means lower risk in this database.

The situation of maritime transport is expressed by D9-D11. D9: Port access is used to represent the accessibility of the port from main city. The summation of lead time of export in the origin and lead time of import in the destination is inputted. In addition, "Port infrastructure level index" is a proxy used to represent how much port infrastructure of the origin and destination are developed (D10). This index ranges from 1 to 7 and measures business executives' perception of their country's port facilities. To represent a frequency of maritime transport between the origin and destination, "Linear shipping connectivity index" derived from World Bank is used (D11). Liner Shipping Connectivity Index captures how well countries are connected to global shipping networks based on five components of the maritime transport sector: number of ships, their container-carrying capacity, maximum vessel size, number of services, and number of companies that deploy container ships in a country's ports. The index generates a value of 100 for the country with the highest average index in 2004.

3. Results and discussion

3.1 All sample case

All correlation of coefficient between explanatory variables is less than 0.7, therefore firstly analysis by all samples with all variables is conducted and result is shown in Table 2 as case (a). By omitting 3 variables with unexpected sign (A1: GDP/capita, C6: Number of border and D10: Port infrastructure level) and 3 samples with more than 3 or less than -3 of absolute value of standardized residual error, the model used for residual analysis in the next section is obtained as case (b). Case (b) has more than 60% of adjusted R square and 8 factors gets significance. Furthermore, by omitting C8: Country risk, A1: GDP per capita gets significance since their correlation coefficient is relatively high (0.66). Unfortunately, the significance of C6: Number of border and D10: Port infrastructure level cannot be found in anyway by this model.

3.2 Excluding 2 inter regional case

2 European related inter regional case (European Union&Western Asia, Other European country& Western Asia) has high land ratio even though they have many border crossings. By excluding these samples, the sample size turns out to be 207 and the significance of C6: Number of border is confirmed as shown in case (c). Therefore, it can be said that in the regions except the European countries, number of border is also significant factor to facilitate cross-border land corridor.

3.3 Stratification analysis

Since border crossing is obviously significant factor as mentioned above, stratification analysis using same variables is conducted by separating the samples into 2 groups: the OD locating neighbor and OD locating non neighbor. In neighboring case, the OD pairs that either origin or destination is landlocked country are excluded

Table 2: Estimation results (*: 10%, **: 5%, ***: 1% significance)

	(a)			(b)			(c)			(d)			(e)		
R square	0.580			0.619			0.520			0.561			0.645		
Adjusted R square	0.563			0.608			0.506			0.537			0.631		
	Coeffici ent	t-value	signifi cance	Coeffici ent	t-value	signifi cance	Coeffici ent	t-value	signifi cance	Coeffici ent	t-value	signifi cance	Coeffici ent	t-value	signifi cance
Intercept	-4.6910	-3.67	-	-2.5139	-3.56	-	0.6244	1.27	-	0.6741	1.15	-	-1.6915	-1.50	-
A1	0.0000	-1.52		-			0.0000	3.07	(***)	0.0000	2.71	(***)	-		
A2	1.5170	4.76	(***)	1.3593	4.55	(***)	0.9396	2.04	(**)	-			1.5482	4.29	(***)
B3	0.0189	3.77	(***)	0.0190	4.07	(***)	0.0122	2.66	(***)	0.0153	2.33	(***)	0.0210	4.01	(***)
C4	-0.0009	-11.05	(***)	-0.0008	-13.06	(***)	-0.0007	-8.31	(***)	-0.0010	-8.23	(***)	-0.0007	-10.46	(***)
C5	1.6433	6.13	(***)	1.5005	6.49	(***)	-			-			-		
C6	0.2220	2.70	(***)	-			-0.5063	-5.56	(***)	-			-		
C7	0.3059	1.55		0.6988	4.49	(***)	-			-			0.7832	4.03	(***)
C8	0.0685	5.18	(***)	0.0513	5.17	(***)	-						0.0568	4.51	(***)
D9	0.1093	2.19	(**)	0.0959	2.16	(**)	0.0694	1.44		0.1213	2.00	(**)	-		
D10	0.1756	0.75		-			-			-			-0.2080	-0.94	
D11	-0.0127	-1.91	(*)	-0.0135	-2.53	(**)	-			-			-0.0166	-2.55	(**)
Num of samples	280			277			207			79			187		

from a set of the samples since these OD pairs have high land ratio without discussion. The result of neighboring case is (d) with 79 samples while non-neighboring case is (e) with 187 samples.

Comparing both groups, non-neighboring case has higher adjusted R square and more variables with significant. D9: Port access is significant only in neighboring case. Since maritime transport time is relatively shorter, higher accounting ratio of time on port access makes D9: Port access crucial in neighboring case. D10: Port infrastructure has expected sign only in non-neighboring case since higher port infrastructure level is required for longer maritime transport time.

4. Residual analysis

4.1 Low and high residual error

By logistic regression analysis, residual error can be calculated by subtraction of the predicted value from actual value. It can be assumed that the samples with low residual error is expressed well by the set of explanatory variables and the samples with high residual error is not, therefore other factors to explain high residual error should be investigated. The following figure shows histogram of the standardized residual error by case (b) in Table 2. In this study, the samples with standardized residual error ranges from -0.5θ to 0.5θ is considered to have low residual error and sensitivity analysis is conducted. Furthermore, the samples with more than 2θ or less than -2θ of standardized residual error is considered to have high residual error, and detailed analysis is carried out.

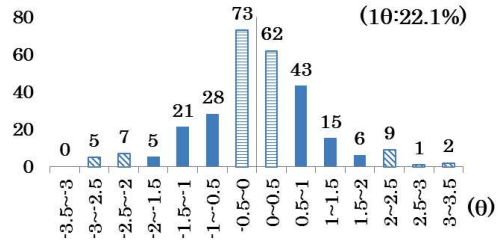

Figure 1: Histogram of standardized residual error

4.2 Sensitivity analysis

Sensitivity analysis is a technique that examines the impact of input change on output. To comprehend the potential each variable has to change the land ratio, B3: Export (manufacturing), C7: Infrastructure level, and C8: Country risk, D9: Port access and D11: Frequency of maritime are changed ranging from maximum to minimum value of a set of samples shown in Table 1. The residual error initially each sample has is assumed to be fixed even when each input variable is changed.

The result of Brazil (export) - Chile (import) whose actual land ratio is 10.3% is shown in Figure 2. It can be said that infrastructure level has the biggest potential to increase the land ratio by almost 40% in this case.

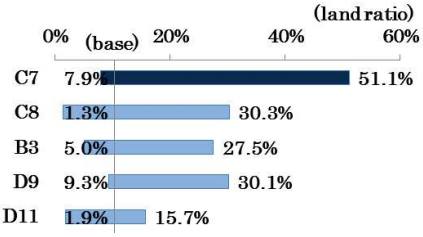

Figure 2: Tornado chart (Export: Brazil, Import: Chile)

4.3 Detailed analysis

The samples with high residual error including omitted 3 samples are shown in Table 3. The reason why these samples have high residual error can be classified into 5 issues as follows.

[1] Land infrastructure level

In EU&Western Asia and North America, the actual value is higher than predicted value. As shown in Table 4, the average of infrastructure level in EU&Western Asia is much higher than all samples and this makes the land ratio possible to be high. North America has lower infrastructure level contrary to the expectation since one of the indexes used to composite variable is total road length per land area and countries in North America have large land area so that the value gets lower than the real situation. Both cases contain long distance, so it can be implied that distance is not a

Table3: Samples with high residual error

Issue	Region	Export	Import	Actual value	Predicted value	Residual error
[1]Land infrastructure level	EU&Western Asia	Spain	Turkey	81.2%	34.5%	46.7%
		Turkey	Spain	80.8%	36.2%	44.6%
		Finland	Turkey	80.6%	27.5%	53.1%
		Turkey	Portugal	79.9%	30.0%	50.0%
		Portugal	Turkey	79.8%	30.6%	49.3%
		Turkey	Finland	79.8%	28.2%	51.6%
	North America	Mexico	Canada	87.6%	30.7%	57.0%
		Canada	Mexico	85.9%	17.9%	68.0%
[2]Frequency of maritime	East Asia	Thailand	Singapore	26.7%	74.1%	-47.4%
[3]Detailed commodity	Western Asia	United Arab Emirates	Bahrain	2.5%	46.9%	-44.4%
	Central America &North America	El Salvador, Honduras, and Nicaragua	Mexico	89.3%	36.6%	52.7%
		Costa Rica and Panama	Mexico	83.5%	13.2%	70.3%
		Mexico	Costa Rica and Panama	78.9%	26.5%	52.4%
	South America	Brazil	Costa Rica and Panama	82.3%	lower	+
[4]Geographical features	Africa	Algeria	Burkina Faso, Mali, and Niger	4.8%	57.7%	-52.9%
		Burkina Faso, Mali, and Niger	Algeria	4.1%	60.8%	-56.7%
		Libya	Burkina Faso, Mali, and Niger	4.1%	59.3%	-55.2%
		Burkina Faso, Mali, and Niger	Libya	3.8%	63.2%	-59.4%
	South America	Bolivia	Brazil	98.8%	54.1%	44.7%
		Argentina	Chile	21.7%	70.0%	-48.2%
		Chile	Argentina	18.2%	64.6%	-46.4%
[5]Specific country risk	Africa&Western Asia	Egypt, Arab Rep.	Saudi Arabia	6.0%	55.2%	-49.2%
		Israel	Libya	5.1%	65.8%	-60.7%
		Egypt, Arab Rep.	Israel	7.1%	higher	—
		Israel	Egypt, Arab Rep.	5.5%	higher	—
	Central America & North America	Costa Rica and Panama	Colombia	7.9%	68.7%	-60.8%
	Indian Subcontinent &Western Asia	Pakistan	Other Western Asia (Iran,Iraq)	3.6%	68.0%	-64.3%

critical issue if land infrastructure is developed enough.

Table 4: Average of infrastructure level

	EU&Western Asia	North America	All samples
C7: Infrastructure level	1.0502	-0.2085	-0.1895

[2] Frequency of maritime

East Asia has extremely high frequency of maritime transport (the average of East Asia: 90.5, the average of all samples: 40.7) since Malacca strait is a choke point of world supply chain. In fact, 9 out of top 10 world container port locate in East Asia such as Shanghai, China and Singapore in 2014.

[3] Detailed commodity

Most of Western Asia country except Turkey export mineral fuels more than 50% of total trade and this can be the reason of causing high residual error since mineral fuel is a mode captive commodity of maritime transport. As for Mexico-Central America and Brazil – Costa Rica and Panama case, according to UNcomtrade[4], Mexico mainly exports manufacturing products to Central America and Brazil also exports manufacturing products to Costa Rica and Panama ,even though B3: Export (manufacturing) of Brazil is not as much high (34.8%). This is the phenomena caused by a big economical gap between those countries. Additionally, it can be considered that Central America exports the lower value commodity to Mexico by truck to reduce the unloaded return truck.

[4] Geographical features

Burkina Faso, Mali and Niger are landlocked country but the land ratio with North Africa is not high since Atlas Mountain and Sahara desert exists along the route. In contrast, route between Bolivia and Brazil is relatively flat so actual value is higher than predicted value. Andes Mountain existing between Chile and Brazil makes the land ratio gets lower as well.

[5] Specific country risk

Even though indicator of country risk is included in the model, it is hardly to be said the score represents country risk of land corridor itself perfectly for some countries. For example, the score of Israel is 66.8 and better than the average but, in Israel there is area called “Gaza” specifically dangerous and this area locates close to the freight route between Africa and Western Asia. In addition, in Panama, Darien Gap locates where rebel army have activity and this area is a missing link of Pan-American corridor. Furthermore, in Pakistan, Iran and Iraq, there is much terrorism and Islamic extremist such as Taliban base around here.

5. Conclusion

In this study, to generalize the important factors to select cross-border land corridor in competition with maritime transport, logistic regression analysis was conducted and 8 variables were identified as the significant factor. Some variables were found to be significant in the specific cases. Sensitivity analysis showed a big potential of land infrastructure. By detailed analysis, importance of land infrastructure, high frequency of maritime transport in East Asia, detailed commodity, geographical features and specific country risk were found as region-specific issue.

References

[1] Database
Online available: https://www.ihs.com/index.html
[2] World Bank Development Indicator
Online available: http://wdi.worldbank.org/table
[3] Euromoney Country Risk
Online available:
http://www.euromoneycountryrisk.com/Home/Return/Countries
[4] UNcomtrade
Online available: http://comtrade.un.org/

CAMERA CALIBRATION USING GLOBAL PROJECTION TRANSFORMATION

Student Number:14M18247 Name:Yang Chen Supervisor:Yukihiko YAMASHITA

大域的射影変換を用いたカメラキャリブレーション

陳 陽

本研究では, Zhang が提案した平面オブジェクトのカメラキャリブレーション法に基づき, 実世界の座標と画像座標の間のホモグラフィの推定に, 大域的射影変換 (GPT) 相関法を適用することを提案する。GPT 相関法は画像自体のマッチングによりホモグラフィを求めるため，特徴点が求まりにくい画像でもホモグラフィを求めることができる。そのため，キャリブレーションオブジェクトの選択がより柔軟になる。また，画像全体でマッチングを行うため，高精度化が期待できる。さらに本研究では，キャリブレーション実験により，提案手法の有効性を確かめた。

1 Introduction

Computer vision is a technology which makes the machine to have an ability of recognizing the world from images. This technology can be used to recognition, tracking, and measuring. With the development of computer vision, it has been applied for medical science, robotics, character recognition, military reconnaissance, scene measurement, and so on.

Camera calibration is a necessary step in 3D computer vision. It is a process to estimate the internal and external parameters of a camera. The accuracy of camera calibration effects the correctness of the following steps in computer vision directly. It has been studied extensively in photogrammetry community and computer vision.

Tsai proposed a camera calibration method by observing a 3D object. The calibration object consists of two planes orthogonal to each other. This method is very efficient. But because we need to know the geometry of the object in 3D space with a very high precision, it requires expensive calibration equipments and delicate setup.

For this issue, Zhang did abundant study and proposed a new flexible method [3] for camera calibration in 1999. Zhang's method requires the camera observing a planar pattern under different orientations. Then estimating the homography between each image and the world by matching several feature points, and the internal and external parameters of a camera can be estimated form those homography. Zhang's method is quite flexible and easy to setting up, so that it has been implemented in OpenCV. OpenCV is an open source library aiming at real-time computer vision, which was developed by Intel, and later supported by Willow Garage. The library is written in C and C++ and runs under various OSs. It has a high capability for calculating images and matrixes. However, in Zhang's method, since the first step is to check out several feature points for matching, the calibration result correctness is usually effected by the accuracy of the coordinates of the extracted points.

In this research, I propose using the global projection transformation (GPT) correlation method to estimate the homography between an image and the world coordinates. Since GPT correlation method is a region matching method, images without feature points also can be used to estimate the homography, so that it will make the choice of calibration objects more flexible. And the improvement of accuracy also could be expected.

2 Camera Calibration

2.1 Camera Model

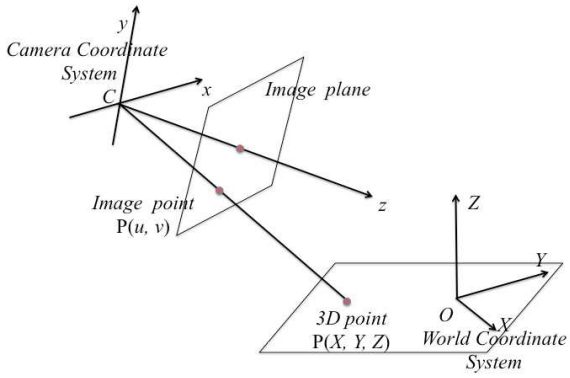

Figure 1: Camera model

Figure 1 shows the relationship among the coordinates of a camera model. We assume that a 3D point P in the world coordinate system is represented by M=$[X, Y, Z]^T$. Its projected point in the image coordinate system is represented by m = $[u, v]^T$. The relationship between M=$[X, Y, Z]^T$ and m = $[u, v]^T$ is given by

$$s \begin{bmatrix} u \\ v \\ 1 \end{bmatrix} = \boldsymbol{A}[\boldsymbol{R}\ \boldsymbol{t}] \begin{bmatrix} X \\ Y \\ Z \\ 1 \end{bmatrix}, \quad (1)$$

$$\text{with } \boldsymbol{A} = \begin{bmatrix} \alpha & \gamma & u_0 \\ 0 & \beta & v_0 \\ 0 & 0 & 1 \end{bmatrix},$$

where s is an arbitrary scale factor, $\boldsymbol{R}$ and $\boldsymbol{t}$ is the rotation matrix and the translation vector which relate the world coordinate system to the camera coordinate system, and $\boldsymbol{A}$ is the internal parameter matrix of a camera, with (u_0, v_0) the coordinates of the origin of an image, α and β the scale factors, and γ the skewness of the two image axes.

Camera calibration is to estimate the parameters in $\boldsymbol{A}$, $\boldsymbol{R}$, and $\boldsymbol{t}$.

2.2 Zhang's Method

Zhang's method is based on eq.(1). It just uses several (at least 2) photos taken by observing a planar pattern under different orientations. Either the camera or the planar pattern can be moved freely. The motion does not need to be known.

First, we can assume the template plane satisfies $Z = 0$. Then we can rewrite eq.(1) as follow:

$$\begin{aligned} s\begin{bmatrix} u \\ v \\ 1 \end{bmatrix} &= \mathbf{A}[\mathbf{r_1}\ \mathbf{r_2}\ \mathbf{r_3}\ \mathbf{t}]\begin{bmatrix} X \\ Y \\ 0 \\ 1 \end{bmatrix} \\ &= \mathbf{A}[\mathbf{r_1}\ \mathbf{r_2}\ \mathbf{t}]\begin{bmatrix} X \\ Y \\ 1 \end{bmatrix}. \end{aligned} \quad (2)$$

From eq.(2), we can get a relationship between a 3D point M and its projection point m by a homography $\mathbf{H}$, with $\mathbf{H} = \mathbf{A}[\mathbf{r_1}\ \mathbf{r_2}\ \mathbf{t}]$. The homography can be estimated by an image of a template.

We denote $\mathbf{H}$ by its column vectors as $\mathbf{H} = [\mathbf{h_1}\ \mathbf{h_2}\ \mathbf{h_3}]$. Then we have

$$[\mathbf{h_1}\ \mathbf{h_2}\ \mathbf{h_3}] = \lambda\mathbf{A}[\mathbf{r_1}\ \mathbf{r_2}\ \mathbf{t}], \quad (3)$$

where λ is an arbitrary scalar. Because $\mathbf{r_1}$ and $\mathbf{r_2}$ are orthonormal, we have

$$\begin{aligned} \mathbf{h}_1^T\mathbf{A}^{-T}\mathbf{A}^{-1}\mathbf{h}_2 &= 0, & (4)\\ \mathbf{h}_1^T\mathbf{A}^{-T}\mathbf{A}^{-1}\mathbf{h}_1 &= \mathbf{h}_2^T\mathbf{A}^{-T}\mathbf{A}^{-1}\mathbf{h}_2. & (5) \end{aligned}$$

From eqs.(4) and (5), we can solve the internal parameters by a closed-form solution. Let

$$\begin{aligned} \mathbf{B} &= \mathbf{A}^{-T}\mathbf{A}^{-1} \equiv \begin{bmatrix} B_{11} & B_{12} & B_{13} \\ B_{12} & B_{22} & B_{23} \\ B_{13} & B_{23} & B_{33} \end{bmatrix} \quad (6)\\ &= \begin{bmatrix} \frac{1}{\alpha^2} & -\frac{\gamma}{\alpha^2\beta} & \frac{v_0\gamma - u_0\beta}{\alpha^2\beta} \\ -\frac{\gamma}{\alpha^2\beta} & \frac{\gamma^2}{\alpha^2\beta^2} + \frac{1}{\beta^2} & -\frac{\gamma(v_0\gamma - u_0\beta)}{\alpha^2\beta^2} - \frac{v_0}{\beta^2} \\ \frac{v_0\gamma - u_0\beta}{\alpha^2\beta} & -\frac{\gamma(v_0\gamma - u_0\beta)}{\alpha^2\beta^2} - \frac{v_0}{\beta^2} & \frac{(v_0\gamma - u_0\beta)^2}{\alpha^2\beta^2} + \frac{v_0^2}{\beta^2} + 1 \end{bmatrix}. \end{aligned}$$

Because $\mathbf{B}$ is symmetric, it can be defined by a 6 dimensional vector

$$\mathbf{b} = [B_{11}, B_{12}, B_{22}, B_{13}, B_{23}, B_{33}]^T. \quad (7)$$

By using $\mathbf{h}_i = [h_{i1}, h_{i2}, h_{i3}]^T$, we have

$$h_i^T\mathbf{B}h_j = v_{ij}^T\mathbf{b} \quad (8)$$

with
$v_{ij} = [h_{i1}h_{j1}, h_{i1}h_{j2} + h_{i2}h_{j1}, h_{i2}h_{j2}, h_{i3}h_{j1} + h_{i1}h_{j3}, h_{i3}h_{j2} + h_{i2}h_{j3}, h_{i3}h_{j3}]^T$.

From eqs.(4) and (5), it can be obtained that

$$\begin{bmatrix} v_{12}^T \\ (v_{11} - v_{22})^T \end{bmatrix}\mathbf{b} = \mathbf{0} \quad (9)$$

as

$$\mathbf{V}\mathbf{b} = \mathbf{0}. \quad (10)$$

For n images of a template, there will be $2n \times 6$ equations. Since $\mathbf{V}$ is known, $\mathbf{b}$ can be solved. After $\mathbf{b}$ is estimated, all internal parameters of the camera can be calculated as follows:

$$\begin{aligned} v_0 &= (B_{12}B_{13} - B_{11}B_{23})/(B_{11}B_{22} - B_{12}^2) \\ \lambda &= B_{33} - [B_{13}^2 + v_0(B_{12}B_{13} - B_{11}B_{23})]/B_{11} \\ \alpha &= \sqrt{\lambda/B_{11}} \\ \beta &= \sqrt{\lambda B_{11}/(B_{11}B_{22} - B_{12}^2)} \\ \gamma &= -B_{12}\alpha^2\beta/\lambda \\ u_0 &= \gamma v_0/\alpha - B_{13}\alpha^2/\lambda \end{aligned} \quad (11)$$

After $\mathbf{A}$ is estimated, the external parameters for each image could be calculated. From eq.(3), we have

$$\begin{aligned} \mathbf{r}_1 &= \lambda\mathbf{A}^{-1}\mathbf{h}_1 \\ \mathbf{r}_2 &= \lambda\mathbf{A}^{-1}\mathbf{h}_2 \\ \mathbf{r}_3 &= \mathbf{r}_1 \times \mathbf{r}_2 \\ \mathbf{t} &= \lambda\mathbf{A}^{-1}\mathbf{h}_3 \end{aligned} \quad (12)$$

with $\lambda = 1/||\mathbf{A^{-1}h_1}|| = \mathbf{1}/||\mathbf{A^{-1}h_2}||$.

3 Global Projection Transformation Correlation Method

GPT correlation method is an extension of GAT (Global Affine Transformation) correlation method.

GPT correlation method uses the normalized cross-correlation as a matching measure. By applying GPT to the input image, a high correlation can be obtained with the target image. The projection transformation parameters between the input image and the target image can be obtained when the correlation value is the maximum.

3.1 2D Projection Transformation

2D projection transformation is given by

$$\boldsymbol{x}' = \frac{A\boldsymbol{x} + \boldsymbol{b}}{1 + \langle \boldsymbol{c}, \boldsymbol{x} \rangle}. \quad (13)$$

Here, $\langle \boldsymbol{c}, \boldsymbol{x} \rangle$ is the inner product between $\boldsymbol{c}$ and $\boldsymbol{x}$. This function can be divided into the affine transformation (AT) part and the partial projection transformation (PPT) part as follows:

$$\begin{aligned} \boldsymbol{x'} &= A\boldsymbol{x} + \boldsymbol{b} & (14)\\ \boldsymbol{x'} &= \frac{\boldsymbol{x}}{1 + \langle \boldsymbol{c}, \boldsymbol{x} \rangle} \quad (\equiv P(\boldsymbol{x})) & (15) \end{aligned}$$

The AT parameters A, $\boldsymbol{b}$, and the PPT parameter $\boldsymbol{c}$ can be calculated respectively.

3.2 Calculating Affine Transformation Parameters

Let's denote an input gray-scale image as $f(x)$, a template image as $g(x)$, and the transformed input image as $f'(\boldsymbol{x})$. From eq.(14), the correlation value between the input image and the transformed image is given by

$$C(f', g) = \int_{\boldsymbol{K}} \frac{1}{|A|} f(A^{-1}(\boldsymbol{x} - \boldsymbol{b}))g(\boldsymbol{x})d\boldsymbol{x}. \quad (16)$$

Because A and $\boldsymbol{b}$ are directly in the variable of function f, it is difficult to determine A and $\boldsymbol{b}$. Therefore, I change the function to eq.(17) by using the Gaussian window function.

$$C(f', g) = \iint_K G(A\boldsymbol{x}_1 + \boldsymbol{b} - \boldsymbol{x}_2) f(\boldsymbol{x}_1) g(\boldsymbol{x}_2) d\boldsymbol{x}_1 d\boldsymbol{x}_2. \tag{17}$$

Here, A and $\boldsymbol{b}$ appear only in the Gaussian window function.

In order to achieve a higher process speed, I also introduce the edge direction function. So the final correlation function is given by

$$C_{\mathrm{GAT}}(f, g) = \iint_K G(A\boldsymbol{x}_1 + \boldsymbol{b} - \boldsymbol{x}_2) \delta(\nabla f(\boldsymbol{x}_1), \nabla g(\boldsymbol{x}_2)) f(\boldsymbol{x}_1) g(\boldsymbol{x}_2) d\boldsymbol{x}_1 d\boldsymbol{x}_2. \tag{18}$$

The necessary condition of maximization of $C_{\mathrm{GAT}}(f, g)$ yields that both derivatives of $C_{\mathrm{GAT}}(f, g)$ with A and $\boldsymbol{b}$ equal to zero. Then A and $\boldsymbol{b}$ can be calculated.

3.3 Calculating Partial Projection Transformation Parameters

The function $f_p(\boldsymbol{x})$ which is transformed by the partial projection transformation is given by

$$f_p(\boldsymbol{x}) = \left| P^{-1}(\boldsymbol{x}) \right| f\left(\frac{\boldsymbol{x}}{1 - \langle \boldsymbol{c}, \boldsymbol{x} \rangle} \right), \tag{19}$$

where $|P^{-1}(\boldsymbol{x})|$ is the Jacobian of $P^{-1}(\boldsymbol{x})$.

First, I substitute $f_p(\boldsymbol{x})$ into eq.(16). Next, I also introduce the Gaussian window function and the edge direction function to get an objective function. Finally, the objective function is given by

$$C_{\mathrm{PPT}} = \iint_{\boldsymbol{K}} G(\frac{\boldsymbol{x}_1}{1 + \langle \boldsymbol{c}, \boldsymbol{x}_1 \rangle} - \boldsymbol{x}_2) \delta(\nabla f(\boldsymbol{x}_1), \nabla g(\boldsymbol{x}_2)) f(\boldsymbol{x}_1) g(\boldsymbol{x}_2) d\boldsymbol{x}_1 d\boldsymbol{x}_2. \tag{20}$$

The factor $\boldsymbol{c}$ can be calculated when the derivative of $C_{\mathrm{PPT}}(f, g)$ by $\boldsymbol{c}$ equals to zero.

To determine the optimal GPT factors, I use the successive iteration method. As for the whole algorithm, I calculate the affine transformation part and the partial projection transformation part alternatively until the correlation becomes maximum. Then, output the maximal correlation value and the transformation matrix.

3.4 Estimation of Homography

The transformation matrix represents the relationship between the input image and the template image. And the homography between the camera and the world coordinates can be represented as follow:

$$\begin{bmatrix} u \\ v \\ 1 \end{bmatrix} = \begin{bmatrix} a_{11} & a_{12} & b_1 \\ a_{21} & a_{22} & b_2 \\ c_1 & c_2 & 1 \end{bmatrix} \begin{bmatrix} \frac{1}{dx} & 0 & u_0 \\ 0 & \frac{1}{dy} & v_0 \\ 0 & 0 & 1 \end{bmatrix} \begin{bmatrix} X \\ Y \\ 1 \end{bmatrix} = \mathbf{H} \begin{bmatrix} X \\ Y \\ 1 \end{bmatrix}.$$

Therefore, n kinds of $\mathbf{H}$s can be estimated by n images of a template. Then substituting them into eq.(4) and eq.(5), the parameters of a camera can be calculated.

4 Experiments Results

In experiments, I test many kinds of templates, such as chessboards, circles, and squares. The templates are printed on a A4 paper and attached to a board. The input images are taken by iPhone6 Plus with an original size as 2448×2448 and they are transformed into 200×200 gray scale images.

The process of the experiment are as follows:

1. Make a template image and print it out.
2. Take a few (at least 2) pictures of the template under different orientations.
3. Make the photos to be the same size with the template image as the input images.
4. Match each input image with the template image to get the transform matrix.
5. Estimate the homography between the image coordinate and the world coordinate of the print.
6. Calculate the length between 2 points on the print from the input image, and compare it with the actual length to evaluate the accuracy of the proposed method.

Figures 2 – 5 show some transformed images by GPT correlation method. Tables 1 and 2 show the results of the original correlation value, the GPT correlation value, the estimated length, and the actual length. Table 3 shows the comparison of the length calculated by GPT correlation method and Zhang's method in OpenCV.

From the results, we can see that the template images witch transformed by GPT correlation method become very similar to the input images. The correlation values are all improved to 0.9 by GPT correlation method. I also calculated the length of 2 points on the input images by the estimated homography, and compared the length with the true length. There is about 10% error. The length shows the availability of GPT correlation method to estimate homography between the images and the world coordinats.

However, the calculated length still has some errors. The calculating time was also increased a lot along with the size of an image.

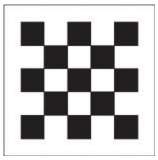

Figure 2: Template of chessboard pattern

Table 1: Results of chessboard pattern

	Original Cor.	GPT Cor.	Calculated Length	True Length
(a)	0.347	0.937	19.10	22
(b)	0.323	0.953	21.63	22
(c)	0.277	0.940	19.80	22

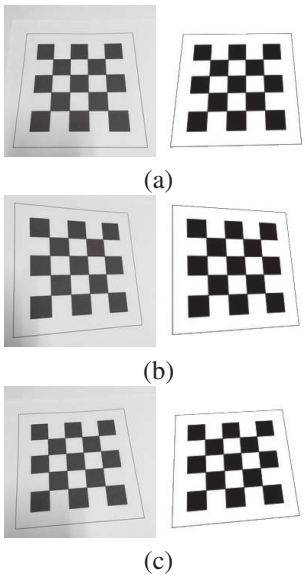

Figure 3: Left:input images Right:transformed images by GPT

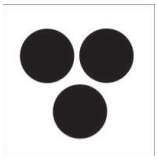

Figure 4: Template of circles

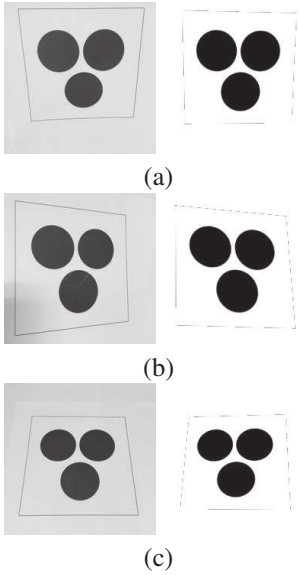

Figure 5: Left:input images Right: transformed template images

Table 2: Results of circles

	Original Cor.	GPT Cor.	Calculated Length	True Length
(a)	0.566	0.943	127.44	112
(b)	0.611	0.922	116.98	112
(c)	0.520	0.944	100.97	112

Table 3: Calculated lengths by GPT and Zhang's methods

	Length by GPT	Length by Zhang's method	True length
(a)	19.10	21.51	22
(b)	21.63	23.32	22
(c)	19.80	21.45	22

5 Conclusions

In this paper, I proposed an application of GPT correlation method to camera calibration. We can easily estimate the homography between the image and the world coordinates. The experimental results show the effectiveness of GPT correlation method for image matching. From the calculated length of 2 points of the input image, we can prove the availability of homography estimated by GPT correlation method. We can use a template without feature points such as circles for camera calibration. It makes the choice of calibration object more flexible.

For the feature works, we need to improve the algorithm of GPT correlation method to reduce the error. And accelerating the calculating speed is also an important task.

References

[1] R.Y. Tsai, "A versatile camera calibration technique for high-accuracy 3D machine vision metrology using off-the-shelf TV cameras and lenses," IEEE J. Robotics and Automation, vol. 3, no. 4, pp. 323-344, Aug. 1987.

[2] Wakahara, T.; Yamashita, Y., "Acceleration of GAT correlation for distortion-tolerant image matching," 21st International Conference on Pattern Recognition (ICPR 2012), pp.746-749, 11-15 Nov. 2012.

[3] Zhengyou Zhang, "A flexible new technique for camera calibration," IEEE Transactions on Pattern Analysis and Machine Intelligence, vol.22, no.11, pp.1330-1334, Nov. 2000.

[4] Wakahara, T.; Kimura, Y.; Tomono, A., "Affine-invariant recognition of gray-scale characters using global affine transformation correlation," IEEE Transactions on Pattern Analysis and Machine Intelligence, vol.23, no.4, pp.384-395, Apr. 2001.

Energy Transfer in Adhesive Contact between PDMS Plate and Glass Lens

Student Number: 14M18253 Name: Guanda FU Supervisor: Kunio TAKAHASHI

シリコンゴムとガラスレンズの凝着接触におけるエネルギー授受

傅　冠達

シリコンゴムとガラスレンズの凝着接触におけるエネルギー授受について研究された。変位を制御しながら力と接触半径が測定された。実験結果からシリコンゴムのヤング率、ガラスレンズの曲率半径、計測系の剛性及び凝着仕事を推定し、接触過程においての各エネルギーを計算した。Loading 過程において、接触面で蓄えた界面エネルギーがシリコンゴムの弾性エネルギーと散逸エネルギーに渡し、一方、unloading 過程において、蓄えた弾性エネルギーが界面エネルギーと散逸エネルギーに渡すことが分かった。

1 Introduction

Understanding of adhesion phenomena of polymers is significant in engineering filed such as designing grip-release devices e.g. adhesive tape[1] and wall climbing robots[2]. Furthermore, the adhesion phenomena is also important in dealing with micro-scale objects[3]. Hertz[4] first introduced the contact theory of two elastic spheres (or one sphere and one flat surface) pressed against each other. Base on the Hertz theory, Johnson, Kendall and Roberts[5] analyzed the adhesion behavior between a soft elastic sphere to a flat rigid body or, conversely ,a hard rigid sphere to a soft elastic flat surface. Furthermore, Takahashi, Mizuno and Onzawa[6] added the consideration of the stiffness of the measurement system to the JKR contact model[5]. These studies were based on the stable equilibrium condition of the total energy of the contact system. However, during real contact experiments, the difference of force curve (i.e. the relationship of force and displacement) in the loading and unloading (or approaching and detaching) process has been observed. The contact process is irreversible due to the energy dissipation which is involved as adhesion hysteresis. The study of adhesion hysteresis is important for clarifying the adhesion phenomena and designing applications.

Adhesion hysteresis is observed and discussed in the experiment of elastic contacts by many authors[7-11], however, the mechanism of adhesion hysteresis is not clear. An impressive study was introduced by Baek *et al.*,[12]. They attempted to clarify the mechanism of adhesion hysteresis under the energy unstable equilibrium condition, which means the energy dissipation is separated from the energy of contact system. And a quasi-static (having a duration between each step of applying a displacement) was conducted between a PDMS and a silica glass lens. The results showed that the energy dissipation during unloading process is proportional to the radius of contact area. The energy dissipation is a result of energy transfer (elastic energy, interface energy, etc.) during the contact process. However, how energy transfered have not been investigated. In the present study, the way of transfer during the contact process between each type of energy is clarified.

As an approach to the object of this study, TMO point contact model[6] is used to discuss the energy transfer during the contact process. Force and contact radius are measured under the control of displacement by the experimental apparatus during the contact process (i.e., duration time in fixed displacement). Other parameters such as Young's modulus, stiffness etc. that needed to calculate each energy are determined. Then elastic energy, interface energy, stiffness energy and energy dissipation are calculated and the energy transfer is discussed.

2 Theoretical consideration

An schematic illustration of the contact system is shown in Fig. 2.1. It is assumed that a axisymmetric parabolic body contacts on a semi-infinite elastic body and their is no friction between two bodies.

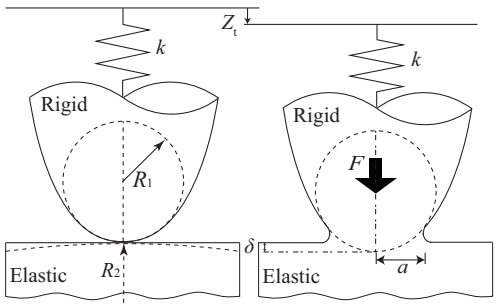

Fig. 1: Schematic illustration of the TMO contact model. Z_t is the gross displacement that applied by experimental apparatus, a spring with stiffness k is represented of the stiffness of the measurement system, F is the force between rigid body and elastic body, a is the radius of contact area, R_1 is the radius of curvature of the rigid body, R_2 is the radius of curvature of the elastic surface, δ is the penetration depth of the rigid body into the elastic body.

In Fig. 1, the force F between rigid body and semi-infinite elastic body is balanced as a relation of $F = P_H - P_B$, where P_H is force of Hertz's distribution and P_B is the force of Boussinesq's distribution. F can be expressed as

$$F = \frac{2Ea}{1-\nu^2}\left(\delta - \frac{a^2}{3R}\right), \tag{1}$$

where E and ν are Young's modulus and Poisson's ratio of the semi-infinite elastic body. R is an effective radius of curvature that can be expressed by

$$\frac{1}{R} = \frac{1}{R_1} + \frac{1}{R_2}, \tag{2}$$

R_1 and R_2 are the radius of curvature of the rigid body and semi-infinite elastic body. In the perfect condition, which means that the elastic surface is flat, R_2 is infinite, so that $R = R_1$. δ is the displacement of the tip of rigid body, and a is the radius of contact area. The displacement δ is not the gross displacement that we can control under the consideration of stiffness of the measurement system. Thus, a spring

with k is considered as the stiffness of the measurement system, and the gross displacement Z_t is expressed as

$$Z_t = -\delta - \frac{F}{k}, \tag{3}$$

together with Eq.(2), we can get the new relationship that can be expressed as

$$F = \frac{2kEa}{(1-\nu^2)k + 2Ea}\left(-Z_t - \frac{a^2}{3R}\right). \tag{4}$$

The force F, contact radius a and gross displacement Z_t are measured simultaneously by experimental apparatus. The Young's modulus E, radius of curvature R and stiffness k can be determined using Eq.(5).

The elastic energy stored in the elastic body due to the elastic deformation is expressed as

$$U_{\text{elastic}} = \frac{4Ea^5}{45(1-\nu^2)R^2} + \frac{1-\nu^2}{4Ea}F^2. \tag{5}$$

The interface energy stored in the contact area is expressed as

$$U_{\text{interface}} = -\pi a^2 \Delta\gamma, \tag{6}$$

$\Delta\gamma$ is the work of adhesion, means the work needed to separate unit area of the interface. The stiffness energy stored in the measurement system is expressed as

$$U_{\text{stiffness}} = \frac{F^2}{2k}. \tag{7}$$

The energy of the contact system is expressed as

$$\begin{aligned}\Delta U_{\text{external}} &= \Delta U_{\text{elastic}} + \Delta U_{\text{interface}} \\ &\quad + \Delta U_{\text{stiffness}} + \Delta U_{\text{dissipation}}.\end{aligned} \tag{8}$$

The strain energy release rate G_{Z_t} (i.e. the energy variation per contact area) during the fixed gross displacement Z_t, is defined and expressed as

$$G_{Z_t} = \frac{\Delta U_{\text{elastic}} + \Delta U_{\text{stiffness}}}{\Delta(\pi a^2)} = \frac{\Delta U_{\text{dissipation}}}{-\Delta(\pi a^2)} + \Delta\gamma. \tag{9}$$

G_{Z_t} can be calculated by

$$G_{Z_t} = \frac{(P_H - F)^2}{6\pi R P_H}, \tag{10}$$

where P_H is force of the Hertzian contact that is expressed as $4Ea^3/3(1-\nu^2)R$. The energy dissipation $\Delta U_{\text{dissipation}}$ can be calculated using Equation (2.11), since the work of adhesion $\Delta\gamma$ has been determined. The determination of $\Delta\gamma$ will be described in section 4.

3 Experiment

The schematic illustration of experimental apparatus is shown in Fig.2. The experimental apparatus was set in a clean bench on a vibration-isolated table. Contact experiment was conducted in the environment of 20°C. The gross displacement Z_t was applied by the motorized stage(a) by 1μm per step. There were 60 seconds of duration of waiting time between each step(fixed gross displacement Z_t). The force and contact radius were measured by electronic balance(c) and microscope(d) 4 times in one second. The measurement error of electronic balance and microscope are ±0.01g and $\pm 1 \times 10^{-5}$m. A polydimethylsiloxane(PDMS) plate was fabricated as the semi-infinite elastic body by heated the mixture of two kinds of liquid (base polymer and cross-linking, Sylgard 184 Silicone Elastomer Kit). The contact experiment began at the loading process i.e. glass lens and PDMS plate were approaching each other. The gross displacement was set to 0μm when the glass lens and PDMS plate contacted firstly. There were 20steps during the loading process. In the unloading process, the motorized stage applied displacement towards detachment of the glass lens and PDMS plate. During the unloading process, the motorized stage conducted until the glass lens and PDMS plate fully detached from each other.

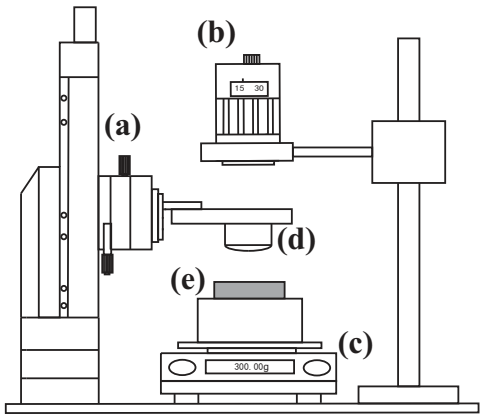

Fig. 2: Schematic illustration of the experimental system. (a) Motorized stage: motorized vertical movement with resolution of 1μm; (b) Microscope: resolution of 1600×1200 pixel; (c) Electronic balance: strain gauge type with resolution of 0.01g; (d) Lens: silica glass lens with radius of curvature R_1 = 0.2076m and diameter of 30mm; (e) PDMS plate: with the dimension of 60 × 60 × 15mm.

4 Result and discussion

4.1 Experimental result

The force F between PDMS and glass lens and radius of contact area a are shown in Figure 3. The force that measured by the electric balance is shown in Figure 3(a). The force when first jumped to contact was negative, means that the adhesive force mainly acted because the force from Boussinesq's contact was greater that the force from Hertz's contact. During the waiting time, the force decreased. After the waiting time of 60 seconds, 1μm of displacement was loaded by the motorized stage, so that the force from Hertz's contact became larger instantaneously and then decreased again in the waiting time. In the unloading process, the motorized stage conducted the opposite direction to the loading process. When the motorized stage unloaded 1μm, the applied force became smaller instantaneously. During the waiting time, the force kept almost the same value at the first several steps. After that, the force during the waiting time increased which is the opposite to the loading process. As the unloading process progressed, the applied force became the smallest which is referred as the largest adhesive force before the detachment.

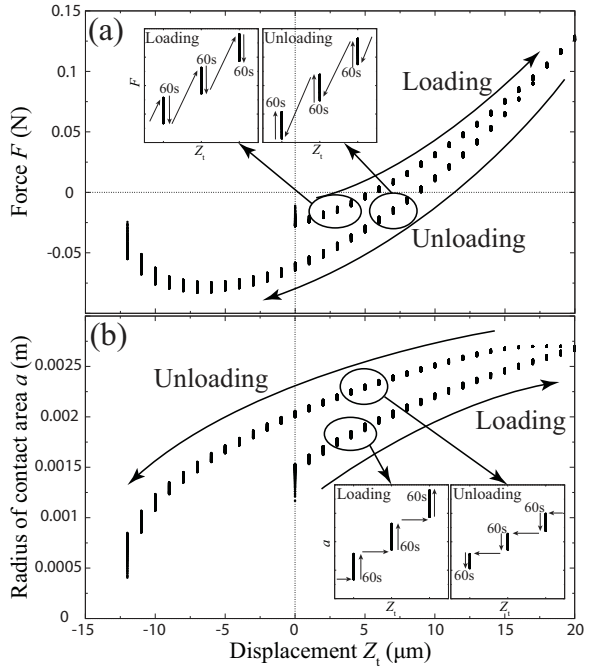

Fig. 3: (a) Measurement force F between PDMS and glass lens at each displacement. (b) Radius of contact area a at each displacement.

4.2 Determination of R, E, k

About the effective curvature R, we can not ensure that the PDMS surface is perfectly flat which means R_2 has infinite value, so that the R need to be evaluated. The effective radius of curvature R can be determined using Equation (5) when applied force $F = 0$, therefore,

$$R = -\frac{a^2}{3Z_t}\bigg|_{F=0}. \tag{11}$$

The result is $R = 0.2076$m, it is the same value with the radius curvature of the glass lens. So it can be assumed from Equation (3) that the PDMS plate has a nearly flat surface.

According to the assumption in this study, the measured force F, radius of contact area a and gross displacement must satisfy the relationship of Equation (5). The value of radius of contact area a, effective radius curvature R and Poisson's ratio ν were assigned to Equation (5). The parameters needed to be evaluated (i.e. E, k,) were also assigned to Equation (5) using experienced value. Thus a calculated force F_{cal} can be obtained. E, k were adjusted to make calculated value F_{cal} close to the measured value F using least squares method. The parameters is determined as $E = 2.01$(MPa), $k = 6.00 \times 10^6$(N/m). The comparison with measured force F and calculated force F_{cal} is shown in Fig.4. It is suppose that F_{cal} is well fitted with F.

4.3 Determination of $\Delta\gamma$

The work of adhesion $\Delta\gamma$ is determined using strain energy release rate G_{Z_t} in Equation (10). It is assumed that the energy dissipation $\Delta U_{\mathrm{dissipation}} \geq 0$ during both loading and unloading process. The change of contact area $\Delta(\pi a^2)$ is positive as the contact radius a advanced, and it became negative as the contact radius a receded. Therefore, from Equation (9), the value of $\Delta\gamma$ is determined to the value of

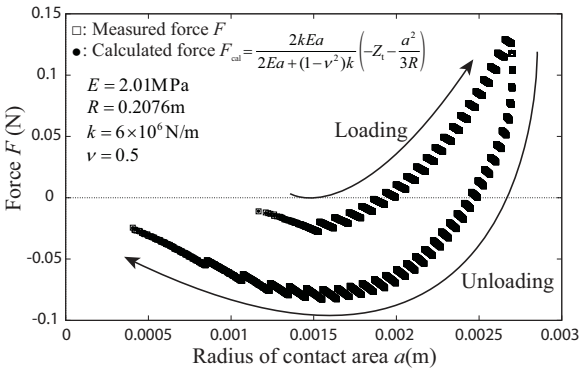

Fig. 4: Fitting result of measured force F and calculated force F_{cal} plotted with radius of contact area a. The values of E, R, k, ν were applied to the equation in this figure. F_{cal} is well fitted to F.

G_{Z_t} at the boundary between advancing and receding of contact radius. That means the value of $G_{Z_t}|_{a_{\max}}$ is the value of $\Delta\gamma$. The strain energy release rate is shown in Fig.5 as a function of contact radius. The region of $\Delta a \geq 0$ and $\Delta a \leq 0$ is not clear in the circle part of Fig.5 due to the measurement error of the contact radius. Thus, that region is the boundary of increasing and decreasing of contact radius. Therefore, $\Delta\gamma$ can be estimated as $0.037 \leq \Delta\gamma \leq 0.047$. We assumed the intermediate point where $\Delta\gamma = 0.042$(J/m^2) in this study.

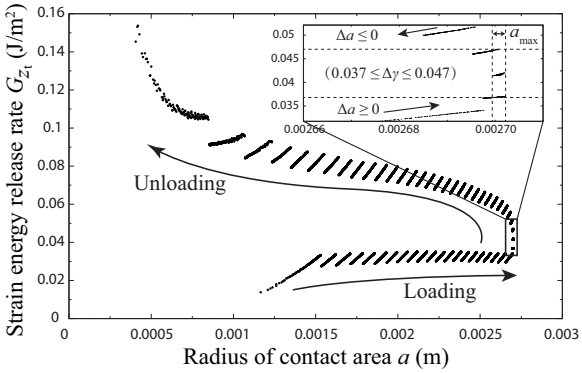

Fig. 5: Strain energy release rate plotted as a function of contact radius. The work of adhesion $\Delta\gamma$ is determined at the boundary of increasing and decreasing of contact area.

4.4 Results of energy calculation

Since all the parameters were measured and determined in Section 4.2 and 4.3, each type of energy in contact system can be calculated. The calculation results plotted with contact radius is shown in Fig.6. It is observed from Fig.6 that the external work done by the experimental apparatus is received as the elastic energy by PDMS plate and as the stiffness energy by the measurement system. The stiffness energy negligible since the order of magnitude of stiffness energy is 3 times less than other types of energy. Therefore, the external energy is almost transfered as elastic energy of the PDMS plate at the moment of applying a displacement.

4.5 Energy transfer in duration of fixed Z_t

Energy transfer is occurred in the duration between each displacement. However, in a critical area in unloading process at the displacement of 19μm to 17μm, the energy can

not be judged as increasing or decreasing because the variation of elastic energy and contact radius (interface energy) are within the margin of error. So that the energy transfer is negligible at the beginning of unloading process. From the displacement of 16μm, the contact radius and elastic energy have a tendency of decreasing, meas the energy transfer began.

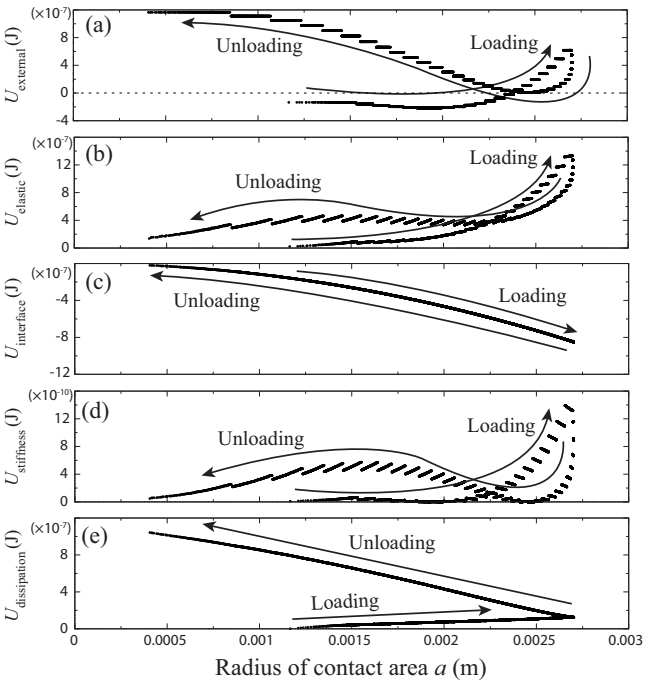

Fig. 6: Each type of calculated energy with the relation of contact radius during whole contact area. (a) External energy that done by experimental apparatus. (b) Elastic energy stored in the PDMS plate. (c) Interface energy stored at the interface between PDMS and glass lens. (d) Stiffness energy stored in the experimental apparatus. (e) The amount of dissipated energy.

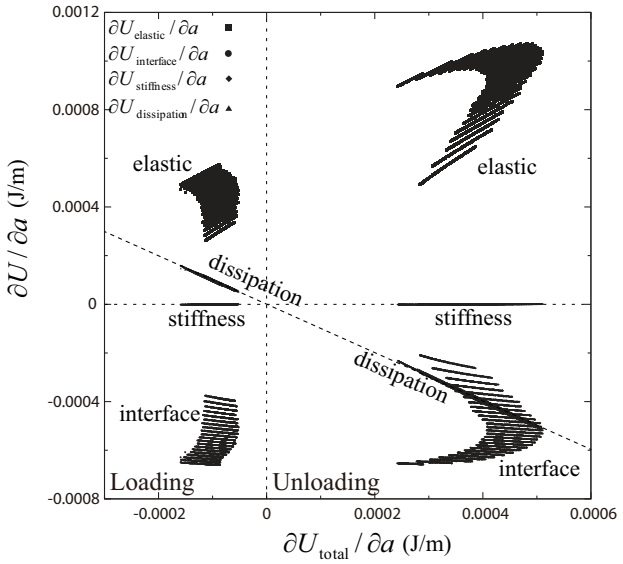

Fig. 7: Gradient of each type of energy plotted with gradient of total energy. The region of $\partial U_{\text{total}}/\partial a \geq 0$ represents loading process, region of $\partial U_{\text{total}}/\partial a \leq 0$ represents unloading process. Furthermore, the positive value of energy gradient in loading process means giving energy; the negative value of energy gradient means receiving energy, this is contrary to the unloading region.

Energy gradient is calculated at loading and unloading processes for the discussion of energy transfer. Fig.7 shows the relation between gradient of each type energy and gradient of total energy U_{total}. The total energy is the energy stored in the contact system which is defined as

$$\Delta U_{\text{total}} = \Delta U_{\text{elastic}} + \Delta U_{\text{interface}} + \Delta U_{\text{stiffness}}. \qquad (12)$$

We can get $\Delta U_{\text{total}} \leq 0$ in the duration time of fixed Z_t during both loading and unloading process due to the assumption of $\Delta U_{\text{dissipation}} \geq 0$. Because $\Delta a \geq 0$ during loading process, the negative value of $\partial U_{\text{total}}/\partial a$ correspond to the loading process. Similarly, the positive value of $\partial U_{\text{total}}/\partial a$ correspond the unloading process.

In the region of loading process ($\partial U_{\text{total}}/\partial a \leq 0$), the gradient of elastic energy and energy dissipation have positive values($\partial U_{\text{elastic}}/\partial a > 0$, $\partial U_{\text{dissipation}}/\partial a > 0$), means that they received energy. Whereas the gradient of interface energy is negative($\partial U_{\text{interface}}/\partial a < 0$), means that interface energy transferred to elastic energy and energy dissipation in the duration time of fixed gross displacement Z_t. The change of stiffness energy can be negligible due to the small order of the energy gradient. On the contrary, the elastic energy stored in the PDMS plate transfered to the interface energy and energy dissipation in the duration time of fixed gross displacement Z_t.

5 Conclusion

All kinds of energy were calculated by measuring the force F, contact radius a, displacement Z_t and determining Young's modulus E, radius of curvature R, stiffness k and work of adhesion $\Delta\gamma$. In loading process, the interface energy stored at the contact area transfered to the elastic energy of PDMS plate and energy dissipation. A stable equilibrium state exists at the beginning of unloading process which means the energy transfer does not occur. Then, in the rest of unloading process, the elastic energy stored in the PDMS lens transfered to the interface energy and energy dissipation.

References

[1] W. Hawkes *et al.,Trans. on Mechs.*, **2013** Vol.18, No.2.

[2] M. P. Murphy *et al.,* small **2009**, 5, No. 2, 170.

[3] Z. Wei *et al., Chin. Phys. Soc.*, **2004** Vol.13, No.8.

[4] H. Hertz, Macmillan London **1896**, p.156.

[5] K. L. Johnson, *et al., Proc. R. Soc. Lon., Ser. A* **1971** 324, 301.

[6] K. Takahashi, *et al.,J.Adhesion Sci.Tech.* **1995**, Vol.9, No.11, 1541.

[7] P. Silberzan,*et al.,Langmuir* **1994**, 10, 2466.

[8] G. Y. Choi, *et al.,Langmuir* **1997,** 13, 6333.

[9] A. N. Gent, *Langmuir* **1996,** 12, 4492.

[10] E.Charrault, *et al., Langmuir* **2009,** 29(10), 5847.

[11] D. Maugis,*et al.,J. Phys. D: Appl. Phys.,* **1978** Vol. 11, No. 14

[12] D. Baek *et al.,*, "Mechanism of adhesion hysteresis in the elastic between a silicone rubber and a silica glass lens" a master thesis of Tokyo Institute of Technology**(2013)**.

Performance Comparison Of Space-time Coding On Polarized and Non-Polarized Line-Of-Sight Multiple Input Multiple Output (MIMO) Propagation Channels

Student Number: 14M18307 Name: Djiby Marema Diallo Supervisor: Jun-ichi Takada

Abstract

Performance evaluation of an open loop 22 MIMO (Multiple Input Multiple Output) system under Rician fading conditions is studied in this paper. First, through spatial multiplexing technique and spatial Space Time Trellis Code (STTC) technique, and the use of a BPSK (Binary Phase Shift Keying) modulation, the BER (Bit Error Rate) is computing in each case to evaluate the channel performance. Second, by using co-located and dual-polarized antennas, we also evaluate the channel performance by considering the dual-polarized multiplexing technique and the dual-polarized diversity technique. In order to characterize these two schemes discussion on the SNR per bit is considering. We Compare of performance of 22 MIMO spatial, and dual polarized STTC and multiplexing schemes based on how the performance of these systems are affected by the Rician K factor.

1 Introduction

Recently, due to the high demand of mobile communication system in increasing data rates, reliability and efficient usage of the spectrum, the use of multiple antennas at both side transmitter and receiver appears as a breakthrough to meet these challenges. Even though the Multiple-Input Multiple-Output has demonstrated its importance to meet these challenges faced by the wireless communication designers through the multiplexing and the diversity technique, its capacity may be reduced when the transmitter does not have any knowledge about the channel propagation, when the line-of-sight (LOS) component is dominant. Even though improvement of the MIMO system can be achieve under these limits using some techniques such as beamforming, multiplexing technique in close loop system with the presence of the LOS component, correlated channel, the performance degradation cannot be avoided in open-loop MIMO system with the presence of LOS. The LOS component is known to reduce the system performance due to the high correlation of the individual channel it causes. Since orthogonal polarizations ideally may offer a complete separation between the individual channel of the propagation environment, therefore the use of co-located orthogonally-polarized antennas appears as a space and cost cost effective alternative. In this thesis, the performance evaluation of a spatially separated co-polarized and co-located dual polarized in the presence of LOS component is proposed. Specifically the performance of an open-loop MIMO system will be analyzed based on the bit-error-rate (BER). While modeling a MIMO transmission system, the Rician factor represents the ratio of the power in the LOS component and the power in the non-line-of sight component. Therefore, in order to analyze the degradation performance due to the presence of the LOS component, we will conduct simulation against the Rician K factor. Diversity technique The validation of this extended framework will be evaluated in the future work.

2 Channel Modeling

Our goal in this work is to evaluate the performance of MIMO transmission system using different antenna configuration, under Rician fading environment. Therefore we will provide the MIMO channel representation in the case where antennas are co-located and the case where they are spatially separated. The representation of the channel matrix for a MIMO system with N_T transmit antennas and N_R receive antennas is given by the $N_T \times \mathrm{N}_R$ matrix:

$$\mathbf{H}=\begin{bmatrix} h_{1,1} & h_{1,2} & \cdots & h_{1,M_T} \\ h_{2,1} & h_{2,2} & \dots & h_{2,M_T} \\ \vdots & \vdots & \ddots & \vdots \\ h_{M_R,1} & h_{M_R,2} & \cdots & h_{M_R,M_T} \end{bmatrix}$$

Each individual elements of the matrix $h_{j,i}$ represent the channel gain from the transmit antenna of index i to receive antenna of index j. Thus the mathematical representation of the MIMO system is given by the following equation:

$$\mathbf{y} = \mathbf{Hx} + \mathbf{n} \tag{1.1}$$

Where **y,x,n** are the received signal vector, the transmitted signal vector, and the noise vector respectively. In this work, the different elements of the channel matrix are supposed to be independent and identically distributed (i.i.d.) zero-mean, unit variance, complex circularly Gaussian random variables. The MIMO channel propagation is composed of the Line-of-sight (LOS) component and the Non-line-of-sight (NLOS) component. At the mobile receiver, when a signal is affected by several scattering objects, random attenuations, and delays due to the radio propagation environment, then the signal is called a NLOS component. And when the signal travels from the transmitter to the receiver without any obstructing object, it is called a LOS component. When only NLOS are present in the MIMO channel propagation, therefore the matrix coefficients can be modeled as complex Gaussian variables with zero mean. The individual elements follows

the Rayleigh distribution and the channel is called a Rayleigh MIMO channel. Rayleigh MIMO channel matrix has proven to be a very instrumental tool for the computation of the average capacity of NLOS channel like in macrocells of mobile communication systems[2],[3]. Although useful, this approach is not suitable to describe communication environment with LOS components. The Rice fading model is more appropriate as it include the LOS component.
Since we are evaluating the performance of a channel in a LOS environment therefore the Rician fading channel modeling will be adopted.

2.1 Spatially Co-Polarized MIMO Channel Model

A Rician fading environment is a propagation environment having both direct signal components and scattered signal component. The channel matrix of the Rician fading environment is given by:

$$\mathbf{H} = \sqrt{\frac{K}{K+1}}\mathbf{H_{LOS}} + \sqrt{\frac{1}{K+1}}\mathbf{H_{NLOS}} \qquad (1)$$

Where K is the Rice factor and is the power ratio in the LOS component of the channel to the power in the fading component.

2.2 Co-located Dual Polarized MIMO Channel Model

The Rician channel modeling in dual polarized MIMO system is given by te following equation:

$$\mathbf{H} = \sqrt{\frac{K}{K+1}}\mathbf{X_c}\mathbf{H_{LOS}} + \sqrt{\frac{1}{K+1}}\mathbf{X_c}\mathbf{H_{NLOS}} \qquad (2)$$

$\mathbf{X}_c$ represents the antenna depolarization matrix and is given by:
$\mathbf{X}_c$ represents the antenna depolarization matrix and is given by:

$$\mathbf{X}_c = \begin{bmatrix} 1 & \sqrt{\chi}_c \\ \sqrt{\chi}_c & 1 \end{bmatrix}$$

Where χ_c is the antenna cross-polar coupling and is assumed to be as equal to 0.

3 Space-Time coding for MIMO System

3.1 Diversity Gain

In wireless communication,the information is carried by the electromagnetic waves. Electromagnetic waves are attenuated due to some mechanism that are reflection, scattering induced by the propagation environment: this phenomena is called fading. At the receiver, the signal which is the superposition of all multipath components is degraded due the fading. Increasing the power transmission, or the antenna size, or antennas height are possible solution but not pragmatic. Since the signal is degraded at the received, if several copies of the same signal, therefore the probability that at least one copy is not corrupted is increased. This scheme of transmission and reception is called diversity and is one of the most important technique in MIMO transmission system to mitigate the effects of fading in wireless communications.

3.2 Space-Time Trellis Coding

The design criteria for Space-Time Trellis codes (STTC) was derived in [8] by Tarokh, Seshadri and Calderbank over slow frequency non selective fading channels under the assumption of a large signal-to-noise-ratio (SNR). This concept became extremely popular due its effectiveness of combating fading effects. The STTC can provide maximum diversity and coding gain with spectral efficiency over fading channels by using simple decoding techniques. The coding offered by the STTC itself is different of that provided by the achieved by the block or the convolution codes. A typical STTC designed for a wireless communication system has an encoder, pulse shaper, modulator and multiple antennas at the transmitter, and the receiver has one or more receive antennas.

3.3 Encoder structure for STTC

The encoder for a STTC is composed of one input block of n bits and v memory blocks of n bits. At each time t, the encoder maps the information bit to modulation symbols, where the mapping function is described by a trellis diagram. All the bits of a block are replaced by the n of the previous block. The i^{th} bit $b_i^{t\text{-}j+1}$,i=1,...n of the j^{th} block, j=1,... v+1, is associate to n_T multiplier coefficients $g_{i,j}^k \in Z_{2^n}$, k= 1,...n_T. Where n_T is the number of antennas. A space-time trellis encoder is defined by its generator matrix $\mathbf{G}$.

$$\mathbf{G} = \begin{bmatrix} \mathrm{g}_{1,1}^1 & \cdots & \mathrm{g}_{n,1}^1 & \cdots & \mathrm{g}_{1,v+1}^1 & \cdots & \mathrm{g}_{n,v+1}^1 \\ \vdots & \cdots & \vdots & \cdots & \vdots & \cdots & \vdots \\ \mathrm{g}_{1,1}^k & \cdots & \mathrm{g}_{n,1}^k & \cdots & \mathrm{g}_{1,v+1}^k & \cdots & \mathrm{g}_{n,v+1}^k \\ \vdots & \cdots & \vdots & \cdots & \vdots & \cdots & \vdots \\ \mathrm{g}_{1,1}^{n_T} & \cdots & \mathrm{g}_{n,1}^{n_T} & \cdots & \mathrm{g}_{1,v+1}^{n_T} & \cdots & \mathrm{g}_{n,v+1}^{n_T} \end{bmatrix}$$

4 Performance Criteria

We consider a mobile communication system with n_T transmit antennas and m_T receive antennas We assume a the STTC codeword:

$$c = c_1^1 c_1^2 c_1^3 .... c_1^n c_2^1 c_2^2 ... c_2^n ... c_L^1 c_L^2 ... c_L^n$$

Where L is the frame length. The erroneous codeword is given by:

$$e = (e_1^1 e_1^2 e_1^3 .... e_1^n e_2^1 e_2^2 ... e_2^n ... e_L^1 e_L^2 ... e_L^n).$$

In order o obtain a maximum diversity order m.n, the (n×L) difference matrix B(c,e)

$$B(\mathbf{c},\mathbf{e}) = \begin{bmatrix} e_1^1 - c_1^1 & e_2^1 - c_2^1 & \dots & e_L^1 - c_L^1 \\ e_1^2 - c_1^1 & e_2^1 - c_2^1 & \dots & e_L^1 - c_L^1 \\ e_1^3 - c_1^1 & e_2^1 - c_2^1 & \dots & e_L^1 - c_L^1 \\ \dots & \dots & \dots & \dots \\ \vdots & \dots \vdots & \dots \vdots & \dots \vdots \\ e_1^{n_T} - c_1^1 & e_2^1 - c_2^1 & \dots & e_L^1 - c_L^1 \end{bmatrix}$$

4.1 rank criterion

The rank criterion will optimize the spatial diversity gain r.m achieved by a STTC over all possible codeword pairs **c** and **c** by maximizing the rank of matrix A(c,e). The minimum rank of matrix A taken over all codeword pairs is also called the the rank of the code.

4.2 Determinant criterion

The determinant criterion optimizes the coding gain. The coding gain corresponds to the minimum r^{th} root of the sum of the determinants of all r×r co-factors of $A(c,e) = B(c,e)B^*(c,e)$ taken over all pairs of distinct codewords c and e [10]. The coding corresponds is therefore specified by $(\lambda_1\lambda_2\lambda_3....\lambda_r)^{\frac{1}{r}}$ where $\lambda_1\lambda_2\lambda_3....\lambda_r$ is the absolute value of the sum of determinants of all the principal $(r \times r)$ co-factors of A. To maximize the determinant of A(c,e) taken over all possible codeword pairs c and e is equivalent to achieve full rank r=n.

4.3 Performance Analysis

4.3.1 Spatially Separated Co-Polarized System

The system performance evaluation is done based on the Rician K factor. It is observed that when the Rician K factor is varying between -10 and 0 which correspond to the pure Rayleigh fading channel propagation, the performance of the spatially- separated Co-polarized MIMO approaches the performance of a single-input single-output propagation channel where the bit-error rate is deterministic in any case. When increasing K between 0 and 7 which correspond to the Rician fading channel where both LOS and NLOS components are present, the spatially-separated Co-polarized 2×2 MIMO system outperforms. Finally when K equals 10dB which corresponds to the pure LOS environment, the performance of the spatially- separated Co-polarized MIMO is almost the same as AWGN channel.

4.3.2 Co-located Dual-Polarized System

Similarly to the case of spatially-separated Co-polarized MIMO system, the performance evaluation is done based on the Rician K factor. Although the bit-error-rate (BER) is in different in the case of dual-polarized MIMO, the trend is the same.In pure

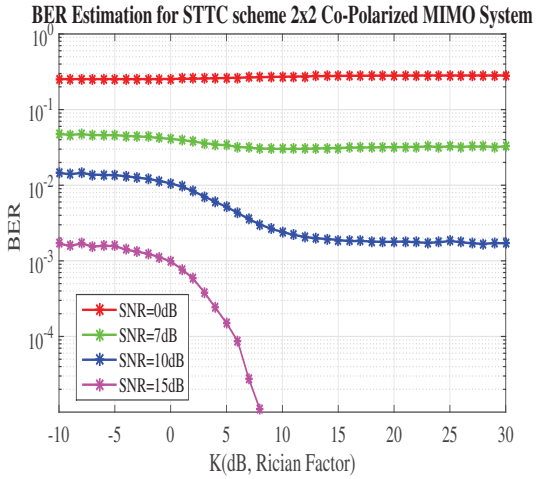

Figure 1: Co-Polarized STTC scheme

Rayleigh fading channel propagation, the performance of the Co-located dual-polarized MIMO approaches the performance of a single-input single-output propagation channel where the bit-error rate is deterministic in any case. When increasing K between 0 and 7 which correspond to the Rician fading channel where both LOS and NLOS components are present, the Co-located dual-polarized 2×2 MIMO system outperforms. Finally when K equals 10dB which corresponds to the pure LOS environment, the performance of the Co-located dual-polarized MIMO is almost the same as AWGN channel.

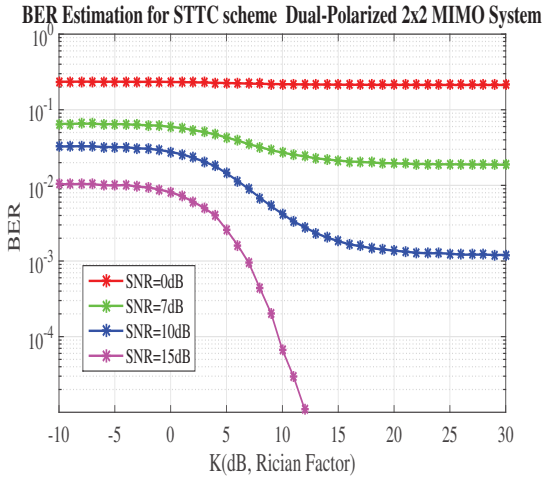

Figure 2: Dual-Polarized STTC scheme

5 Summary

The performance evaluation of a STTC spatially separated co-polarized and co-located dual-polarized MIMO system is performed in this chapter. This performance evaluation is based on the Rician K factor which determines the importance of the LOS component in the channel propagation. While spatially separated co-polarized should be preferred for rich scattering MIMO system, the co-located dual-polarized MIMO is recommended for the LOS environment.

References

[1] C.Oestges, Propagation Channel, Capacity and Error Probability with Dual-Polarized Wireless Transmissions, Indian Journal of Radio and Space Physics, vol. 36, pp. 411417, 2007

[2] Emre Telatar, "Capacity of Multi-antenna Gaussian Channels" , *European Transactions on Telecommunications*, Vol. 10, No 6, pp. 585-595, Nov/Dec 1999

[3] K. Yu, M.Bengtsson, B. Ottersten and M. Beach, Narrowband MIMO Channel Modeling for LoS Indoor Scenarios,Proceedings $XXVII^{th}$ Triennial General Assembly of the International Union of Radio Science, (URSI) Maastricht, the Netherlands, Aug. 2002.

[4] Andrea Goldsmith, Wireless Communications, Cambridge University Press, 2005.

[5] F.Bohagen, P.Orten, and G.E.Oien,On Spherical vs. Plane Wave Modeling of Line of Sight MIMO Channels, *IEEE TRANSACTION ON COMMUNICATIONS*, Vol.57, No. 3,pp. 841-849, 2006.

[6] C.Oestges and B. Clerckx, *MIMO Wireless Communications, From Real Word Propagation to Space Time code Design*. Elsevier Ltd., 2007

[7] W.L.Stutzman, Polarization in Electromagnetic Systems. Arttech House,1993

[8] W.L.Stutzman, Polarization in Electromagnetic Systems. Arttech House,1993

[9] V.Tarokh, N Seshadri, and A.R. Calderbank,"Space-Time Trellis Codes for Wireless Communications: Code Construction", IEEE 47^th Vehicular Technology Conference, vol.2, pp.637-641, Phoenix, Arizona, 4-7 May 1997.

[10] V.Tarokh, N Seshadri, and A.R. Calderbank,"Space-Time Trellis Codes for High Data Rate Wireless Communications: Performance Criterion and Code Construction" IEEE Transactions on Information Theory, vol.44, no.2,pp. 744-765, March 1998

[11] Z.Chen, J. Yuang, and B. Vucetic, "An improved Space-Time Trellis Coded Modulation Scheme on Slow Rayleigh Fading Chanels", IEEE International Conference on VCommunications, 2001. ICC 2001. Vol.4, pp. 1110-1116, Helsinki, Finland, 11-14 June 2001.

[12] N. Yuen, "Performance Analysis of Space-time Trellis codes," Master of Engineering report, University of British Columbia, April 2000.

[13] G.J. Foschini and M.J. Gans,"On limits of wireless communications in a fading environment when using multiple antennas," Wireless Personal Communications, vol. 6, pp. 311-335,1998.

[14] M.Kang and M. Alouini Performance Analysis of MIMO MRC System over Rician Fading Channels, IEEE VTC2002 fall, pp. 869873, 2002. 1, 7

[15] E.Biglieri, R.Calderbank, A.Constantinides, A.Goldsmith, A.Paulraj, and H. Poor, MIMO Wireless Communications. Cambridge University Press, 2007. 1

[16] S.Zhou and G.B.Giannakis, Optimal Transmitter Eigen-Beamforming and Space Time Block Coding Based on Channel Mean Feedback, IEICE TRANS.COMMUN., vol. E95-B, no. 11, pp. 34983508, 2012.

[17] K.Kobayashi, Ohtsuki.T, and Kaneko.T, Precoding for MIMO Sytems in Line-Of-Sight Environment, IEEE GLOBECOM 2007, 2007

[18] A. Paulraj and T. Kailath, Increasing capacity in wireless broadcast systems using distributed transmission/directional reception (dtdr), 1994. US Patent 5,345,599

[19] F.Bohagen, P.Orten, and G.E.Oien, Construction and Capacity Analysis of High Rank Line of Sight MIMO channel, IEEE COMMUNICATIONS SOCIETY/WCNC, vol. 1, pp. 432437, 2005.

[20] M.Taguchi, K.Murayama, T.Shitomi, S.Asakura, and K.Shibuya, Field Experiments on Dual-polarized MIMO Transmission with Ultra-multilevel OFDM Signals Toward Digital Terrestrial Broadcasting for the Next generation, BMSB, IEEE international symposium, pp. 15, 2011.

[21] Z. Chen ,J. Yuan and B. Vucetic An improved Space-time Trellis Coded Modulation Scheme on Slow Rayleigh Fading Channel, 0-7803-7097-1/01/10.00 copyright 2001 IEEE

GEOMETRY BASED DYNAMIC CLUSTERING OF THE DOUBLE-DIRECTIONAL WIDEBAND MULTIPATHS ESTIMATED FROM AN INDOOR MEASUREMENT AT 11 GHZ

Student Number: 14M18313 Name: Panawit Hanpinitsak Supervisor: Jun-ichi Takada

Abstract

This work proposes clustering approach utilizing scattering points (SPs) obtained from the measurement-based ray tracer (MBRT). After that, multipath components (MPCs) were classified into clusters according to those SPs. The cluster centroids were tracked along the mobile station (MS) route exploiting 2 cluster tables. The cluster characteristics were extracted from 11 GHz channel sounding data in an indoor environment. The clustering accuracy of this algorithm was assessed against the conventional clustering method. The simulation results showed that MPCs were classified into the clusters and the centroids were tracked accurately. Moreover, the cluster assessment results implied that the proposed method achieved more accuracy.

1 Introduction

Recently, the data traffic in the mobile communication has increased rapidly due to the increase of various services. To increase the network capacity, the next generation mobile communication system such as the 5th generation(5G) system has been proposed. In 5G system, the higher frequency band above 10 GHz is expected to be utilized for the mobile communications. Then the higher order multiple-input, multiple-output (MIMO) transmission technologies which utilize the several antennas will be realized in the those bands.

Since the MIMO performance strongly depends on the propagation environment, an accurate channel model is necessary for system design. Recent channel models also assumes that the multipath components (MPCs) arrives in clusters with similar characteristics. Thus, in order to create an accurate cluster based channel models, it is important that clusters should be properly defined. Conventionally, KPowerMeans (KPM) [1] algorithm has been widely used. However, the drawback is that the physical locations of interacting objects (IO) in the environment was not considered which decreases clustering accuracy. Thus, this research aims to focus on clustering in indoor environment based on scattering points (SPs).

2 Proposed Clustering Method

2.1 Scattering Points Estimation

Firstly, the measurement was conducted by using 11 GHz channel sounder [2] which output the result as superposition of paths. Then, space alternating generalized expectation maximizations (SAGE) [3] algorithm was applied to get each path parameters from measured data. The parameters of each paths consist of propagation delay, angle-of-departure (AoD) from transmitter (Tx) and angle-of-arrival (AoA) from receiver (Rx). The SPs of MPCs were estimated by measurement based ray tracer (MBRT) [4]. It inputs the path parameters obtained from the parameter estimation along with the map of the environment into the ray tracing algorithm so that the SPs and corresponding IO locations can be estimated. The algorithm was simplified to consider in the azimuth plane. Moreover, only single bounce (SB) and double bounce (DB) MPCs were considered. SB MBRT algorithm is as follows

1. Launch rays from both Tx and Rx according to its AoD and AoA with angular sweep of ± 3 degree. Find all possible SPs from all combinations of AoD and AoA sweep.

2. For each SP, calculate two values: 1. the distance between SP and the nearest IO and 2. the delay error which is absolute difference between SAGE estimated delay and theoretical delay calculated from the location of SPs.

3. If the minimum distance between the walls and SPs is significantly small, the SPs that minimize this distance are selected. Otherwise, SP that minimize the delay error are selected.

4. In case the launched rays from both Tx and Rx do not intersect, or the intersection point is more than 1 m outside the room, these MPCs are regarded as the double bounce clusters.

For DB MBRT, the algorithm is as follows

1. Launch ray from Tx according to the Anngle-of-Departure (AoD), find the intersection point between this ray and all possible objects blocking its paths. This intersection point is called the SP seen from Tx side (SPTX).

2. The same can be done from the Rx side. The intersection point in this case is called SP seen from Rx side (SPRX).

3. After obtaining SPTXs and SPRXs found in the first step, find all possible MPC travelling distances from all possible combinations of SPTXs and SPRXs

4. Calculate the delays from those distances obtained in step 3. by dividing them with the speed of light.

5. Select only one pair of all SPTXs and SPRXs where the delay is closest to the measured delay which was obtained by SAGE algorithm.

6. If the error between the SAGE delay and calculated delay is than some threshold (in this research, 10 ns was used), adjust the SPTX and SPRX. If the calculated delay is more than SAGE delay, iteratively move the SPTX and SPRX one step closer to the Tx and Rx until the error is less than 10 ns, otherwise iteratively move them further away from Tx and Rx. The step value used here is 0.2 m

2.2 Clustering and Tracking Method

After the MBRT calculated the SPs of SB and DB MPCs, these SPs were used for clustering. The concept of this clustering method is based on KPM [1]. In KPM algorithm, the clusters are identified by their centroid positions. After that, it iteratively optimizes the position of centroid in order to minimize the multiplication between multipath component distance (MCD) of centroid and MPC and path power. In conventional method [5] , MCD is defined as the Euclidean distance between 2 parameter vector which is expressed as

$$\mathbf{x}_{l,c} = [\tau_l, \cos\phi_l^{\mathrm{AoD}}, \sin\phi_l^{\mathrm{AoD}}, \cos\phi_l^{\mathrm{AoA}}, \sin\phi_l^{\mathrm{AoA}}]. \quad (1)$$

where τ_l, ϕ_l^{AoD} and ϕ_l^{AoA} denote delay time, AoD and AoA respectively. Each dimension in $\mathbf{x}_{l,c}$ is normalized to have zero mean and unit variance. In case of proposed method, this distance metric or scattering point distance (SPD) is defined as the distance between SPs. Thus, parameter vector for SB and DB MPCs are expressed as

$$\mathbf{x}_{l,SB} = [s_{x,l}, s_{y,l}]. \quad (2)$$

$$\begin{aligned} \mathbf{x}_{l,DB,Tx} &= [s_{x,l}^{Tx}, s_{y,l}^{Tx}] \\ \mathbf{x}_{l,DB,Rx} &= [s_{x,l}^{Rx}, s_{y,l}^{Rx}] \\ \mathbf{x}_{l,DB} &= [\mathbf{x}_{l,DB,Tx}, \mathbf{x}_{l,DB,Rx}] \\ &= [s_{x,l}^{Tx}, s_{y,l}^{Tx}, s_{x,l}^{Rx}, s_{y,l}^{Rx}]. \end{aligned} \quad (3)$$

where $s_{x,l}$, $s_{y,l}$, represent SB SP in x- and y-coordinates. Similarly, in case of double bounce, $s_{x,l}^{Tx}$, $s_{y,l}^{Tx}$ denotes the x- and y-coordinates of SPTX and $s_{x,l}^{Rx}$, $s_{y,l}^{Rx}$ denotes the x- and y-coordinates of SPRX. For each snapshot s, l-th MPC is denoted by $\mathbf{x}_l^{(s)}$ and the n-th SP based cluster centroid (SBCC) is denoted by $\mathbf{c}_n^{(s)}$. All the MPCs and SBCCs are stored in matrix $\mathbf{X}^{(s)} = [\mathbf{x}_1^{(s)}, \mathbf{x}_2^{(s)}, ..., \mathbf{x}_L^{(s)}]^T$ and $\mathbf{C}^{(s)} = [\mathbf{c}_1^{(s)}, \mathbf{c}_2^{(s)}, ..., \mathbf{c}_N^{(s)}]^T$ respectively where L is the number of MPC and $N = \left|\mathbf{C}^{(s)}\right|$ is the number of cluster. $\mathbf{X}_n^{(s)}$ denotes the subset of $\mathbf{X}^{(s)}$ which belongs to cluster $\mathbf{c}_n^{(s)}$. Please note that $\mathbf{x}_l^{(s)}$ is either $\mathbf{x}_{l,SB}^{(s)}$ or $\mathbf{x}_{l,DB}^{(s)}$ depending on which type of clusters are being considered. The same applies for other variables. In case of DB clusters, $\mathbf{x}_{l,Tx}^{(s)}$ and $\mathbf{x}_{l,Rx}^{(s)}$ are the simplified version of $\mathbf{x}_{l,DB,Tx}^{(s)}$ and $\mathbf{x}_{l,DB,Rx}^{(s)}$ and they are stored in matrix $\mathbf{X}_{Tx}^{(s)}$ and $\mathbf{X}_{Rx}^{(s)}$. The n^{th} SBCC in DB clusters are expressed as $\mathbf{c}_n^{(s)} = [\mathbf{c}_{n,Tx}^{(s)}, \mathbf{c}_{n,Rx}^{(s)}]$

2.2.1 Cluster Centroid Initialization

This step was done to guess initial centroid location. Deterministic initialization [6] was used in the first snapshot. The strongest path is initialized to be the first centroid. Then, for each MPC, calculate the minimum distance to the centroids available. Finally, the MPC having the maximum distance is chosen to be the next centroid. For the subsequent snapshots s, the SBCCs were initialized using the previous snapshot $s-1$ SBCCs as shown in the following

1. Set the parameter $Choice$ according to which type of MPC is being determined. Set to 0 for SB and 1 for DB.
2. Set $m \leftarrow 0$

for $n = 1$ to $\left|\mathbf{C}^{(s-1)}\right|$ **do**
  a. Find the minimum SPD between the MPC in the current snapshot s and centroid obtained in previous snapshot $s-1$
  if $Choice = 0$ **then**
    $d \leftarrow \min\{\mathrm{SPD}(\mathbf{c}_n^{(s-1)}, \mathbf{X}^{(s)})\}$
  else
    $d_{Tx} \leftarrow \min\{\mathrm{SPD}(\mathbf{c}_{n,Tx}^{(s-1)}, \mathbf{X}_{Tx}^{(s)})\}$
    $d_{Rx} \leftarrow \min\{\mathrm{SPD}(\mathbf{c}_{n,Rx}^{(s-1)}, \mathbf{X}_{Rx}^{(s)})\}$
  end if
  b. Initialized this centroid if this distance is less than some threshold
  if ($d < \epsilon_2$ **and** $Choice = 0$) **or** ($d_{Tx} < \epsilon_2$ **and** $d_{Rx} < \epsilon_2$ **and** $Choice = 1$) **then**
    $m \leftarrow m + 1$, $\mathbf{c}_m^{(s)} \leftarrow \mathbf{c}_n^{(s-1)}$
  end if
end for
3. Assign minimum number of cluster and initialize the centroids
$K_{\min} \leftarrow m$, $\mathbf{C}^{(s)} \leftarrow [\mathbf{c}_1^{(s)}, \mathbf{c}_2^{(s)}, ..., \mathbf{c}_m^{(s)}]^T$

where ϵ_2 is the threshold. It is set to 1.5 (SB) and 1 (DB).

2.2.2 Main Clustering Algorithm

As in conventional KPM, the minimum ($K_{\min}$) and maximum ($K_{\max}$) number of clusters need to be specified. Since $K_{\min}$ is already determined, only $K_{\max}$ needs to be determined. $K_{\max}$ was set to 10 for SB and 15 for DB. The proposed algorithm for snapshot s is as follows

1. Set the parameter $Choice$ according to which types of MPC is being determined. Set to 0 for SB and 1 for DB.
for $K = K_{\min}$ to $K_{\max}$ **do**
  2. Initialize additional SBCC if K is more than $K_{\min}$
  if $K > K_{\min}$ **then**
    Initialize the additional $K - K_{\min}$ SBCC using deterministic initialization [6]
  end if
  3. Cluster using KPM algorithm
  4. Check whether the resulted SBCC is compact or not, break the iteration if it is already compacted
  for $n = 1$ to $\left|\mathbf{C}^{(s)}\right|$ **do**
    if $Choice = 0$ **then**
      $\mathbf{l}(n) \leftarrow \max\{\mathrm{SPD}(\mathbf{X}_n^{(s)}, \mathbf{c}_n^{(s)})\}$
    else
      $\mathbf{l}_{Tx}(n) \leftarrow \max\{\mathrm{SPD}(\mathbf{X}_{n,Tx}^{(s)}, \mathbf{c}_{n,Tx}^{(s)})\}$
      $\mathbf{l}_{Rx}(n) \leftarrow \max\{\mathrm{SPD}(\mathbf{X}_{n,Rx}^{(s)}, \mathbf{c}_{n,Rx}^{(s)})\}$
    end if
  end for
  if ($\max\{\mathbf{l}\} < \epsilon_3$ **and** $Choice = 0$) **or** ($\max\{\mathbf{l}_{Tx}\} < \epsilon_3$ **and** $\max\{\mathbf{l}_{Rx}\} < \epsilon_3$ **and** $Choice = 1$) **then**
    break
  end if
end for

where ϵ_3 is the threshold. It is set to 0.5 (SB) and 3 (DB).

2.2.3 Optimal Cluster Number Selection

Optimal cluster number was selected by calculating and combining several cluster validation indices (CVIs) using average rank aggregation [5]. In this method, the indices of all

possible cluster numbers are calculated. After that, the rank number is attach for each type of index. If the CVI is optimized based on maximizing the index, the highest rank number is given to the maximum value, the second highest number is then given to the second maximum value and so on. If the CVI is optimized based on minimizing the index, the rank number assignment is reversed. Finally, these rank numbers are summed up for each cluster number. The optimal cluster number is then selected based on maximum number of that summation. Seven validation indices which are Xie-Beni, PBM, Calinski-Harabasz, Davies-Bouldin, Silhouette, Kim-Parks, and Dynamic indices were used.

2.2.4 Shape Pruning

Shape pruning [1] was done to remove outlier MPCs in DB clusters. Firstly, weak singleton clusters were removed until the power is less than 95 % of original power of all MPCs. After that, outlier MPCs for other clusters were removed by removing the MPC that has maximum distance from the centroid until the total MPC power is less than 90 % of original power of all MPCs.

2.2.5 Cluster Tracking Method

After all clusters in all measurement snapshots were calculated, all the cluster centroids were used for cluster tracking which is based on 2 types of tables: 1. Cluster database table (CDT) and 2. Instantaneous cluster table (ICT).

CDT keeps the databases of cluster centroid's location of every snapshots. After each snapshot, the resultant cluster centroids were input into this table. The row and column of this table are cluster indices and snapshot numbers respectively. If a cluster does not exist in some snapshot, the table is filled with an empty vector.

ICT provides the information of the clusters instantaneously at each snapshot. An example of this table is shown in Table 1. There are three columns in this table:

1. Cluster index: This column provides the information which cluster is active at that particular snapshot.

2. Position: This column gives the geometrical position of cluster centroids.

3. Counter: This number shows how many snapshots has gone without this cluster appears. This number is reset to zero if the cluster is found. If Counter exceeds some predefined value, this cluster is discarded from this table.

The criteria to track the cluster centroids is the Euclidean distance between the current and previous cluster centroids. If this distance is significantly small, the clusters are regarded to be the same. This threshold was set to 1 m for SB and 3 m for DB. The disappearance and reappearance of clusters are controlled by Counter. This value is incremented by one after each snapshot if a cluster disappears. If a cluster disappears for several snapshots, this cluster is discarded from the ICT.

3 Results and Discussion

The proposed method was validated with channel sounding data in an indoor hall environment in 11 GHz band [2]. The configuration of the sounder is shown in Fig. 1. The channel was measured continuously while the transmitter (Tx) was moved along the course at 0.25 m/s. Before running the algorithm, the Line-of-Sight (LOS) path and MPC where the delay is around the LOS delay were removed as there is no IO associated with them. Fig. 2 and 3 shows the environment floor plan and panorama photo seen from Tx at the first snapshot and Table 2 shows the specification of channel sounder used.

Fig. 4 and 5 shows locus plot of SB and DB clusters respectively in the environment. Each tracked cluster is denoted by different combination of marker and color. The clustering results shows that most of the tracked clusters are associated with one IO or few IOs which means that the proposed method can estimate cluster locations very accurately. However, some clusters are still sparse in DB results. This is because the threshold to track the cluster centroid for DB is more than SB.

Table 1: An Example of an Instantaneous Cluster Table

Cluster index	Position	Counter
1	$[x_1, y_1]$	0
4	$[x_4, y_4]$	1
5	$[x_5, y_5]$	3

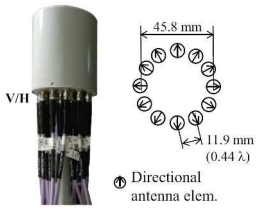

Figure 1: Channel sounder antenna array.

Table 2: CHANNEL SOUNDER PARAMETERS

Parameter	Value
Frequency, Bandwidth	11 GHz, 400 MHz
Tx/Rx antenna arrays	12 elements dual-polarized UCA
Antenna gain, Tones number	6 dBi, 2048

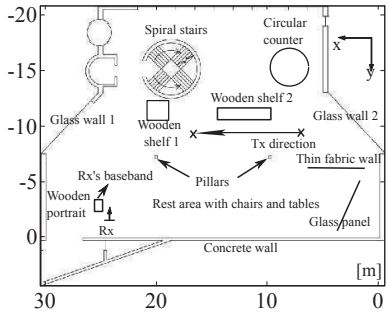

Figure 2: The considered indoor environment.

Figure 3: Panorama photo of measurement environment.

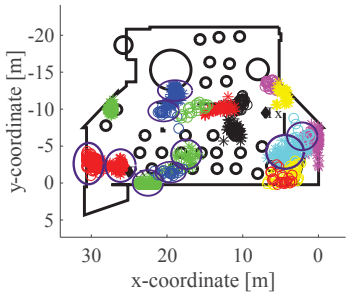

Figure 4: SPs locus of single bounce clusters.

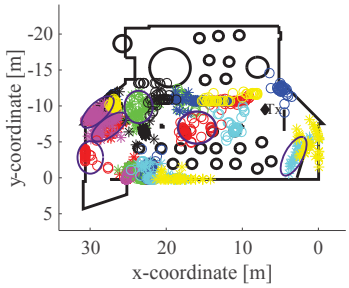

Figure 5: SPs locus of double bounce clusters.

Table 3: Cluster distribution for channel simulation

Parameters	Distribution
AoA, AoD, EoA, EoD, delay	Laplace
Power, polarization ratio	Normal
Phase (ϕ)	Uniform

Moreover, since DB clusters have to undergo double bounce, the probability that non-specular scattering occurs is higher which makes the cluster characteristics changes rapidly.

The proposed clustering results was validated and compared with the conventional method where $\mathbf{x}_{l,c}$ from equation 1 was used. The assessment was done by generating 11 MPCs for each cluster according to the distribution in table 3. After that, channels were reconstructed for both MPCs obtained from proposed and conventional clustering by superposing the MPCs. Singular value decomposition (SVD) were applied to these channel matrices and also SAGE reconstructed channel matrices to obtain all 24 eigen values of all snapshots. These eigen values are the square of channel gain which describe how much gain is achieved if MIMO channel is decomposed into parallel independent channels. Thus, they are the good indicator for modeling accuracy evaluation. The median of these Eigen-values are shown in Fig. 6. In case of first two eigen values, proposed and conventional method have similar performance. However, from the third eigen value onward, conventional method overestimates the channel. This is because some clusters from the conventional method might be the mixture of strong clusters scattered from different IOs. This makes that cluster has a very high power, angular and delay spread with centroid location not corresponding to any of the IO. Thus, the MPCs generated from this cluster would have higher power than usual which strongly contributes to the overestimation of eigen values.

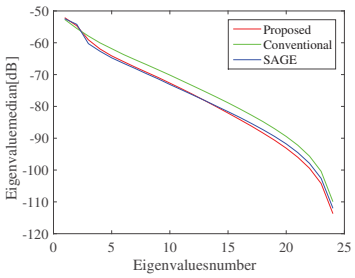

Figure 6: Median of Eigen-values comparison between proposed and conventional method.

4 Conclusion

This work presented a novel clustering method exploiting MBRT. Utilizing the SPs in the clustering algorithm, an accurate clustering and tracking could be achieved. All the tracked behaviour of clusters could be accurately justified from the location of Tx, Rx and IOs associated with them. The eigen value comparison between proposed and conventional clustering method also implied that the proposed method achieved higher accuracy by around 4 dB. These information would be vital for the analysis of the channel characteristics and modeling at 11 GHz in the future.

References

[1] N. Czink, P. Cera, J. Salo, E. Bonek, J. P. Nuutinen, and J. Ylitalo, "A framework for automatic clustering of parametric mimo channel data including path powers," in *IEEE 64th Vehicular Technology Conference (VTC 2006 Fall)*, Sept 2006, pp. 1–5.

[2] Y. Konishi, Y. Chang, M. Kim, and J. Takada, "Versatile radio channel sounder for double directional and multi-link mimo channel measurements at 11 ghz," *IEICE Transactions on Electronics*, vol. E97-C, no. 10, pp. 994–1004, Oct 2014.

[3] B. Fleury, M. Tschudin, R. Heddergott, D. Dahlhaus, and K. Ingeman Pedersen, "Channel parameter estimation in mobile radio environments using the sage algorithm," *IEEE J. Select. Areas Commun.*, vol. 17, no. 3, pp. 434–450, Mar 1999.

[4] J. Poutanen, K. Haneda, J. Salmi, V. Kolmonen, A. Richter, P. Almers, and P. Vainikainen, "Development of measurement-based ray tracer for multi-link double directional propagation parameters," in *3rd European Conference on Antennas and Propagation, 2009. EuCAP 2009.*, March 2009, pp. 2622–2626.

[5] L. Materum, J. Takada, I. Ida, and Y. Oishi, "Mobile station spatio-temporal multipath clustering of an estimated wideband mimo double-directional channel of a small urban 4.5ghz macrocell," *Eurasip J. Wireless Commun. Networking*, vol. 2009, no. 1, p. 804021, 2009.

[6] S. Mota, M. Garcia, A. Rocha, and F. Perez-Fontan, "Clustering of the multipath radio channel parameters," in *Proceedings of the 5th European Conference on Antennas and Propagation (EUCAP)*, April 2011, pp. 3232–3236.

Interannual variation of sea-breeze in Kanto-plain in summer

Student Number: 14M18135 Name: Yuta Nejime Supervisor: Manabu Kanda

夏期東京湾海風の長期年代変化

寝占　祐太

卒論において、過去の長期間の気象観測データの分析から、東京湾海風の内陸への侵入時刻が有意に変化していることを示し、それが気候変動と都市化の両方の影響によることを示唆した。本論文は、夏期の東京湾海風について、1960 年代と 2010 年代の土地利用や気候条件を再現し、都市化や気候変動に伴って、東京湾海風や相模湾海風の挙動がどのように変動したのかを、WRF（Weather Research and Forecasting Model）を用いて、数値計算によって解析したものである。

1. Introduction

The impact of urbanization to sea-breeze behavior has been a topic of interest [1] due to its mitigation effect on urban heat island. Both simulations [2] and data analyses [3] have suggested that urbanization near the coast delays sea-breeze penetration inland. However, another study, statistical comparison [4] of sea-breeze penetration time between 1960s and 2010s in Tokyo, suggests that,

- Sea-breeze penetration inland of Tokyo was delayed by ~30 min. due to surface drag from dense urban areas; and
- Sea-breeze in 2010s tends to pass the shoreline earlier than it was in 1960s due to the increasing land-sea pressure gradient possibly triggered by global climate change.

The findings were based solely from analyses of point observation data. Simulation is another tool to validate the earlier findings in Tokyo. Conversely, no study has included an accurate reconstruction of past real land morphology and climate, with specific focus on interannual variation of sea-breeze.

The objective of this research are as follows,

- To re-create 1960s' urban and climate condition.
- To find the separate effect of climate change and urbanization to the sea breeze behavior in Kanto-plain.

2. Methodology

The effect of 1960s' and 2010s' climate, and 1960s' and 2010s' land morphology to sea breeze was investigated using the weather model, Weather Research and Forecasting Model (WRF).

2.1 Reconstruction of 1960s' land morphology

To reconstruct 1960s' land morphology for weather simulation, it was necessary to construct a distribution of the following parameters [5] (additional description can be found in [6]),

- Land use category
- Plain Area Index (λ_p)
- Frontal Area Index (λ_f)
- Average Building Height (H_{ave})
- Roughness length (z_0)
- Displacement Height (d_0)
- Anthropogenic Heat Emission (AHE)

The earliest digital map of land use produced by MLIT (Ministry of Land, Infrastructure, Transport and Tourism) was retrieved for the year 1976 with high

spatial resolution, 100m × 100m, and was assumed to have the same land use as 1960s.

λ_p and H_{ave} were estimated from family-unit density in 1970 produced by MIC (Ministry of Internal Affairs and Communications). λ_f, z_0 and d_0 are estimated by λ_p and H_{ave} using regression formula [5]. Then, AHE was estimated [7] using Final Energy Consumption in Japan, 1965. The Fig.1 shows assumed H_{ave} in current and 1960s.

2.2 Reconstruction of 1960s' climate condition

In this research, a reverse approach of the Pseudo-global Warming Method [8] (PGW) was used to re-create 1960s' climate. The climate difference (ex. Temperature, horizontal and vertical wind velocity and humidity) between 2010s' and 1960s' were calculated by subtracting from 10-yr average of 2010s (2004-2013) to that of 1960s (1960-1969). Then, 1960s' daily climate data were re-created by subtracting it from 2010s' daily climate data (Fig.2). For this method, JRA-55 (Japanese 55 years Reanalysis) was used because it has available records from 1958 with a relatively high spatial resolution is 0.5° × 0.5°.

Sea breeze is driven by pressure gradient generated by the temperature differences between the land and sea. Thus, it was necessary to apply the reversed PGW approach to sea surface temperature as well. For this purpose, MGDSST (Merged satellite and in situ data Global Daily Sea Surface Temperature) was introduced. The spatial resolution is 1.0° × 1.0° and its temporal resolution is monthly.

2.3 Simulation setting

In this research, the modified [6] WRF-ARW ver.3.3.1 was used with 7 days spin-up days, and the simulation domain and resolution are shown in Fig.3 and Table1, respectively. 18 days with clear sea-breeze were statistically analyzed [4].

Three cases were simulated in this research (Table.2). "Control" case had simulated with 1960 urban morphology and 2010 climate. Urbanization's influence to sea-breeze behavior could be represented by the comparison of "Current" and "Control". On the other hand, climate change effect could be represented from the comparison of "Past" and "Control" cases.

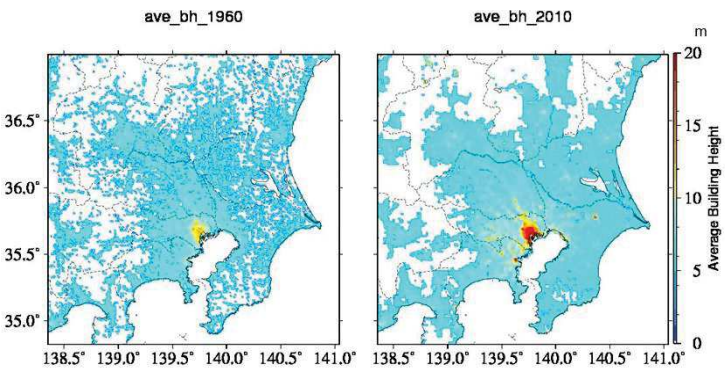

Fig.1 Average Building height
(lefe:1960s', right:2010s')

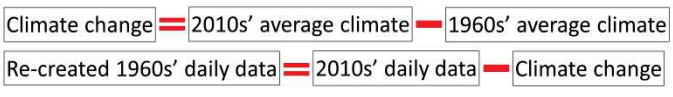

Fig.2 Modified PGW method for 1960s' climate

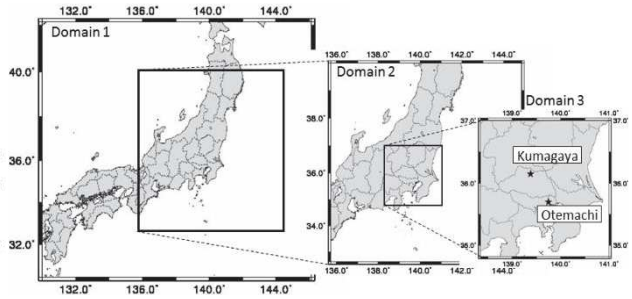

Fig.3 Simulation domain

Table.1 domain information

	Number of grid	Grid size
Domain 1	62×56×61	30000
Domain 2	171×171×61	6000
Domain 3	201×181×61	1200

3. Result

3.1 Climate differences

Fig.4 shows the temperature and wind difference between 2010s and 1960s on August; and Fig.5 shows that of sea surface temperature (SST). Left figure shows the wider domain (domain 1 in Table 1) and right figure shows domain 3 which is Kanto region. Positive value means the temperature and wind were more intense in 2010s compared to that of 1960s.

The temperature in Japan had increased about 0.3 to 0.7°C (Fig. 4). Especially in North-west side of Kanto area, the increment of temperature exceeds 1.0°C. Southwesterly winds were enhanced above the sea in 2010s'. This means that easterly winds were stronger in the 1960s'.

According to Fig.5, SST has increased around Japan, especially at northern part. SST at Tokyo and Sagami-bay also increased about 0.2~0.3°C. The increment of SST was found to be smaller than that of surface temperature above Kanto region.

3.2 Statistical result

Here, effect of urbanization and climate effect are discussed statistically based on the simulation. Sea-breeze arrival at Otemachi from Tokyo bay are 5 cases and at Kumagaya from Tokyo and Sagami bay are 9 cases. Because Sagami bay sea-breeze are dominant to penetrate to Kumagaya. In Other cases, there are rainfall event or wind from Kashima-bay and so on. The average time of sea-breeze arrival at Otemachi and Kumagaya are shown in Table.3. At Otemachi, sea breeze arrival in "Past" case is earlier than others due to the climate effect. Fig.6 shows that the ensemble average of 2-m temperature and wind distribution around Otemachi (star) at 9. Sea breeze in the "Control" case was weaker due to climate change (Fig.4). In terms of urbanization (Current v.s Control), temperature difference between land and sea in "current" are higher

Table.2 Combination of urban and climate

	Current	Past	Control
Urban	2010	1960	1960
Climate	2010	1960	2010

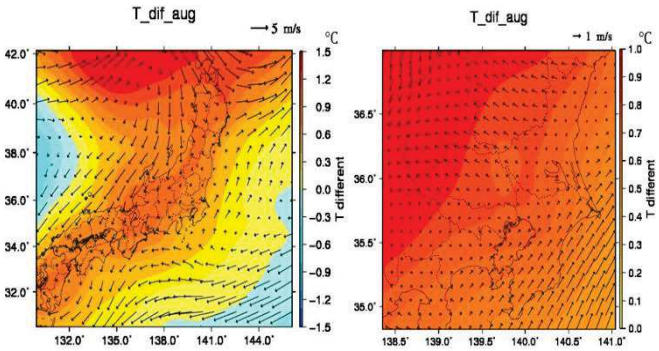

Fig.4 Temperature and wind difference between 2010s and 1960s on Aug

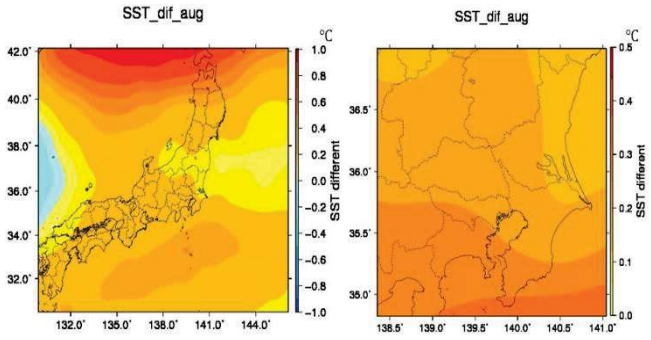

Fig.5 Sea Surface Temperature between 2010s and 1960s on Aug

Table.3 Average time of sea breeze arrival

	Current	Control	Past
Otemachi	9:06	8:51	8:22
Kumagaya	15:12	14:33	14:27

than in "Control" case. It can be deduced from this large temperature differences that sea breeze tend to penetrate in "Current" case. However, sea-breeze penetration above land in "current" case is much slower than that in "Control" because of the surface drag.

Fig.7 shows that same as Fig.6, but in whole Kanto-plain at 15:00 local time. Due to the urbanization, 2-m height temperature in "Current" is highest and temperature gradient between land and sea is higher. However winds were weaker because of surface drag.

So, the sea-breeze arrival time at Kumagaya in "Current" case are slower than the others. On the other hand, sea breeze arrival time in "Past" and "Control" don't have so much difference. Inland temperature gradient in the "Control" was higher than in the "Past" resulting to a more intensified acceleration of sea breeze in the "Control" than in the "Past". This can be obvious at the later time when sea-breeze front in "Control" has caught up with that of the "Past" case. As shown in Table 3, sea-breeze arrival time at Kumagaya shows little difference between "Past" and "Control".

4. Conclusion

- Land modification and climate in the 1960s was reconstructed to study separate effects of urbanization and climate change to sea breeze behavior;
- It is difficult for sea breeze to penetrate inland in the present because of the enhanced surface drag due to increasing building volume and extent in Kanto region (urbanization);
- Sea-breeze penetration tends to be delayed in the present climate at Otemachi when no change in urban areas is assumed; However,
- Inland temperature is warmer in the present climate (assuming 1960s urban areas) resulting to larger temperature gradient. Consequently, sea-breeze arrival time at Kumagaya in the present climate becomes similar as that of the "past" (in spite of the earlier penetration of sea breeze at Otematchi).

5. Reference

[1]. Yamamoto, H. et al.: Journal of Geography, 2011.

[2]. Kusaka, H. et al.: Journal of Meteorological Society of Japan, 2000.

[3]. Yoshikado, H. et al.: Boundary-Layer Meteorology, 1989.

[4]. Nejime, Y. et al.: Journal of Japan Society of Civil Engineers, 2015.

[5]. Kanda, M. et al.: Boundary-Layer Meteorology, 2013.

[6]. Varquez, C, G, A. et al.: Boundary-Layer Meteorology, 2014

[7]. Dong, Y. et al.: (Preparation for Submission).

[8]. Hara, M. et al.: Journal of Japan Society of Fluid Mechanics, 2010.

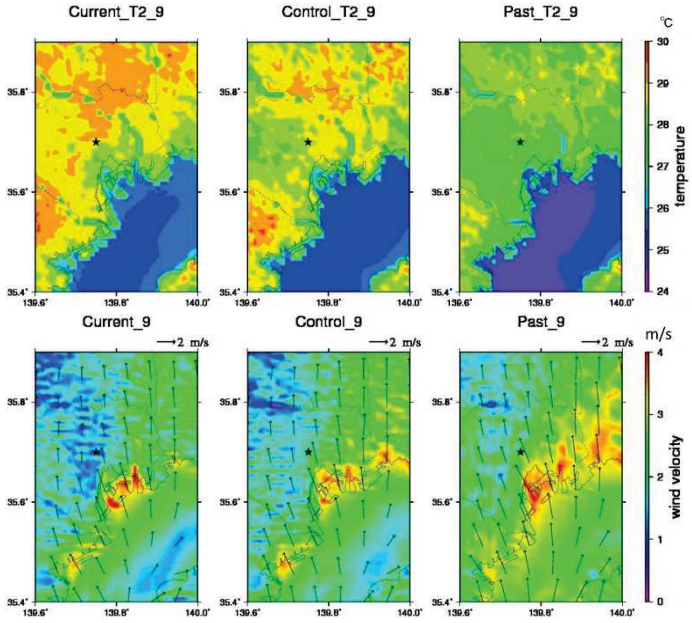

Fig.6 2-m height of temperature (upper) and wind distribution (lower) at Otemachi at 9

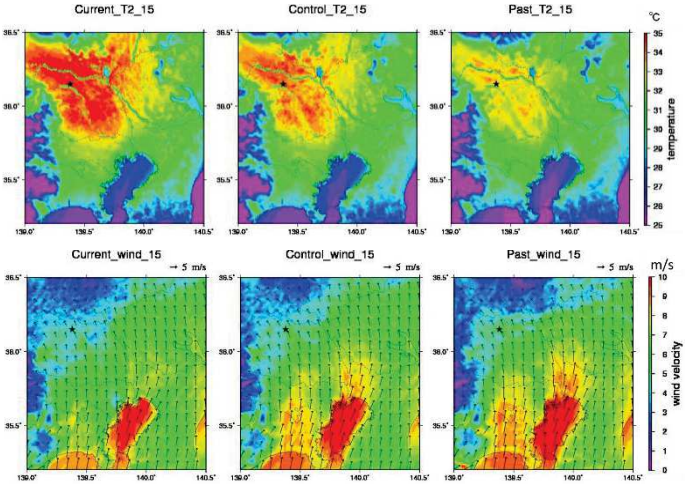

Fig.7 2m height of temperature (upper) and wind distribution (lower) in Kanto at 15

SATELLITE-DERIVED URBAN AERODYNAMIC PARAMETERS FOR MESOSCALE MODELING IN MEGACITIES

Student Number: 14M18299 Name: Nisrina Setyo DARMANTO
Supervisor: Manabu KANDA, Alvin C. G. VARQUEZ

衛星画像を用いた都市パラメータの算定とメガシティーにおける
メソスケール都市気候モデルへの応用

ダルマント　ニスリナ　セティヨ

This research aims to derive 1km high-resolution urban parameters from global satellite images as foundation on calculating WRF urban aerodynamic parameterization scheme. Empirical equations in deriving satellite images into urban geometric parameters were developed and resulted in good agreement with real ones. Simulations on Jakarta and Istanbul megacities were done by utilizing the new satellite-derived urban parameters to assess their performance in advanced WRF. Simulation results in these two megacities showed that application of satellite-derived urban parameters improves model results in representing temperature, wind speed, and other urban atmospheric phenomena.

1 Introduction

Urbanization, despite offering improved living standards and signifying rapid economic growth for the country, it also introduces social, economic, and environmental threats. One of the major environmental impacts of urbanization is modification of urban climate due to increase of heat and pollutant emissions, and changes in surface cover. The most discussed phenomenon in urban climate is urban heat island (UHI), a condition where an urban area is significantly warmer than its surrounding rural areas due to anthropogenic heat and complex urban morphology.

Recently, the said phenomenon is analysed by using state-of-the-art 3D weather and climate model which capable on medium to fine resolution such as mesoscale model. One of the sophisticated mesoscale model widely used in urban climate research is Weather Research and Forecast (WRF) model due to its capability to directly couple with urban canopy models (UCM).

From large-eddy simulation of real buildings in Tokyo, a new urban aerodynamic feedback parameterization [1] in displacement height d and aerodynamic roughness length z_0 parameters which can adequately consider the heterogeneity of urban geometry within a grid (bulk indices). Calculation of these parameters requires the urban morphology represented in five geometric parameters: plane area index λ_p (i.e., the ratio of the plane area occupied by buildings to the total floor area), the frontal area index λ_f (i.e., the ratio of the frontal area of buildings to the total floor area), the average building height H_{ave}, the maximum building height H_{max}, and the standard deviation of building height σ_H. Incorporating the new urban aerodynamic feedback parameterization in 1km resolution to WRF mesoscale model coupled with modified single layer UCM for Tokyo resolved the sea breeze fairly well along with the surface wind speed reductions at densely built-up areas [2].

Although weather modelling of urban areas improve upon inclusion of realistic parameters, distributed urban parameter data for most cities is still scarce. Setting up the urban parameters often requires realistic building data which is not available for all cities, especially those in developing countries. On the other hand, there is high potential to define two dimensional urban morphology λ_p from recent LANDSAT 8 satellite imagery due to its 30m resolution and more sensitive sensors in differentiating land use/cover. Furthermore, Digital Elevation Model (DEM) satellite ASTER launched in 2011 has tendency to give offset biases on measuring ground elevation due to forest or buildings canopy [3]. Thus, it is very likely that building canopy height could be determined by subtracting these offsets with real ground elevation. GMTED2010 was proofed in providing real ground elevation correctly [4] and will be utilized together with ASTER in estimating H_{ave}.

In this study, we aim to calculate λ_p, λ_f, H_{ave}, d and z_0 in megacities. This is a novel method in creating detailed high resolution 1km urban parameters from satellite images and prospected to be applied for global extent. Furthermore, high-resolution 1km urban climate simulation using WRF coupled with modified single-layer UCM with urban parameterization scheme was done. These simulations were conducted for Istanbul and Jakarta and is aimed to assess the capability of these satellite-derive urban parameters in defining the megacities actual urban climate condition.

2 Urban Parameters Construction for Megacities

2.1 Determining empirical equation on λ_p from LANDSAT 8

Before deriving satellite images to λ_p and λ_f, land use classification in defining types of land use/cover (e.g., water, vegetation, bare soil, and agriculture area) from these images should be done. To classify the land use from LANDSAT 8 image, supervised classification process was conducted. This process was done by using Semi-Automatic Classification (SCP) plugin available for QGIS [5]. For this work LANDSAT 8 Band 2–Band 7 were used. This classification concept is using image corrections and Spectral Angle Mapping (SAM)

algorithm. The method will maintain the classified land use in 30m LANDSAT 8 resolution.

This classification method applies the concept of machine learning by selecting Region of Interests (ROIs) as learning samples. SCP is supported with region growing algorithm during the ROIs collection which detect similar pixels value on surrounding areas. In creating an area-specified ROIs, user needs to give attention during the creation to define high-representation of real land use data. This could be done by match it with high-resolution satellite image (i.e., Google satellite image). The collected ROIs for each different land use classification is then averaged to create spectral signatures. These spectral signatures will be the based for land use classification itself by using spectral angle mapping algorithm. Since this method utilized an area-specific ROIs, the spectral-signatures will be valid in a specific area of study. There are 10 classified Region of Interests (ROIs) as the base in making the spectral wavelength; water, 3 vegetation classes (e.g., mix-vegetation, grassland, mix-forest), 2 bare soil classes (e.g., general bare soil and quarry), agriculture, and 3 urban classes (e.g., medium-dense, high-dense, and industrial/commercial) (Figure 1).

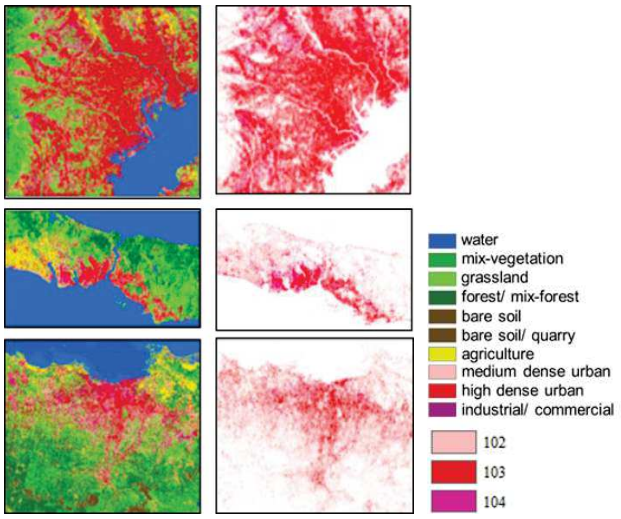

Figure 1: Land use classification (left column) and extracted urban land use (right column)

From the created urban extracted area (Figure 1), we created urban ratio which later used in comparison with λ_p real to satellite-derive λ_p predict. Urban ratio is the ratio of total area occupied with certain urban class to the total area of all urban and non-urban value in 1km grid. Therefore, there will be 3 urban ration in area inside approximately 1km resolution grid and derived as:

$$r_{102} = \frac{total\ area\ of\ 102\ in\ 1km\ grid\ km^2}{total\ area\ of\ 1km\ grid\ in\ km^2}\ , \qquad (1a)$$

$$r_{103} = \frac{total\ area\ of\ 103\ in\ 1km\ grid\ km^2}{total\ area\ of\ 1km\ grid\ in\ km^2} \qquad (1b)$$

$$r_{104} = \frac{total\ area\ of\ 104\ in\ 1km\ grid\ km^2}{total\ area\ of\ 1km\ grid\ in\ km^2}\ , \qquad (1c)$$

where r_{102}, r_{103}, and r_{104} denote medium density urban ratio, high density urban ratio, and commercial urban ratio. The result of each urban ratio in one 1km grid will be compared to λ_p real in the same corresponding grid. λ_p for Tokyo were taken from MAPCUBE provided by Pasco Geospatial (http://www.pasco.co.jp/eng/products/3d_city/). λ_p for Istanbul were taken from Istanbul real building data provided by Turkey government. λ_p for Jakarta were extracted from map image provided on Nokia Here map by using simple image processing to extract building footprint from the map.

Ordinary Least Squares (OLS) method was utilized to determine coefficient value on each urban ratio as regressor variables towards λ_p value from original building data as dependent variable. In this OLS method, we used seven real λ_p database (Table 2.2): Tokyo real λ_p; Istanbul real λ_p; Jakarta real λ_p; Tokyo and Istanbul combined real λ_p; Tokyo and Jakarta combined real λ_p; Jakarta and Istanbul combined real λ_p; and Tokyo, Jakarta, and Istanbul combined real λ_p. We used OLS prediction equation (2) to find three coefficients $\alpha_1, \alpha_2, \alpha_3$ which corresponding directly to r_{102}, r_{103}, and r_{104} respectively. Range of applicable $\alpha_1, \alpha_2, \alpha_3$ to be used in deriving λ_p value from Landsat 8 images on other cities are: $\alpha_1 = 0.01{\sim}0.03$, $\alpha_2 = 0.4{\sim}0.5$, and $\alpha_3 = 0.1{\sim}0.3$.

$$\lambda_{p_{predict}} = \alpha_1(r_{102}) + \alpha_2(r_{103}) + \alpha_3(r_{104})\ , \qquad (2)$$

Equation (2) has been proofed to have >0.86 Pearson R correlation coefficient of real λ_p and predicted λ_p in Tokyo, Istanbul, and Jakarta.

To create frontal area index λ_f, we directly derived it following λ_f empirical equation correlation with function of λ_p (2.3) (Kanda et. al., 2013). λ_f predict created from λ_p predict has Pearson R value of 0.87 with λ_f real in Tokyo, which conclude that this method is impressive to represent real 1km λ_f in urban area.

$$\lambda_f = 1.42\lambda_p^2 + 0.4\lambda_p\ , \qquad (3)$$

2.2 Determining empirical equation on H_{ave} from ASTER GDEM, GMTED2010, and Nightlight DMSP

To create empirical equation in deriving 1km H_{ave}, the satellite images used are: 30m ASTER GDEM, 7.5 arc-second GMTED2010 – and calibrated nightlight images – 1km Nightlight Defense Meteorological Satellite Program (DMSP) satellite image for Tokyo area. ASTER GDEM and GMTED2010 –interpolated into 30-m resolution- satellite images (Fig. 2(a) and (b)), both with 1-m vertical resolution were utilized as primary images in this method. Nightlight data interpolated into 30-m resolution (Fig. 2(c)) was utilized as secondary since its high potential in correcting average building height on high-rise commercial area which is analyzed lacked from ASTER GDEM and GMTED2010 due to inadequacy on urban morphology detection [6]. For validation, 1-km spatially averaged building height data from MAPCUBE was utilized. 1km average building height created from MAPCUBE then will be called H_{ave} real.

From 1-km gridded spatially average raster data of ASTER GDEM and GMTED2010, we subtract ASTER value with GMTED2010 value on the same grid. The result is filtered with urban area mask (λ_p). Nightlight data also filtered with urban area mask to be paralleled with ASTER-GMTED data. OLS of ASTER GDEM, GMTED2010 and Nightlight as

regressors variable and H_{ave} real as dependent variable was conducted to estimate a formula that define the correlation among them. The OLS result is shown in (4a), with adjustment apply for H_{ave} predict >19m as stated in (4b). This adjustment was done since (4a) tends to underestimate high-rise building value. H_{ave} predict was calculated as follows:

$$H_{ave}predict = 0.305(H_{ASTER}) + 0.01(NL) - 1.42 \quad , \qquad (4a)$$

$$H_{ave}predict > 19m = 6.37 \times (H_{ave}predict)^{0.53} \quad , \qquad (4b)$$

where H_{ASTER} denotes the value of ASTER subtracted by GMTED2010 (in meters), and NL denotes digital number value of nightlight images.

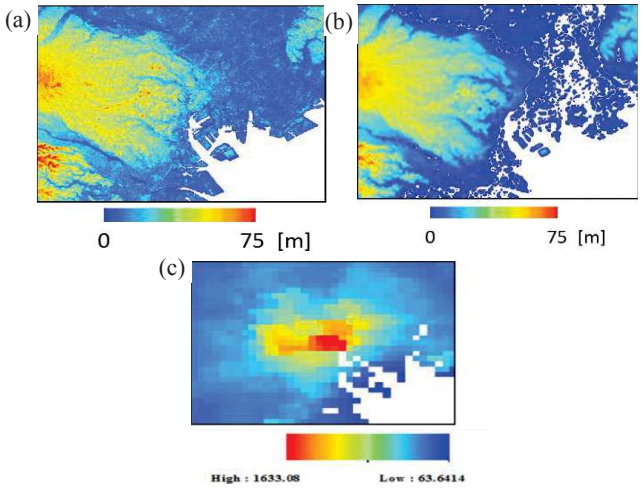

Figure 2: ASTER GDEM (a), GMTED2010(b), and Nightlight DMSP (c) for Tokyo

Correlation between H_{ave} real and H_{ave} predict has Pearson correlation R value of 0.67 for Tokyo which is considerably acceptable for this study purpose. However, for Istanbul, application of equation (4a 4b) gives low Pearson correlation value of -0.10. Based on spatial distribution (Figure 3) the spatial distribution of real and predicted H_{ave} has similar pattern in Tokyo. Nonetheless, Istanbul shows different pattern of real and predicted H_{ave}. This problem is likely due to different timestamp of real H_{ave} –which was taken on 2005- and predicted H_{ave} –which was taken on 2011-. The real H_{ave} Istanbul in 2005 was underestimate compared with 2011 building data, since this city builds significant number of skyscrapers that was just finished around late 2010 until early 2011. For Jakarta case, since there is no available real building height data such as Tokyo and Istanbul, equation (4a and 4b) were directly applied.

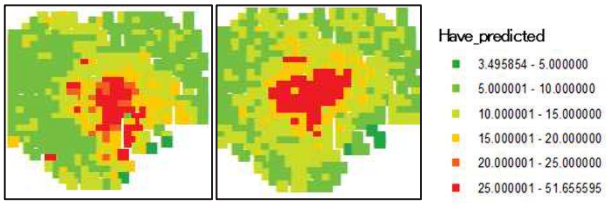

Figure 3: Spatial distribution of H_{ave} from MAPCUBE real 3D building data (left) and satellite-derived H_{ave} (right) for Tokyo

2.3 Urban Feedback Aerodynamic Parameters: d and z_0 construction

Two urban feedback aerodynamic parameters of displacement height d and roughness length z_0 were calculated using method 1 in new aerodynamic parameterization for real urban surfaces as stated in equation (5) with $a_0 = 1.29$, $b_0 = 0.36$, $c_0 = -0.17$ and (6) with $a_1 = 0.71$, $b_1 = 20.21$, $c_0 = -0.77$ [1]. Required urban morphology parameters in these equations were taken from satellite-derive urban morphology parameters described before.

$$\frac{d}{H_{max}} = c_0X^2 + \left(a_0\lambda_p^{b_0} - c_0\right)X \; ; \; X = \frac{\sigma_H + H_{ave}}{H_{max}} \; , 0 \le X \le 1.0 \qquad (5)$$

$$\frac{z_0}{z_0(mac)} = b_1Y^2 + c_1Y + a_1 \quad ; \quad Y = \frac{\lambda_p\sigma_H}{H_{ave}} \; , 0 \le Y \qquad (6)$$

3 WRF Simulation using Satellite-derived Urban Parameters

In this work, simulation on Jakarta megacity was done. Another one simulation was done for Istanbul [7]. Two nested domains and one parent domain with 30km, 6km, and 1.2km resolution for Domain 1, Domain 2, and Domain 3 respectively with one-way nesting system were set. There are 3 validation points in this simulation: Kemayoran station (KMY) 106.8133E,6.1833S; Priok station (PRK) 106.8778E,6.111S; and Cengkareng station (CGK) 106.65E,6.167S.

Two cases of simulation were conducted in this work to analyze the effect of urban parameterization on Jakarta urban climate. One case was coupled with satellite-derived urban parameterization –next will be called as Urban_case-, and another one was done without urban parameterization –next will be called as Control_case-. Both cases used updated MODIS 15' 20-categories land use on urban area and Anthropogenic Heat Flux (AHF) generated from global AHF estimation based on population and Nightlight intensity [8]. For initial and lateral meteorological boundary condition on both cases, National Centers for Environmental Prediction Final (NCEP-FNL) archive data in 1° and 6-hour resolution were used. Both used 25-days spin-up time. MODIS 4km resolution gridded Sea Surface Temperature (SST) data was used in both cases to improve NCEP-FNL low-resolution SST. Both cases used same physical settings: short wave radiation follows Dudhia scheme, long wave radiation follows RRTM scheme, microphysics follows New Thompson scheme, cumulus parameterization follows Kain-Fritsch scheme, and planetary boundary layer follows Mellor-Yamada 2.5 scheme.

The simulated result on Jakarta was compared with observation data –hourly synoptic report- from 3 stations mentioned before. Figure 4 shows temperature validation graphs for Control_case and Urban_case on KMY and CGK on fine days on August 22-30 2014. Figure 5 shows wind speed validation graphs on August 22-30 2014.

Figure 4 shows that Control_case and Urban_case has similar performance in predicting maximum temperature in Jakarta and both of them are very close to observation value. Urban_case predicts minimum temperature better than Control_case as clearly seen on KMY and CGK stations. Table 1 shows simulation and observation averaged Root Mean

Squared Error (RMSE) from 3 observation stations. Urban_case simulation decreased error between simulation and observation with 1.53 RMSE value for Urban_case and 1.77 for Control_case. This shows that adding satellite-derive urban temperature in Jakarta in modified WRF could improve simulation performance as its getting closer with point observation value.

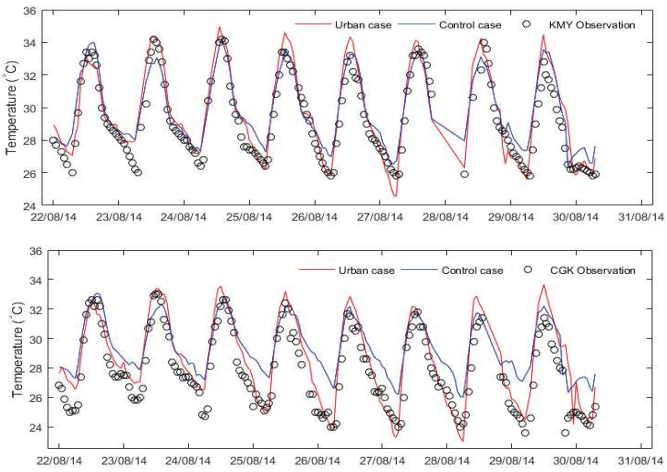

Figure 4: Temperature comparison of Jakarta simulation cases with observation

Figure 5 shows that simulation result overestimates observed data both in KMY and CGK, which is happened due to WRF sensitivity in analysing near-ground wind speed. As shown in Figure 5, Urban_case predicted lower near-ground wind speed, thus made it more similar with observed data. From Table 1, Urban_case has significant lower RMSE value compared to Control_case.

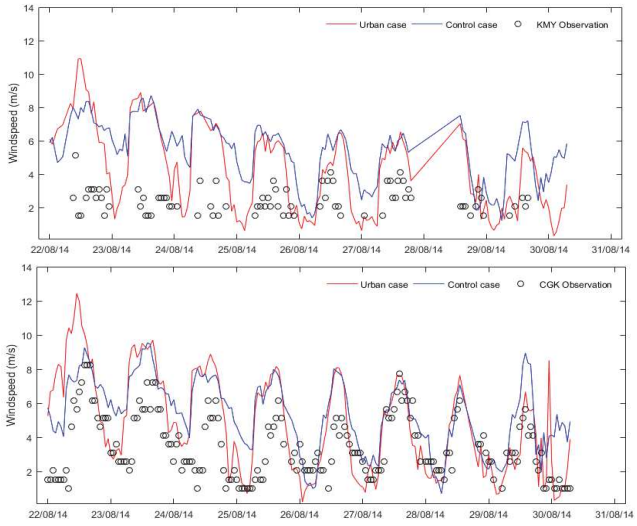

Figure 5: Wind speed comparison of Jakarta simulation cases with observation

Table 1: Average RMSE for both cases on observation data

Jakarta cases	Average Temperature RMSE	Average Wind speed RMSE
Control_case	1.77	3.53
Urban_case	1.53	2.80

4 Conclusions

Empirical equations in deriving LANDSAT 8 satellite images into λ_p and λ_f were proposed. Validation with real urban parameters were conducted and it resulted in good agreement between the real urban parameters and satellite-derived one. Validation other than mentioned cities is still in progress since it is a difficult matter to collect the data. ASTER GDEM, GMTED2010, and DMSP Nightlight image were combined to create empirical equation in deriving urban geometry parameters of H_{ave} from satellite images based on Tokyo area. Validation on H_{ave} gave a good agreement between real and satellite-derived urban parameters in Tokyo.

Two simulation cases were conducted in Jakarta to evaluate satellite-derived urban parameters performance in WRF model coupled with modified single-layer urban canopy model for urban aerodynamic parameterization scheme. It appears that simulation results using urban parameters have better agreement on temperature and wind speed with observed data compared to another case which not utilizing urban parameters. It concludes that satellite-derived urban parameters have promising potential for being source dataset in creating urban parameters, especially for most cities without distributed building morphological information.

References

[1] Kanda, M., Inagaki, A., Miyamoto, T., Gryschka, M. and Raasch, S. (2013) 'A New Aerodynamic Parameterization for Real Urban Surfaces', *Boundary-Layer Meteorology*, 148(2), pp. 357–377.

[2] Varquez, A. C. G., Nakayoshi, M. and Kanda, M. (2014) 'The Effects of Highly Detailed Urban Roughness Parameters on a Sea-Breeze Numerical Simulation', *Boundary-Layer Meteorology*, 154(3), pp. 449–469.

[3] Tachikawa, T., Kaku, M. and Iwasaki, A. (2011) *ASTER GDEM Version 2 Japan's Validation Report*.

[4] Carabajal, C. C., Harding, D. J., Boy, J.-P., Danielson, J. J., Gesch, D. B. and Suchdeo, V. P. (2011) 'Evaluation of the global multi-resolution terrain elevation data 2010 (GMTED2010) using ICESat geodetic control', *International Symposium on Lidar and Radar Mapping 2011: Technologies and Applications*.

[5] Congedo Luca, Munafò Michele, Macchi Silvia (2013). "Investigating the Relationship between Land Cover and Vulnerability to Climate Change in Dar es Salaam". Working Paper, Rome: Sapienza University.

[6] Makabe, T., Nakayoshi, M., Varquez, A. C. G. and Kanda, M. (2014) 'Database of meteorological urban geometric parameters of Japan and extension to global scale', *Japan Society of Civil Engineers*, 70(4), pp. 331–336. (in Japanese)

[7] Yucel, M., Varquez, A.C.G., Darmanto, N., Kanda, M. (2015) 'Improvements of urban representation in weather models using global datasets', *Journal of Hydraulic Engineering, JSCE,* 72.

[8] Dong, Y., Varquez, A.C.G., Kanda, M. 'Global high spatial resolution anthropogenic heat flux database' (*to be submitted*).

Process to Recover Unreacted Alcohol in Biodiesel Fuel Production from Inedible Oils

Student Number: 14M18282 Name: Zhenqiang SHI Supervisor: Ryuichi EGASHIRA

非食用油を原料としたバイオディーゼル燃料製造における未反応アルコール回収プロセス

石　振强

モデル混合物およびジャトロファ油をエステル交換して得られた実混合物を用いて液液平衡を実測した。それぞれの成分の平衡関係を明らかにし，またバイオディーゼル相と副生成物であるグリセリン相に存在するメタノールの物質量は同程度であり両相からメタノールの回収が必要であることを確認した。これらの実験結果に基づいて，バイオディーゼル相からのメタノール回収に蒸留，水による抽出，あるいはグリセリンによる抽出を適用した3つの異なるプロセスを合成し，これらを模擬計算により比較した。所要エネルギーおよび必要な操作の観点においてグリセリンによる抽出を用いたプロセスが最も優れていた。

1. Introduction

The production of biodiesel fuel has been intensively studied as an alternative and carbon neutral diesel fuel made from renewable biological sources such as vegetable oils and animal fats. Nonetheless, biodiesel fuel commercialization has not sufficiently been promoted due to the limitation on feed supply and its high cost of production. To make the variety options of feed oils, the used frying oil and inedible plant oils have been popular due to its lower price and environmentally friend resource for biodiesel fuel production[1]. For the production process, the transesterification of the feed oil with lower alcohol is reversible reaction and excessive alcohol is required to attain higher conversion of triglycerides[2]. The recovery of the excessive unreacted alcohol is one of the important challenges to improve the production efficiency. The distillation is popular method to recover the unreacted alcohol from biodiesel and glycerol phases after the transesterification[3]. The solvent extraction has also been studied as a promising method of alcohol recovery, in which water or glycerol, a byproduct in transesterification, was used as solvent[4]. However the alcohol recovery process by solvent extraction has not sufficiently been studied yet.

The objective of this study was to develop the appropriate process for recovery of unreacted alcohol for its reuse in the biodiesel fuel production. In the first, the liquid-liquid equilibrium appearing in this production was studied. Secondly, based on the above liquid-liquid equilibrium study, possible alternatives of the alcohol recovery process were synthesized, simulated, and compared. In these studies, jatropha oil, inedible vegetable oil, and methanol, one of the widely used alcohols, were considered as feed oil and alcohol for transesterification.

2. Liquid-liquid equilibrium in Biodiesel Fuel Production

2.1 Experimental

Transesterification: The composition of jatropha oil is shown in **Table 2.1** together with those of other vegetable oils. The free fatty acid, water, etc. contained in the feed jatropha oil used here were removed before the transesterification[5]. Thus purified jatropha oil and methanol were transesterified with the catalyst of sodium hydroxide under 333 K to obtain fatty acid methyl ester, i.e., biodiesel, and glycerol[5]. The glycerol phase was washed by aqueous solution of H_3PO_4 to remove salt (soap).

Measurement of liquid-liquid equilibrium: The liquid-liquid equilibrium appearing in the downstream after transesterification were measured. The conditions of the measurements are summarized in **Tables 2.2** and **2.3**. Methyl palmitate (PAME), methyl stearate (SAME), methyl oleate (OAME), and methyl linoleate (LAME) were selected as fatty acid methyl esters (FAME), since the precursors of these FAMEs were major contents in the typical vegetable oils as given in **Table 2.1**. Each single FAME of them or the mixture of all these FAMEs was used as a model biodiesel phase. The phase immiscible with biodiesel was glycerol or water to simulate the heterogeneous system just after the transesterification

Table 2.1 Four Feeding FAMEs in Biodiesel Made from Vegetabale Oils

	Rapeseed Oil [wt%]	Soybean Oil [wt%]	Palm Oil[wt%]	Peanut Oil [wt%]	Jatropha Oil[wt%]
Methyl Palmitate(PAME, C16:0)	4.30	10.5	43.5	9.40	4.20
Methyl Stearate (SAME, C18:0)	2.09	4.44	4.30	2.65	6.90
Methyl Oleate (OAME, C18:1)	61.7	22.6	36.6	46.8	43.1
Methyl Linoleate (LAME, C18:2)	19.0	51.0	9.10	33.4	34.3

Table 2.2 Experimental conditions of Liquid-liquid equilibrium

Feed		FAME, Methanol, Glycerol(or Water)
Methanol/FAME mass ratio	[-]	0 ~ 5
Glycerol(or Water)/FAME mass ratio	[-]	1
Experimental temperature	[K]	333.5
Stirring speed	[rpm]	500
Stirring time	[hours]	24

Table 2.3 Experimental conditions of MBD Liquid-liquid equilibrium

Feed		MBD, Methanol, Glycerol
Total Feed Weight	[g]	71.48
Methanol:Glycerol:MBD mass ratio	[-]	1.56:1.43:10
Experimental temperature	[K]	333.5
Stirring speed	[rpm]	500
Stirring time	[hours]	24

or in the extraction recovery of methanol in the downstream. The methanol was added to this heterogeneous liquid-liquid system to measure the equilibrium. The equilibrium in the heterogeneous system obtained after the above transesterification was measured as well.

2.2 Results and discussion

Figures 2.1 and **2.2** show the phase diagrams in the cases with single FAME component. The methanol distributed more in glycerol or aqueous phase than in FAME phase in all cases. The two-phase region in the diagram shrunk, that is, the solubilities among the components increased, as the number of double bond between carbons in a molecular of FAME increased.

These results were correlated using UNIFAC method. The UNIFAC method is one of the thermodynamic techniques to estimate activity coefficients in liquid phase with interaction parameters between functional groups composing molecular of component and so on. The correlations in the case of LAME are shown in **Figures 2.3** and **2.4** as examples. The UNIFAC method could favorably estimate the liquid-liquid equilibrium by adjusting the parameters. The parameters are tabulated in **Table 2.4**.

The distribution coefficient and mass distribution ratio of methanol, m_{MeOH} and MR_{MeOH}, were defined as,

$$m_{\mathrm{MeOH}} = x_{\mathrm{MeOH,Gly}} / x_{\mathrm{MeOH,BDF}}$$

$$MR_{\mathrm{MeOH}} = M_{\mathrm{Gly}}\, x_{\mathrm{MeOH,Gly}} / (M_{\mathrm{BDF}}\, x_{\mathrm{MeOH,BDF}})$$

with mass fractions of methanol, $x_{\mathrm{MeOH,Gly}}$, $x_{\mathrm{MeOH,BDF}}$, and masses of phases, M_{Gly}, M_{BDF}. **Table 2.5** shows the results in the case with the mixture of four FAMEs. Although it was confirmed that the distribution coefficient of methanol, m_{MeOH}, was much higher than unity also in this system, the mass of methanol in two phases were comparable because mass of biodiesel phase was much larger than that of glycerol phase in the practical production. The similar results were obtained in the case of the system just after the transesterification as presented in **Table 2.6**. Hence, it was necessary to recover unreacted methanol from not only glycerol but also biodiesel phases.

Table 2.4 UNIFAC interaction parameters employed selected groups

Mairoup	CH_2	$C=C$	OH	H_2O	$CCOO$
CH_2	0	189.66	644.6	1300	-164.04
$C=C$	-95.418	0	724.4	896	1857
OH	328.2	470.7	0	28.73	195.6
H_2O	342.4	220.6	-122.4	0	-6.32
$CCOO$	326.04	498.8	180.6	385.9	0

Selected subgroups' R_k and Q_k parameters

Subgroup	R_k	Q_k
CH_3	0.6325	1.0608
CH_2	0.6325	0.7081
CH	0.6325	0.3554
$CH=CH$	1.2832	0.7000
OH	1.2302	0.8927
H_2O	1.7334	2.4561
CH_3COO	1.2700	1.6286

Table 2.5 Results of Liquid-liquid equilibrium by MBD

	Glycerol Phase		Biodiesel Phase	
	Mass Fraction[-]	Mole Fraction[-]	Mass Fraction[-]	Mole Fraction[-]
Methanol	0.444	0.698	0.058	0.359
Glycerol	0.551	0.301	0.003	0.007
PAME	0.001	0.0001	0.163	0.119
SAME	0.001	0.0002	0.037	0.025
OAME	0.001	0.0002	0.366	0.238
LAME	0.003	0.0005	0.373	0.252
Distribution coefficient of Methanol		[-]		7.66
Mass ratio of Methanol between two phase		[-]		1.643
Glycerol phase/Biodiesel phase mass ratio		[-]		0.216

Table 2.6 Results of Transesterification by Jetropha oil

	Glycerol Phase		Biodiesel Phase	
	Mass Fraction[-]	Mole Fraction[-]	Mass Fraction[-]	Mole Fraction[-]
Methanol	0.425	0.681	0.044	0.291
Glycerol	0.537	0.305	0.003	0.007
PAME	0.004	0.001	0.094	0.075
SAME	0.001	0.004	0.026	0.019
OAME	0.013	0.004	0.381	0.277
LAME	0.019	0.005	0.452	0.331
Distribution coefficient of Methanol		[-]		9.73
Mass ratio of Methanol between two phase		[-]		1.657
Glycerol phase/Biodiesel phase mass ratio		[-]		0.248

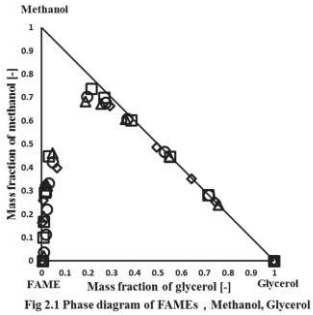

Fig 2.1 Phase diagram of FAMEs , Methanol, Glycerol

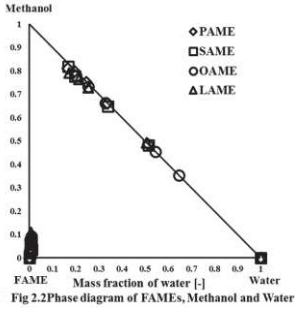

Fig 2.2Phase diagram of FAMEs,Methanol and Water

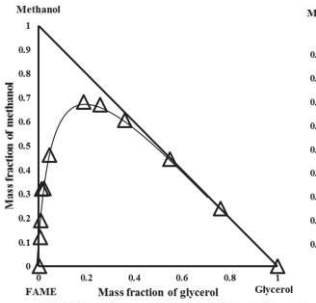

Fig 2.3 Phase diagram of LAME , Methanol, Glycerol

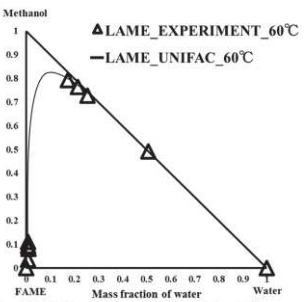

Fig 2.4 Phase diagram of LAME , Methanol, Water

3. Process to Recover Unreacted Alcohol

3.1 Process outline

The schematic diagrams of three processes, Processes a, b, and c, are presented in **Figures 3.1**, **3.2**, and **3.3**, respectively.

Process a: The unreacted methanol in both phases are recovered by distillation. Recovered methanol is reused in transesterification as feed. After distillation, the biodiesel phase is washed by

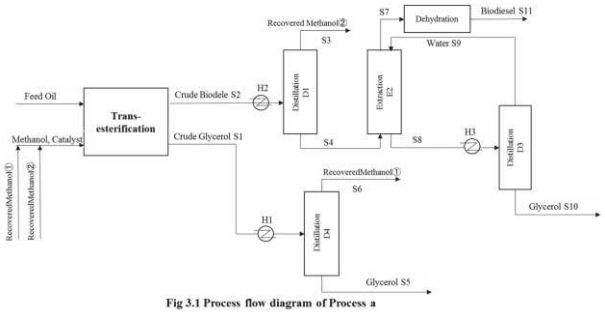

Fig 3.1 Process flow diagram of Process a

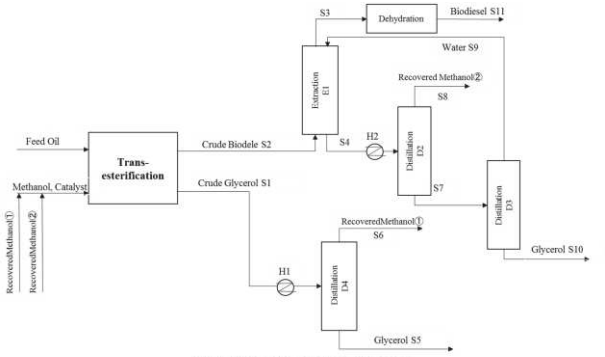

Fig 3.2 Process flow diagram of Process b

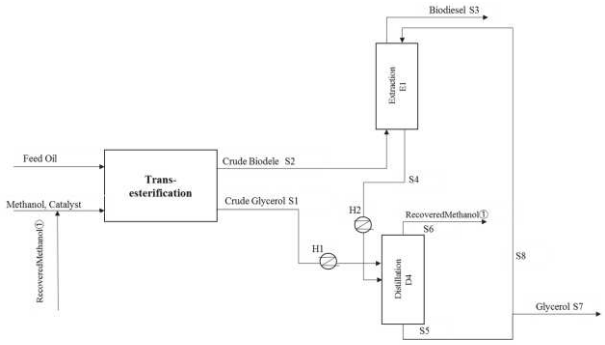

Fig 3.3 Process flow diagram of Process c

water to remove glycerol. Then the water and glycerol are separated by another distillion. Biodiesel fuel product is obtained after dehydration. Recovery of unreacted methanol by distillation is the most normal way in biodiesel production.

Process b: The unreacted methanol in byproduct glycerol phase is recovered by distillation, while biodiesel phase is firstly extracted by water to remove the methanol and glycerol. Then biodiesel fuel product is obtained after dehydration. Methanol and glycerol are separated from water by distillations. Thus recovered methanol is reused in transesterification as feed and water reused in extraction.

Process c: The unreacted methanol in crude biodiesel phase is firstly extracted by purified glycerol, then this glycerol phase is distillated with the crude glycerol phase to recovery the methanol in. Recovered methanol is reused as feed in transesterification.

3.2 Calculation

The equations of material balances, enthalpy balances, equilibrium relationships, and so forth formulated for the process were solved simultaneously under the assumptions of ideal stages for solvent extraction and distillation. The program written in Visual Basic was used for the calculation of solvent extraction, where the equilibrium was estimated by UNIFAC method with the parameters shown in **Table 2.4**. The distillation was calculated by a commercial process simulator (PRO/II, Invensys).

The operating conditions and specifications for the products are shown in **Table 3.1**. The heats consumed by heat exchanger and ditillation reboiler were regarded as the energy requirement for the process.

3.3 Results and discussion

Figures 3.4-3.7 show the effects of the number of stages in the extraction on necessary S/F ratio and energy requirement for the process in Processes b and c. The S/F ratios and energy requirements decreased with the numbers of stages and were almost constant, where the numbers of stages were more than five. The numbers of extraction stages in the both processes were, thus, fixed at six, hereafter.

Tables 3.2 shows the product results in three processes. The yield of methanol in Process a was highest at 0.995. The purity and yield of glycerol in Process c were the highest at 0.974 and almost unity with the methanol yield of 0.98. The yield of biodiesel of three processes were all over 0.99.

The energy requirements for the respective processes are summarized in **Table 3.3**. Under the same conditions and specifications, the energy

Table 3.1 Calculation conditions of processes

Equipment	Process a	Process b	Process c
	E2	E1	E1
Feed	Biodiesel Phase	Crude Biodiesel	Crude Biodiesel
Solvent	Water	Water	Glycerol
Column Temperature [K]	333	333	333
Column Stages [-]	1	1 ~ **6**	1 ~ **6** ~ 12
Extraction Specification	$x_{R,Glycerol} = 0.002$	$x_{R,MeOH} = 0.002$	$x_{R,MeOH} = 0.002$
	D1	D2	
Column Pressure [atm]	1	1	-
Column Stages [-]	5	10	-
Feed Tray	3	9	-
Distillation Specification			
Yield of Methanol [-]	0.999	0.999	-
Methanol Purity [-]	0.99	0.99	-
	D3	D3	
Column Pressure [atm]	1	1	-
Column Stages [-]	5	5	-
Feed Tray	2	1	-
Distillation Specification			
Yield of Water [-]	0.999	0.999	-
Water Purity [-]	0.99	0.99	-
	D4	D4	D4
Column Pressure [atm]	1	1	1
Column Stages [-]	5	5	5
Feed Tray	2	2	2, 3
Distillation Specification			
Yield of Methanol [-]	0.999	0.999	0.999
Methanol Purity [-]	0.99	0.99	0.99

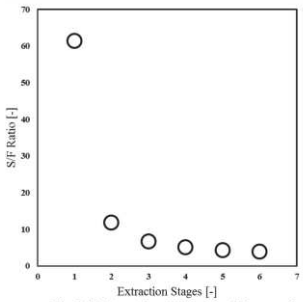

Fig 3.4 Extraction S/F Ratio of Process b

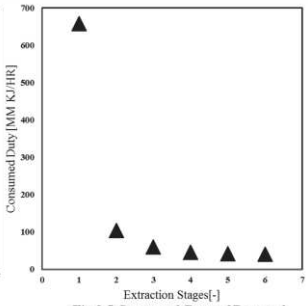

Fig 3.5 Consumed Duty of Process b

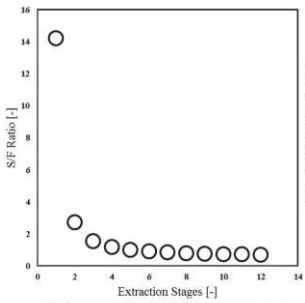

Fig 3.6 Extraction S/F Ratio of Process c

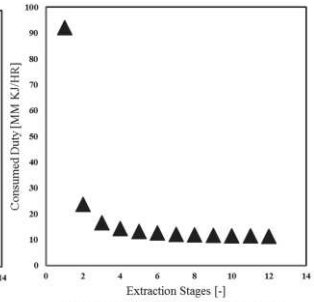

Fig 3.7 Consumed Duty of Process c

Table 3.2 Product results of each process

		Process a	Process b	Process c
Biodiesel	Purity [-]	0.998	0.998	0.996
	Yield [-]	0.987	0.987	0.987
Methanol	Purity [-]	0.999	0.999	0.999
	Yield [-]	0.995	0.973	0.980
Glycerol	Purity [-]	0.875/0.999	0.875/0.412	0.974
	Yield [-]	0.972	0.965	1.00

required for Process a and Process b were aboutdouble and triple of that for Process c, namely, Process c could be operated with much lower energy than Processes a and b.

The unit operations necessary for the respective processes are presented in **Table 3.4**. The number of operations, especially distillation, in the case of Process c was smaller than those of the other processes. Also in this point of view, Process c was superior to the other processes.

4. Conclusions

The liquid-liquid equilibriums in the biodiesel fuel production were clarified and it was confirmed that unreacted methanol should be recovered from not only glycerol but also biodiesel phases.

Three synthesized processes using extraction and distillation methods to recover the unreacted methanol after transesterification were calculated. Process using by-product glycerol as extraction solvent requires lower energy and fewer equipments than others with a high yield and purity of glycerol, methanol and biodiesel.

Table 3.3 Results of Energy Required in Process

	Engergy Duty [MM KJ/HR]		
Items	Process a	Process b	Process c
Heat Exchanger			
H1	2.929	2.929	2.929
H2	18.028	17.502	9.129
H3	0.486	-	-
Distillation Reboiler			
D1	1.954	-	-
D2	-	15.25	-
D3	0.136	4.291	-
D4	0.612	0.612	0.465
Total	24.145	40.584	12.523

Table 3.4 Equipments Required in Process

Equipment	Process a	Process b	Process c
Extraction Column	1	1	1
Distillation Column	3	3	1
Dehydration	1	1	0
Heat Exchanger	3	2	2
Total	8	7	4

Nomenclature

M	=	mass	[g]
m	=	distribution ratio	[–]
MR	=	mass ratio	[–]
S/F	=	flow rate ratio of solvent relative to feed	[–]
x	=	mole fraction in phase	[–]

<Subscipt>

BDF	=	Biodiesel Fuel
D	=	Distillation Column
E	=	Extraction Column
FAME	=	Fatty Acid Methyl Ester
H	=	Heat Exchanger
i	=	Component i
LAME	=	Methyl Linoleate
MeOH	=	Methanol
OAME	=	Methyl Oleate
PAME	=	Methyl Palmitate
R	=	Raffinate
S	=	Stream
SAME	=	Methyl Stearate

Literature Cited

1) S. Eguchi *et al.*; *J. Cleaner Pro.*, 101, 245-250, (2015)
2) B. Freedman *et al.*; *J. Am. Oil Chem. Soc.*, 61, (10), 1638-1643, (1984)
3) A. Anton *et al.*; *Apply Energy*, 99, 146-153, (2012)
4) J. Ye. *et al.*; *Biosource Technology*, 102, 4759-4765, (2011)
5) P. Sinthupinyo; Master Thesis, Tokyo Tech (2007)

ROLE OF PARATRANSIT MODES ON ACCESSIBILITY IN KHULNA, BANGLADESH

Student Number: 14M18201 Name: DHRUBO Alam Supervisor: Shinya HANAOKA

Paratransit is an informal transportation mode which includes non-motorized transport; quite popular and widely used in many developing cities. Khulna, is the 3rd largest city of Bangladesh, with high number of paratransit traffic among its' total vehicle fleet. The main objectives of the study are: explaining the traffic situation of Khulna in the context of Bangladesh and develop a mode choice model for various modes including the paratransits. Mode choice depends on travel time for shorter trips. In case of longer trips, fare is also significant. The important socioeconomic factors are house ownership and house type as proxies for income.

1. Introduction

Paratransit is generally, informal, privately owned, runs without subsidy, either door-to-door or shared and includes Non-Motorized Transport (NMT). They are also often unregulated, poorly managed and designed (both the service and vehicles). But it provides accessibility in developing cities, sometimes even with the presence of a transit mode, usually at a relatively low cost and investment; but probably at the expense of travel time and safety.

Many midsized developing cities of the world face serious issues in providing transport accessibility, especially to the poor, with their limited budget. Khulna, Bangladesh has the following special characteristics of its socioeconomic situation and transport system: (i) it has high number of paratransit traffic among its' total vehicle fleet (ii) large proportion of low income people among inhabitants, also presence of high number of students, industrial workers, refugees and existence of many slums etc. (iii) prevalence of walking as a mode (iv) no Compressed Natural Gas (CNG) fueled vehicle, poor bus service with only one route operating in north-south direction. Also there is no urban rail (v) important effect of gender while choosing transport modes.

It is the 3rd largest city of Bangladesh and also a divisional headquarters. It is located in the southwestern part of the country. The city is situated in the northern part of the district, and is mainly an expansion of trade centers close to the Rupsha and Bhairab rivers. The Central Business District (CBD) is in the south and the industrial zone is in the north. One of the main reasons for having such high number of paratransit (especially battery bikes) is the proximity of the Mongla sea port, which is about 50 km south from the city. Almost all of the battery bikes are from China and imported via the port, resulting in cheaper price and high availability.

This study elaborately describe and explain the contribution, characteristics and transit pattern of paratransit modes and its network in a midsized developing city (in terms of population and area), taking Khulna as a case study. The sub objectives of the study are as per following: (i) explaining the traffic situation in the context of Bangladesh (ii) develop the mode choice model for various modes (including the paratransits like rickshaws, battery bikes, auto-rickshaws etc).

So far, there has been not much published research on transposition system of Khulna, specially focusing on paratransit. Common researches on Khulna include road accident and traffic safety, analyzing efficiency of certain roads, and modeling Spacio-temporal land cover growth dynamics. Also, no mode choice model or utility function for Khulna has been developed. Mode choice models developed for Dhaka in the recent past by Hasan [1], Rahman et al. [2] and Enam [3], are important in this context. But, none of them includes all the paratransit modes (e.g. battery bikes, rickshaws, autorickshaws etc.) individually; many socioeconomic factors (e.g. gender, income, household type etc.) or the phenomenon of mode changes during a trip with single trip purpose have been analyzed.

2. Methodology

2.1. Survey Design and Data Collection

A questionnaire survey has been conducted for data collection in Khulna from 6 to 12 December, 2015. Basic socioeconomic information (e.g. monthly income, occupation, etc.) along with trip information was collected. Also, a survey on drivers was conducted at the same time, to get the situation from the supply sides' perspective and their situation. The uniqueness of the data was it includes the information of the number of mode change and the involved modes in details. In Khulna, significant numbers of trips with a single trip purpose are made involving more than one mode and changes.

2.2. Model Development

A discrete choice modeling (Multinomial logit model) is used to estimate the utility parameters of different choice. The utility of a choice set i of individual n can be expressed as in Equation (1)

$$U_{in} = \beta_i * X_{in} + \varepsilon_i, \forall\ i \in C_n \quad (1)$$

Where, X_{in}: Socioeconomic characteristics of the individual n and attributes of different modes i, β_i: Coefficient of X_{in}, ε_i: Random error term and C_n: Universal choice set or the choice set determined deterministically for individual n.

For the basic model, two candidate variables were used, they are: (1) travel time, and (2) fare. In here, the travel time means in-vehicle travel time. The definition of the trip is following; a single trip can only have one trip purpose with a distinct origin and a

distinct destination. The trip maker can change the mode, one or more than one time at different locations, but if the trip purpose remains same, it is considered as a single trip with that Origin-Destination (OD) pair, involving different mode combination. Walk is considered as a mode only when it is more than 5 minutes.

The wards (an administrative unit), has been used as zones. The 31 wards are considered as zones and also for trips from outskirts of the city some neighboring zones were also considered. The distances between the zones are calculated by GIS software between the centroids of the zones.

In case of non-chosen alternative modes for each OD pair and each mode, the cost (fare) and travel time are calculated by multiplying average value of cost (fare) per km and travel time per km with distance respectively, the distances between the OD pairs are used. The cost (fare), travel time and distance are in Taka, minute and km respectively. While calculating average value of cost (fare) per km and travel time per km of a mode; in case of linked trips with changes, travel time and cost (fare) of the unlinked part of the trips are averaged for each different mode between the zones, similarly like the direct trips with OD pair. For motorcycles, fuel efficiency (km/liter) for Indian cities and fuel price (96 Taka/liter) of Bangladesh are used. In case of students, a flat rate of fare of 3 taka per trip is used. This is because students generally pay around 1,000 Taka per year for bus use (1USD=70 Taka, 1 Taka=1.54 JPY).

3. Results

3.1. Travel Behavior Survey

The initial sample size was 1,800. It came down to 1,534 after removing the erroneous ones and wrong entries. Most (74%) of the trips made were direct and 26% of them had at least one change (mostly, with one change, 22% of all). For trips with mode changes, the main mode or dominating mode is considered as the one which takes longer travel time.

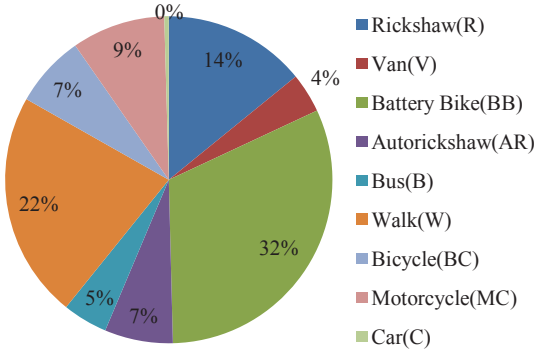

Fig 1: Mode distribution in case of direct trips (N=1,128) (both intra and inter zone)

As seen from Fig 1, in case of direct trips, the highest number of trips is made by battery bikes (32%), followed by walk, and rickshaws. The mode shares of other modes are less than 10%. The modal share of car is very low (<1%), so it is ignored in modeling.

Fig 2 shows, in case of modes with at least one change, the significant combinations are W_BB, BB_BB and BB_W. In case of trips with changes, it can be observed that, in most cases, at least one of the modes from trips from the origin or to the destination is NMTs (e.g. rickshaws, vans, etc.) or walks, which are mainly used for short distances; they contribute as an access or egress mode. So, only BB_BB is considered for the model.

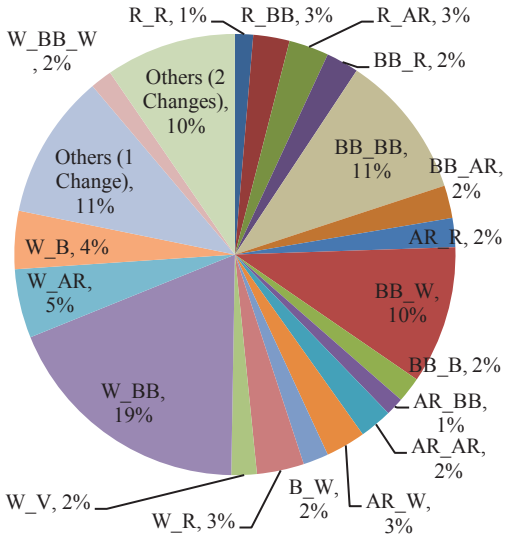

Fig 2: Mode distribution in case of trips with at least one change (N=408) (both intra and inter zone)

Fig 3 shows, most of trips made were work, school, shopping, recreational and business trips. Bazaar trips (which means going to the groceries) are mostly walking, because people do their groceries nearby. Almost 30% of the trips are made by battery bikes, irrespective of the trip purpose.

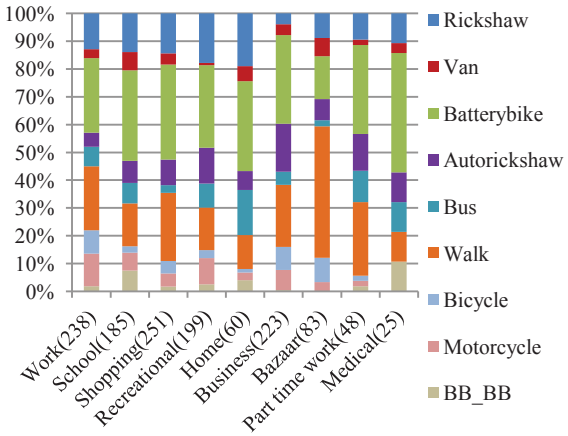

Fig 3: Modal share vs. trip purpose (both intra and inter zone)

It is observed from Fig 4, that people with less income, like 1,000 taka or less, tend to walk more. Richer people can afford motorcycles, and use them more often. A lot of the respondents (249) did not

answer the income related question, or rather did not answer honestly.

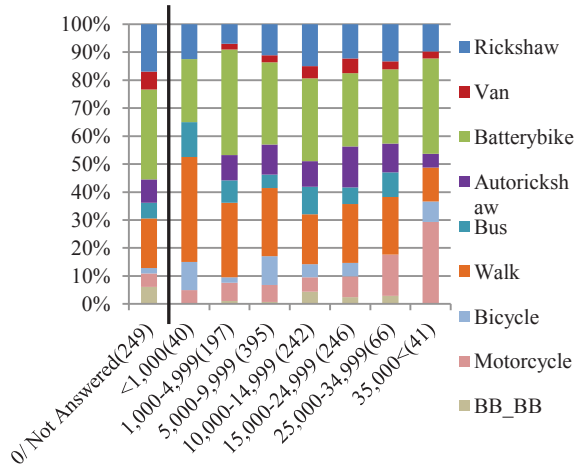

Fig 4: Modal share vs. monthly household income level (in Taka) (both intra and inter zone)

It is shown in Fig 5 that, the mode choice changes significantly when the distance get over 4 km or 6 km. People use bus and autorickshaw for longer distances. Also, as expected walking distance is generally less than 6 km and use of battery bikes decrease with distance. So, 4 km and 6 km are used as a threshold value to stratify the inter-zonal samples into two groups for modeling.

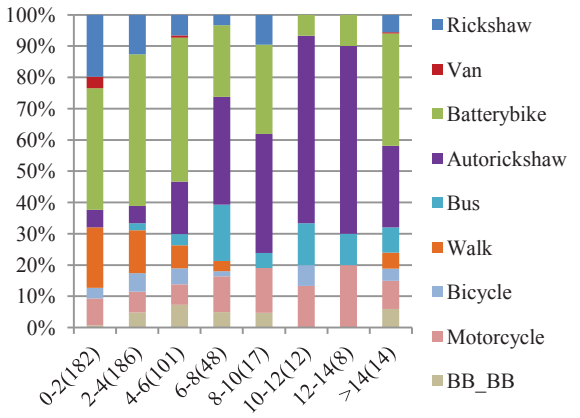

Fig 5: Modal share vs. trip distances (in km) (only inter zone)

Finally, for the multinomial logit model, 9 transportation modes are considered, namely: (1) auto-rickshaw (AR), (2) bus (B), (3) battery bike (BB), (4) bicycle (BC), (5) motorcycle (MC), (6) rickshaw (R), (7) van (non-motorized 3-wheeler) (V), (8) walk (W) and a combination (9) battery bike and battery bike (BB_BB). In case of the combination, a trip with single trip purpose is made, with one change during the trip.

3.2. Driver's Survey

Daily income for the 90% of the driver is less than 1,000 Taka, 70% of them drive battery bikes and 80% of them do not own the vehicle, so they rent from the businessmen. Almost 85% of the drivers solely depend on this income. It is quite common for the owner to carry the fuel expenses in case of battery bikes; so it is then included in the rent. As a result, 50% of the drivers have no fuel cost. In other cases, the daily fuel cost is less than 200 Taka, which is quite low. This is also because the battery bikes do not have a high fuel cost like petrol or octane. The daily rent is quite high, in half of the cases; it is about 400-700 Taka.

More than half of the garages (from where the driver rent their vehicle and keep at night) have 6-20 vehicles per garage. The autorickshaw drivers are more experienced, licensed and in most cases, driven something else before. In case of battery bikes, the drivers are new; less experienced and have no license. The battery bike driver or owners have too many organizations or co-operative societies among themselves, but none of them has the complete control (e.g. fare determination, routing decisions etc.) over their operations. On the other hand, there are two autorickshaw associations (one in north and the other in southern part of the city).

3.3. Mode Choice Model

Only inter zone trips were used for analysis. Also, long distance (inter-district) trips are excluded as the study focus is on urban mode choice model. The number of inter and intra zonal trips are 807 and 727 respectively.

People tend not to give income information as it is considered a sensitive issue in Bangladesh. Also, women, children and aged persons are dependent on others, like their husbands, parents and children respectively. In these cases, they do not know or do not have any income. So, house ownership and house type are used as proxies for income.

Table 1: Dummy variable description

No	*Variable*	*Observations*
1.	Vehicle ownership	1: if the person owns a motorcycle or bicycle 0: Those who do not own a motorcycle or bicycle
2.	Occupation	1: If the person is a student 0: anyone other than student
3.	Gender	1: Female 0: Male
4.	House ownership	1: if the person owns a house 0: Those who do not own a house
5.	House Type	1: if the person live in a built up house 0: if the person do not live in a built up house

The following tables (Table 2, 3 and 4) are the results of basic models and model with dummy variables with stratified (based on trip distances) inter-zonal data samples. From Table 2 and 3, it is observed that, travel time is important for mode choice for shorter trips (less than 6 km) and both travel time and fare is significant in case of comparatively longer trips

(more than 4 km). Their coefficients are negative for both cases, which is logical and expected. The model for less than 6 km trip distances shows better result than the other model, as it has only one mode (BB_BB combination) insignificant. So, for the next step, this model is used with dummy variables and the results are shown in Table 4. (*), (**) and (***) denotes 10%, 5% and 1% significance level respectively for all the tables.

Table 2: Utility parameters for basic model (trip distances less than 6 km)

Parameters	***Value***	***t-test***	***Significance Level***
Alternative Specific Constants:			
autorickshaw	0	-	-
bus	-2.430	-5.420	***
battery bike	2.080	10.810	***
BB_BB	0.727	1.620	
bicycle	2.170	4.650	***
motorcycle	1.580	4.840	***
rickshaw	1.810	7.300	***
van	-1.000	-2.770	***
walk	1.420	5.350	***
Fare	-0.005	-0.310	
Travel Time	-0.120	-8.050	***
Number of observation: 475 Number of estimated parameters: 10 Null log-likelihood: -865.711 Final log-likelihood: -613.969 Adjusted rho-square: 0.279			

Table 3: Utility parameters for basic model (trip distances more than 4 km)

Parameters	***Value***	***t-test***	***Significance Level***
Alternative Specific Constants:			
autorickshaw	0	-	-
bus	-5.650	-6.330	***
battery bike	3.490	5.690	***
BB_BB	2.450	3.230	***
bicycle	4.160	2.090	**
motorcycle	-1.360	-1.400	
rickshaw	5.740	2.520	***
van	-4.790	-0.420	
walk	0.350	0.200	
Fare	-0.120	-1.890	*
Travel Time	-0.330	-6.130	***
Number of observation: 210 Number of estimated parameters: 10 Null log-likelihood: -411.123 Final log-likelihood: -66.679 Adjusted rho-square: 0.813			

Table 4 shows that, house ownership and housing type are the most significant socioeconomic factor for mode choice. The dummy variables are used with only the modes stated next to them enclosed by brackets in Table 4. People with higher income, use private mode motorcycle) and tend to use rickshaws more often instead of walking. Bus is preferred by students and autorickshaw and van by women. People, who do not own any vehicle, (generally poorer households), use bus and van, and tend to walk more. Adding the dummy variables in the model makes BB_BB combination significant.

Table 4: Utility parameters for the model with dummy variables (trip distances less than 6 km)

Parameters	***Value***	***t-test***	***Significance Level***
Alternative Specific Constants:			
autorickshaw	0	-	-
bus	-2.270	-4.210	***
battery bike	2.930	9.100	***
BB_BB	1.550	3.000	***
bicycle	2.850	5.200	***
motorcycle	0.915	2.050	**
rickshaw	2.090	5.100	***
van	-0.809	-2.100	**
walk	2.590	6.220	***
Travel Time	-0.118	-7.790	***
Dummy and Socioeconomic Variables:			
Gender (AR, V)	0.417	1.200	
House Ownership (AR, MC, V)	1.230	4.070	***
House Type (B,MC)	0.847	3.110	***
Income (W)	-0.000	-1.290	
Occupation (B, AR)	0.511	1.470	
Vehicle Ownership (AR, B, W)	-0.562	-1.710	*
Number of observation: 475 Number of estimated parameters: 16 Null log-likelihood: -865.711 Final log-likelihood: -594.014 Adjusted rho-square: 0.295			

4. Conclusion

This study describes the key features of Khulna's transportation, trip behavior and developed a mode choice model including almost all the modes in Khulna. Most of the trips made are direct (74%) and less than 6 km in length (72%). The drivers' profit is not quite high, but almost all of them (85%) solely depend on this income. Also, most (62%) of the businessmen of the paratransit sector are relatively small to midsized (operating 11 to 20 vehicles). Apart from the trip attributes (travel time and fare), most important socioeconomic aspects for mode choice are house ownership and housing type. In case of other dummy variables, their signs are also logical, even though they are not always as significant as these two. Some socioeconomic factors like age and permanent residency do not have influence on mode choice. These results can be used for measuring accessibility and be a stepping stone for transportation equity mapping in future.

References

[1] Hasan, S., 2007, Development of a travel demand model for Dhaka city, M.Sc. Thesis, Department of Civil Engineering, Bangladesh University of Engineering & Technology, Dhaka.

[2] Rahman, M.S., Fujiwara, A. and Zhang, J., 2008, Development of travel mode choice models for commuting trips in Dhaka city, Proceedings of the International Conference on Sustainable Transport for Developing Countries, Dhaka.

[3] Enam, A. and Charishma, F. C., 2011, Methodological issues in developing mode choice models for Dhaka city, Transport Research Record, Journal of the Transport Research Board: 84-92.

APPLICATION OF WIRELESS SENSOR NETWORK FOR CROWD DYNAMICS MONITORING

Student Number: 14M51664 Name: Stanislav LYKOV Academic Advisor: Shinya HANAOKA and Yasuo ASAKURA

This study is dedicated to investigation of possibility of utilization of wireless sensor network as a core component of crowd monitoring system aimed to track crowd dynamics. Based on limitations and shortcomings of contemporary crowd monitoring approaches, as well as the specificity of the problem, modified positioning algorithm for wireless sensor network, combined with noisy data preprocessing technique is proposed. Furthermore, several physical principles of interaction between pedestrians and sensor network were analyzed in details. Moreover, various mathematical models of crowd dynamics had been analyzed in order to choose the most appropriate one. Additionally, an experiment was conducted to demonstrate the concept of data collection technique aimed to obtain relevant information regarding crowd movement. This experiment was coupled with simulation to demonstrate how obtained data could be processed and visualized.

1 Introduction

One of the major trends of 21st century is intensive urbanization process. This process is leading to increasing urban population all over the world. As a result cities are becoming more congested, therefore the probability of dangerous situations is increasing. Especially, public venues such as train stations, stadiums, airports etc. are highly vulnerable to so-called crowd related disasters, such as stampede during mass events or emergency situations during rush hours.

As an example, one can consider a deadly stampede during the Hajj in Saudi Arabia in 2015, where over 700 people died and nearly 900 were injured [1]. Notable that this tragedy occurred despite the fact that modern surveillance systems were being used and a lot of preparation work had been done in order to provide safety.

Among many other reasons, the key challenge is the complexity of the problem. Crowd behavior is difficult to predict, describe and analyze, since people (especially during emergency situations) do not follow strict movement rules. Therefore, it is clear that more advanced systems need to be introduced, and safety aspect should be considered first with more attention.

Despite the fact that modern surveillance systems are highly advanced, several major shortcomings are still exist. Coupled with the complexity of the task, this may lead to failure of these systems.

In order to overcome some of these limitations this study propose the concept of the system based on Wireless Sensor Network (WSN) as a solution for crowd dynamics monitoring. Under the term WSN we assume spatially distributed autonomous sensors to monitor physical or environmental conditions, and to cooperatively pass their data through the network.

The ultimate goal of current study is to propose a concept of a system which could be used in order to track crowd dynamics and analyze crowd behavior. There are two main objectives under the scope of this study:

1. To investigate the possibility of utilization of WSN as a core component of crowd monitoring system, coupled with the analysis of physical principles of interaction between WSN and the crowd.
2. To develop a prototype of data collection system aimed to gather information regarding crowd dynamics, and experimentally validate the created model.

2 Methodology

2.1 Proposed Solution

The solution based on wireless sensor network as a core component of crowd monitoring system is proposed. This solution is inspired by “Smart Dust” project, introduced by the researchers from the University of Berkeley starting from 1990s. According to the authors [2], this is a *"... system of many tiny microelectromechanical systems (MEMS) such as sensors, robots, or other devices, that can detect, for example, light, temperature, vibration, magnetism, or chemicals."*.

2.2 Proposed Positioning Algorithm

One of the key challenges in sensor networks is positioning. Positioning has to be done in order the network to function as intended. Due to specificity of the solution, network could be affected with noise, which may result in decreasing of applicability, therefore noisy data pre-processing has to be considered. Moreover, since “Smart Dust” concept assume a huge number of devices, we cannot use common approach such as GPS for positioning, since it would be costly. More precisely, in our model we assume that following entities exist: tiny devices (ref. as MOTEs) equipped with several sensors, and user-related devices such as smartphones or wearable devices. This section is dedicated to the description of modified positioning algorithm, combined with noisy data pre-processing.

1. *Phase 0. Assumptions*
   - 1.1. Small number of fast moving BEACONs (user-related devices, equipped with GPS)
   - 1.2. Large number of slowly moving MOTEs, equipped with several sensors.
   - 1.3. While BEACONs are moving in vicinity of MOTE, MOTE remains motionless.
   - 1.4. BEACONs periodically broadcast the following

information: ID, current GPS coordinates.

1.5. MOTEs receive this information and use it for the purpose to determine the position.

2. *Phase 1. Data Smoothing*
   2.1. Objective: find time slot when BEACONs are inside MOTE's sensing radius.
   2.2. Problem: due to existence of obstacles received data from BEACONs could be noisy.
   2.3. Solution: using smoothing cubic spline (SCS) to smooth noisy observations.
3. *Phase 2. MOTEs position estimation*
   3.1. Objective: estimate MOTEs position using received information from BEACONs
   3.2. Solution: using least-squares circle fit (LSCF) for positioning.
4. *Phase 3. Cooperative positioning*
   4.1. Objective: position estimation of MOTEs which did not receive any signal from BEACONs.
   4.2. Solution: geometric location based on time-difference-of-arrival (TDOA).
5. *Phase 4. Dynamic position update*
   5.1. Objective: update MOTEs positions, since their location could change over time.
   5.2. Solution: newly arrived BEACONs broadcast their position information to MOTEs, so that adjust their position. Further, if MOTE's position had been changed, this information also broadcasted to nearby MOTEs and so on. This process repeated continuously.

2.3 Positioning Algorithm Simulation Results

Simulation had been done using JAVA programming language in order to investigate the influence of noisy data pre-processing on positioning accuracy and investigate the performance of positioning algorithm according to the MOTEs density. The proposed algorithm had been tested using 50, 100 and 150 "hypothetical" observations from BEACONs. Existence of obstacles (leading to noisy observations) were emulated using non-uniform distributed observations. As for the results, the proposed algorithm demonstrated 29.92% (50 observations); 25.62% (100 observations); 24.26% (150 observations) better results than without noisy data pre-processing.

3 Experiment and Simulation

3.1 Proposed Approach

As a validation part, an experiment was conducted in order demonstrate the concept of data collection system. Coupled with simulation, this experiment demonstrates the way how to obtain the data related to pedestrian's movement and how to use this data in order to describe and visualize the dynamics of a crowd. In this chapter the detailed description of experiment, simulation setups, as well as results is proposed.

3.2 Experiment Objectives

The most important objective is to examine proposed data collection concept and show how to use obtained data for the purpose of crowd dynamics description. However, examination of practical issues that arose during the experiment also was subject to investigation.

3.3 Experiment Setup

The targeted region of interest was represented as rectangular area 10m x 5m indoors. Since engineering aspects were not considered in current research project, instead of using tiny devices which were described above, Raspberry Pi 2 Model B [3], four items, had been used. Each of the devices had Planex GW-USNANO2A LAN adapter, so that all of them were connected. As for client side, LG Nexus 5, five items, had been used. Via MQTT communication protocol, which is extremely lightweight publish/subscribe messaging protocol, clients and MOTEs communicated.

3.4 Experiment Roadmap

The key idea of the experiment is utilization of Wi-Fi received signal strength indicator (RSSI) as a metric for determining the distance between MOTEs and clients. The roadmap of the experiment is shown on the figure below:

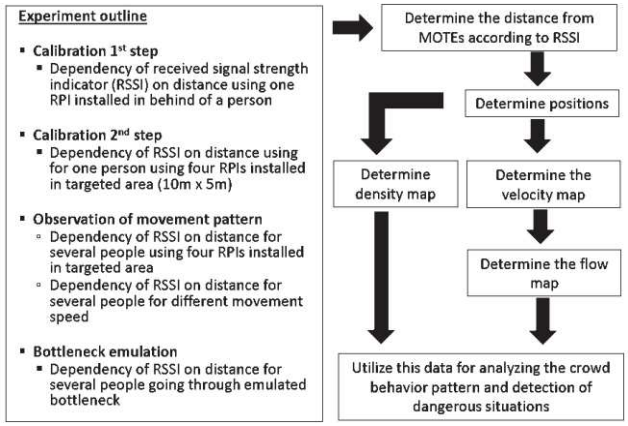

Figure 1. Experiment roadmap.

3.5 Experiment Results

First of all, the dependency of RSSI according to time was measured. The result is shown on figure below.

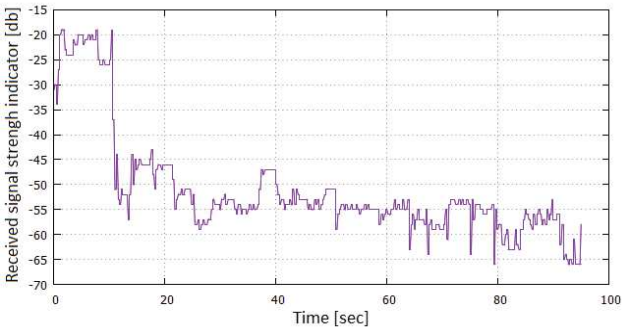

Figure 2. Observations of received signal strength indicator according to time.

This figure is showing the result of observations for pedestrian moving away from the RPI. The dependency of RSSI according to distance, as intended follows the exponential attenuation law, which was theoretically proved.

However, more interesting and practically useful results are shown on two picture below, where the dependency of RSSI according to distance is shown. The observations had been done for five trials. The result is shown below.

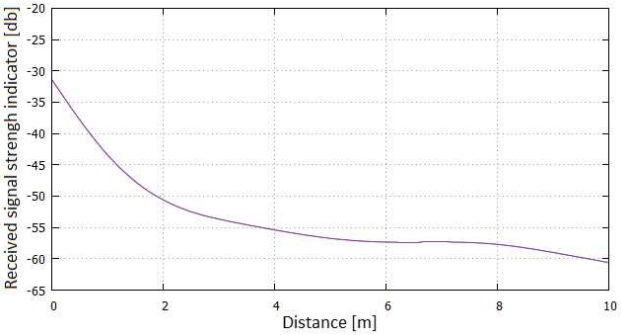

Figure 3. Observations of RSSI according to distance (average).

According to this figure, the chosen equipment could be used, for example, up to 1.85 meters (in case of -50 db. drop) and 3.68 meters (in case of -55 db. drop).

Additionally, simultaneous observations using four RPIs installed in targeted area had been done. The main objective of this phase was to demonstrate the chosen equipment and MQTT communication protocol allow to obtain meaningful results. The result is shown below.

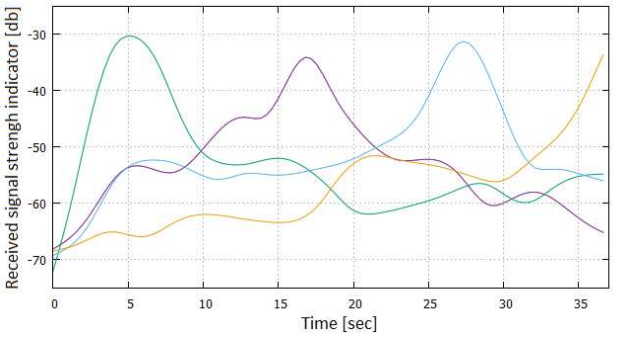

Figure 4. Observations of RSSI using four RPIs according to time

According to the results, RSSIs from all the RPIs have similar pattern, therefore the proposed system could be used in order to obtain RSSIs from all devices simultaneously, which is an important aspect for proposed positioning scheme. Moreover, the shape of peaks are similar (corresponds to the situation when pedestrians are in vicinity of RPIs).

Additionally, under the scope of the experiment, an artificial bottleneck had been created. In the center of targeted area a narrow corridor was setup. Five people were moving simultaneously towards this bottleneck, and then waited for each other, while one of them were passing through. The objective of this phase was to observe the RSSI from all the RPIs in order to detect this bottleneck. The results of the observations of RSSI are shown below.

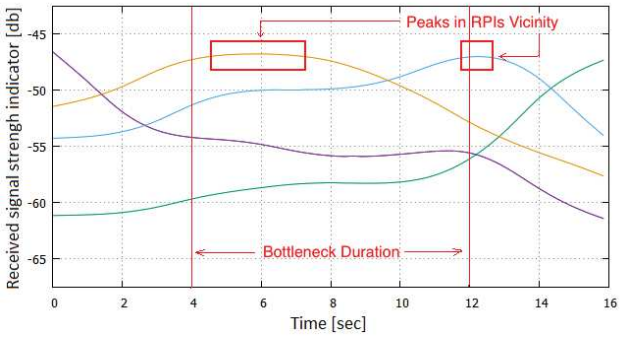

Figure 5. Observations of RSSI according to distance for bottleneck scenario.

As clearly see from the figure, there is a region from 4th till 12th seconds (which corresponds to bottleneck), when the pedestrian had to wait before enter the bottleneck. This waiting near the entrance also widens the peaks (marked red on figure), so that the signal level remains the same during the waiting time. Of course, more precise detection and analysis is essential to consider for the purpose of more accurate detection, however, the objective of this scenario was to show the applicability of proposed technique, so obtaining the precise results was not the main goal.

3.6 Model of Crowd Dynamics

Another important point is mathematical representation of crowd dynamics [4]. In other words, this model is a link between the data collection system and quantitative analysis. Herein, we assume that targeted area is divided into the grid:

$$\Omega = \sum_{nm} G_{nm} \; \forall n, m = \overline{1, N} \tag{1}$$

Further, for each grid element, every time step and also for each of the pedestrians we define coordinate and velocity vectors, as it shown below:

$$\overrightarrow{r_{ik}} = [x_{ik}, y_{ik}]^T, \overrightarrow{v_{ik}} = [u_{ik}, w_{ik}]^T, \forall k = \overline{0, T} \tag{2}$$

Using the equations above, we could calculate local density map:

$$\rho(\vec{r}_{nm}, t_k) = \sum_{j \in G_{nm}} f(\vec{r}_j - \vec{r}_{nm}) \quad f(\vec{r}_j - \vec{r}_{nm}) = \frac{1}{\pi R^2} exp(-\frac{||\vec{r}_j - \vec{r}_{nm}||^2}{R^2}) \tag{3}$$

Further, we also can calculate local velocity map:

$$\vec{V}(\vec{r}_{nm}, t_k) = \frac{\sum_{j \in G_{nm}} \vec{v}_j f(\vec{r}_j - \vec{r}_{nm})}{\sum_{j \in G_{nm}} f(\vec{r}_j - \vec{r}_{nm})} \tag{4}$$

Moreover, as one of the most important results is calculated flow map, which describe the crowd dynamics in targeted area:

$$\vec{Q}(\vec{r}_{nm}, t_k) = \rho(\vec{r}_{nm}, t_k) \vec{V}(\vec{r}_{nm}, t_k) \tag{5}$$

3.7 Simulation Results

The simulation had been done in order to process and visualize the data. The simulation dealt with data, obtained from "hypothetical" experiment. Need to mention that the data used for simulation had the same structure, as data obtained from the real experiment. More precisely, during the experiment the RSSI dependency according to distance is obtained. Further, using calibration results and triangulation, current position and velocity of pedestrians are calculated. These results are used as input parameters for simulation. The simulation had been done for two setups. First, the crowd was uniformly distributed inside targeted area. The density map is shown on the figure below.

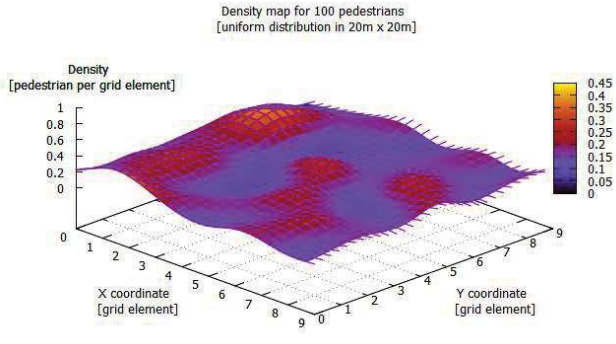

Figure 6. Density map in case of uniformly distributed crowd

The second setup describe the situation when crowd is non-uniformly distributed inside the targeted area and concentrated near the center. In this case, the peak represents the highest concentrations of pedestrians. The result is shown on the figure below.

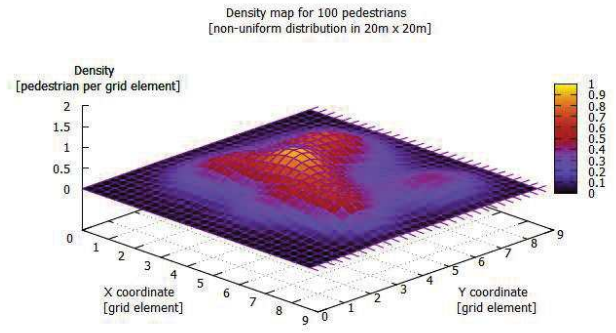

Figure 7. Density map in case of non-uniformly distributed crowd

Besides density maps, the trajectory information could contain an important information and particularly useful for the analysis of movements of pedestrians inside area of interest. The trajectory information for two pedestrians, arbitrary moving inside targeted area is shown on the figure below.

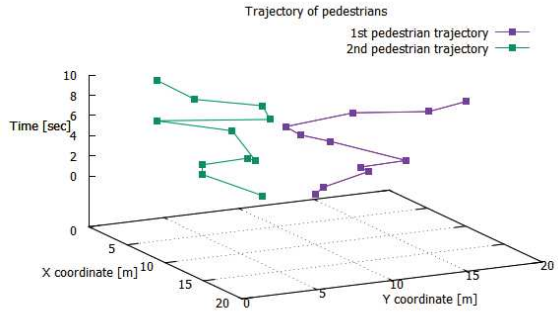

Figure 8. Trajectory of pedestrians according to time

4 Conclusion

This study had an attempt to incorporate the idea of "Smart Dust" into the concept of crowd monitoring system. For this purpose, the solution based on wireless sensor network, as a core component of crowd monitoring system was proposed. Relevant challenges regarding this application of wireless sensor network had been investigated and analyzed. More precisely, modified positioning algorithm, combined with noisy data pre-processing technique was presented. Additionally, experiment had been conducted for the purpose to test and demonstrate the concept of data collection system aimed to obtain the relevant information regarding crowd movement behavior inside the targeted area. This experiment was coupled with the simulation in order to demonstrate how the obtained experimental data could be used. The key novelty of this study is the attempt to merge several promising technologies, and the attempt to use their synergy performance as the approach for crowd monitoring problem, which require more comprehensive data gathering techniques, and data processing methods.

References

[1] Holly Y. *"717 people dead: what caused the Hajj stampede?"* CNN official report. 2015. [2]

[2] Warneke B., Last M., Liebowitz B., Pister. K.S.J., *"Smart Dust: communication with a cubic-millimeter computer"*. IEEE Computer, 34:44-51. 2001.

[3] Official Raspberry Pi Page. *"Raspberry Pi model B hardware general specifications"*. 2015.

[4] Cristiani E. et al. *"An overview of the modeling of crowd dynamics. Multiscale Modeling of Pedestrian Dynamics"*. Springer, pp. 73-107. 2014.

Effect of sub-critical water treatment of raw material on the composting

Student Number: 14M18141 Name: Takahiro HINOMIZU Supervisor: Kiyohiko NAKASAKI

コンポスト原料を亜臨界水処理することによるコンポスト化への効果

樋水　孝弘

有機性廃棄物をコンポスト化する際、廃棄物原料を亜臨界水処理することの効果について検討をおこなった。160℃、200℃、240℃の亜臨界水で前処理したモデル食品廃棄物のコンポスト化をおこなったところ、前処理するとコンポスト化８日目で Germination Index(GI)は 80%以上に達し、コンポスト化が高速化され、悪臭の原因であるアンモニアの発生を抑制できることが明らかとなった。また、従来のコンポスト化において、コンポスト化の温度を高め微生物の活性を高めても 10 日間では GI が 80%に達しないことから、亜臨界水処理でコンポスト化が高速化されると結論した。

1 Introduction

Composting is one of the methods for treating organic waste. Among waste materials, organic fractions such as food waste originating from households, restaurants, and food processing factories can be reclaimed as compost for agricultural use [1]. Development of an accelerated composting method has been expected to treat a large amount of food wastes rapidly. In recent years, food wastes has been treated by sub-critical water based on an assumption that the breaking up of the food waste by the pretreatment using sub-critical water would make the food wastes more easy to be degraded by the microorganisms. In this study, we investigated the effect of the sub-critical water pretreatment of the model food waste on the performance of the composting using the pretreated food waste as raw material. Four composting runs, Run A, B, C and D were carried out in this study. Three of the four runs were the composting using the raw mixture treated by sub-critical water for 30 min at 160°C (Run A), 200°C (Run B) and 240°C (Run C). Run D was the run using the raw mixture without sub-critical water treatment.

2 Material & Methods

2.1 Sub-critical water pretreatment of compost material

The rabbit food and rice were mixed at a ratio of 4:1 to prepare the representative model of food waste. 4 kinds of organic acids are characteristic of food waste: acetic acid, propionic acid, butyric acid, and lactic acid [2]. These were all added to the reaction mixture to achieve adjusted concentrations of 2.90, 3.02, 2.43, and 12.45g/kg-ds for acetic acid, propionic acid, butyric acid, and lactic acid, respectively. The model food waste and sawdust were mixed at a ratio of 10:9 to prepare the raw mixture and then, the total 20g-ws of the raw mixture was treated by sub-critical water for 30 min at 160, 200 and 240ºC.

2.2 Composting of food wastes pretreated by sub-critical water with different temperature conditions

The mixtures prepared were mixed with seeding material of compost products at a ratio of 19:1 to prepare the compost raw materials. The pH of the compost raw materials was adjusted to 5.0. A fungus having the ability to degrade fran compounds, *Paecilomyces* sp FA13 that was isolated in our

laboratory was inoculated to the compost raw material. The concentration of FA13 was adjusted to 10^5 CFU/g-ds in the compost raw material. At the start of composting, approximately 10 g of each compost raw material was put into the mini reactor (Fig. 1). The temperature was controlled at 30°C until the day 5 and then, raised to 60°C at a constant rate of 2.5 °C h^{-1}, and the 60°C was maintained until the day 10. On the day 5 of composting, the pH was adjusted to 8.0. The composting runs were carried out for 10 days. The conversion of carbon at a given composting time was defined as a molar ratio of carbon loss (as CO_2) to the total carbon present in the rabbit food and rice of compost raw material. The concentrations of organic acids and fran compounds in the compost samples were determined by high performance liquid chromatography (HPLC).

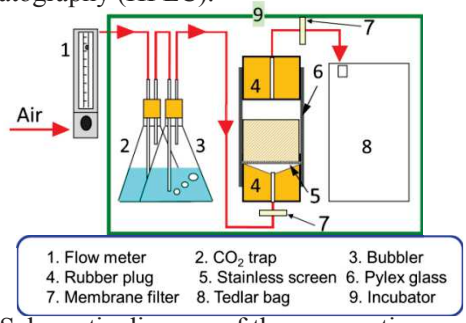

Fig. 1 Schematic diagram of the composting system.

2.3 Composting of model food waste with different temperature.

The compost raw material and composting condition were same as 2.2. The temperature was controlled at 40°C until the day 5 and then, raised to 60°C at a constant rate of 2.5 °C h^{-1}, and the 60°C was maintained until the day 10 (Run E).

2.4 Seed germination test

Seed germination test was conducted to evaluate the maturation of compost material. Aqueous extracts of compost samples were prepared by shaking 4g subsamples with 40 ml distilled water in a 200 ml flask for 1h, 150rpm, using a shaker. Suspensions were centrifuged and then, filtered through No.2 Whatman filter paper. Nine ml of the filtrate was poured into the disposable petri dishes containing 50 komatsuna seeds (Takii. co. Ltd, Kyoto, Japan) attached on the germination sheet (Fujihira. co. Ltd, Tokyo, Japan). Distilled water was used as control, and petri dishes were covered and kept in the dark for 4 days at 25°C. At the day 4, Germination Index (GI) of the compost samples were evaluated by counting the number of germinated seeds and the length of the root. GI was calculated according to the following formula[3].

Germination index (%)

$$= \left(\frac{G}{Gc}\right) \times \left(\frac{L}{Lc}\right) \times 100$$

G: the number of seed germination in extract of compost sample

Gc: the number of seed germination in distilled water

L: the root length in extract of compost sample

Lc: the root length in distilled water

3 Results and discussion

3.1 Composting of representative model food waste pretreated by sub-critical water at different heating condition

It was reported that the fran compounds that inhibit the microbial activity were generated during the sub-critical water pretreatment. In this study, to overcome the problem of fran compounds generation, a fungus having the ability to degrade fran compounds, *Paecilomyces* sp FA13 that was isolated in our laboratory was inoculated at the start of composting. Decrease in the concentration of the fran compounds was monitored by HPLC and it was confirmed that the fran compounds were completely degraded until day 8 of composting. The courses of CO_2 evolution rate during the composting are shown in Fig. 2.

In all runs, CO_2 evolution rate was almost 0 at day 10, suggesting that almost all the decomposing

organic matter was degraded until day 10.

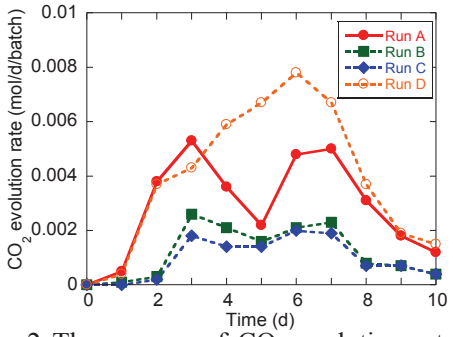

Fig. 2 The courses of CO_2 evolution rate during the composting for Run A, B, C and D.

Conversion of carbon during composting is shown in Fig. 3. The higher temperature sub-critical water pretreatment resulted in the higher conversion of C on day 0. On the other hand, conversion of C in Run A was 39.0%, in Run B was 33.9%, in Run C was 39.4% and in Run D was 45.7% on day 10 and Run D showed the highest value of conversion of C among 4 experimental runs and At first, it was expected that the breaking up of the food waste by the pretreatment using sub-critical water would make the food wastes more easy to be degraded by the microorganisms. However, it was suggested that a parts of organic matter was changed into hardly decomposing material for microorganisms by sub-critical pretreatment.

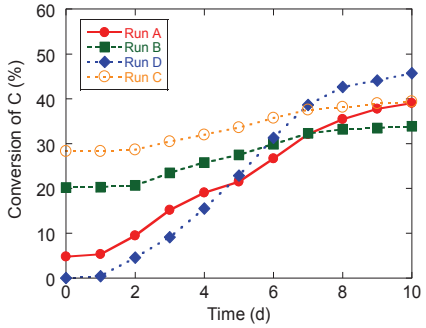

Fig. 3 The courses of conversion of C during the composting for Run A, B, C and D.

The course of the cumulative emission of ammonia is shown in Fig. 4. Almost no ammonia emission was observed in the composting runs using the raw mixture treated by the sub-critical water whereas significant amount of ammonia was emitted in Run D using the raw material without the sub-critical water pretreatment. The results of the conversion of C indicated the change of the organic matter to the hardly decomposing material by the sub-critical water pretreatment and it was also considered that the organic matter containing nitrogen was changed to the material that was hardly converted to the ammonia by the microbial decomposition.

Suppression of the ammonia emission can be observed when the ammonia is consumed considerably by the microorganism as the nitrogen source. However, the results of the cell density of microorganisms shown in Fig. 5 showed that the highest cell density of microorganism was generally attained in Run D denying the above hypothesis.

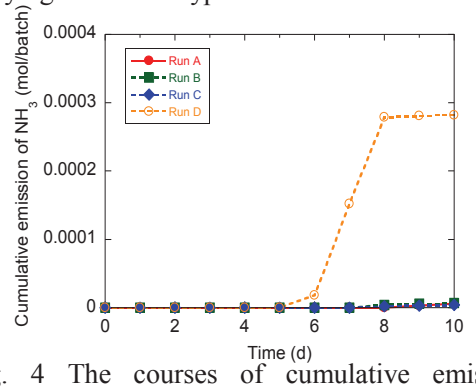

Fig. 4 The courses of cumulative emission of ammonia during the composting for Run A, B, C and D.

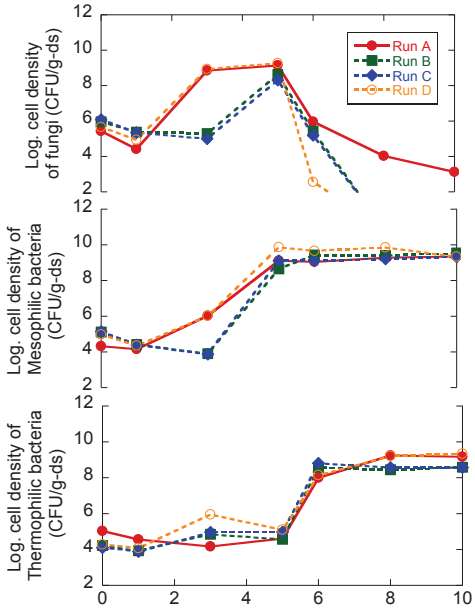

Fig. 5 The courses of log cell density of fungi, mesophilic and thermophilic bacteria during the composting for Run A, B, C and D.

3.2 Germination index

The germination index of compost samples during composting are shown in Fig. 6. It was reported that the GI for mature compost was over 80%. The GI was 0% in Run A, B and C on day 0 though conversion of C increased after the sub-critical water pretreatment. The concentrations of fran compounds and organic acids increased after the sub-critical water pretreatment and it was considered that those compounds attributed the low GI value. The concentrations of fran compounds and organic acids decreased with the progress of composting, on day 8 of composting, all those compounds were below the detectable level and GI of the compost samples attained highest value in Run A, B and C. GI at the end of composting on day 10 was 33.6% in Run A, 111.8% in Run B and 81.9% in Run C and they were higher than the GI in Run D of 6.6%. These results suggested that compost product of the food waste with sub-critical water pretreatment became mature compost without containing the germination and growth inhibitor.

The germination index of compost samples during composting are shown for Run D and E in Fig. 7. The temperature was controlled at 30℃ and 40℃ until the day 5 in Run D and Run E respectively. The GI was improved in Run E compare with that in Run D. However, The GI at day 10 was 73% in Run E.

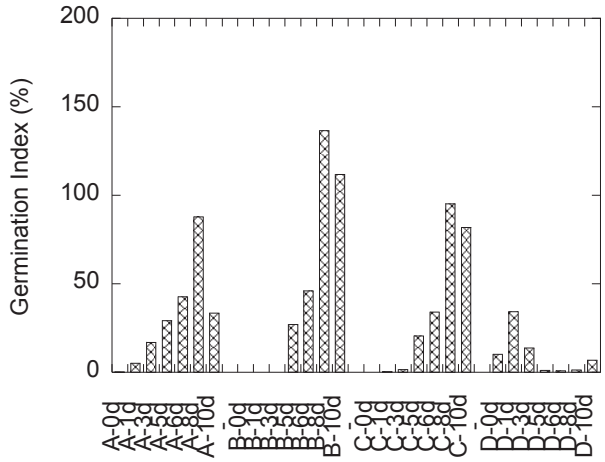

Fig. 6 The GI of compost products for Run A, B, C and D at day 0, 1, 3, 5, 6, 8 and 10.

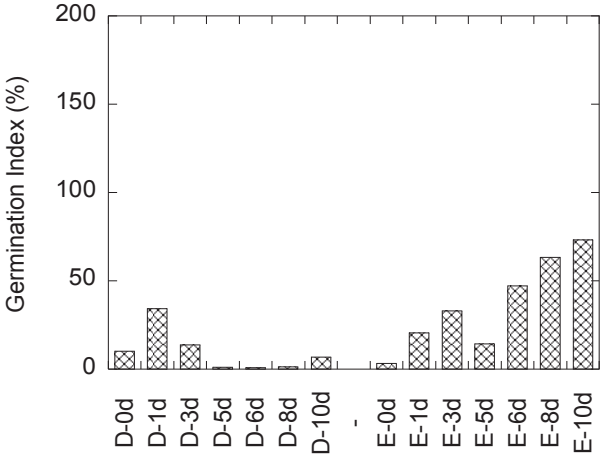

Fig. 7 The GI of compost products for Run D and E at day 0, 1, 3, 5, 6, 8 and 10.

4 Conclusions

In this study, it was revealed that sub-critical water pretreatment was effective to suppress the emission of ammonia. Furthermore, the compost samples of the raw mixture treated by sub-critical water pretreatment at 160, 200 and 240℃showed high GI value in short period.

References

[1] K. Nakasaki, S. Araya, H. Mimoto, Inoculation of *Pichia kudriavzevii* RB1 degrades the organic acids present in raw compost material and accelerates composting, Bioresour Technol (2013).

[2] C. Sundberg, I. Franke-Whittle, S. Kauppi, D. Yu, M. Romantschuk, H. Insam, H. Jönsson, Characterisation of source-separated household waste intended for composting. Bioresour Technol, 102, 2859-2867 (2011).

[3] F. Zucconi, A. Monaco & M. De Bertolodi, Biological evaluation of compost maturity, BioCycle, 22, 27-29 (1981).

Field Survey and Numerical Simulation of Inundation in the Mekong Delta's Largest City

Student Number: 14M18112 Name: Chiaki Tsurudome Supervisor: Hiroshi TAKAGI

メコンデルタ都市部における氾濫現象の調査と数値シミュレーション

鶴留　千晶

Abstract

カントー市はメコンデルタにおける最大の都市で河口から 80km 内陸に位置する．上流からの河川流量と河口からの海洋潮汐により，カントーでは度々洪水が発生し，住民の日常生活に影響を及ぼしている．しかし、氾濫のメカニズムや被害状況はこれまで十分に研究されていない．本研究では，洪水の実態を明らかにするため市内で住民インタビュー調査を行った．また地形測量を行い詳細な地形モデルを作成し，市街地における氾濫を解析し，観測した水位と比較したところ雨季・乾季ともによく一致することが示された．更に，海面上昇と地盤沈下を考慮した複数の水位上昇シナリオを想定し，将来氾濫域がどのように変化するかを検証した．モデル内の道路総延長に対する氾濫の割合は，現在はまだ限られた範囲であるが，乾季では 40 cm の水位上昇で 7.1 %, 80 cm 上昇で 40 %, 100 cm 上昇で 90 %，雨季では 40 cm 上昇で 81 %, 60 cm 以上の水位上昇で 100 %と急激に増加することが示された．

1 Introduction

The Mekong Delta widely spreads from the south of Phnom Penh towards Vietnam, with approximately a 400-km^2 basin. About 50% of the national rice production is reaped in the Mekong Delta [1], boosting Vietnam to be ranked at top five in the world with production of around 44 million tons as of 2014 [2]. While the delta is rich in agricultural products, the region is prone to natural disasters. More than 70% of the population is at risk of water disasters, such as tropical storms, floods, and storm surge [3]. Mekong River Commission [4] estimated that flooding which occurred during 2000 and 2003 in Vietnam had caused the agricultural losses estimated at 200 to 300 million US$.

Figure 1.1 Urabn floods in Can Tho City

It is necessary to investigate the flood risk and the impact of future environmental changes such as sea level rise (SLR) and land subsidence in the Mekong Delta, which plays an important role as a place for livelihood and food supply. This study focuses on Can Tho City that suffers from seasonal flooding (Figure 1.1). Can Tho is the largest city in the Mekong Delta located 80 km inland from the river mouth (Figure 1.2) and its population is 1.2 million.

Huong and Pathirana (2013) [5] simulated the influence of SLR, rainfall and urbanisation in Can Tho City, showing that flood level will drastically increase under the significant change in river level. Takagi et al. (2014) [6] carried out the field survey and analysed the tidal elevation data in Can Tho and showed that the ocean

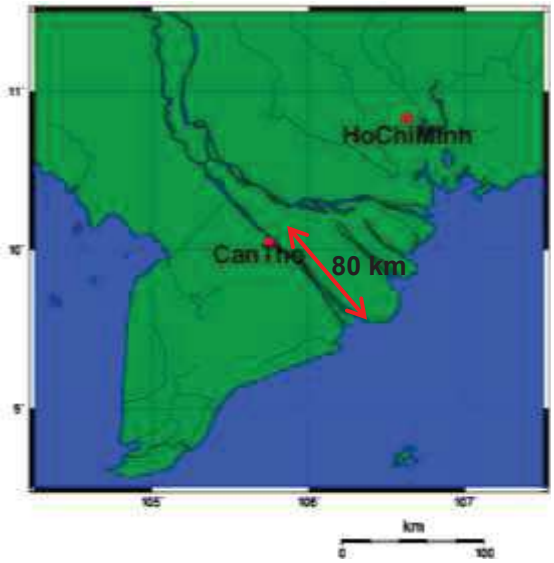

Figure 1.2 Map of Can Tho City

tides dominantly determined water elevation, although Can Tho is located 80 km inland from the river mouth. Furthermore, they revealed that the river discharge effectively caused tidal damping and lessened the tidal energy from the river mouth particularly in a rainy season. Fujihara et al. [7] analysed the water levels from 1987 to 2006 observed at the 24 monitoring stations in the Mekong Delta, showing that the river inflow hardly affected water-level rise and that the maximum and minimum water elevation is strongly influenced by tidal regime.

However, the mechanism of flooding in Can Tho has not been sufficiently investigated. This study investigates the present flood level and frequency in this city through the field survey and also, examine local people's awareness to floods and SLR. Moreover, this research investigates how the inundation takes place and intrudes into the streets in the Can Tho downtown area under future environmental scenarios considering SLR and land subsidence.

2 Methods

The present study is consisted of three components: (1) interview with local residents, (2) field survey, and (3) numerical simulation, all aiming at revealing the real danger of flood in the downtown area of Can Tho city.

2.1 Interview

The interview was held at An Binh on 11th and 14th August in 2014, Nin Kieu on 14th August in 2014, Tan An on 10th March in 2015. The total number of the respondents was 60. The questionnaire comprised of multiple choices was prepared in Vietnamese printed together with English translations. A part of the questionnaire is shown in Figure 2.1. The questionnaire was specifically designed for asking the questions about frequency and extent of inundations around their residents and the respondents' knowledge, experience and awareness to flood events.

2.2 Field Survey

In order to create a precise elevation map for simulation, a topographical survey was conducted. The depth of the main river and tributaries and the ground elevation in Can Tho were all measured by the authors themselves.
Actual inundation was visually observed twice a day at a riverbank park in the downtown Can Tho. Inundation depths were measured by a measuring staff. The ground elevation in the downtown area was examined using a laser distance meter. The ground elevation was measured at a large number of locations with an interval of 10-15 meters. The depth of the Hau River and its tributaries was measured using a potable echo-sounder. Measurement was conducted at three points per cross-section. The depth used in the numerical simulation was finally determined by taking an average of the values.

2.3 Numerical Simulation

Delft-3D was applied to the detailed simulation of inundation in the downtown area with the bathymetry and topography in the downtown created from the field survey data. The topography of those outside of the downtown area was reproduced from the satellite data of SRTM 90 m Digital Elecation. Since flooding in Can Tho is greatly influenced by tides traveling upstream, the tidal variation was inputted on the downstream boundary in the model. The basic calculation settings are listed in Table 2.1. In order to examine the accuracy of the model, the authors performed the simulations on 13th August and 7th November, 2014 in a rainy season and 9th March, 2012 in a dry season.

Table 2.1 Basic calculation settings

Item	Description
Grid size	10 meter
Time step	0.01 minute
Boundary conditions (downstream, upstream)	Tide boundary Riemann boundary
Roughness (Manning's *n* value)	River bottom: 0.02 Land surface: 0.05

2.4 Future Scenarios

Flood extent over the downtown Can Tho are predicted under the five future water level rise (WLR) scenarios due to the combination of SLR and land subsidence, WLR of (1) 20 cm, (2) 40 cm, (3) 60 cm, (4) 80 cm, and (5) 100 cm from the present typical water level in dry and rainy seasons.

3 Results

3.1 Interview

The interview reveals that nearly all the respondents understand the phenomenon of flood, while only less than half of the respondents recognise storm surge or SLR. Seventy five percent of the respondents replied that a maximum of 20-50cm depth water flooded their houses in their life. One of the queries about how they react when such a flood occurs found that 95% of the respondents would stay home, whereas nobody answered that they would evacuate. Even if water level rises by 50cm in the future, 92% of the respondents would not relocate their residents into a safer place. Only one person who lives in the downtown area in Can Tho answered moving to other place.

3.2 Topographical Survey

The inundation depth was measured at the riverside park in the downtown in the morning on 14th August, 2014 (Figure 3.1). The maximum depth reached around 40cm from 7:00 A.M. to 8:00 A.M. in local time. In measurement of ground elevation, the total number of the observation points was 102.
The heights measured all along the pass were finally adjusted to minimise errors by the closing the traverse. The lowest elevation measured in the closed pass was 0.1 m lower than the elevation of the riverside park, where which was set to be 0 m as a base level. The centre of the main river was 19-meter deep and the bank side of the river was 3-meter deep, demonstrating that the river slope is steep.

Figure 3.1 Measurement of the inundation depth at the park. Photo taken on 11th August, 2014

3.3 Verification of the model

Using topographical data from the field survey and SRTM 90 m Digital Elevation data, the model for numerical simulation was created (Figure 3.2). The bathymetry used in the simulation was modified by lowering the original elevation by 60 cm in order to

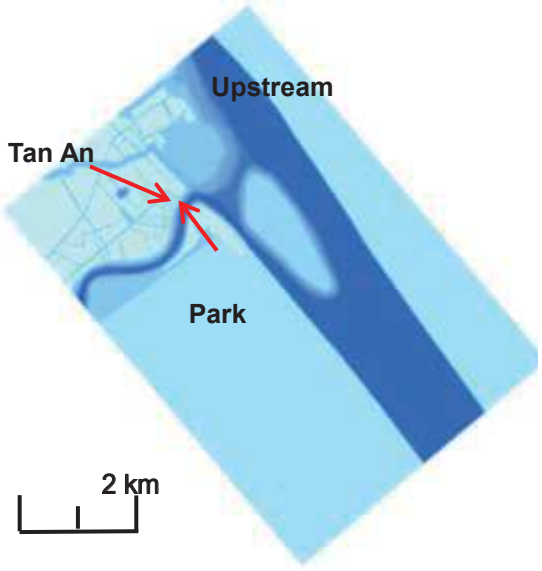

Figure 3.2 The bathymetry model

adjust to the mean water levels at Can Tho. The simulation was performed for a whole day between 15:00 on 14th and 15:00 on 15th August in 2014. Figure 3.3 shows that the calculated depth at the park coincided the observed inundation depth. Therefore, it is not necessary to calibrate the bottom boundary in the model.
In November 2014, the authors found that the inundation reaches even Tan An where flooding rarely occurs in a dry season. The simulation for a typical flood season, covering from 10:00 on 7th to 10:00 8th on November in 2014, shows that most roads in Can Tho were inundated and Tan An was also inundated by a maximum of 20 cm. Flood in a typical dry season were also investigated by simulating for a one-day period from 10:00 on 9th to 10:00 on 10th March in 2012. The result shows that the flooding did not occur in any place of Can Tho.

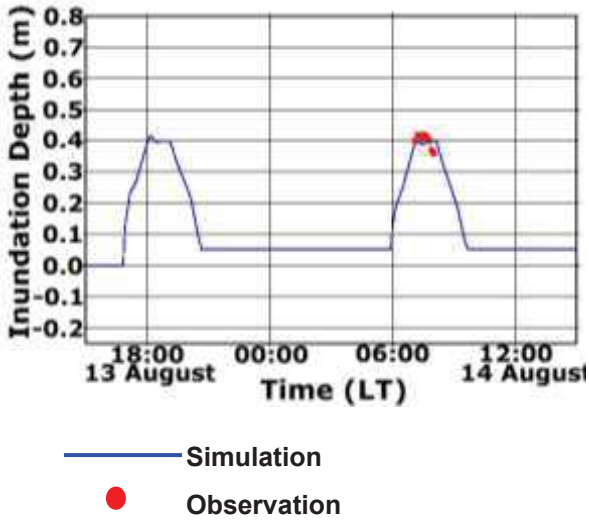

Figure 3.3 Comparison between the simulated depth and the observation at the park

Given these results obtained, the authors confirm that the model would be sufficiently reliable in simulating flood over the downtown area of Can Tho.

3.4 Future scenarios

If water level will rise up more than 80 cm, the inundation areas would significantly expand from the situation under 20-cm rise in a future dry season (Figure 3.4). The downtown would be totally inundated under WLR 80 cm scenario in a future rainy season (Figure 3.5). Figure 3.6 shows how rapidly the percentage of the inundated roads will increase as water level rise in case of both rainy and dry seasons. Particularly, it changes dramatically when WLR exceeds 20 cm.

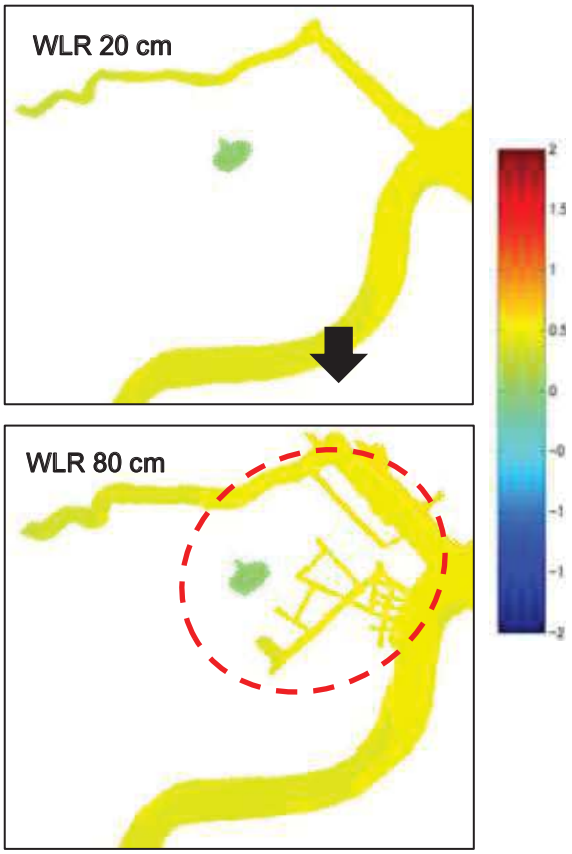

Figure 3.4 Increase of inundated area compared with WLR 20 cm and 80 cm in a future dry season

Figure 3.5 Colour contour map of water elevation with WLR 80 cm scenario in a future rainy season

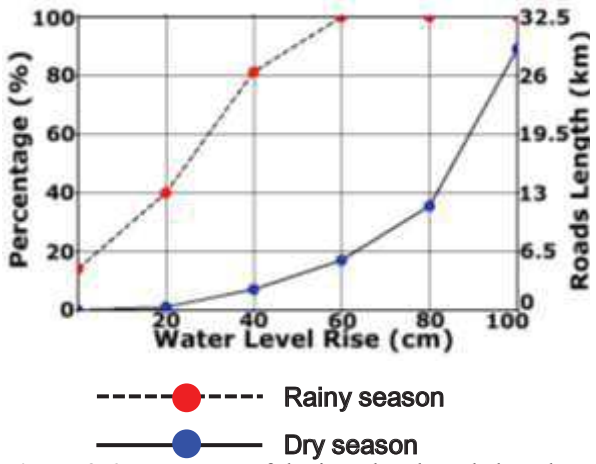

Figure 3.6 Percentage of the inundated roads length to the total roads length in Can Tho

4 Discussion

The interview survey revealed that local inhabitants in the Mekong Delta accept flooding as a usual event, even though their daily life has been obviously annoyed by such frequent inundations. They would not evacuate themselves from their houses even flood levels further increase in the future.

The simulation suggest that local authorities may mitigate inundation by raising roads or constructing dykes if the water level rise is limited (less than 20 cm). In August in 2015, the local authority has raised the banks along the Can Tho River by about 70cm (Figure 4.1). It seems that any visible inundation did not take place because of this reinforcement of the flood protection when the authors visited the city again on 29th August in 2015, unlike the substantial inundations that we have observed in August 2014. This observation may demonstrate the effectiveness of the dyke constructed. If the rise was remarkable (higher than 20 cm), however, the inundated area will significantly and rapidly spread throughout the downtown area of Can Tho. The current countermeasures should not be enough to prevent flooding in the future, which would be exacerbated by SLR and land subsidence. Once the water from the river overflows the dykes and pours into the city, the water will first flood a lower part of the city and cause a persistent inundation which has a great impact on the life of local population. Given the unawareness of local people to potential disasters, it is necessary to take an immediate action for planning an effective disaster management.

5 Conclusions

The interview revealed that 75 % of the respondents experienced a maximum of 20-50 cm depth inundation in their life. 95 % of the respondents stay home even if flooding occurs. Moreover, even if water level will rise up to 50 cm in the near future, 92 % of them would not relocate their houses to a safer place. We developed the numerical model which uses the precise topography data obtained through our field surveys. The model was verified with observed water levels in both rainy and dry seasons and then applied to the projections under future water level scenarios. The results showed that the inundated area would significantly spread if water level will rise up to 20 cm or higher, which suggests that immediate actions are necessary to be undertaken in the coming years before the situation becomes unmanageable.

Figure 4.1 The new protection at the park along the Can Tho River, taken by the author on 29th August in 2015

References

[1] P. T. T. Hanh and M. Furukawa, Impact of sea level rise on coastal zone of Vietnam, Bull. Fac. Sci., University of Ryukyu, No.84, 45-59, 2007

[2] Food and Agriculture Organization (FAO), Statistics Division, http://faostat3.fao.org/home/E, accessed on 27th, December, 2015

[3] T. L. Nguyen and D. T. Bui, Flood Monitoring of Mekong River Delta, Vietnam Using ERAS SAR Data, 22nd Asian Conference on Remote Sensing, 5-9 November 2001, Singapore, 6pp, 2001

[4] Mekong River Commission (MRC), State of the Basin Report 2010, 232 pp, 2010

[5] H.T.L. Huong and A. Pathirana, Urbanization and climate change impacts on future urban flooding in Can Tho city, Vietnam, Hydrology and Earth System Sciences, 17, 379-394, 2013

[6] H. Takagi, T.V. Ty, N.D. Tao and M. Esteban, Ocean tides and the influence of sea-level rise on floods in urban areas of the Mekong Delta, Journal of Flood Risk Management, Vol 7 Issue 1, 2014

[7] Y. Fujihara, K. Hoshikawa, H. Fujii, A. Kotera, T. Nagano and S. Yokoyama, Analysis and attribution of trends in water levels in the Vietnamese Mekong Delta, Hydrological Processes, 33 pp, 2015 (Accepted), doi: 10.1002/hyp.10642

TRANSIT CHOICE OF ASIAN HUB AIRPORTS IN INTERCONTINENTAL FLIGHTS

大陸間フライトにおけるアジアのハブ空港のトランジット選択

Student Number: 14M18276 Name: Shuyang KANG Supervisor: Shinya HANAOKA

International passengers include those of departure, arrival and transit and only transit passengers among hub airports have a competition each other. This study focuses on long distance (more than 13,000 km, 13 hours) continental transit flights between North America and Southeast Asia through Asian hub airports. Firstly, the current transit situation among hub airports is analyzed. Secondly, possible factors affecting transit passengers' flight choice are selected and its weight are estimated by analytic hierarchy process (AHP). Finally, flight routes of certain ODs are evaluated by TOPSIS among main Asian hub airports.

1 Introduction

International passenger volume based on airport is the sum of passengers who are taking an international flight that "departure from", "arrive at" or "transit at" a certain airport. The international passenger volume of "departure from" or "arrive at" a certain hub airport is affected not only by the flight attributes but also by macro factors such as the country's attractiveness, visa policy and economic development. The international passenger volume of "transit at" a certain hub airport is affected by flight attributes, airlines attributes and transit airport attributes which shows competition among airlines and hub airports.

This study focuses on the long distance continental transit flight through hub airports. Long distance here indicate transit flight which is more than 13,000 km, 13 hours. Figure 1-1 shows the routes for transit.

Until now, the longest direct flight is around 14,000 km, 16 hours from/to Sydney and Dallas. Airlines may not serve any more direct flights if the distance and total travel time are longer than this flight. Such situation happens mostly in the long distance OD like North America – Southeast Asia. The reason of choosing this OD is to transit at Asian hub airport.

International transit passenger volume is one of the most visible and important attribute to show the competition among hub airports and transit routes. Although Narita's international transit passenger volume is seemed to be decreasing during the past several years, transit competitiveness of routes through Narita and other Asian hub airports are unclear, which is necessary to be evaluated and compared. Furthermore, from the demand side, the factors affecting transit passengers' choice behavior are also uncertain.

To make a brief summary of above research problems, there are 3 main objectives in this study.

1) To analyze the current transit situation between North America and Southeast Asia.
2) To estimate the factors and their weights that affect passengers' long distance transit flight choice behavior.
3) To evaluate the transit flight routes through main Asian hub airports.

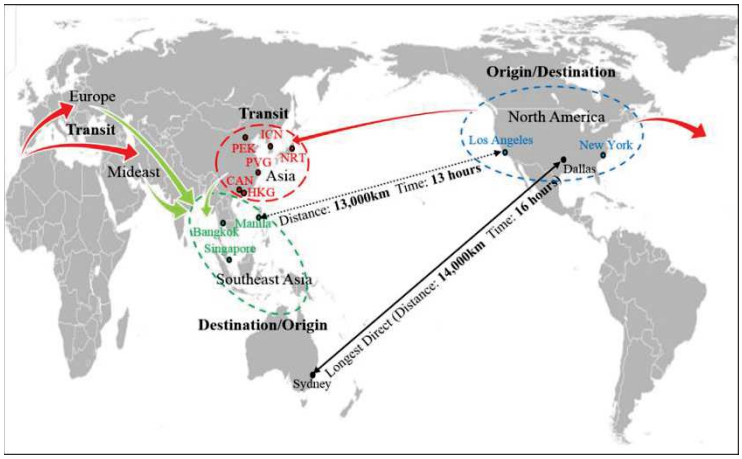

Figure 1-1: Direct and transit flights between North America and Southeast Asia

2. Methodology

AHP can help to calculate the weight of each explanatory factor even if the factors are supposed to be insignificant or qualitative. Compared with ANP (Analytic network process), an extension method of AHP, samples can be collected widely from not only experts but also transit passengers who experienced transit flight several times. Although ANP may explain the relationship between factors more clearly and reasonably, sample may be unavailable due to the increase of the number of comparison sets. Furthermore, co-relationship between factors is difficult to define.

TOPSIS would be suitable for cases with a large number of attributes and alternatives, and especially handy if the given data is objective or quantitative. In this study, because evaluation scenarios are divided by several indicators such as trip purposes and ODs, pairwise comparison is complicated to structure for evaluation. Although the number of attributes and alternatives are not many, large number of scenarios makes the evaluation complex and detailed. Therefore, TOPSIS is chosen as the flight routes evaluation method in this study.

2.1 Factors estimation method

Analytic hierarchy process (AHP) is a structured

technique for organizing and analyzing complex decisions based on mathematics and psychology. It has particular application in group decision making and is used in a wide variety fields such as government, business, industry, healthcare, shipbuilding and education. It can be also commonly used in the normal daily life.

There are mainly 3 steps of AHP method. The first step is to structure the decision hierarchy by defining the decision problem and developing the conceptual framework. Factors which are necessary to estimate need to be selected and divided into multiple criteria. The second step is to collect the data from experts or respondents who have the related experience. Relative importance of every two factors, which is called pair-wise comparison are judged by the respondents. The third step is to estimate the relative weights and mean weights of main criteria and sub criteria. Degree of consistency is also necessary to be checked in this step.

The objective of AHP is to estimate relative weights of elements. In the next table, group A are the elements to be compared. Group a are the relative importance of each 2 elements. For example, A_1 is a_{12} times important than A_2.

A	A_1	A_2	A_3	…	A_n
A_1	1	a_{12}	a_{13}	…	a_{1n}
A_2	$1/a_{12}$	1	a_{23}	…	a_{2n}
A_3	$1/a_{13}$	$1/a_{23}$	1	…	a_{3n}
…	…	…	…	1	…
A_n	$1/a_{1n}$	$1/a_{2n}$	$1/a_{3n}$	…	1

The following formula (1) shows the way of geometric mean method to calculate the weight. (2) and (3) helps to check the consistency of the AHP result.

$$w_i = \frac{(\prod_{j=1}^{n} a_{ij})^{\frac{1}{n}}}{\sum_{i=1}^{n}(\prod_{j}^{n} a_{ij})^{\frac{1}{n}}} \quad (1)$$

$$\lambda_{max} = \frac{1}{n}\sum_{i=1}^{n}\left[\frac{\sum_{j=1}^{n} a_{ij} w_j}{w_j}\right] \quad (2)$$

$$CI(Consistency\ Index) = \frac{\lambda_{max}-n}{n-1} < 0.1 \quad (3)$$

2.2 Flight routes evaluation method (TOPSIS)

The Technique for Order of Preference by Similarity to Ideal Solution (TOPSIS) is a multi-criteria decision analysis method. TOPSIS is based on the concept that the chosen alternative should have the shortest geometric distance from the positive ideal solution and the longest geometric distance from the negative ideal solution. It is a method of compensatory aggregation that compares a set of alternatives by identifying weights for each criterion, normalizing scores for each criterion and calculating the geometric distance between each alternative and the ideal alternative, which is the best score in each criterion. There are 3 main steps in TOPSIS. The first step is to create an evaluation matrix which is made up of criteria weight data, score data of transit airports and airlines and flight information, and then normalized it. The second step is to calculate the weighted normalized decision matrix and determine the worst and the best alternatives. The third step is to calculate the similarity to the worst condition which is also the final scores result and rank the alternatives based on the scores.

3. Data collection

AHP questionnaire was designed based on the criteria in Figure 3-1. Relative importance was selected to show respondents' priority between 2 factors. Respondents chose which factor is more important and how much the relative importance is to themselves.

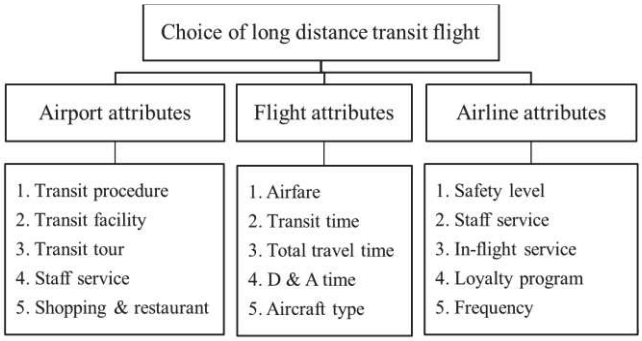

Figure 3-1 AHP decision hierarchy

Survey was conducted in Tokyo Narita International Airport in 2 days from 4th to 5th, January, 2016. Survey target are divided into 2 groups including the people who have ever used a long distance transit flight 1st, 2nd or 3rd and more than 3 times which are belong to the effective sample group and only more than 3 times which is belongs to the high reliability group. In this study, samples from respondents are divided into 6 segments by 2 indicators. The first indicator is trip purpose which includes business, sightseeing and visiting friends and relatives (VFR). The second is residence which includes North America and the others. The sample size is shown in the Table 3-1. Finally, 148 effective samples are analyzed with good balance. 83 effective samples of North America are used as AHP output and 98 high reliability samples are used as TOPSIS input.

Table 3-1 Sample size

Trip Purposes	Sample type	North America	Others
Business	Collected	27	25
	Effective	24	24
	High reliability	16	13
	CI	2.1%	4.6%
Sightseeing	Collected	33	16
	Effective	32	14
	High reliability	21	11
	CI	2.3%	8.7%
Visit Friends or Relatives (VFR)	Collected	28	28
	Effective	27	27
	High reliability	16	21
	CI	3.3%	5.9%

4. Results and analysis

4.1 Current transit situation

Figure 4-1 shows the direct and transit volume change through 4 main Asian hub airports. They are Narita Airport in Tokyo (NRT), Incheon Airport in Seoul (ICN), Hong Kong Airport (HKG) in Hong Kong and Taoyuan Airport in Taipei (TPE). In this figure, although volume through NRT was ranked 1st in 2004, it decreased year by year and dropped to 4th in 2014. On the other hand, ICN and TPE increased dramatically in this 10 years. Although volume through HKG decreased from 2009 to 2014, it increased from 2004 to 2014.

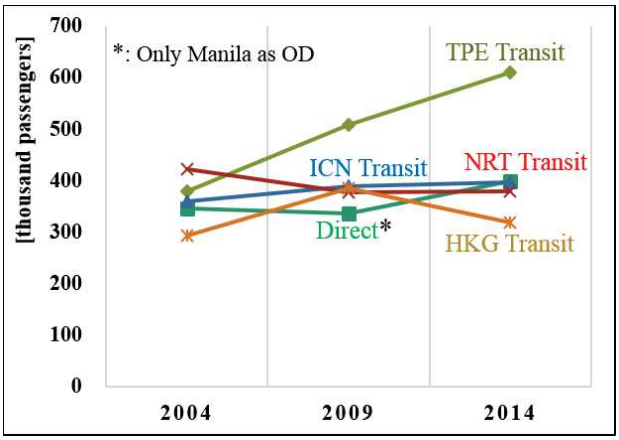

Source: NAA

Figure 4-1 Transit volume through main Asian hub airports

Figure 4-2 shows the results of transit passenger volume change based on certain ODs which are the top 19 that have the most transit passenger volume. The volume through NRT of MNL-LAX, MNL-SFO, BKK-LAX, BKK-JFK and BKK-JFO decreased which are taken by ICN, HKG and TPE. MNL is the hub airport in Manila, Philippines. BKK is the hub airport in Bangkok, Thailand. LAX is the hub airport in Los Angeles, Western US. SFO is the hub airport in San Francisco, Western US. JFK is the hub airport in New York, Eastern US. Because there is an obvious change of the transit volume through every main hub airport among BKK-LAX, MNL-JFK and BKK-JFK, flight routes based on these 3 ODs are chosen to be evaluated by the TOPSIS.

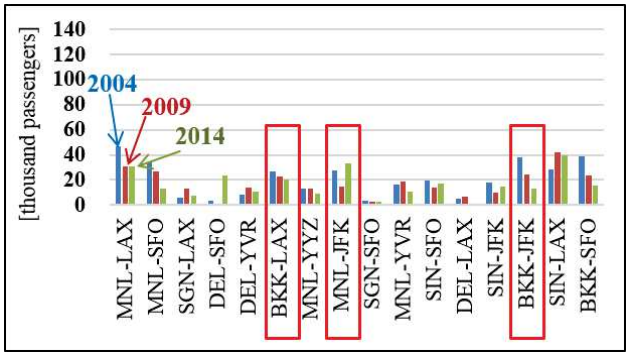

Source: NAA

Figure 4-2 Transit passenger volume change through NRT

4.2 Transit choice factors weighting result

Factors weighting are calculated based on 148 samples. Main criteria weight results of respondents living in Southeast Asia are also calculated in Figure 5-21. The result of weight criteria of sightseeing and VFR purpose is unexpected because the weight of airport attributes takes relatively large and the weight of flight attributes takes relatively small. The reason may be because of few sample size and misunderstanding on the definition of airport attributes in this situation. Therefore, criteria weight results of North America respondents are utilized to be the TOPSIS input to evaluate the transit flight routes.

Figure 4-3 shows the main criteria weighting result of North American segment. From the result, business travelers choose airlines as their priority while sightseeing and VFR passengers consider flight. Detailed reason are shown in the Figure 4-4, 4-5 and 4-6.

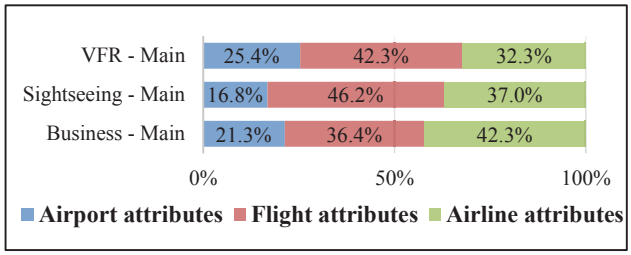

Figure 4-3 Main criteria weight of North American respondents

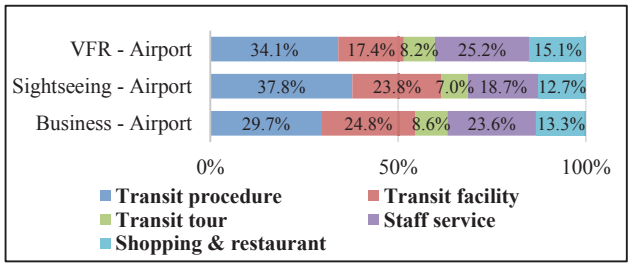

Figure 4-4 Airport attributes weight of North American respondents

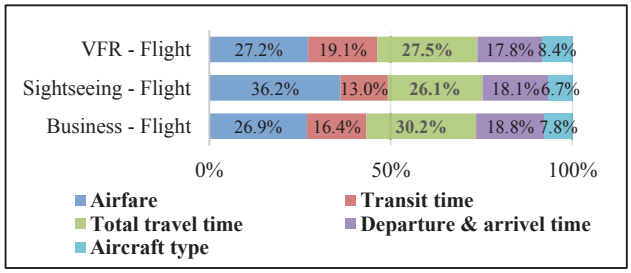

Figure 4-5 Flight attributes weight of North American respondents

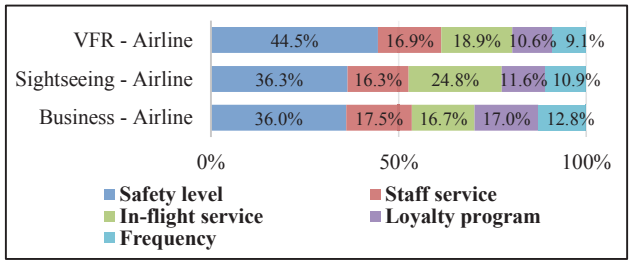

Figure 4-6 Airline attributes weight of North American respondents

For airport attributes, transit procedure, facility and staff service are mainly considered. Business passengers prefer a better transit facility condition, sightseeing passengers prefer a satisfied transit procedure and VFR passengers consider the shopping and restaurant most. As an optional choice, transit tour is not considered significantly by all the passengers. For flight attributes, airfare is significant for sightseeing travelers and total travel time is considered mostly by business travelers. For airline attributes, safety level is concerned mostly by all the passengers. Business passengers prefer a better loyalty program. Sightseeing passengers consider in-flight service more.

4.3 Flight routes evaluation results

TOPSIS sample data are made up of 3 parts. They are scores of hub airports for transit judged by transit passengers, flight information on April 1st, 2016 and airline scores from SKYTRAX. Table 4-1 shows the average scores of 4 main Asian hub airports. Table 4-2 shows the example of long distance transit flight information through 4 main Asian hub airports on April 1st, 2016. Table 4-3 shows the airlines score of 5 sub criteria except frequency that is from the flight information. Frequency in Table 4-3 is the data of LAX- BKK. Airfare, transit time and total travel time are collected by 2 directions and the mean value of one day flight information are calculated as input. Departure & arrival time is the number of available departure time period. Flight routes evaluation results are calculated based on 18 scenarios. These 18 scenarios are divided by 3 trip purposes, 3 ODs and 2 directions which is showed in the Table 4-4. For each scenario, flight routes choice through NRT, ICN, HKG and TPE are evaluated and ranked. The transit routes evaluation results are compared with current transit situation. For details, the route evaluation result between LAX and BKK is same as the current transit situation. On the other hand, for results between JFK and MNL, JFK and BKK are different with the current situation especially transit routes through ICN and HKG in the Southeast Asia departure scenarios. Low score may mainly be due to the high airfare which has a big variation in different ODs.

Table 4-1 Scores of Asian hub airports based on 5 sub criteria

Airports attributes	NRT	ICN	HKG	TPE
Transit procedure	4.364	4.235	4.250	4.091
Transit facility	4.409	4.176	4.200	3.455
Transit tour	3.364	3.529	3.450	3.091
Staff service	4.318	3.765	3.600	3.636
Shopping & restaurant	4.045	4.000	4.250	3.545

Table 4-2 Transit flight information through Asian hub airports

LAX-BKK	NRT	ICN	HKG	TPE
Airfare ($)	2194.6	1295.8	866.2	579.4
Transit time (h)	6.2	11.3	13.8	8.5
Total travel time (h)	25.1	30.3	32.9	27.5
Departure & arrival time	4	3	3	5
Aircraft type	8	7	5	6

Source: Google flight 1st, April

Table 4-3 Scores of airlines through Asian hub airports

Airline attributes	NRT	ICN	HKG	TPE
Safety level	4.500	4.000	4.750	4.250
Staff service	4.637	4.215	4.400	4.065
In-flight service	4.322	4.023	4.357	4.044
Loyalty program	4.000	4.000	4.000	4.000
Frequency	13	9	32	18

Source: SKYTRAX, Google flight 1st, April

Table 4-4 Flight routes evaluation results of 18 scenarios

Purpose / Route	B	S	V
LAX-BKK	Rank	Rank	Rank
NRT	4	4	4
ICN	3	3	3
HKG	2	2	2
TPE	1	1	1
BKK-LAX	Rank	Rank	Rank
NRT	3	3	2
ICN	4	2	3
HKG	2	4	4
TPE	1	1	1
JFK-MNL	Rank	Rank	Rank
NRT	3	3	3
ICN	4	4	4
HKG	1	1	1
TPE	2	2	2
MNL-JFK	Rank	Rank	Rank
NRT	1	2	2
ICN	2	1	1
HKG	3	4	3
TPE	4	3	4
JFK-BKK	Rank	Rank	Rank
NRT	2	2	1
ICN	3	4	3
HKG	1	1	2
TPE	4	3	4
BKK-JFK	Rank	Rank	Rank
NRT	2	3	2
ICN	1	1	1
HKG	4	4	4
TPE	3	2	3

Transit situation LAX⇔BKK

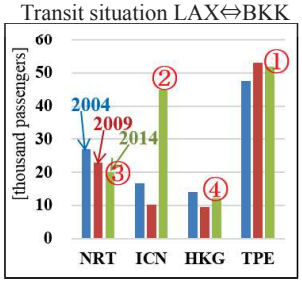

Transit situation JFK⇔MNL

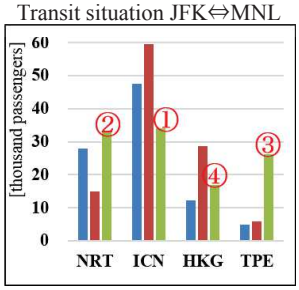

Transit situation JFK⇔BKK

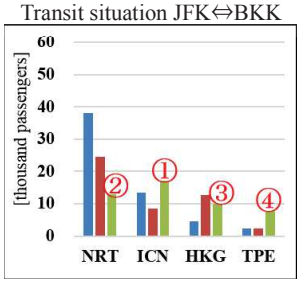

5. Conclusion

Transit passenger volume through NRT, ICN, HKG and TPE have had an obvious competition in the past 10 years. From main criteria, flight attributes are selected as priority by most transit passengers. From sub criteria, airfare, total travel time and airline safety are mostly concerned by the transit passengers. Optimal flight route choice change due to different route directions, which is affected by the high weighted factors such as airfare and total travel time. There is always an optimal transit flight route choice under the conditions of different trip purposes, origins and destinations.

Reference

[1] Chang, Y. (2003). Performance evaluation of international airports in the region of East Asia. Proceedings of the Eastern Asia Society for Transportation Studies, Vol.4.

[2] Kopytov, E., Abramov D. (2012). Multiple-criteria analysis and choice of transportation alternatives in multimodal freight transport system. Transport and Telecommunication, 13(2), 148-158.

LIFETIME PREDICTION METHOD USING ACCELERATION TEST FOR PAINT-COATED STEEL AND MORTAR-COVERED STEEL IN MARINE ENVIRONMENT

Student Number: 14M18081 Name: Kyohei Shimura Supervisor: Nobuaki Otsuki

促進試験を用いた塗装鋼材およびモルタル被覆鋼材の海洋環境における寿命推定方法

志村　恭平

海洋環境においては塗装鋼材やモルタル被覆鋼材の腐食が問題となっている．そこで適切な補修間隔の決定やライフサイクルコストの算出のために劣化過程や劣化速度について把握し,寿命を推定する方法が必要とされている．既往の研究[1]によって,フタル酸系塗装鋼材とタールエポキシ系塗装鋼材の劣化過程および劣化促進試験を用いた寿命推定方法が提案された．しかし，塗料種類が異なる塗装鋼材やモルタル被覆鋼材にも適用できるのかなどその汎用性については検討が不十分であった．

以上の背景を踏まえ，本研究では促進試験を用いてポリウレタン系塗装鋼材およびモルタル被覆鋼材の劣化過程および劣化速度について検討を行い，模擬実環境中における劣化速度との比較から促進倍率を算出し，寿命推定を行った．その結果，①ポリウレタン系塗装鋼材の潜伏期においてはフタル酸系塗装鋼材およびタールエポキシ系塗装鋼材と同様の促進倍率が得られ，寿命推定結果の妥当性が確認された．しかし，②ポリウレタン系塗装鋼材の潜伏期以降においてはフタル酸系塗装鋼材およびタールエポキシ系塗装鋼材と異なる劣化過程を示すことが確認された．③モルタル被覆鋼材では，促進試験で寿命推定を行うことができなかったが，鉄筋コンクリートの寿命推定方法と同様の方法で妥当な寿命推定結果が得られた．

1. Introduction

Steel is easy to corrode in marine environment. To protect steel from corrosion, paint-coated steel are often used. It is important to know deterioration process and deterioration speed and establish lifetime prediction method of these steel for appropriate repair time and life-cycle cost estimation.

In previous study[1], the influence of temperature and solution on deterioration speed of defective paint-coated steel was investigated, deterioration process and lifetime prediction method of defective paint-coated steel was proposed.

However, in the study, only 2 types of paint-coated steel (Phthalic type, Tar epoxy type) were used. So its applicable range was not investigated. In actual environment different type of paint-coated steel and mortar-covered steel are also used. Therefore, to make the lifetime prediction method more usable, investigation on deterioration speed and deterioration process of other type of paint-coated steel and mortar-covered steel are also needed.

From the above background, the objectives of this study are as following:

1. To know deterioration process and deterioration speed of polyurethane type paint-coated steel and mortar-covered steel using acceleration test.
2. To obtain magnification of acceleration comparing the deterioration speed in acceleration environment and simulated actual environment.
3. To conduct lifetime prediction and examine the validity of predicted lifetime.

2. Previous Study (Phthalic, Tar Epoxy)

Annaka[1] proposed the influence of f temperature and solution on deterioration speed and deterioration process of defective paint-coated steel and as below.

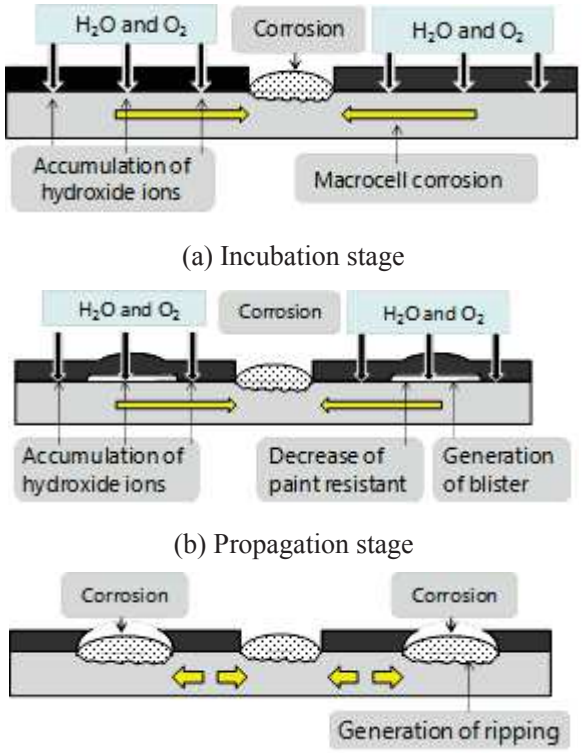

Fig.1 Deterioration process　defective paint-coated steel in submerged zone

(a) Deterioration process of defective paint-coated steel

From exposure test in off Suruga Bay and Futtsu, and consideration of mechanism, deterioration process could be proposed as shown in **Fig.1**.

(b) Influence of temperature

Temperature was estimated by activation energy. Magnification of acceleration was estimated by equation (1).

$$\frac{V_1}{V_2} = \exp\left(\frac{\Delta E_a}{R}\left(\frac{1}{T_2} - \frac{1}{T_1}\right)\right) \quad (1)$$

Where, V: corrosion current (μA/cm2), ΔEa: activation energy (cal/mol), R: gas constant (1.99 kcal/mol/K), T: temperature.

From the experimental result, ΔEa was estimated as 11.0kcal/mol. So, the magnification of acceleration between 20˚C and 50˚C was estimated at 5.8.

(c) Influence of solution

The magnification of acceleration between Sea water and 3%Nacl was estimated at 2.3.

3. Experimental procedures

In this study, to investigate deterioration mechanism and deterioration speed, and specimens are submerged in acceleration environment. And to obtain magnification of acceleration, specimens are also submerged in simulated actual environment.

3.1 Environments

Acceleration environment is set as the air saturated 50℃ 3wt% NaCl water (JSCE standard[2]). Simulated actual environment is set as the 20℃ artificial sea water.

According to Chap.2, magnification of acceleration should be 13 .3times.

3.2 Paint-coated steel specimen

In this study, steel plates (thickness: 3.2mm, width: 0.9mm) divided into rings were provided as shown in **Fig.2 (a)**. Soldering was conducted to the backside of each steel plate as shown in **Fig.2 (b)**. Steel plate was embedded in epoxy resin as shown in **Fig.2 (c)**. By connecting lead wire, the divided steel plates were considered as one circulated plate. Center circulated steel was called "R-0". Other steel plates were called "R-1" to "R-5" from inside. The area of each steel plate is as shown in **Fig.2 (d)**. After painting, φ8mm defect was added to R-0. Divided specimen is used to measure microcell and macrocell corrosion current density at defect part.

Not divided steel plate specimen (defective and not defective) is also used to understand paint coating deterioration.

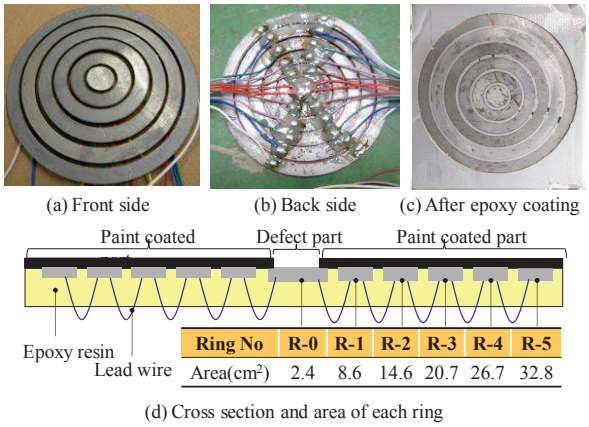

Fig.2 Paint-coated steel specimen

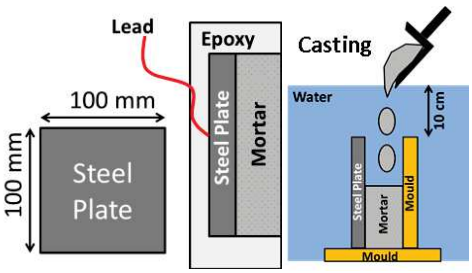

Fig.3 Mortar-covered specimen

In this study, polyurethane paint (PU) are used. Different from Phthalic and Tar epoxy paint, polyurethane paint has undercoat (50μm) and overcoat thickness was controlled. Paint thickness is set as 300, 500, 700, 900μm.

3.3 Mortar-covered specimen

In case of mortar-covered specimen, steel plates (thickness: 3.2mm, 10mm×10mm) were used. Soldering was conducted to the backside. Same as actual case, anti-washout mortar is used and casted in artificial sea water (**Fig.3**). Curing was conducted for 1day in artificial sea water. Then back and side surface was covered with epoxy resin. Mix proportion of mortar is shown in **Table.1**. Covering thickness was set as 1cm, 2cm, 3cm.

Table.1 Mix proportion of mortar

Air (%)	W/C (%)	S/C	Unit Weight (kg/m3)						
			W	C	S	Admixture			
						AE Admixture	SP	Viscosity Agent	Defoaming Agent
3.0	45.0	1.2	360	800	931	2.50	8.00	3.88	0.12

3.4 Measuring method

In this study, appearance observation was conducted to understand deterioration of paint coating or mortar covering.

Polarization resistance was measured by alternating current impedance method. Microcell current density was calculated as Stern-Geary constant (In this study, 0.0209V) divided by Polarization resistance.

Macrocell current was measured by zero resistant ammeter connecting between each ring.

4. Discussion and experimental results

4.1 Polyurethane paint-coated steel

(1) Appearance observation

Fig.4 shows appearance, blisters were oseraved on defective polyurethane paint-coated steel and their distribution looked concentrating near the defect. Paint-coating was disbonded at large area. Even at not blistered part, paint-coating was disbonded and paint thickness didn't affect disbonding width from defect. Spot rusts were observed under disbonded paint-coating. However, there was no rust under big blister around defect, so it is considered that the area around defect was cathod part.

(2)P aint thickness and duration until blistering

As shown in **Fig.5**, relation between paint thickness and duration until blistering of polyurethane paint-coated steel was obtainesd as y = 0.0139x in 50℃NaCl water and y = 0.1478 in 20℃ Seawater. Then magnification of acceleration was

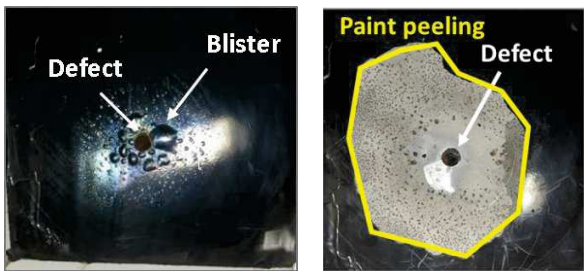

Fig 4Polyurethane paint-coated steel (50℃NaCl water, 300μm, 140th day)

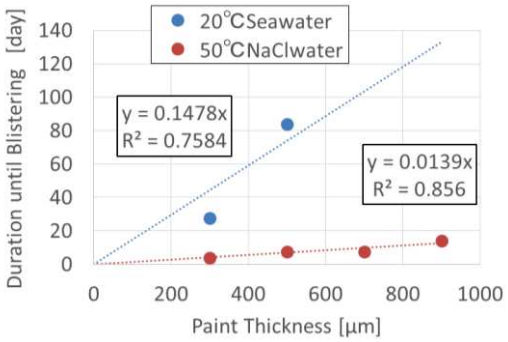

Fig.5 Relation between paint thickness and duration until blistering

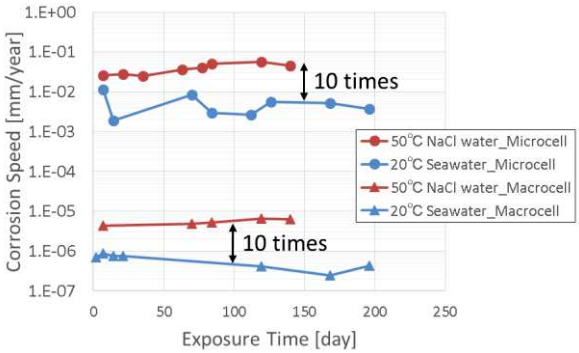

Fig.6 Corrosion speed of polyurethane paint-coated steel at defect part (incubation stage)

obtained as 10.6 times.(y: Duration until blistering, x: Paint thickness)

(3) Influence of defect on duration until blistering

In case of Polyurethan paint-coated steel (300μm), blister occurred on defective specimen at 4th day and blister didn't occur on not defective specimen at 140th day. Then influence of defect existence was obtained as over 35 times.

(4) Corrosion speed in incubation stage

Fig.4.3 shows microcell and macrocell corrosion speed of polyurethane paint-coated steel. As shown in **Fig.6**, magnification of acceleration of both of microsell and macrocell corrosion speed was about 10 times.

(5) Proposal of deterioration process of polyurethane paint coated steel

Deterioration process of polyurethane paint-coated steel was proposed in **Fig.7** After incubation stage, it shows different deterioration process from Phthalic and Tar epoxy paint type.

4.2 Mortar-covered steel

(1)Appearance observation

In this study, deterioration of mortar-covered steel couldn't

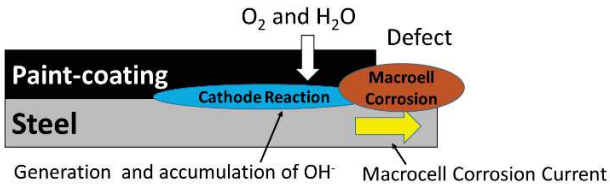

(a) Incubation stage

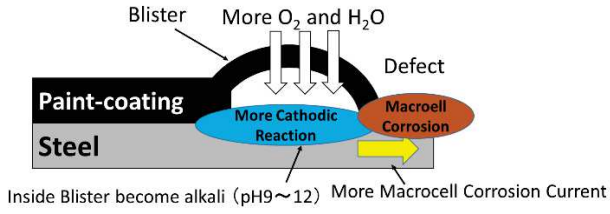

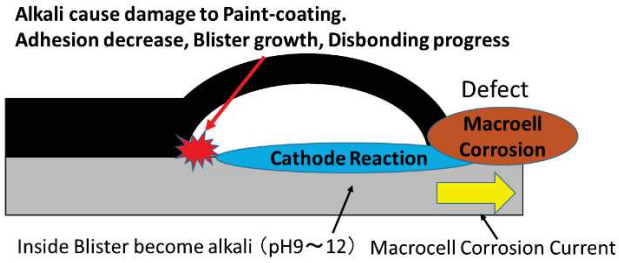

(b) Propagation stage

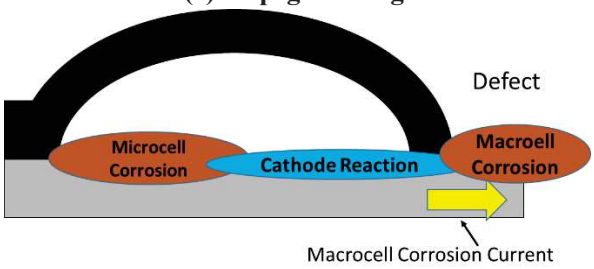

(c) Acceleration stage

Fig.7 Deterioration process of polyurethane paint coated steel

investigated by using acceleration test.

So lifetime prediction of mortar-covered steel was conducted in the same way as lifetime prediction of reinforced concrete[3].

(2) Chloride ion diffusibity in mortar-covering

Chloride ion content of mortar surface, chloride ion diffusion coeficient and initial chloride ion content in 20℃ seawater are obtained experimentaly as 10 [kg/m^3], 3.3 [cm^2/year] and 1.2 [kg/m^3]. And threshold chloride ion content is 2.1 [kg/m3][4]

(3) Oxygen permeation amount and corrosion speed

Oxygen permeation amount of mortar-covered steel (20℃ Seawater, 3cm) was obtained as 1.7E-12 [mol/cm^2/s]. This can be converted to corrosion speed as 0.94 [mg/cm^2/year].[5]

(4) Relation between corrrosion amount and adhesion

Adhesion force of electrolytic corroded mortar-covered steel was measured. As the result, adhesion force decreased by 95% at 10 [mg/cm^2] corrosion amount.

(5) Corrosion amont at mortar cracking

As actual structure, mortar-covered steel pipe pile(ϕ 100cm, covering thickness = 10cm) was modeled. Then its corrosion

amount at mortar cracking was obtained as 21.2 [mg/cm^2] by Nonlinear finite element analysis.

(6) Deterioration process of mortar-covered steel

Fig.8 shows deterioration process of mortar-covered steel.

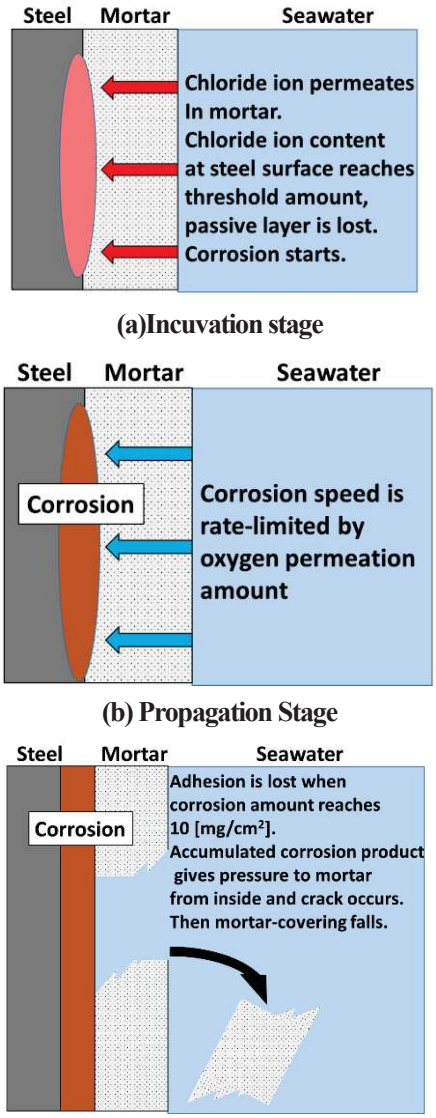

Fig.8 Deterioration process of mortar-covered steel

4.3 Lifetime prediction of polyurethane paint-coated steel and mortar-covered steel

In case of polyurethane paint-coated steel, lifetime was defined as incubation stage. In case of mortar-covered steel lifetime was defined as incubation + propagation stage. Lifetime prediction procedure is shown in **Table.2.** (Phthalic: Defective, 150μm, Tar Epoxy: Defective, 675μm, Polyurethane: Not defective, 2500μm, Mortar : Steel pipe pile[φ100cm, covering thickness = 10cm])

5. Conclusions

1. The magnification of acceleration of polyurethane paint-coated steel in incubation stage was about 10 times. This is almost same to the magnification of acceleration of Phthalic and Tar epoxy paint-coated steel. And predicted life time of polyurethane paint-coated steel was close to actual lifetime.
2. Deterioration process of polyurethane paint-coated steel after incubation period was different from that of Phthalic and Tar epoxy paint-coated steel.
3. In this study, deterioration of mortar-covered steel couldn't investigated by using acceleration test. And lifetime prediction method for reinforced concrete was not valid. As future work, more appropriate lifetime prediction method for mortar-covered steel should be studied.

References

1) T. Annaka, "Research on Corrosion Mechanism and Influential Factors of Paint Coated Steel with Defect in Submerged Zone", 2013
2) JSCE, "Guideline of efficiency evaluation about durability and load resistance of marine steel structures in marine environment"
3) H. Ohara, "Lifetime Prediction of Concrete Mixed with Seawater against Chloride Attack and Carbonation", 2013
4) JSCE, "Concrete standard specifications (design)", 2012
5) S. Maruyama, "Influence of temperature and cement on steel bar corrosion in concrete induced by carbonation", 2002
6) Public Works Research Institute, "Corrosion protection guideline and manual of marine steel structure (Splash zone・Tidal Zone), 1990

Table.2 Lifetime prediction procedure

	Phthalic[1)]	Tar Epoxy[1)]	Polyurethane		Mortar-covered steel	
Lifetime Prediction	23.4~58.5 [day]	2.3~5.7 [year]	Paint thickness	0.0139×2500μm = 34.75 [day]	Incubation stage	**5.3 [year] ※1**
			Defect	Over 35 times	Propagation Stage	**22.6[year] ※2**
			Magnification of Acceleration	10.6 times	Total	**27.9[year]**
			Total	over 12900 [day] = **over 35.3 [year]**		
Actual Lifetime	**37 [day]**	**1~5 [year]**	**About 40 [year][6)]**		**About 50 [year][6)]**	
Accuracy	**63.2~158%**		**88.3 %**		**55.8 %**	

※1 Calculated from the results shown in 4.2(2) and Fick's law

※2 Corrosion amount at cracking 21.2 [mg/cm2] / Corrosion speed 0.94 [mg/cm2/year]

STUDY ON SUSTAINABLE MANAGEMENT OF PONDS AND WETLANDS IN WORLD HERITAGE USING GIS: CASE OF LUANG PRABANG, LAO PEOPLE'S DEMOCRATIC REPUBLIC

Student Number: 14M18017 **Name**: Norifumi IRIE **Supervisors**: Shinobu YAMAGUCHI and Jun-Ichi TAKADA

GIS を用いた世界遺産地域における湿地帯の持続可能な管理に関する研究: ラオス人民民主共和国ルアンプラバンの事例を用いて

入江　憲史

本研究では世界遺産ルアンプラバン地域における湿地帯の事例を用い、近年その価値が国際的に見直されつつある湿地帯の保全について、現地遺産局のニーズを元に様々な視点から取り扱う。具体的に、地理情報システムを用いた湿地帯変化の視覚化及び分析、質的なアプローチによる現地住民が培ってきた知識について分析する。また Mixed-methods アプローチを導入し住民の湿地帯保全に関する意識調査を実施し、湿地帯の持続的保全について考察する。

1. Introduction

Luang Prabang, the first World Heritage site in Lao PDR, is situated in the confluence of the Mekong and Nhamkhan river. The ponds and wetlands in the town have been playing an important role with its various functions promoting flood prevention, water retention, and healthy environment with rich biodiversity. Its water network compliments the unique townscape. 183 ponds and wetlands were registered in the inventory within Natural and Landscape Zone (ZPP-N) of the safeguard and enhancement plan (PSMV) as part of the Outstanding Universal Values of World Heritage.

Since the heritage inscription in 1995, the town experienced the hike of tourist visits and rapid development. This resulted in increasing pressure on the heritage property including the inventory ponds and wetlands. Department of World Heritage in Luang Prabang (DPL) has been continuously implementing preservation programs on ponds and wetlands supported by international organizations under multiple projects until 2009. With the reason of recent growing attention to the ponds and wetlands preservation in the Greater Mekong Sub-regions where the decrease of wetlands have been increasingly reported, the collaboration team between Tokyo Institute of Technology (Tokyo Tech) and DPL conducted a preliminary survey in 2014. The survey result identified the needs of updating the available data, visualizing temporal changes of the ponds and wetlands, and understanding the reasons of the change as well as the local residents' situation.

Following such needs, three specific research objectives were developed as follows: 1) to visualize temporal changes of the ponds and wetlands from 2001 to 2015 using GIS; 2) to identify reasons behind the change of the ponds and wetlands; and 3) to understand people's attitude toward ponds and wetlands preservation.

2. Literature Review

2.1. Analysis on temporal changes using GIS

With the recognized value of ponds and wetlands preservation, Geographic Information System (GIS) has been applied to detect the temporal changes of ponds, wetlands, and their surrounding area.

There are two common methods on GIS applied to measure the temporal changes: 1) inspection of geo-referenced multi-temporal satellite images; and 2) comparison analysis on land cover or use types in the location at different time points [1]. There are also unique methods available depending on the study context. For example, the shift of the number of patches of land cover types was studied over years to see the temporal change of wetlands in China [2].

2.2. Environmental attitude

Incorporating the environmental attitude into decision making process will help achieve a long term preservation of nature [3]. Environmental attitude is traditionally composed of three factors, namely, *cognitive (knowledge)*, *affective (feeling)*, and *conative (behavioral)*. Meanwhile, recently diverse factors were identified. For instance, demographical characteristics such as age and education level were identified factors [4]. Bonita L. Mc Farlane insisted that *value*, the worth of the object, has a certain degree of linkage to environmental attitude [5]. Another

study suggested there exist connection between *perceived access* to green pathway and environmental attitude [6]. Balram then emphasized on the importance of context-based studies as the attitude components vary depending the context [7]. This study follows this argument and, thus, considers the importance of "context" in understanding people's attitude toward the ponds and wetlands preservation in Luang Prabang.

3. Methodology

The theoretical framework adapted an instrument developed by Balram to analyze contextualized environmental attitude [7]. The study takes the following five specific steps.

First, the temporal changes in a pilot site are visualized and analyzed using GIS to provide evident information on the changes and update data on the ponds and wetlands. The pilot site for the analysis covers Mano and Phonkham villages located in ZPP-N with the area of approximately 1 km^2. This study analyzed the temporal changes by comparing various types of data including: 1) green space observed in the satellite images; 2) land cover types; and 3) usage types of the ponds at three different time points (2001, 2008, 2014/2015). A vector map in 2014 is newly delineated for comparison and updated systematically by inspecting observable changes in the field and referring to available spatial data.

Second, interviews are conducted with selected stakeholders with two purposes: 1) to explore reasons behind the changing tendency of the ponds and wetlands; and 2) to identify possible factor components affecting the attitude of people toward ponds and wetlands preservation. Twelve open-ended questions are developed based on the common factors of attitude found in existing studies and suggestions from DPL and Tokyo Tech. The interview content is translated from Lao to English and stored as text data.

Third, a local workshop is organized with the experts of DPL to share the results. There are two purposes for the discussion as follows: 1) to confirm the validity of the results and findings discovered in the previous two steps; and 2) to reflect opinions and ideas of local experts onto this study.

As the forth step, the identified possible factor components are further explored through a questionnaire survey. The questionnaire has two sections: attitude measurement and demographic profile section. The attitude measurement section includes multiple 5-point Likert scale items in which the level of agreement is measured. Those questionnaire items are reflected from the current literatures and the possible factor components identified in the previous step. The demographic profile section consists of job occupation, gender, age, education level, and income level. The expected respondents include 10 DPL experts, 10 Urban Development Administrative Agency members, and 40 pond owners. The questionnaires are distributed in the drop-off survey style.

Finally, quantitative analysis on survey responses is conducted. Three objectives for the analysis are highlighted: 1) to identify what ideas people mostly agree or disagree with; 2) to explore the latent factors of the attitude of people towards ponds and wetlands preservation; and 3) to comprehend the significance level of the latent factors.

The mean value of the questionnaire items is analyzed to find patterns in the items. Factor analysis is conducted to understand latent attitude factors contextualized in Luang Prabang. Item-total correlation, Kaiser-Meyer-Olkin Measure of Sampling Adequacy (KMO), and Bartlett tests are performed for data cleansing. For factor extraction, EFA adapts Principal Components Analysis (PCA). The reliability of the factors is assured through Cronbach's Alpha that demonstrates the level of inter-correlation in each factor.

To interpret the level of significance among the identified factors, the average mean value of each factor is compared and analyzed. In addition, Sample T-test and Demographic analysis of variance (ANOVA) are employed to identify differences in attitude across various demographic variables such as age and gender.

4. Data analysis

First, the green space observed in the satellite image of 2002, 2008 and 2014 were compared on GIS. The decrease of the green space and wetlands was visually detected. Second, the area proportion of land cover types including building zone and green space was calculated based on the vector map of 2002, 2008 and 2015 using area calculation tool of GIS (Figure 1). There were three findings: 1) green space had decreased while building zone had increased; 2) green space had shrunk more rapidly between 2008 and 2015 than before; and 3) other land cover types had rapidly increased between 2008 and 2015.

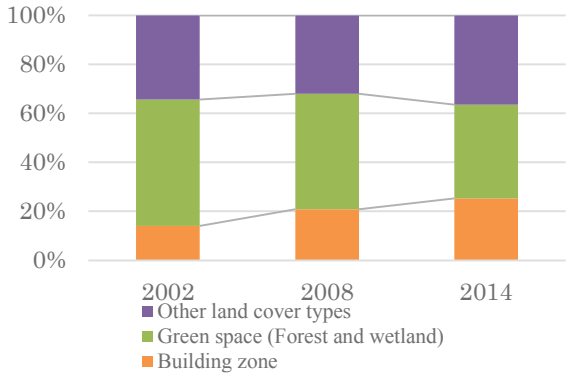

Figure 1: Land cover types' area percentage (2001 – 2014)

Third, the comparison analysis of the usage types of inventory ponds at three different points (2001, 2008 and 2015) identified three key findings: 1) ponds with no activities had increased from two to 13 between 2001 and 2015; 2) one pond with no activities in 2008 was converted into land; and 3) once ponds became unused, those ponds tend to be abandoned.

Interviews were conducted between March and May 2015 with 13 interviewees. The interview contents were analyzed following Grounded Theory. The reasons of the decrease of ponds and wetlands were categorized into two major factors: man-made or natural factors. Man-made factors include unintentional loss due to new constructions and intentional reclamation. Natural factors include three components: landslides near ponds; mud accumulation in the bottom of ponds; and continuous droughts due to the long dry season. Most of the respondents agreed that the pond quality has become lower compared to the past.

The qualitative analysis identified 21 possible factor components affecting people's attitude toward ponds and wetlands preservation such as *usefulness in agricultural activities*, *knowledge about ponds' history*, and *good atmosphere coming from the beauty and relaxing effect*. These components were classified into five categories, namely, *value*, *knowledge*, *feeling*, *cost* and *others*.

The local workshop was held in May 2015. As for the reasons behind the decrease of the ponds and wetlands, it was emphasized that the man-made and natural factors have been strongly linked with each other. Further, the workshop extracted additional possible factor components such as *land price hike* and *local mythology on ponds*.

A questionnaire with 32 items, reflecting the workshop discussion and existing knowledge on environmental attitude. The questionnaires were distributed between September and October 2015. A total of 61 responses were collected. The data cleansing was performed. As a result, 25 items remained valid for further analyses. Moreover, EFA using PCA techniques and interpretation through Varimax identified six factors. 1) cost of the ponds and wetlands maintenance; 2) pleasant feeling towards the ponds or wetlands; 3) understanding about the ponds and wetlands; 4) importance of the ponds and wetlands preservation; 5) accessibility to the ponds and wetlands; and 6) usefulness of the ponds. The high value of Cronbach's Alpha in every factor indicated that the inter-correlation within the tested factor was reliable.

Through the mean value analysis of the factors, there were particularly four findings in the context of Luang Prabang (Table 1). First, the respondents believe ponds and wetlands are important as *importance of the ponds and wetlands preservation* was the factor with the highest level of agreement (Mean = 1.683). Second, the respondents hold pleasant feeling towards the ponds and wetlands as the factor also marked the high level of agreement. Third, accessibility is one of the reasons for preserving ponds as *accessibility to the ponds and wetland*s showed the high level of agreement. Forth, the cost was highly considered by the respondents as *cost of the ponds or wetlands maintenance* showed the high level of agreement.

Factor	# of items	Mean Value	Standard Deviation
Importance of the ponds and wetlands preservation	3	1.683	0.740
Pleasant feeling towards the ponds or wetlands	4	1.787	0.788
Accessibility to the ponds and wetlands	3	1.934	0.809
Cost of the ponds and wetlands maintenance	7	1.940	0.949
Understanding about the ponds and wetlands	4	2.254	0.847
Usefulness of the ponds	1	2.410	1.006

Table 1: The mean value and standard deviation of factors

ANOVA and T-test found the gap across the governmental officials (UDAA and DPL experts) and pond owners in understanding about the ponds' function as a water network system and about the policies and regulation of DPL.

5. Discussion

As for the visualization of the temporal changes in the ponds and wetlands, the study findings supported the observed trends in ponds and wetlands as well as its surrounding green space around the Greater Mekong Sub-regions [8]. It is often the case in the region that building zone increases typically meanwhile the land cover types indicating a part of the nature decrease [1]

Using the empirical data, this study reinforced the importance of human-centered studies. As the heritage preservation is generally achievable when the participation of the stakeholders in both the public and private sectors is made, understanding various stakeholders' opinions is vital [9]. In fact, this study empirically found that every resident has their own perception, experiences and knowledge on the ponds and wetlands, so classifying their opinions could capture a variety of viewpoints inclusively.

Five out of the identified six factors affecting people's attitude towards ponds and wetlands preservation coincided with the factors of environmental attitude commonly found in the current literatures. An exceptional factor was *cost of the ponds and wetlands maintenance*, which was only found in this study context. It may be because the ponds and wetlands require industrious maintenance work while other natural environments such as forests and agricultural lands do not need the same level of maintenance work. This unique factor proves the importance of contextual research as pointed out by Balram [7].

Further, the findings through the mean value analysis of the factors are expected to be referenced to implement ponds-related projects in the future. It could be a reference to design preservation awareness campaign on ponds and wetlands. One of the common factors *value* was regarded as less important in this study context. In fact, the ponds and wetlands had been less utilized as identified through the interviews and visualization in GIS compared to 2001. It may have resulted from the shift of economic activities as the past studies indicated [1][2].

6. Conclusion

This study serves as significant knowledge base for future decision making on the ponds and wetlands in Luang Prabang. This comprehensive study covered three major topics including temporal changes of ponds and wetlands, the identification of the reasons for the changes and people' attitude towards ponds and wetlands preservation. As one of the few studies taken place in World Heritage sites in developing countries, the findings will also help the future studies to explore topics related to ponds and wetlands in similar settings.

It is recommended to update information subsequently as the situation of ponds and wetlands as well as its stakeholders is constantly changing. Neglecting the data update will cause the obsolescence of information. Another recommendation is expansion of the study area for visualization. Following the same techniques, it is possible to expand the survey scale.

In the end, it is hoped that this study can contribute to the sustainable management of the ponds and wetlands in Luang Prabang and possibly other sites in the Greater Mekong Sub-regions as well as World Heritage sites in the world facing the similar situation.

Acknowledgement

This work was supported by JSPS KAKENHI Grant Number 25303001.

Reference

[1] W. W. Zhang, L. Yao, H. Li, D. F. Sun, and L. D. Zhou, "Research on land use change in Beijing Hanshiqiao wetland nature reserve using remote sensing and GIS," *Procedia Environ. Sci.*, vol. 10, no. PART A, pp. 583–588, 2011.

[2] D. Xiao, B. Tian, K. Tian, and Y. Yang, "Landscape patterns and their changes in Sichuan Ruoergai Wetland National Nature Reserve," *Acta Ecol. Sin.*, vol. 30, no. 1, pp. 27–32, 2010.

[3] F. G. Kaiser, S. Wolfing Kast, and U. Fuhrer, "Environmental attitude and ecological behaviour," *J. Environ. Psychol.*, vol. 19, no. 1, pp. 1–19, 1999.

[4] P. D. L. V. CHRIS LAKHAN, "Use of Loglinear Models to Assess Factors Influencing Concern for the Natural Environment," *Environ. Manage.*, vol. 30, no. 1, pp. 77–87, 2002.

[5] P. C. B. Bonita L. Mc Farlane, "Factors Influencing Forest Values and Attitudes of Two Stakeholder Groups: The Case of the Foothills Model Forest, Alberta, Canada," *Society & Natural Resources*, vol. 13. pp. 649–661, 2000.

[6] G. Lindsey, M. Maraj, and S. Kuan, "Access, Equity, and Urban Greenways: An Exploratory Investigation," *Prof. Geogr.*, vol. 53, no. 3, pp. 332–346, Aug. 2001.

[7] S. Balram and S. Dragićević, "Attitudes toward urban green spaces: integrating questionnaire survey and collaborative GIS techniques to improve attitude measurements," *Landsc. Urban Plan.*, vol. 71, no. 2–4, pp. 147–162, 2005.

[8] B. Matthew and L. Rebelo, "Wetlands play critical role in economic growth of the Mekong," 2015. [Online]. Available: https://wle.cgiar.org/thrive/2015/02/02/wetlands-play-critical-role-economic-growth-mekong.

[9] N. F. N. Azhari and E. Mohamed, "Public Perception: Heritage Building Conservation in Kuala Lumpur," *Procedia - Soc. Behav. Sci.*, vol. 50, no. July, pp. 271–279, 2012.

Evaluation of the effectiveness of the proposed mitigation structures after the 2011 Great East Japan Earthquake

Student Number: 14M18164 Name: Koki MATSUMOTO Supervisor: Hiroshi TAKAGI

東日本大震災後の新設減災構造物の有効性の検証

松本　光希

2011 年に発生した東日本大震災においては．従来の想定を大きく超える津波が襲来し．東北地方を中心に甚大な被害をもたらした．本研究では．津波によって特に大きな被害を受けた宮城県の 2 地域（石巻市および名取・岩沼市）を研究調査対象とし．３度の現地調査を行い．護岸や盛土など減災構造物の復旧・復興状況を調査した．被災前後の護岸形状や地盤高等のデータを詳細に測量し．その結果を反映した津波の遡上再現数値モデルを構築した．この数値モデルを利用して．今後想定される津波に対して．現在建設が進められている減災構造物がどれほど効果的か数値解析に基づき検証した．

1. Introduction

The 2011 Great East Japan Earthquake that occurred on March 11th 2011 triggered a massive tsunami, claiming lives of more than 18,000 people and bringing partial or complete damage to approximately 400,000 building structures. Among several areas that suffered from the wrath of the 2011 event were Ishinomaki and Natori-Iwanuma, both of which are coastal areas in Miyagi Prefecture. The event had afflicted 3,000 deaths in Ishinomaki and more than 1,000 in the cities of Iwanuma and Natori.

According to the tidal records at Ayukawa Station[1], the observed tsunami height was at least 8.6m and the resultant flood extended 73 km^2 inward Ishinomaki City[2]. In the Sendai plains, the tsunami height reached as high as 8.5m[3] as derived from the water mark at Sendai Airport, and the inundation expanded to 29 km^2 inside Iwanuma City and 27 km^2 inside Natori City[2].

This study focuses on investigating the efficiency of the proposed mitigating structures based on the 2011 Great East Japan Earthquake in order to reduce the damage of future tsunami events. The authors expect that the findings in this study can improve the proposed reconstruction plan and thereby contributing to disaster risk reduction plan in the future.

2. Field Survey

Field survey was conducted at three different periods (March 2013, November 2013 and November 2015) in order to collect input data necessary for the tsunami run-up simulation. All three surveys were primarily aimed to collect ground elevation, water depth and dyke height information.

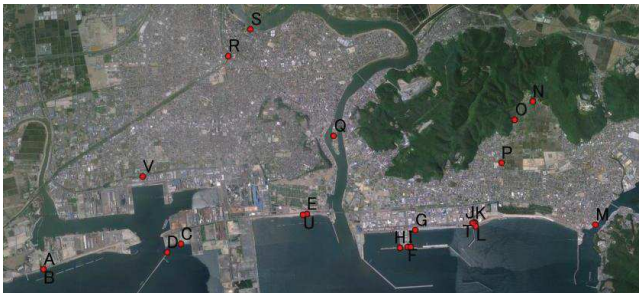

Fig 1 .Field survey points at Ishinomaki

Fig 2. Field survey at Ishinomaki

Fig 3. Field survey points at Natori and Iwnauma

Fig 4. Field survey at Natori and Iwanuma

3. Reconstruction Plan

Efforts to reconstruct and establish new mitigating structures were led by the local government of Ishinomaki, Natori and Iwanuma. The reconstruction plan which started in year 2011 and has been on-going until now was based on the past 1960 Chile tsunami and storm surge event. A three countermeasures reconstruction plan in Ishinomaki contains lining up a 7.2m-high dyke along the coastline as part of the first structure, and accompanied by the second structure that involves the road 1-km away and parallel to the coastline and raising this road by 2.6-4.5m from the ground level. In addition to these, 21 evacuation buildings and an additional 3 evacuation towers will be established as included in the third structure. The spatial distribution of the three countermeasures is illustrated in the figure below, along with the details of each structure's status.[3]

Table 1. Reconstruction plan in Ishinomaki

Name	Type	Height(T.P.)	Color and Line	Condition
First structure	dyke	7.2m	red(solid)	partially complete
Second structure	road	2.6～4.5m	blue(dot)	has not started
River dyke	dyke	4.1～7.2m	green(chain)	partially complete

An identical three countermeasures package was proposed in Natori and Iwanuma. This involves lining up a 7.2m-high dyke along the coastline as part of the first structure. Similarly, the second structure aims at raising the road 1-km away and parallel to the coastline by 8m from the ground level. The third structure incorporates a construction of another road raised 10-m above ground and called "The Highway of Eastern Sendai".[4][5]

Table 2. Reconstruction plan in Natori and Iwanuma

Name	Type	Height(T.P.)	Color and Line	Condition
First structure	dyke	7.2m	red(solid)	almost complete
Second structure	road	8.0m	blue(dot)	has not started
Third structure	road	10.0m	yellow(one dot chain)	completed
River dyke	dyke	7.2m	green(one dot chain)	has not started

4. Model Setup

Delft 3D Flow, a fluid dynamics model, was applied to recreate the lifecycle of the tsunami in 2011 generated from the deep sea, traversing through the shallow water and eventually running up towards inland. The present study employed a 2D horizontal grid equivalent to a non-linear long wave model commonly used for tsunami run-up simulations.

4.1 Calculation Setting and Calculation Area

Table 1 presents the settings used in the simulation. The offshore boundary is set aligned between the two GPS buoys of Central Miyagi and Fukushima. The input data were created by linearly interpolating the observed tsunami elevations at two locations. For the purpose of effectively running the simulation, the computational domains were composed of four areas from (a) to (d) with a 540m, 180m, 60m, and 20m grids, respectively.

Table 3. Calculation Setting and Area

item	
Calculating area	Largest mesh (540m square mesh)
	Second mesh (180m square mesh)
	Third mesh (60m square mesh)
	Fourth mesh (20m square mesh)
Wave	2011 Great East Japan Earthquake and Tsunami
Time step	Δt=0.03s
Tide level condition	Mean sea-level of Tokyo Bay (T.P.+0.0m)
Computation time	2011/3/11 14:46～2011/3/11 17:00
Bathymetric data	Largest mesh: JODC 500m data
	Second mesh: JODC 500m data
	Third mesh: JODC 500m data
	Fourth mesh: プレジャーボート・小型船用港湾案内
Ground levels	5m mesh data of Geographical Survey Institute
Manning's *n* coefficient	water area:0.025
	ground area:0.16(Ishinomaki) 0.08(Natori and Iwanuma)

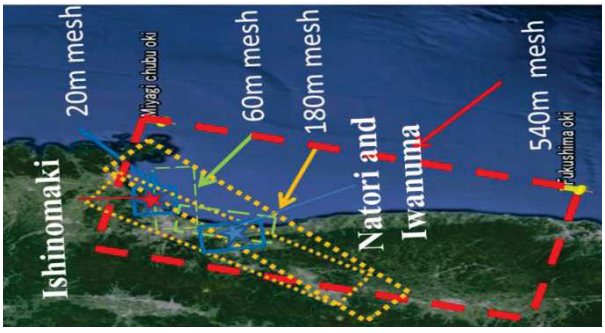

4.2 Selecting Manning's *n* coefficient during tsunami run-up over land

In order to incorporate the varying surface roughness throughout the different stages of flow of the tsunami, separate values of Manning's coefficient for the sea and the land were utilized [6][7]. A uniform Manning's coefficient of 0.025 was set to the sea portion; however, different values must be assigned to each land segment of Ishinomaki and Sendai plains in order to assimilate the difference of land cover of the studied areas. To do so, several calculations were performed employing different values of Manning's coefficient. The simulated inundation height from different Manning values were graphed and cross-checked with the observed values in Figure [8]. The Manning value that generated the best-fit regression line was then selected. It was derived that the Manning coefficient to be used is 0.16 in

Ishonomaki and 0.08 in Natori and Iwanuma.

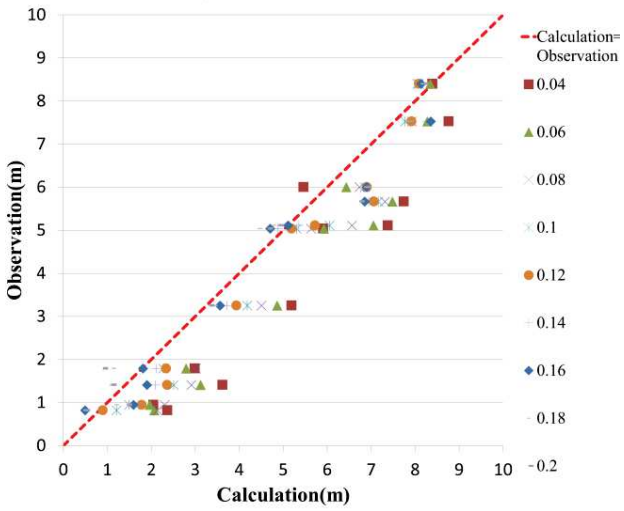

Fig 5.Comparing observed and calculated inundation height data in Ishinomaki

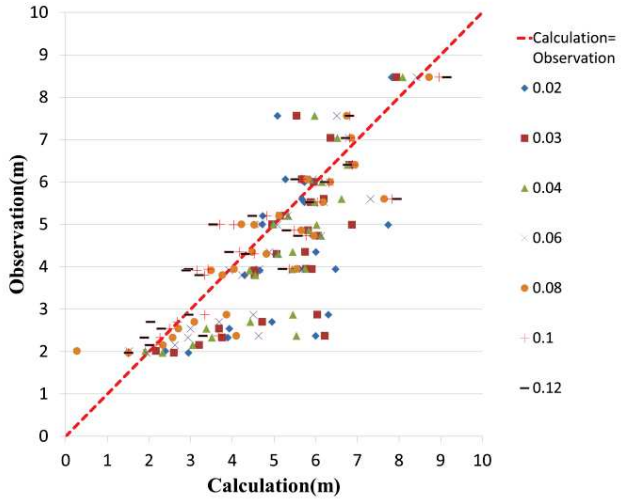

Fig 6. Comparing observed and calculated inundation height data in Natori and Iwanuma

5. Evaluation of the effectiveness of the proposed mitigation structures

In this study, the authors defined three types of tsunami according to the frequency of occurrence: once in a hundred year, once in several hundred years and once in a thousand year. Moreover, three terrain conditions were applied: during pre-tsunami event of 2011, during present condition, and during post-reconstruction of the proposed structures. The run-up height values with different scales were carried out to each terrain case and the spatial distribution of the damage was examined.

5.1 Incident Wave

As mentioned above, the authors opted to divide the simulations into three categories with varying scales of tsunami run-up which are proportioned according to the 9m-high maximum run-up generated during the 2011 event. To illustrate, in Ishinomaki the run-up values of the first category (once in a hundred year occurrence interval) were calculated by proportioning the 9m maximum by 1/4 and 1/3, resulting to 2.25m and 3m-high run-up, respectively. Similarly, the proportions for the second and third group were set to 1/2, 2/3 (corresponding to heights of 4.5m and 6m) and 4/5, 5/5 (corresponding to 7.2m and 9m) with return periods of once in several hundred years and once in a thousand year, respectively. The same procedure was utilized in Natori and Iwanuma with a maximum run-up tsunami height of 5m. Utilizing the identical proportions applied in Ishinomaki, the corresponding incident waves are 1.25m and 1.67 for 1/4 and 1/3 proportions, 2.5m and 3.33m for 1/2 and 4/5 proportions and 4m and 5m for the 4/5 and 5/5 proportions.

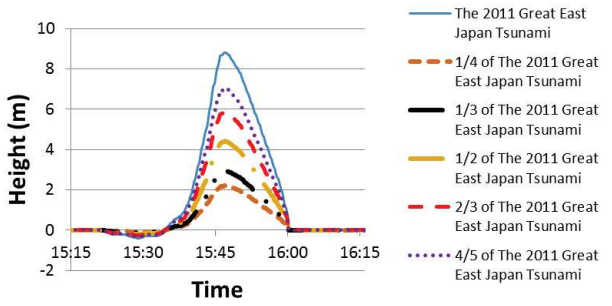

Fig 7.Incident Wave in Ishinomaki

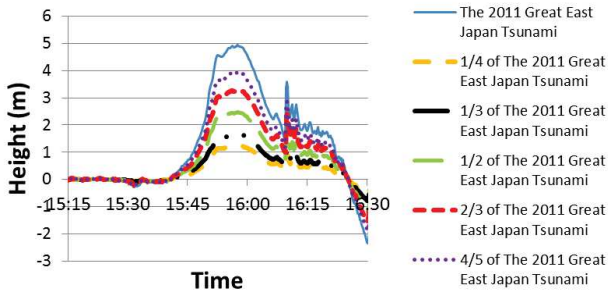

Fig 8. Incident Wave in Natori and Iwanuma

5.2 Calculation Results

The authors ran the simulation for ten different locations and selected the results in Mitsumata in Ishinomaki to show one of the typical trends among all ten locations Fig10-12 show the consequence of each tsunami scale for all three terrain conditions at Mitsumata, a residential area during pre-tsunami and post-tsunami event of 2011. Fig10 suggests that tsunami events with occurrence interval of once in a hundred year will completely disperse the generated waves and hence, will not reach the residential areas. On the other hand, as depicted on Fig11, a tsunami scale of once every several hundred years will induce a run-up wave that may extend towards the residential areas, but the structures may significantly dissipate the energy generated by the tsunami. The energy dissipation may also be attributed to the change in land use after the reconstruction plans. Lastly, tsunamis of scale analogous to that of the 2011 Great East Japan Earthquake may not also inhibit the waves from stretching onto Mitsumata and the energy dissipation caused by the structures are likely to be lower than that of the second case.

Figure 13 illustrates the flood area in Ishinomaki with 1/3 incident wave. It is apparent that the second

structure can prevent the tsunami run-up.

Fig 9. Calculation points (Left: Ishinomaki, Right: Natori and Iwanuma)

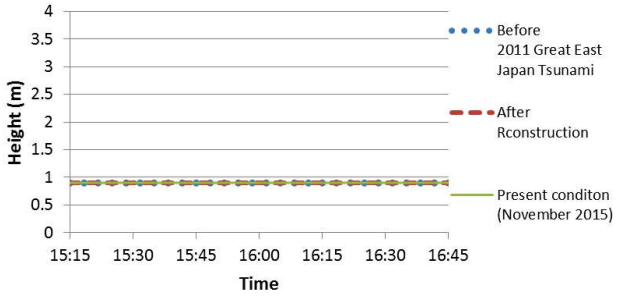

Fig 10. Mistumata (1/4 Incident Wave)

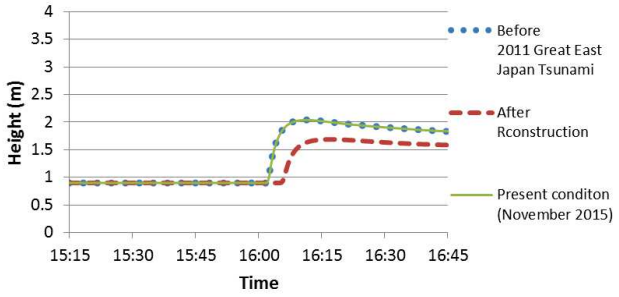

Fig 11. Mistumata (2/3 Incident Wave)

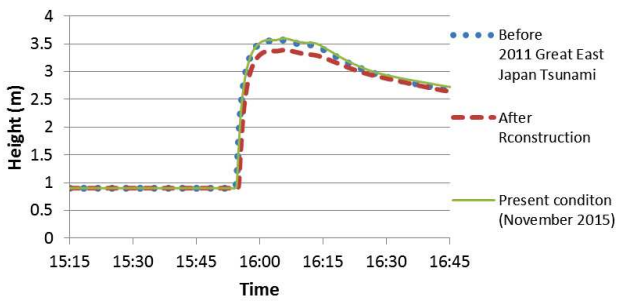

Fig 12. Mistumata (2011 Great East Japan Tsunami Incident Wave)

Fig 13. The flood Area at Ishinomaki in 1/3 incident wave) (Red: Before 2011 Great East Japan, Blue: Present condition, Green: After Reconstruction)

6. Conclusion

Since a full protection from another tsunami event with a magnitude similar from that of the previous one in 2011 is likely to be unrealistic, the intention of the reconstruction plan is to sufficiently dissipate the future tsunamis' run-up to enable the residents to evacuate before the arrival of tsunami, which is further supported by the raised road plan (second structure). Based on the simulation results of this study, the likelihood of future tsunami event reaching the residential area will be less when the proposed new structures are incorporated. Evidently, the likelihood will be much lower when the residents relocate further away from the coastline. Furthermore, the results of the simulation reveal that the configuration of the dyke and the raised road in the non-residential areas of Ishinomaki, Natori and Iwanuma may possibly inflict a larger tsunami run-up due to wave reflection. Accordingly, the authors propose a reconfiguration of the position and alignment of the raised road from the dyke aligned along the coastline.

7. References

[1] Japan Meteorological Agency: http://www.jma.go.jp/jma/press/1106/03b/

[2] The Geospatial Information Authority of Japan: http://www.gsi.go.jp/chirijoho/chirijoho40022.html

[3] 石巻市:東日本大震災からの復興　「最大の被災都市から世界の復興モデル都市を目指して」, https://www.city.ishinomaki.lg.jp/cont/10181000/8235/99.hukkoujyoukyou_2.pdf

[4] 岩沼市:岩沼市震災復興計画マスタープラン, http://www.city.iwanuma.miyagi.jp/kurasi/matidukuri/documents/master-ver2.pdf

[5] 名取市:名取市震災復興計画, http://www.city.natori.miyagi.jp/shinsai/fukkoukeikaku/node_31407/node_33441

[6] Takagi H., Bricker J.. Assessment of The Effectiveness of General Breakwaters in Reducing Tsunami Inundation in Ishinomaki, Coastal Engineering Journal, Vol. 56, No. 4, Page 21, Dec. 2014.

[7] Bricker J., Gibson S., Takagi H., Imamura F.. On the Need for Larger Manning's Roughness Coefficients in Depth-Integrated Tsunami Inundation Models, Coastal Engineering Journal, Vol. 57, page 13, Jun. 2015.

[8] 東日本大震災津波詳細地図　上巻」((2011)原口 強, 岩松 暉著)

Decomposition of nitrous oxide over Cu modified Indonesian natural zeolite

Student number: 14M18030　Name: Ryusuke Katagiri　Supervisor: Hirofumi HINODE

インドネシア産天然ゼオライト担持銅触媒を用いた亜酸化窒素の直接分解

片桐　隆介

本研究では、工業生産過程から排気された N_2O の分解を目的に、産地の異なる 2 種類のインドネシア産天然ゼオライトを担体として、含浸法及びイオン交換法を用いてゼオライト担持銅触媒を調製し、N_2O 分解に対する触媒活性を評価した。また、調製条件である金属担持量、焼成温度による触媒活性の変化を検討した。調製した触媒の中では、含浸法で 500 ℃で焼成した Sukabumi 産天然ゼオライト担持銅(5 wt%)触媒が最も高い触媒活性を示し、N_2O は 300 ℃から分解し始め、550 ℃において完全に分解した。

1 Introduction

Natural zeolite is anticipated to have roles of pollution control catalyst due to its high surface area and chemical resistance. However, natural zeolite has low catalytic activity compared to synthetic zeolite because it is naturally formed from volcanic ash and contains impurities, nevertheless its development is desirable as cheaper pollution control catalyst compared to synthetic catalyst. In previous studies, catalytic activity of natural zeolite is improved by various modifications.

Nitrous oxide (N_2O) is one of the powerful greenhouse gases with 310 times effects of the Global Warming Potential per molecule of CO_2. Moreover, N_2O is also identified as a contributor to the destruction of ozone layer in the stratosphere [1]. The abatement of N_2O emissions from industrial plants (e.g. adipic acid production and combustion process) is probably the most feasible by implementing catalytic processes [2]. However, synthetic zeolite modified with Rh which has high decomposition activity is costly [3]. Previous study showed zeolite supported Cu catalyst was effective on N_2O decomposition [3]. Therefore, in this study, the catalytic activity of natural zeolite modified by Cu was investigated.

2 Experimental

2.1 Pretreatment

In this study, Indonesian natural zeolite (NZ) from different places (Sukabumi and Lampung) was used. They are designated as NZS and NZL, respectively. Before the experiment, NZ was crushed, washed and dried at 120℃ with particle size below 150 μm.

2.2 Catalyst preparation

2.2.1 Impregnation method (IM)

Cu/NZ (NZ=NZS,NZL) catalysts were prepared by impregnation method. In the case of preparation of Cu/NZ,NZ was impregnated in an aqueous solution of $Cu(NO_3)_2{\cdot}3H_2O$ (99.9%, Wako Co.). Each of the solutions was stirred at room temperature for 24 hours followed by 24 hours drying at 80℃. Then the catalysts were calcined at 500℃ for 5 hours under air flow. In order to reduce pressure drop, the catalysts were pelletized, crushed and sieved to between 0.71 mm to 1.00 mm pellet size. The following nomenclature for the catalyst samples are used: Cu(xwt%)/NZ where x means Cu loading levels (e.g. Cu(1wt%)/NZS means NZS with Cu loading of 1wt%).

2.2.2 Ion-exchange method (IE)

Cu-NZ (NZ=NZS,NZL) catalysts were prepared by ion-exchange method. In the case of preparation of Cu-NZ, NZ was added in an aqueous solution of

$Cu(NO_3)_2 \cdot 3H_2O$ (99.9%, Wako Co.). Each of the solutions was stirred at room temperature for one day followed by filtering using vacuuming pump and drying. Then the catalysts were calcined at 500℃ for 5 hours under air flow. The catalysts were pelletized, crushed and sieved to between 0.71 mm to 1.00 mm. Similar to impregnation method, the following nomenclature for the catalyst samples are used: Cu(xwt%)-NZ where x means Cu loading levels (e.g. Cu(1wt%)-NZS means NZS with Cu loading of 1wt%).

2.2 Catalytic activity experiment

The catalytic reaction was carried out in a fixed-bed flow reactor under atmospheric pressure. The reactant gas was prepared by mixing N_2O and He as a balance gas. The mixed gas of 1000 ppm N_2O and He was fed to the catalyst at a flow rate which corresponded to a space velocity of 16000 h^{-1}. Gas chromatography (GC323w; GL Science Co., with Porapak N, Porapak Q and Molecular Sieve 13X columns thermal conductivity detector) was used to analyze N_2O concentration.

2.3 Catalyst characterization

Characterizations of the catalysts were performed by Thermogravimetric Analysis (TG8120), X-ray Diffraction (MultiFlex), Nitrogen Adsorption (Autosorb-1), Scanning Electron Microscope (JSM-6000)-Energy dispersive X-ray analysis (MP-00040EDAP) and inductively coupled plasma atomic emission spectroscopy (SPS7800(Ⅱ)).

3. Results and discussion

3.1 Catalytic activity of catalysts prepared by impregnation method for N_2O decomposition

Figure 1 shows the catalytic activity results of Cu/NZS and Cu/NZL with different metal loading levels for the decomposition of N_2O to N_2. Horizontal axis indicates reaction temperature, and vertical axis indicates N_2O conversion. The decomposition of N_2O inside empty tube was also investigated because N_2O naturally decompose at high temperature. Compared to bare NZL and NZS which only decomposed N_2O 12% and 25% respectively at 700℃, loading of Cu on NZ improved catalytic activity. When Cu loading level was 5wt%, the highest catalytic activity for the decomposition of N_2O was achieved on NZS and NZL. Decomposition of N_2O to N_2 over Cu(5wt%)/NZS catalysts began at 300℃, and the conversion of N_2O to N_2 reached 100% at 550℃. On the other hand, decomposition of N_2O to N_2 over Cu(5wt%)/NZL catalysts began at 300℃, and the conversion of N_2O to N_2 reached 100% at 600℃. NZS showed better activity for N_2O decomposition than NZL at the same Cu loading level.

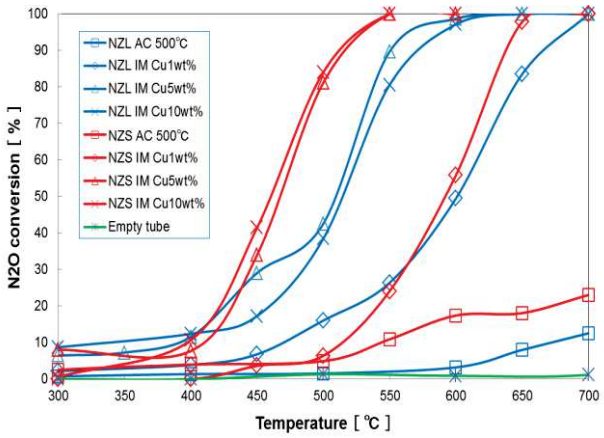

Fig. 1 Catalytic activity of catalysts prepared by impregnation method for N_2O decomposition

The BET specific surface areas of NZS and NZL were 27.9m^2/g and 37.7m^2/g, respectively. The projected area of one molecule of CuO on the surface of TiO_2 was calculated by using the radius of Cu^{2+} ion and O^{2-} ion and the bonding distance of Cu-O molecule (Cu^{2+}: 0.69Å, O^{2-}: 1.40Å, Cu-O: 1.95Å). The projected area of one molecule of CuO on the surface of TiO_2 was calculated to approximately 7.59 $Å^2$ by using the geometrical equation in Eq.1.

$$S=\int_{-1.40}^{1.335}\sqrt{1.40^2-x^2}\,dx+\int_{1.355}^{2.64}\sqrt{0.69^2-(x-1.95)^2}\,dx \quad \text{(Eq.1)}$$

When the surface of NZ was assumed to be uniform and, covered with CuO monolayer, the necessary amount of CuO molecule to make one full layer on the NZ surface could be calculated. Following the assumption, the optimum Cu loading level of Cu/NZ was calculated. They were 3.73wt% (NZS) and 4.98wt% (NZL), respectively which closely in

accordance with experimental value.

3.2 Catalytic activity of catalysts prepared by ion-exchange method for N_2O decomposition

Figure 2 shows the catalytic activity results of Cu-NZS and Cu-NZL with different metal loading levels for the decomposition of N_2O to N_2. Each sample was calcined at 500℃ for 5 h.

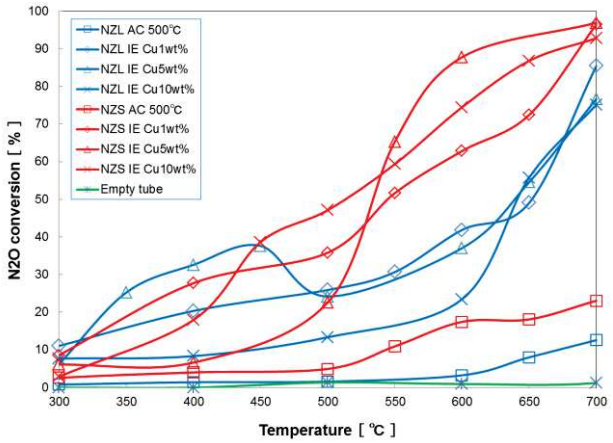

Fig. 2 Catalytic activity of catalysts prepared by ion-exchange method for N_2O decomposition

Decomposition of N_2O to N_2 over Cu(5wt%)-NZS catalysts began at 300℃, and the conversion of N_2O to N_2 reached 97% at 700℃. Also, decomposition of N_2O to N_2 over Cu(5wt%)-NZL catalysts began at 300℃, and the conversion of N_2O to N_2 reached 85% at 700℃. Similar to the result of impregnation method, NZS showed better activity for N_2O decomposition than NZL at the same Cu loading level. Compared to impregnation method, samples prepared by ion-exchange method showed lower activity. Table 1 shows the relationship between the amount of Cu added and Cu ion exchanged capacity of Cu.

Table.1 The amount and rate of Cu exchanged to each sample

sample name	Cu exchanged (mg)	Cu exchanged/ CEC (%)	Cu exchanged/Cu added (%)
SIE 1wt%	4.69	8.4	46.85
SIE 5wt%	8.37	15	16.74
SIE 10wt%	14.6	26.12	14.57
LIE 1wt%	5.96	12.34	59.64
LIE 5wt%	7.67	15.86	15.33
LIE 10wt%	22.32	46.18	22.32

From Table.1, in both NZ, there are increases in the amount of Cu exchanged by loading more Cu precursor. However, the result of the catalyst activity test showed in Fig.2 indicated that there is no significant difference between the catalyst performances.

3.3 The effect of calcination temperature on the catalytic activity for N_2O decomposition

Figure 3 shows the catalytic activity results of the calcined (AC) and uncalcined (BC) NZS and NZL for the decomposition of N_2O to N_2. Calcination temperature is 500℃ and calcination time is 5 h.

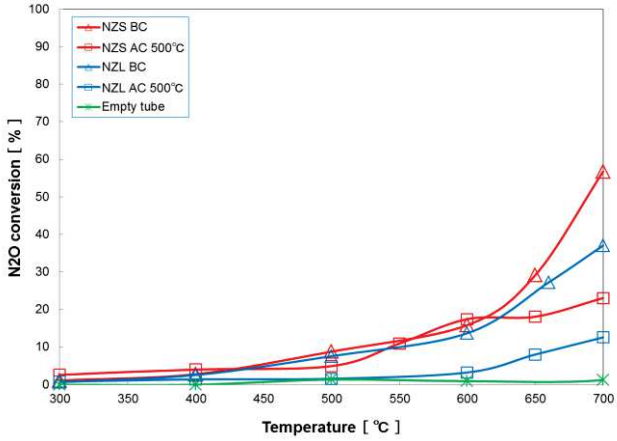

Fig. 3 The effect of calcination on catalytic activity for N_2O decomposition

It is shown that the conversion temperature of N_2O was shifted to slightly lower temperature if the sample is not calcined (BC). Decomposition of N_2O to N_2 over NZS BC began at 400℃, and the conversion of N_2O to N_2 reached 57% at 700 ℃. Also, decomposition of N_2O to N_2 over NZL BC began at 400℃, and the conversion of N_2O to N_2 reached 37% at 700℃. The specific surface area of each sample was NZL (BC): 49.41 m^2/g , NZS (BC): 31.63 m^2/g , NZL (AC): 37.67 m^2/g , and NZS (AC): 27.85 m^2/g . This result indicated that there are decreases of activity site on the surface because of decreasing of surface area by sintering. Also, structural destruction of clinoptiolite was confirmed by XRD analysis.

3.4 The effect of calcination temperature on the catalytic activity for N_2O decomposition

Figure 4 shows the catalytic activity results of NZS and NZL prepared at different calcination temperature for the decomposition of N_2O to N_2. NZS was calcined at 500℃-700℃ for 5 h.

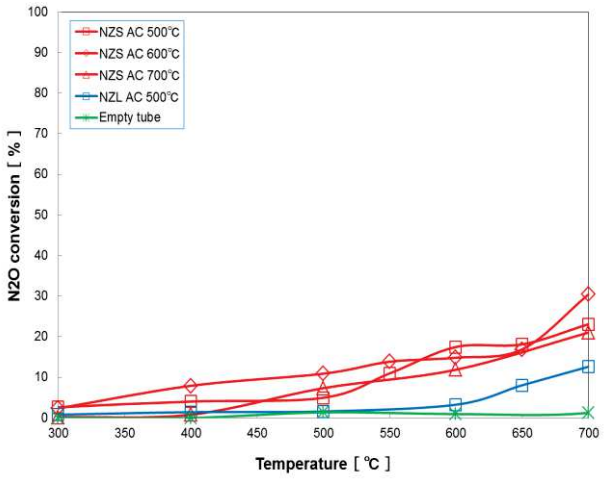

Fig. 4 The effect of calcination temperature on catalytic activity for N_2O decomposition

It is shown that the conversion of N_2O was similar despite the change in calcination temperature. The specific surface area of each sample was NZL AC 500℃: 37.67 m^2/g , NZS AC 500℃: 27.85 m^2/g , NZS AC 600℃: 20.54 m^2/g , NZS AC 700℃: 19.46 m^2/g . They indicate that specific surface area of catalyst did not affect the activity significantly for N_2O decomposition.

3.5 XRD results

Figure 5-7 show the results of XRD analysis of each catalyst.

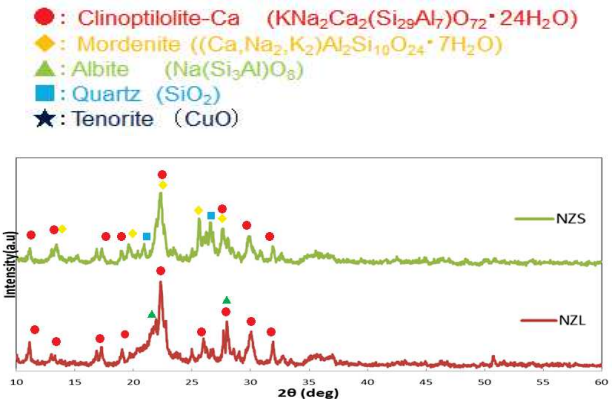

Fig. 5 XRD patterns of NZS and NZL

Figure.5 shows that NZS mainly contains clinoptilolite and mordenite and NZL contains clinoptilolite and albite. In the activity test, NZS catalysts showed higher activity than that of NZL. This might be attributed to structural differences between NZS and NZL. Mordenite structure has big and round pore (0.70 nm× 0.65 nm) in which N_2O molecule can easily enter compared to clinoptilolite (0.72 nm×0.44 nm).

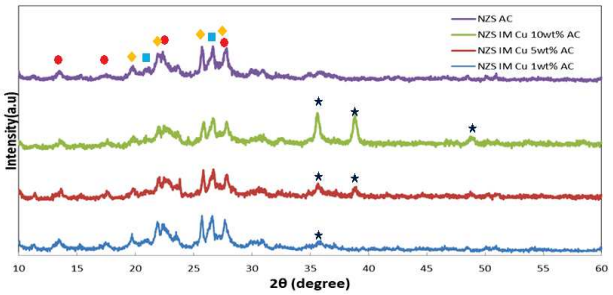

Fig. 6 XRD patterns of Cu/NZS

In Figure 6, increased intensity of CuO peak was observed with increased content of Cu. It indicated Cu exists as CuO on the surface of NZS. It also indicates that NZS is not covered with Cu completely but some of Cu sticks together as can be observed in the SEM-EDS results.

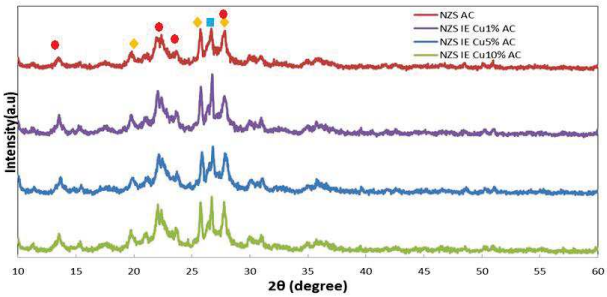

Fig. 7 XRD patterns of Cu-NZS

In Figure 7, no change in the intensity of CuO peak was observed with increased content of Cu. It indicated most of Cu exists as Cu^{2+} in the structure of NZS.

4. Conclusions

Cu(5wt%)/NZS exhibited the highest catalytic activity for N_2O decomposition, and N_2O was decomposed completely at 550℃. In the geometrical calculation, when NZ surface was covered with CuO completely, the catalytic activity for the decomposition of N_2O reached the highest value.

Catalysts prepared by impregnation method showed higher catalytic activity than the catalysts prepared by ion-exchange method. NZS with different calcination temperatures showed similar catalytic activity.

References

[1] S. Kannan, Appl. Clay Sci. 13 (1998) 347
[2] P. Esteves, Y. Wu, C. Dujardin, M.K. Dongare, P. Granger, Catal. Today 176 (2011)
[3] 岩本　正和、　他 編集、“環境触媒ハンドブック”、エヌ・ティー・エス（2001）

Water vapor resistance of Fe-Mn/$(Ti,Zr)_2O_4$ for NO reduction

Student Number: 14M18170　Name: Tomoaki Mitsui　Supervisor: Hirofumi Hinode

Fe と Mn を担持した$(Ti,Zr)_2O_4$複合触媒の NO 選択還元と耐水蒸気性

三井　智章

本研究では、排気ガス内に混在する炭化水素のプロペンを還元剤とした NO の選択還元（HC-SCR）に適応した触媒の実用化に向け、活性と共に耐水蒸気性の向上を目的とした。含侵法、機械的混合法、そして沈着沈殿法によって Fe と Mn を担体の$(Ti,Zr)_2O_4$複合触媒上に担持し、活性及び特性の変化について検討した。3 通りの担持方法全てで担体の$(Ti,Zr)_2O_4$より活性が低下してしまったが、沈着沈殿法で調製した Fe-Mn/$(Ti,Zr)_2O_4$-DP 触媒が特に高い耐水蒸気性を示した。

1. Introduction

Nitrogen oxides (NO_x) are mainly consists of nitric oxide (NO) and nitrogen dioxide (NO_2). NO_x causes atmospheric environmental problems such as photochemical smog, acid rain, ozone depletion and greenhouse effects. Furthermore, presence of nitrogen oxides in the atmosphere might cause problems to human health such as respiratory system illness. Most of the NO_x are emitted from automobiles (52%) and fixed sources (35%) using fossil fuels.

Nowadays, three-way catalysts (TWC) are used to reduce NO_x from automobiles. TWC can reduce NO_x with high efficiency at specific air-fuel ratio (A/F=14.7). However, the development of lean-burn engines (A/F = 20~60) that have higher fuel economy and cleaner emissions requires another type of catalyst for NO_x reduction. One common method to reduce NO_x in exhaust gas is selective catalytic reduction of NO using hydrocarbon as reducing agent (HC-SCR of NO) [1]. Among several applicable methods, HC-SCR using hydrocarbon contained in the exhaust is currently the most studied technology for NO_x reduction.

The main reactions taking place during SCR process are the following:

$$2NO+O_2 \rightarrow 2NO_2 \quad (1)$$

$$3NO+3NO_2+C_3H_6 \rightarrow 3N_2+3CO_2+3H_2O \quad (2)$$

Previous study reported that $(Ti,Zr)_2O_4$ composite used as support material exhibited higher catalytic activity towards HC-SCR of NO when compared to bare TiO_2 [2]. $(Ti,Zr)_2O_4$ is also known of its high surface area and high mechanical strength, and is widely used in many reactions as a catalyst [3].

Another study demonstrated that Mo+$(Ti,Zr)_2O_4$ showed high activity (80% NO removal), however the catalyst was deactivated by the presence of water vapor [4]. On the other hand, Fe-Mn/TiO_2 shows high activity and high water vapor resistance in selective catalytic oxidation of NO. Fe has high water vapor and SO_x resistance and Mn has high activity and selectivity in NO_x reduction [5]. Thus loading Fe and Mn on $(Ti,Zr)_2O_4$ might increase catalyst activity and water vapor resistance.

Therefore, in this study, the catalytic activities of $(Ti,Zr)_2O_4$ impregnated, manual mixed and deposited-precipitated with metal oxides were investigated. Then, catalytic activity and water vapor resistance of catalysts were compared to determine the best method and the optimum ratio of the prepared catalyst for NO_x reduction.

2. Experimental

2.1 Materials

$(Ti,Zr)_2O_4$ catalyst was prepared by co-precipitation method using $Zr(NO_3)_2 \cdot 2H_2O$ and $[(CH_3)_2CHO]_4Ti$ as precursors with the same molar ratio of Ti and Zr. First, $Zr(NO_3)_2 \cdot 2H_2O$ was dissolved in deionized water with continuous stirring and the pH was controlled by addition of HNO_3 (pH=0.5-1.0). Then $[(CH_3)_2CHO]_4Ti$ was added to the solution and the pH was changed by addition of NH_3 solution (pH=9-11). On each steps, the mixed solution was stirred for 30 minutes. The resulting mixture was aged for 8 h, filtered, and dried at 100℃ overnight and then calcined at 550℃ in air for 4 h.

Fe-Mn/$(Ti,Zr)_2O_4$-IMP catalyst was prepared by impregnation (IMP) method using $Fe(NO_3)_3 \cdot 9H_2O$, $Mn(NO_3)_2 \cdot 6H_2O$ and $(Ti,Zr)_2O_4$ as precursors. $Fe(NO_3)_3 \cdot 9H_2O$, $Mn(NO_3)_2 \cdot 6H_2O$ and $(Ti,Zr)_2O_4$ were added to deionized water in a beaker with steady stirring at room temperature for 24 h, then dried at 100℃ overnight, and calcined at 550℃ in air for 3 h.

$Fe_2O_3+Mn_2O_3+(Ti,Zr)_2O_4$-MM catalyst was prepared by manual mixing (MM) using Fe_2O_3, MnO_2 and $(Ti,Zr)_2O_4$. Fe_2O_3, MnO_2 and $(Ti,Zr)_2O_4$ were mixed together manually with ethanol, then dried, and

calcined at 550℃ in air for 3 h.

Fe-Mn/$(Ti,Zr)_2O_4$-DP catalyst was prepared by deposition precipitation (DP) method using $Fe(NO_3)_3 \cdot 9H_2O$, $Mn(NO_3)_2 \cdot 6H_2O$ and $(Ti,Zr)_2O_4$ as precursors. $Fe(NO_3)_3 \cdot 9H_2O$, $Mn(NO_3)_2 \cdot 6H_2O$ and $(Ti,Zr)_2O_4$ were added to deionized water in a beaker and the pH was changed by addition of ammonium carbamate (1 mol/L) until pH = 7 with steady stirring at room temperature for 1 h then dried at 100℃ overnight, and calcined at 550℃ in air for 3 h.

2.2 Catalytic Activity Test

The HC-SCR activity of prepared catalysts was determined in a continuous fixed-bed flow reactor. The reactant gas was composed of 1500 ppm NO, 10% O_2, 1500 ppm C_3H_6 and He as a balance gas. 1.0~1.5 g of catalyst was used with a corresponding space velocity of 13000 h^{-1}. All prepared catalysts were pelletized, crushed and sieved to 0.71-1.00 mm. The temperature was changed stepwise from 150℃ to 500℃ except for $(Ti,Zr)_2O_4$.

The NO and NO_2 concentrations were analyzed by NO_x analyzer (Shimadzu, NOA-7000) while CO_2 was analyzed using gas chromatograph with thermal conductivity detector (GL Science, GC-3200). The catalysts were characterized by TG-DTA, XRD, N_2 adsorption (Autosorb 1MP/TSU, BET analysis) and SEM-EDS.

3. Results and Discussion

3.1 Catalytic Activity

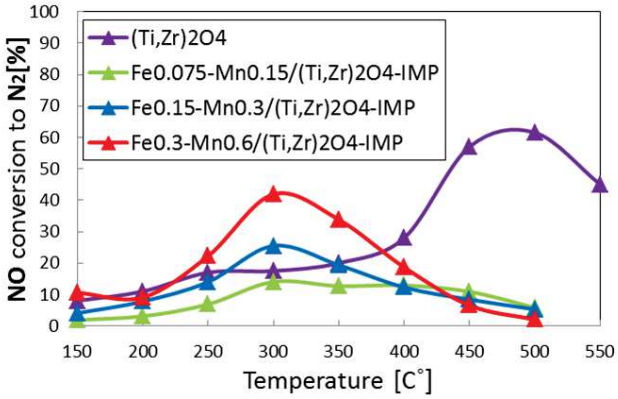

Fig.1 Catalytic activity of Fe-Mn/$(Ti,Zr)_2O_4$-IMP catalyst for the reaction of NO to N_2 using C_3H_6 as a reductant

Fig.1 shows the conversion of NO to N_2 over Fe-Mn/$(Ti,Zr)_2O_4$ catalyst by IMP method with Fe and Mn loading levels of 0.075-0.3 and 0.15-0.6 molar ratios, respectively, compared to $(Ti,Zr)_2O_4$ catalyst. Metal loaded catalyst showed lower catalytic activity than unloaded $(Ti,Zr)_2O_4$ catalyst. However, among IMP catalysts, the higher the loading metal content, the higher the activity of catalyst. Furthermore, addition of Fe and Mn have lowered the required reaction temperature for the reaction to proceed.

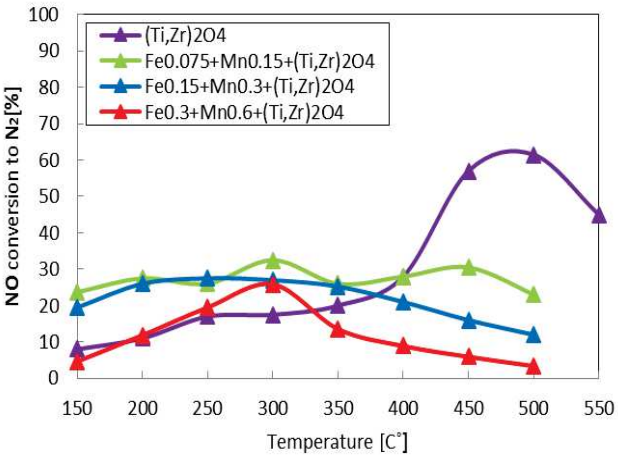

Fig.2 Catalytic activity of Fe_2O_3+Mn_2O_3+$(Ti,Zr)_2O_4$ catalyst for the reaction of NO to N_2 using C_3H_6 as a reductant

Fig.2 shows the conversion of NO to N_2 over Fe_2O_3+Mn_2O_3+$(Ti,Zr)_2O_4$-MM catalyst by MM method. MM catalysts show decreasing activity as the loading metal content increased. MM catalysts have wide temperature zone at which it shows activity. However, MM method does not lead to activity improvement, similar to IMP method.

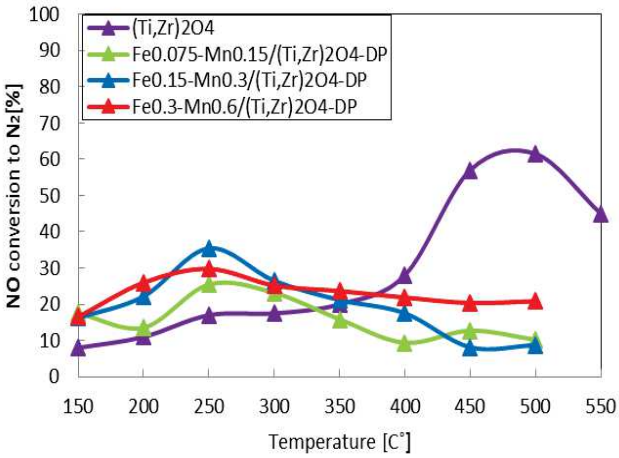

Fig.3 Catalytic activity of Fe-Mn/$(Ti,Zr)_2O_4$-DP catalyst for the reaction of NO to N_2 using C_3H_6 as a reductant

Fig.3 shows the conversion of NO to N_2 over Fe-Mn/$(Ti,Zr)_2O_4$ catalyst by DP method. DP method does not lead to activity improvement, similar to the other 2 methods. Differences with the other 2 methods are that loading levels do not give significant effect to activity and that the temperature of activity is 50℃ lower than the other 2 methods.

3.2 Effect of Water Vapor

In this section, only the result of catalysts which are loaded with 0.3 of Fe and 0.6 of Mn for each loading methods are shown.

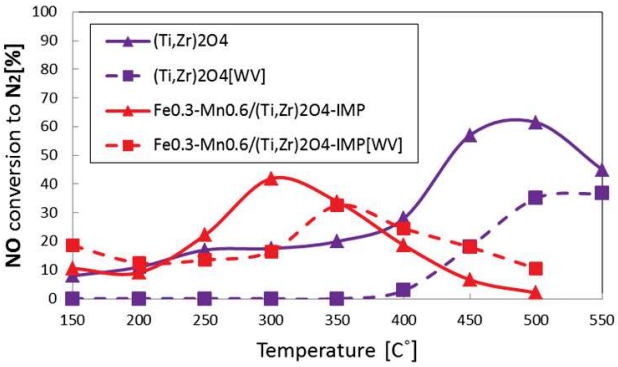

Fig.4 Activity comparison of Fe0.3-Mn0.6/(Ti,Zr)$_2$O$_4$-IMP and Fe0.3-Mn0.6/(Ti,Zr)$_2$O$_4$-IMP [WV] for the reaction of NO to N$_2$ using C$_3$H$_6$ as a reductant (WV means Water Vapor was introduced to the system)

Fig.4 shows the effects of water vapor on Fe0.3-Mn0.6/(Ti,Zr)$_2$O$_4$-IMP catalyst. In the system where water vapor exists, the peak of NO reduction shifts to higher temperature.

Fe0.3-Mn0.6/(Ti,Zr)$_2$O$_4$-IMP catalyst shows high water vapor resistance which is 77.6% and has activity throughout the temperature range of the experiment compared to (Ti,Zr)$_2$O$_4$ catalyst which shows no activity between 150~350℃.

Fe0.3-Mn0.6/(Ti,Zr)$_2$O$_4$-IMP catalyst shows 32% No to N$_2$ conversion which is the highest activity among 3 loading methods tested with 10% water vapor.

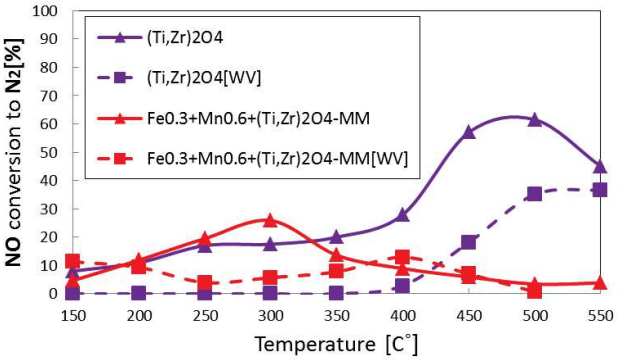

Fig.5 Activity comparison of Fe0.3+Mn0.6+(Ti,Zr)$_2$O$_4$-MM and Fe0.3+Mn0.6+(Ti,Zr)$_2$O$_4$-MM[WV] for the reaction of NO to N$_2$ using C$_3$H$_6$ as a reductant

Fig.5 shows the effects of water vapor to Fe0.3+Mn0.6+(Ti,Zr)$_2$O$_4$-MM catalyst. Similarly, the peak of NO reduction shifts to higher temperature and Fe0.3+Mn0.6+(Ti,Zr)$_2$O$_4$-MM catalyst shows 50% water vapor resistance. MM catalysts have wide temperature zone which shows activity despite the presence of water vapor.

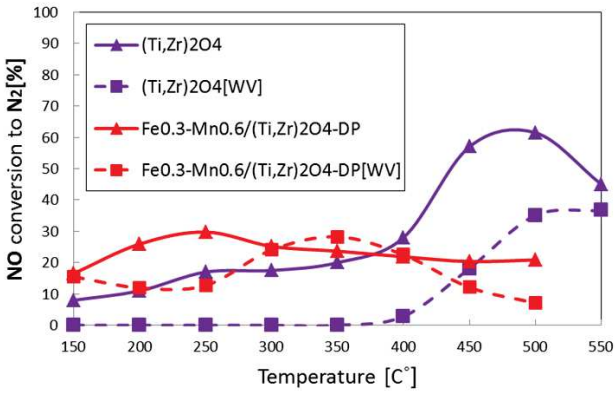

Fig.6 Activity comparison of Fe0.3-Mn0.6/(Ti,Zr)$_2$O$_4$-DP and Fe0.3-Mn0.6/(Ti,Zr)$_2$O$_4$-DP [WV] for the reaction of NO to N$_2$ using C$_3$H$_6$ as a reductant

Fig.6 shows the effects of water vapor to Fe0.3-Mn0.6/(Ti,Zr)$_2$O$_4$-DP catalyst. Like in IMP and MM methods, the peak of NO reduction shifts to higher temperature. Fe0.3-Mn0.6/(Ti,Zr)$_2$O$_4$-DP catalyst has the highest water vapor resistance which is 95.0%.

Table.1 Comparison of water vapor resistance

	Fe0.075-Mn0.15	Fe0.15-Mn0.3	Fe0.3-Mn0.6
IMP	63.1%	65.5%	77.6%
MM	45.2%	60.9%	50.0%
DP	59.6%	76.8%	95.0%

Table.1 shows the comparison of water vapor resistances of all catalyst. Here, water vapor resistance is defined by max NO reduction activity [WV] divided by max NO reduction activity. For comparison, water vapor resistance of (Ti,Zr)$_2$O$_4$ catalyst is 59.7%. Table.1 showed that compared to (Ti,Zr)$_2$O$_4$ catalyst two of the DP catalysts have higher water vapor resistance while one has similar resistance. DP catalysts also showed the highest water vapor resistance. All IMP catalysts have higher resistance, and one of MM catalysts has a higher water vapor resistance. Therefore, it is concluded that the water vapor resistance performance of catalysts is as follows, DP catalysts > IMP catalysts > MM catalysts.

3.3 Catalyst Characterization

TG-DTA, XRD, N$_2$-adsorption method and SEM-EDS are used to characterize each catalyst. Depending on the loading methods and levels, characteristics varies. In this section, the significant characteristics of the catalysts are discussed. It is thought that characteristic which affects activity of NO reduction mostly is shown by SEM-EDS analysis data.

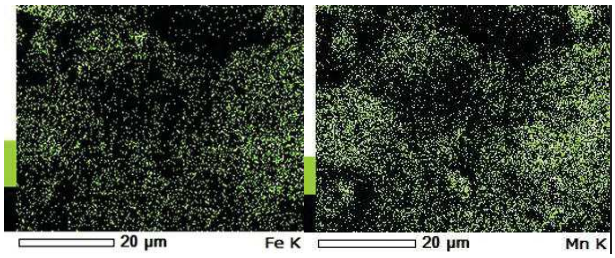

Fig.7 EDS data of IMP catalysts about Fe and Mn

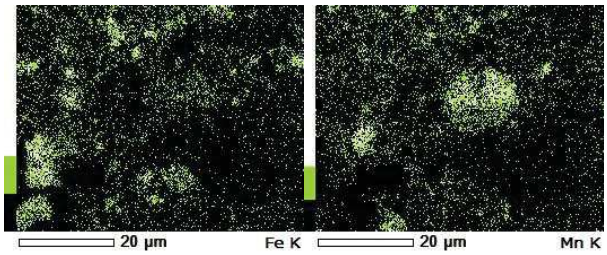

Fig.8 EDS data of MM catalysts about Fe and Mn

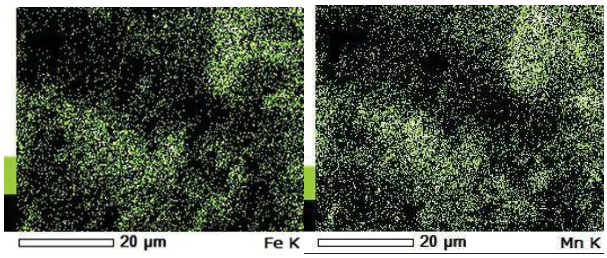

Fig.9 EDS data of DP catalysts about Fe and Mn

Fig.7 to Fig.9 show Fe and Mn distribution on support surface for each of three loading methods. From Fig.7, Fe and Mn are highly dispersed but concentrations of Fe and Mn on the surface of the support are low from IMP catalysts. From Fig.8, Fe and Mn are concentrated locally for MM catalysts. In other words, dispersion of Fe and Mn is the poorest in this method. From Fig.9, Fe and Mn are highly dispersed and concentrations of Fe and Mn on support surface are the highest for DP catalysts.

These characteristics affect the activity in the presence of water vapor, however, it does not affect the activity when the water vapor is not present.

In general, it is said that the higher the specific surface area the catalysts have, the higher the catalysts activity. However, according to the data in Table.2, specific surface area is not connected to NO reduction activity in this study.

For example, IMP catalyst that has the highest activity has low specific surface area. This is because the pores were filled by Fe oxides and Mn oxides, as a result of Fe ions and Mn ions penetration in pores, therefore the specific surface area decreased.

Table.2 Comparison of specific surface area

Sample	Surface Area
$(Ti,Zr)_2O_4$	240.3 m^2/g
Fe0.075-Mn0.15/$(Ti,Zr)_2O_4$-IMP	16.5 m^2/g
Fe0.15-Mn0.3/$(Ti,Zr)_2O_4$-IMP	16.9 m^2/g
Fe0.3-Mn0.6/$(Ti,Zr)_2O_4$-IMP	90.4 m^2/g
Fe0.075+Mn0.15+$(Ti,Zr)_2O_4$-MM	210.9 m^2/g
Fe0.15+Mn0.3+$(Ti,Zr)_2O_4$-MM	169.6 m^2/g
Fe0.3+Mn0.6+$(Ti,Zr)_2O_4$-MM	177.4 m^2/g
Fe0.075-Mn0.15/$(Ti,Zr)_2O_4$-DP	160.0 m^2/g
Fe0.15-Mn0.3/$(Ti,Zr)_2O_4$-DP	155.4 m^2/g
Fe0.3-Mn0.6/$(Ti,Zr)_2O_4$-DP	151.1 m^2/g

4. Conclusions

As Fe and Mn have ability to improve low temperature activity, activity became better at low temperature by adding Fe and Mn. However, maximum activity of Fe-Mn/$(Ti,Zr)_2O_4$ catalyst did not exceed maximum activity of $(Ti,Zr)_2O_4$ catalyst for all loading methods.

Water vapor resistance in NO reduction was increased by adding Fe and Mn. The best water vapor resistance of Fe-Mn/$(Ti,Zr)_2O_4$ is 95.0% (Fe0.3-Mn0.6/$(Ti,Zr)_2O_4$-DP catalyst) compared to water vapor resistance of $(Ti,Zr)_2O_4$ (59.7%).

The order of water vapor resistance is as follows, DP catalysts > IMP catalysts > MM catalysts.

The most important factor influencing the activity of catalyst in the presence of water vapor is dispersion and concentration of loaded metals on support surface. Specific surface area did not affect the activity significantly.

References

[1] R.Burch et al, Appl.Catal.B, 11, (1997) 207
[2]M.Haneda et al, Catal. Today, 42, 127-135 (1998)
[3]B.M.Reddy et al, Appl. Catal. A, 228 (2002) 269-278
[4]Kim Dongil, Master Thesis, Tokyo Institute of Technology (2014)
[5]Mengying Zhang, et al, Appl. Surface Science 300 (2014) 58-65

STUDY OF CONSTRUCTION PERFORMANCE AND DURABILITY OF SEAWATER MIXED ANTI-WASHOUT CONCRETE IN COLD ENVIRONMENT

Student ID: 14M18193 Name: Yuma YOSHIDA Supervisor: Nobuaki OTSUKI

寒冷環境における海水練り水中不分離性コンクリートの施工性能と耐久性の検討

吉田　祐麻

本論文では，年間の平均気温が氷点に近い寒冷環境において水中不分離性コンクリートの練混ぜ水に海水を用いた場合の，施工性能（強度，流動性）と塩害に対する耐久性の基礎検討を行った．強度については材齢初期の硬化促進があり，寒冷環境においてはその効果がより顕著になるため，海水の練り混ぜ水への利用は有利となった．耐久性については水中打設時に多量の塩化物イオンが鉄筋に付着することから，腐食速度に対する海水練りの影響が小さくなった．また，寿命を算出したところ，寒冷環境における海水練りした水中不分離性コンクリートのかぶり 70mm の RC の場合 32.5 年となった．そのため，本研究では寒冷地における水中不分離性コンクリートへの海水利用は十分可能であると結論付けた．

1. Introduction

1.1 Background

Recent years, a long term plans to exploit the vast natural gas are scheduled in Arctic region, for example Yamal peninsula, Russia, and large amount of concrete will be used. Arctic region has less rainfall and cold temperature, and construction sites exist in backcountry. These conditions are disadvantageous for water procurement. Because LNG plant site is at the seaside, seawater is easy to get. So, if seawater is available to use, construction cost will be reduced. However, seawater use as mixing water of concrete is prohibited because of containing chloride ion which makes reinforcement corrode.

Seawater using affects to some property of concrete. In term of construction performance, several ions which are included in seawater accelerate the hardening of cement. Consistency of seawater mixed concrete tends to be worse. In term of durability, according to the Arrhenius theory, temperature affects to speed of chemical reaction and diffusion, in brief low temperature makes them slow. It is believed that this theory also can be applied to the corrosion of reinforcement, so low temperature condition contributes to prevention of corrosion. In past studies, the temperature dependency of corrosion is obtained. But, it has been studied only at temperatures above room temperature (20℃) [1].

1.2 Objectives

In this study, the target is underwater anti-washout concrete, and following objectives have been set for discussing the use of seawater as mixing water in cold environment. In this study, cold environment means 0℃ which is the average temperature of seawater around the Yamal peninsula.

1. To clarify the construction performance (in this study, compressive strength and consistency) of seawater mixed anti-washout concrete in cold environment.
2. To clarify the durability against chloride attack of seawater mixed anti-washout concrete in cold environment.

2. Experiment outlines

2.1 Compressive strength test

The φ50x100mm cylinder mortar specimens are used for measuring the compressive strength. The mix proportion have 2 levels of mixing water (freshwater, seawater), 3 levels of cement (OPC, BFC, FA mix), and each specimens are cured in 2 temperatures (0℃, 20℃).

While the casting, shown as Fig.1, mold is set under the artificial seawater whose water level is set above the 10cm of top of mold, fall the mortar into mold by spoon, and cast without tamping and vibration. Each specimen is cured in the artificial seawater until the test age. Temperature is controlled while the casting and curing. The tests are done at the time of 3, 5, 7, 14, 28, and 91 day age.

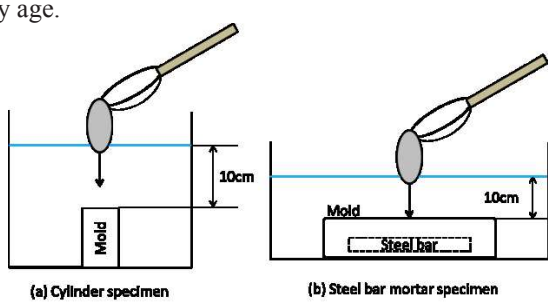

Fig.1 Casting of anti-washout mortar under water

2.2 Consistency test

OPC mortar whose mix proportion have 2 levels of mixing water (freshwater, seawater) and 3 levels of water content (350, 365, 380 kg/m^3) are used. For control the temperature, flow test was done in the water. From the result of preliminary experiment, there was no significant difference in the in water and in the air.

2.3 Cl^- diffusion coefficient calculation

The φ50x100mm cylinder mortar specimens are used for calculating the chloride ion diffusion coefficient. The mix proportions have 2 levels of mixing water (freshwater, seawater). Temperature is controlled while casting-curing and exposure (20℃and 20℃, 20℃and 0℃, 0℃and 0℃). Cement type is only OPC. Specimens

were casted under the artificial seawater same as section 2.1 specimens.

Specimens are coated with epoxy resin except top surface, exposed to artificial seawater which temperature is controlled among 3 months.

2.4 Oxygen permeability calculation and corrosion behavior measurement

The steel bar mortar specimens are used for oxygen permeability calculation and corrosion behavior measurement. φ9x100mm SR235 steel bar is set in the center with cover depth is 10mm. To control the cover depth, sides are covered with epoxy resin. Specimens were casted as section 2.1 specimens (steel bars were once exposed to seawater).

The mix proportion have 2 levels of mixing water (freshwater, seawater), 3 levels of cement (OPC, BFC, FA mix), and each specimens are cured in 2 temperatures (0℃, 20℃). W/C is 50% which is the maximum while use in marine environment.

Specimens are exposed artificial seawater which temperature is controlled and measurement by corrosion monitor will be done continuously among the 5 months. Until the finish of exposure, self-potential and polarization resistance was measured in each month. After the exposure, the polarization curve for oxygen permeability, Cl^- content on steel bar and mortar matrix are measured.

3. Performance of anti-washout concrete mixed with seawater in cold environment

3.1 Compressive strength

Fig.2 shows the strength development and 91days compressive strength. According to time series of 0℃ case, strength increases continually. This indicates that frost of concrete did not occur.

In early age, cases of seawater mixed show higher strength than freshwater. However, difference of mixing water did not appear at the 91 day.

At 91 material day, difference of strength between 20℃ and 0℃ is 2-6N/mm^2, the hydration delay of cement types which is added admixture was large compared with OPC. However every mix proportions in 0℃ have more over 20 N/mm^2 strength.

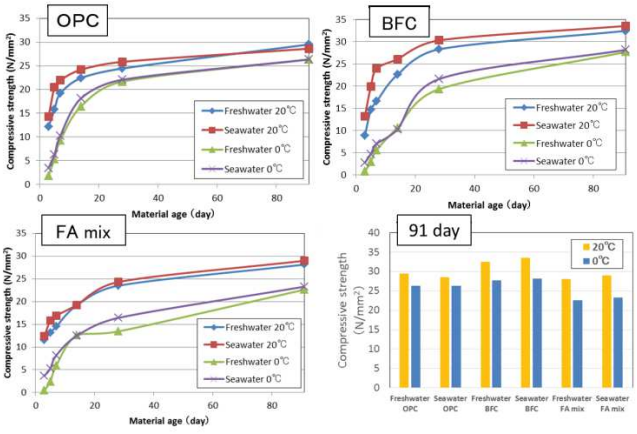

Fig.2 Result of compressive strength test

To evaluate the seawater effect of strength development promotion in cold environment, strength prediction curve were made with using the maturity (Eq.1) and Gomperz curve (Eq.2).

$$M = \sum (T + 10) \cdot \Delta t \qquad \text{(Eq.1)}$$

$$f_c' = F \exp\{-\alpha \exp(-\beta \log M)\} \qquad \text{(Eq.2)}$$

Note: M :Maturity (℃・day),
Δt : Material age (day),
T : Temperature (℃),
f_c' : Compressive strength (N/mm^2),
F : Ultimate strength
α, β : Constant

From this strength prediction curve, the required days for remolding (strength for remolding is supposed 14N/mm^2) were obtained. Table.1 shows the result of them. From the result, seawater use makes required days 3-6 days faster than freshwater use in cold environment. So, seawater use is advantageous for strength development in cold environment.

Table.1 Required day for remold in 0℃

Cement Type	Mixing water	Day	Difference of mixing water
OPC	Fresh	13.4	3.3
	Sea	10.2	
BFC	Fresh	17.5	6.2
	Sea	11.4	
FA Mix	Fresh	18.6	3.0
	Sea	15.5	

3.2 Consistency

Fig.3 shows the flow value of each experiment case. From this result, both of seawater use and cold temperature contribute to be worse consistency. However, compared with seawater use 0℃ and freshwater 20℃, the same flow value can be obtained by way of water content increase 24kg/m^3. In term of consistency, seawater can be used in cold environment with setting the design of mix proportion.

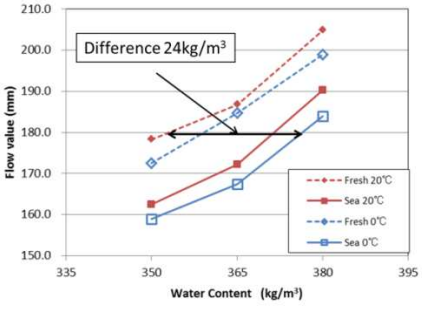

Fig.3 Flow Value

4. Diffusion property of anti-washout concrete mixed with seawater in cold environment

4.1 Cl^- diffusion coefficient

To clarify chloride ion diffusivity, with using specimens shown in section 2.3. The way to evaluation is conform to Japan Society of Civil Engineers JSCE-G 572-2013. And the Fick's diffusion equation was used. Diffusion coefficient was calculated by fitting Cl^- distribution data to the solution of Fick's diffusion equation (Eq.3).

$$C(x,t) = C_0\left\{1 - erf\left(x/2\sqrt{D_{ap}\cdot t}\right)\right\} \quad \text{(Eq.3)}$$

Note: $C(x,t)$: Cl^- content (kg/m^3) at x (cm) from the surface after t (year) exposure time,
C_0 : Cl^- content (kg/m^3) at the surface
D_{ap} : Cl^- diffusion coefficient (cm^2/year)

As shown in Fig.4, chloride ion diffusion coefficient in cold environment is much lower than 20℃, about 4 times. And seawater use makes chloride ion diffusion coefficient lower than freshwater. It might be that initial chloride ion content induced by seawater decrease the difference of chloride ion concentration between mortar and exposure environment. In cold environment, the difference of coefficient between freshwater and seawater is small.

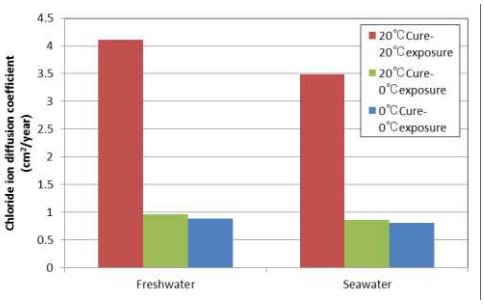

Fig.4 Cl- diffusion coefficient

4.2 O_2 permeability

To clarify oxygen permeability, limit current density obtained from cathodic polarization curve of steel bar in mortar specimens. Oxygen permeability is obtained from the Faraday's law (Eq.4).

$$J = -i_{lim}/nF \quad \text{(Eq.4)}$$

Note: J : Oxygen permeability (mol /cm^2 ・ sec),
i_{lim} : Limit current density (μA /cm^2),
n : Number of electron exchanged (= 4),
F : Faraday constant (= 96500 C/mol)

As shown Fig.5, oxygen permeability in cold was very low compared with 20℃. Then cold environment contribute to delay the steel bar corrosion.

In OPC case, seawater use makes oxygen permeability high, but in BFC and FA case, seawater use makes oxygen permeability low. This trend is the same between 20℃ and 0℃.

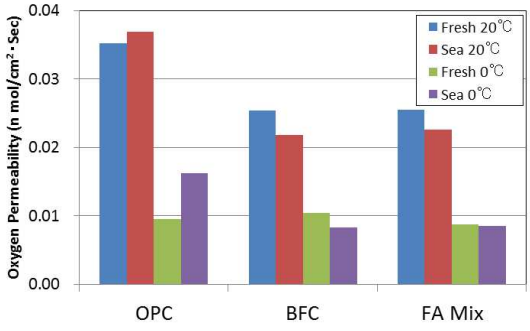

Fig.5 Oxygen permeability

To check the effect of temperature to oxygen permeability, Arrhenius plot shown in Fig.6 was made. From the slope of plot, activation energy was obtained with using (Eq.5).

$$E_a = -A\times(R/\log_{10} e) = -4.58\times A \quad \text{(Eq.5)}$$

Note: E_a : Activation energy (kcal/mol),
A : Slope of the plot,
R : Gas constant (= 1.99×10^3 kcal/K・mol),

As shown in Fig.6, in this study, logarithm of permeability and reciprocal of temperature shows the linear relation and calculated activation energy was about 13-20kcal/mol.

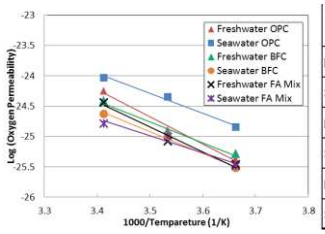

Mix Proportion	Activation Energy (kcal/mol)
Freshwater OPC	20.60
Seawater OPC	14.92
Freshwater BFC	15.87
Seawater BFC	16.36
Freshwater FA Mix	18.70
Seawater FA Mix	12.91

Fig.6 Arrhenius plot and activation energy (Oxygen permeability)

This value is relatively higher than previous study (15℃-35℃) [2] but roughly match. Arrhenius law was also able to be applied in case of anti-washout concrete in cold environment.

5. Corrosion behavior of anti-washout concrete mixed with seawater in cold environment

Until the end of exposure, corrosion current density (I_{corr}) values of every specimen are lower than 0.2μA/cm^2 (value of threshold of corrosion start proposed by CEB).

Fig.7 shows the corrosion rate at the end of exposure. This figure indicates the difference of temperature is very large compared with difference of mixing water. BFC and FA mix shows the higher value than OPC.

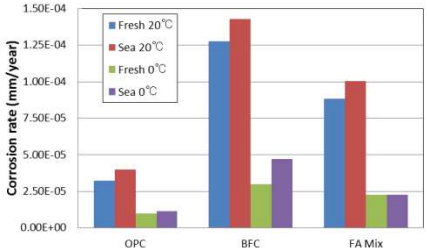

Fig.7 Comparison of corrosion rate (5month)

To clarify this result, chloride ion content on steel bar and in mortar matrix was compared in Fig.8. According to the correlation between I_{corr} and chloride content on steel bar was higher than and in mortar matrix.

While the casting of anti-washout concrete, arranged steel bars are dunk into seawater directly. So, much chloride ion is on the surface of steel bar.

Average of chloride content on steel bar (about 13μg/cm^2) was not changed in each mix proportion. This is why difference of corrosion behavior between freshwater mixed and seawater mixed was small.

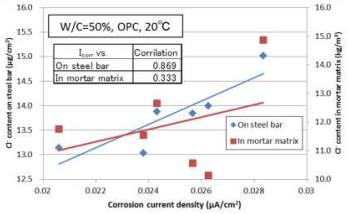

	Correlation I_{corr} vs.	
	Cl^- on steel bar	In mortar
OPC 20℃	0.869	0.333
OPC 0℃	0.868	0.631
BFC 20℃	0.906	0.045
BFC 0℃	0.903	0.099
FA Mix 20℃	0.407	0.117
FA Mix 0℃	0.304	0.030

Fig.8 Comparison of Cl^- effect (on steel vs. in mortar)

To check the effect of temperature to corrosion rate, Arrhenius plot shown in Fig.9 was made. From the slope of plot, activation energy was obtained with using (Eq.5).

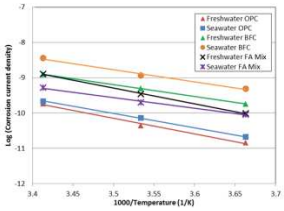

Mix Proportion	Activation Energy (kcal/mol)
Freshwater OPC	20.28
Seawater OPC	18.61
Freshwater BFC	15.36
Seawater BFC	15.85
Freshwater FA Mix	20.27
Seawater FA Mix	13.84

Fig.9 Arrhenius plot and activation energy (Corrosion current density)

As shown in Fig.10, the activation energy of oxygen permeability and corrosion rate is almost the same. This indicates, corrosion rate reaction is oxygen rate-limiting.

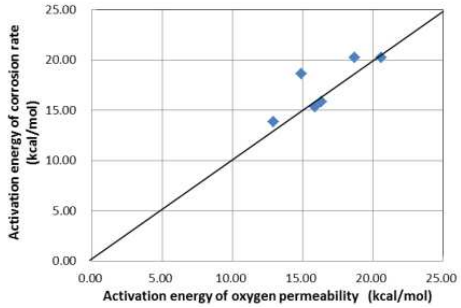

Fig.10 Comparison of activation energy

6. Lifetime prediction of anti-washout RC mixed with seawater in cold environment

As shown in Fig.11, deterioration of RC divided some stage. And critical factor is different in each period. In this study, lifetime is defined the sum of incubation period and propagation period.

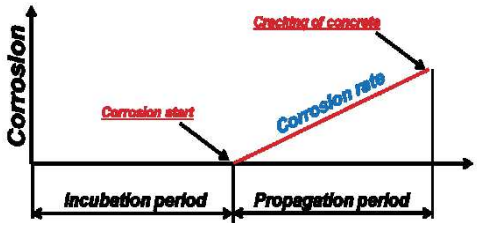

Fig.11 Concept of RC lifetime in term of corrosion

Incubation period is controlled by chloride ion diffusion. For calculation of lifetime of this period, chloride ion diffusivity coefficient which obtained in section 4.1 and chloride ion concentration around the steel bar obtained in chapter 5 are used. In this study, corrosion threshold chloride ion content was not obtained, so latter value was evaluated on the safe side.

Propagation period is controlled by oxygen permeability. For calculation of lifetime of this period, amount of corrosion product for cracking proposed by Yokozeki[3], and corrosion rate during propagation period which is calculated by oxygen permeability obtained from section 4.2 and relationship between oxygen permeability and corrosion rate[4].

Table.2 shows the result of lifetime calculation. As a result, lifetime of seawater mixed anti-washout RC is 32.5 years in cold environment. This is enough long to use. Because of initial Chloride ion content, incubation period of seawater mixed is shorter than freshwater mixed. But, lifetime of propagation period between freshwater mixed and seawater mixed is small.

If more lifetimes are demanded, by changing the cement type from OPC to BFS or FA mix in the mix proportion design propagation period can be longer as shown Table.2, or W/C decreasing because of oxygen permeability decreasing.

Table.2 Result of the lifetime prediction (Cover depth = 70mm)

	Freshwater mixed			Seawater Mixed		
	Incubation	Propergation	Inc + Pro	Incubation	Propergation	Inc + Pro
OPC 20℃	13.5	3.5	17.0	5.0	3.4	8.3
OPC 0℃	61.8	13.2	75.0	20.9	11.5	32.5
BFC 0℃		12.1			15.4	
FA 0℃		14.5			14.8	

7. Conclusion

In this thesis, the performance (compressive strength and consistency) and durability against chloride attack are clarified. From the experiments, conclusions are obtained as follows;

1. Even in cold environment, anti-washout mortar has enough strength (over 20N/mm^2). Because seawater use promotes strength development, required day for remold of seawater mixed is more 3 days faster than freshwater mixed.
2. For consistency, both of cold environment and seawater use makes consistency bad. However, with increasing water content about 24kg/m^3, the same consistency of freshwater mixed in 20℃ can be obtained in case of seawater mixed in 0℃.
3. Difference of corrosion rate after 5 months exposure between freshwater mixed and seawater mixed was small, because steel bar is exposed to seawater while the casting in case of anti-washout concrete.
4. Lifetime of seawater mixed anti-washout RC is 32.5 years in cold environment. Especially, difference of lifetime of propagation period between freshwater mixed and seawater mixed is small.

From these results, seawater can be used as mixing water of anti-washout concrete in cold environment.

8. Reference

[1] Takahiro Nishida, “Influence of Temperature on Deterioration Process of Reinforced Concrete Members Due to Steel Corrosion, Doctoral thesis, 2006

[2] C. L. Page et al., “Kinetics of oxygen diffusion in hardened cement pastes”, Journal of Materials Science 22, pp.942-946, 1987

[3] K. Yokozeki et al., “A Rational Model to Predict Service Life of RC Structures in Marine Environment”, Forth CANMET/ACI International Conference on Durability of Concrete 1, 1997

[4] S. Maruyama, “Influence of Temperature and Cement on Corrosion Rate of Steel Bar under Carbonation”, Master thesis of Tokyo Institute of Technology, 2004 (in Japanese)

Design and control of switching regulator for energy harvesting considering output characteristic of generator

Student Number: 11M18048　Name: Daisuke IWASAKI　Supervisor: Kunio TAKAHASHI

発電機の出力特性を考慮したエネルギーハーベスティング用スイッチングレギュレータの設計および制御方法

岩崎 大輔

本論文では電力源に10V 以下の DC と AC の発電機を用い、一定の回転速度における電流と電圧特性を実験的に計測することにより発電機の最大出力点の推定を行った。更に，等価回路を提案し，発電機内部の抵抗とインダクタンスを実験値から推定することでエネルギーハーベスティング用昇圧型スイッチングレギュレータの設計方法と制御方法について検討した。

1 Introduction

Today the technology of energy harvesting is in the spotlight. For example there are tiny power sources surrounding us like solar power under weak light or a wind power in the breeze. However these power sources can't be used directly because their output are small or influenced by environmental variation. On the while the total amount of these energies in the world can cover our demand on electricity consumption including tiny energy sources. The technology of energy harvesting is to be possible to use this tiny energy.

We can't apply existing wind power generator system for energy harvesting. One of the reasons is that it needs large energy to generate electric power in high efficiency. Sensing wind speed or wind direction, and controlling the blades may consume larger energy than power generation of energy harvesting [1].

Other reason is that power sources of energy harvesting are small and unstable. Existing large-scale wind power generation system is connected to the electricity network. But in the case of energy harvesting it is difficult to connect directly. When we use energy harvesting it is need to control its output or charge to storage device in high efficiency.

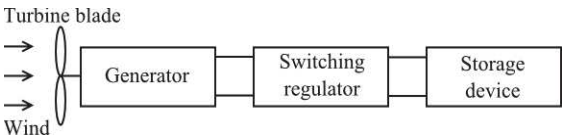

Fig.1 System for energy harvesting by wind power

Figure 1 shows the wind generator system for energy harvesting. The wind power can be converted into mechanical power by the turbine blade, and then into electric power by the generator. Since the generated electric power still has low voltage, a boost switching regulator is required to enable the storage of the generated electric power. The boost switching regulator can control the switching period and duty ratio to boost up the output voltage of the generator and charge to a storage device with high charging-efficiency [2].

The turbine blade and generator have their own output characteristic, such as the maximum power point (MPP) of operation. Therefore, tracking the maximum power point (Maximum Power point tracking, MPPT) is important to raise system's charging-efficiency.

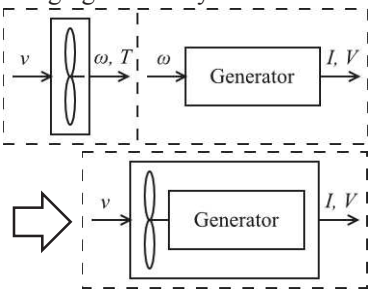

v	Wind speed
ω	Angular Velocity
T	Torque
I	Output current
V	Output voltage

Fig.2 Characteristic of each element

Figure 2 shows that the characteristics of the turbine blade and the generator determine the system's characteristic. To gain high efficient system for energy harvesting it is needed to measure each characteristic and determine optimum method of design and control.

2 Equivalent circuit model

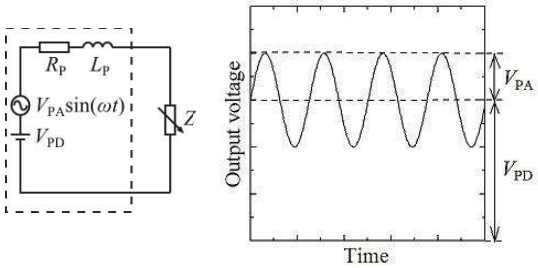

Fig.3 Equivalent circuit model and output wave

Figure 3 shows the equivalent circuit of a generator connected to a load (Z) [2]. The generator consists of a DC voltage supply (V_{PD}), an AC voltage supple of sine wave ($V_{PA}\sin\omega t$), an internal resistance (R_P) and an internal inductance (L_P). Base on the circuit theory, the output current $i(t)$ is obtained as

$$i = \frac{V_{PA}}{\sqrt{(L_P\omega)^2 + (R_P + Z)^2}}\sin(\omega t - \phi) + \frac{V_{PD}}{R_P + Z} \quad (1)$$

$$\phi = \tan^{-1}\frac{L_P\omega}{R_P + Z} \quad (2)$$

Consequently, the output voltage across Z is obtained as

$$V_{in} = \frac{V_{PA}Z}{\sqrt{(L_P\omega)^2 + (R_P + Z)^2}}\sin(\omega t - \phi) + \frac{V_{PD}Z}{R_P + Z} \quad (3)$$

Where, V_{PA}, V_{PD}, R_P, L_P need to be experimentally estimated for several angular frequency (ω).

3 Measurement of I-V characteristics of generation

Two types of generators, such as DC generators (Canon DN22M-12) and AC generator (Shimano DH-2N30JC) are targeted to use in this study. Their output characteristics, i.e. I-V characteristic, internal resistances and inductances are estimated from experiments as follow.

3.1 I-V characteristics

Figures 4 and 5 show the experimental set up to examine the I-V characteristics of the DC generator and AC generator, respectively.

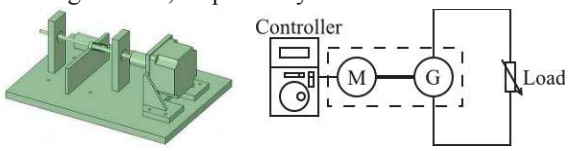

Fig.4 Experimental device with Canon DN22M

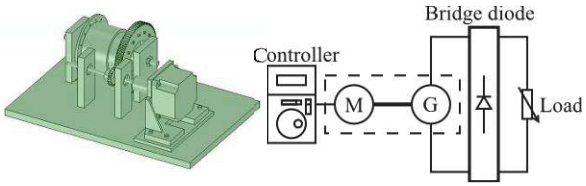

Fig.5 Experimental device with Shimano DH-2N30JC

The generators are driven by a servo motor (Oriental motor NexBL BMU series) via a gear or belt at a constant rotational speed. For the AC generator, shown in Fig.5, a bridge diode were used to rectify generator's output voltage. A variable resistor is used as a load and its across voltage is measured by an oscilloscope (Tektronix TDS2024B).

Figure 6 shows the measurement results of the load's current and voltage while changing the load's resistance and rotational speed.

As shown in Fig. 6, the I-V characteristics of the DC generator has a linear relation, where as that of the AC generator is curved when larger current is output.

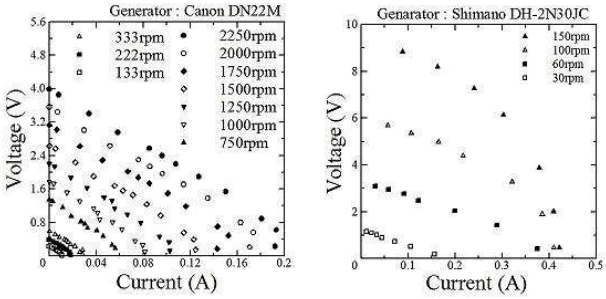

Fig.6 I-V characteristics of generators

Therefore, comparing between the two generators, a wide range of the current and voltage of the DC generator can be considered as the adaptable range for the equivalent circuit model. On the other hand, only a part of the I-V characteristic of the AC generator is able to be approximated to use as the equivalent circuit model. . Consequently, when the generator's

rotational speed is slow, a wide range of the measured I-V characteristics can be used to estimate the internal resistance of the generators, while only a part of the I-V characteristics within the range of high speed and small output voltage is able to use.

3.2 Estimation of Internal resistance

In a part of adaptable range to equivalent circuit model the slope of the measured I-V characteristics shows the internal resistance of the generators.

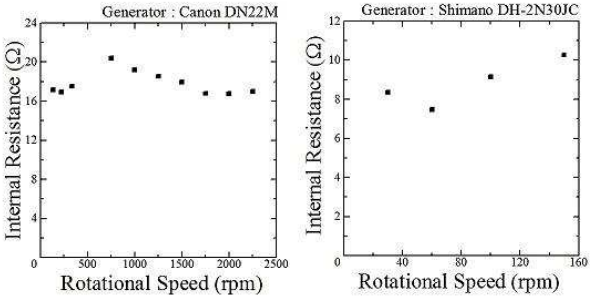

Fig.7 Internal residence of generators

From Fig.7 the values of internal resistance are estimated as shown in table 1, DC is within 20%, AC is within 31% of variation.

Table.1 The average value of internal resistance

Canon DN22M	Shimano DH-2N30JC
17.83Ω	8.81Ω

3.3 Estimation of Internal inductance

The frequency of the measured output current and output voltage are determined by fast Fourier transform (FFT).

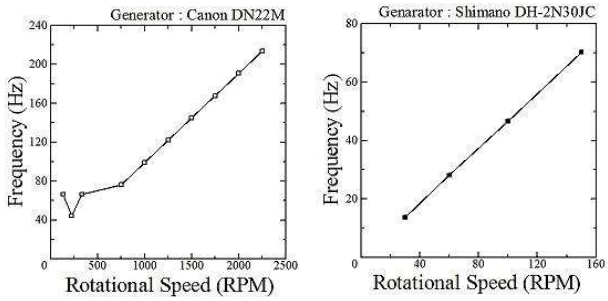

Fig.8 Main frequency of the generators' output voltages

However, in spite of higher order frequency of the output voltage, only the dominant frequency were selected. When the rotational speed is low the waveform of the output voltage fall into disorder and it is difficult to approximate to sine wave. The equivalent circuit model of generators can't apply for these conditions.

Figure 8 shows the relationship of the generators' rotational speed and output voltage's main frequency. When the DC generator (canon DN22M) rotate slowly, the main frequency are not linear because output wave is disorder. Output wave may be influenced by generator's internal brush.

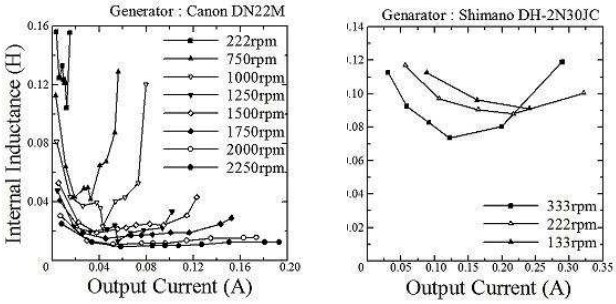

Fig.9 Internal inductance of generators

Therefore, the generator's internal inductance which is estimated by equivalent circuit model are not constant, as shown in table 2.

Table.2 The value of internal inductance

	Canon DN22M	Shimano DH-2N30JC
Mini	0.010H	0.083H
Max	0.156H	0.119H

Table 2 shows the value of internal resistance and inductance of the generators which is rotating are estimated. And the method of designing switching regulator which is connected with generator is proposed.

4 Control of switching regulator

Using the circuit of switching regulator with generator which is designed by above method.

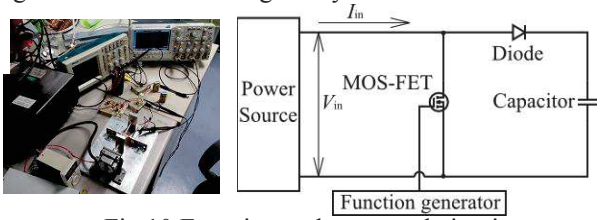

Fig.10 Experimental setup and circuit

Power source is the DC generator (Canon DN22M) because its adaptable range is wide. The output voltage of power source is boosted by switching regulator and the capacitor (EPCOS 10000μF) is charged. Output voltage and current are measured by the oscilloscope (Tektronix DPO2024B) and the capacitor's voltage is measured by oscilloscope (Tektronix TDS2012). Switching period and duty ratio is controlled by the function generator (WAVE FACTORY WF1943).

The switching duty ratio can controlled the boosted voltage and the range of power source's output swing. It is considered that if the range of output swing included the maximum power point the speed of charging capacitor will be fast.

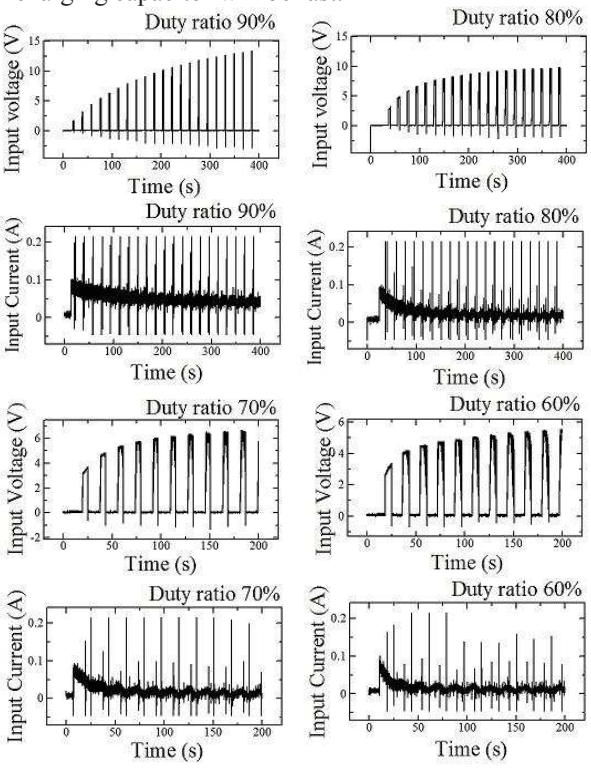

Fig.11 Input current and voltage of Power Source (Duty ratio 90%, 80%, 70%, 60%)

Figure11 shows that switching regulator's input voltage are getting increased and input current are getting decreased. Input voltage is almost zero when FET is ON. On the other hand input voltage is boosted and capacitor is charged when FET is OFF.

Figure12 shows the relationship between generator's I-V characteristic and input I-V characteristic. The average point of input I-V characteristics are nearly over the generator's I-V characteristic.

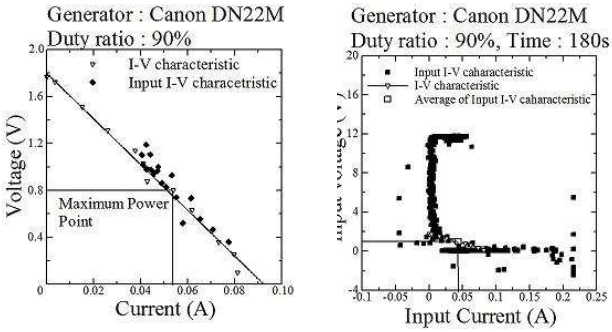

Fig.12 Power source's characteristic and input characteristic

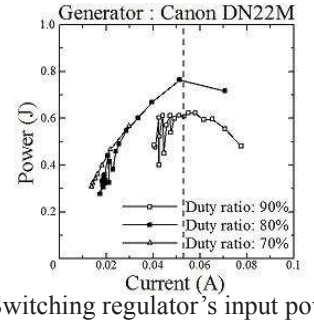

Fig.13 Switching regulator's input power

According Fig.13 the power source's output power is maximum when output voltage and current include the power sources maximum power point. It is necessary that switching duty ratio is controlled to track the maximum power point.

5 Conclusions

In this study the method of design and control for the purpose of charging capacitor using switching regulator with generator are proposed. The range that the equivalent circuit model can adopt is disclosed. Furthermore the internal resistance and inductance when generator is rotating are estimated. It is useful to design switching regulator with generator. Next using switching regulator and capacitor the generator's output can be boosted and charged in the condition of various switching duty ratio. From this analysis it is important to control switching duty ratio which is able to swing output within the range of power source's maximum power point.

References

[1] "A Neural Network Based MPPT Controller for Variable Speed Wind Energy Conversion Systems" 8th Mediterranean Conference on Power Generation, Transmission, Distribution and Energy Conversion MEDPOWER 2012

[2] "Control Method of Boost Switching Regulator for Generators with Voltage Variation" Y. Honda, Master's thesis of Tokyo Institute of technology, 2012

DEVELOPMENT OF DIRECTIONAL CHANNEL SOUNDER USING USRP AND GNU RADIO

Student Number: 14M18218 Name: Tianyang Min Supervisor: Jun-ichi TAKADA

汎用ソフトウエア無線機を用いた指向性電波測定装置の開発

閔 天楊

無線通信において伝搬路特性はシステム設計を行うための重要な情報である．送信信号は伝搬路を通して距離減衰されるばかりではなく，反射や回折，散乱などにより多重波の影響を受ける．特に，到来波角度分布特性はMIMO 伝送評価を行う際に重要な指標であり，近年盛んに伝搬路測定が行われている．これらの特性を測定するために高分解能な指向性伝搬路測定装置が必要となる．現在，伝搬路測定に用いられる測定装置は高価かつ大型であり，伝搬路測定実験は非常に高い費用がかかり，利便性も低いという問題がある．そこで本研究では汎用ソフトウェア無線機（Universal Software Radio Platform) を用いて指向性伝搬路測定装置を開発し，その妥当性に関する検証を行った．本装置は，汎用の測定装置に比べて，安価かつ小型であり，通常の専用装置に比べて，RF 周波数が選択可能であることから柔軟性が優れている．

1 Introduction

Channel sounding is to measure the property of radio propagation channel, and have long held importance for wireless communication system design. Recently, the directional property of the channel has been recognized as an important factor when evaluating the propagation channel. The knowledge of it can be applied to spatial diversity in multi-input-multi-output (MIMO) wireless network.

To measure the directional channel characteristics, the raytracing simulation software (e.g., raplab) has become popular among researchers, which can predict the main line of sight (LoS) path, and major non-line of sight NLoS specular reflected paths. However, a lot of comparison results showed that there still exists a lot of discrepancies between measurement results and raytracing simulation prediction. These kinds of discrepancies are considered as the contribution of scattering phenomenon (such as diffuse scattering) on rough scattering surface, and these diffused components which raytracing simulation can't predict is regarded as important factor that is expected to be utilized in MIMO system. In particular, for higher radio wave frequency, it is easier to interact with small scattering objects and more dense multipath components (DMC) is expected to be observed. The phenomenon mentioned above is very difficult to be reproduced by raytracing simulation. Alternatively, Vector network analyzer（VNA) can also be used to conduct channel sounding measurement so as to save the development cost and additional calibration workload. However, VNA is designed that both transmitter and receiver modules are combined inside one equipment body, it has the limitation that it can be utilized only in short distance measurement environment (indoor environment). Because transmitter and receiver are separately set far away, it's very difficult to use VNA for outdoor measurement. So in reality, channel sounder is necessarily to be designed to conduct outdoor channel sounding measurement. But development of conventional directional channel sounder is very high-cost, and the channel sounder is also huge size, inconvenient and not flexible for RF frequency.

Considering all these respects mentioned above, this thesis abstract presents a development of low-cost and compact directional channel sounder that is able to conveniently and accurately measuring the real propagation channel characteristics. By conducting a comparison indoor channel sounding measurement with VNA, the performance of this work is validated that it can achieve almost the same accuracy as VNA for measuring directional property of the channel. Moreover, this kind of compact and inexpensive channel sounder is expected to be applied for distributed network channel sounding, which requires multiple tranceivers to be allocated to measure the distributed channel in a large scale. Also, with increase of transmission interferences caused by small aircraft (drone) recently, radio propagation channel in the air is necessarily to be clarified. The compact channel sounder is expected to be mounted on a drone, and allocates the mobile stations(MS) in the air so as to measure and investigate the propagation channel above the ground.

2 Structure of channel sounder

2.1 Universal software radio platform

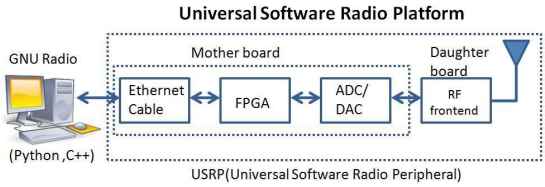

Figure 1: Universal Software Radio Platform

As shown in Figure 1, USRP is comprised of a motherboard and a daughterboard. The complex baseband signals transfered from the host PC are transformed to intermediate frequency (IF) complex signals at near DC by digital-up-converter (DUC) after the processing of interpolation, then IF digital signals are converted into analog signals by using high speed DA converter with 16-bit resolution and 400MS/s sampling rate. Finally, the IF analog signals are streamed into RF up-converter circuits. On the other hand, at the receiver side, the RF received signals are down-converted into IF complex signals at near DC by RF down-converter circuits. Then, IF complex signals are sampled by AD converter with 14-bit resolution and

100MS/s sampling rate, and converted again into complex baseband signals by using digital-down-converter (DDC) inside the FPGA .

2.2 The detail configuration

Figure 2 shows the main structure of channel sounder. The transmit signal was stored in Tx PC, inversely the received signal was stored in Rx PC. Baseband Tx signal is upconverted in FPGA and stream through DAC to be converted into Analog signal. Finally the IF signal is modulated into RF signal by QAM modulation. For receiver side, the received RF signal is demodulated on the daughterboard, then the IF signal is digitalized by ADC and downconverted inside the FPGA into baseband signal. A common external rubidium clock is connected in between transmitter and receiver for frequency synchronization and Pulse-Per-Second (PPS) signal is connected to Tx/RX FPGA ' s clock to trigger the transmitting and receiver at the same timing so as to realize timing synchronization.

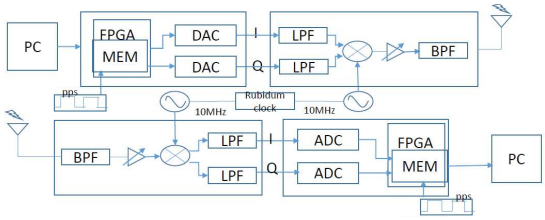

Figure 2: USRP channel sounder structure

2.3 Transmit signal

In this work, a multitone signal was used as a transmit signal. The multitone signal can be represented as

$$s(t) = \frac{1}{\sqrt{N}} \sum_{k=-N/2}^{N/2} \exp(\mathrm{j}2\pi k \Delta_F t + \mathrm{j}\phi_k). \quad (1)$$

where Δ_F means the subcarrier spacing, N denotes the number of the subcarriers. Similarly to orthogonal frequency division multiplexing (OFDM), multitone signal is advantageous over the signal carrier pseudo random (PN) sequence from the view point of the spectrum efficiency although peak-to-average power ratio (PAPR) is higher. A method to minimize PAPR of multitone signal is by introducing the Newman phase condition ϕ_k[2].

2.4 Performance of USRP channel sounder

The performance of developed USRP channel sounder is evaluated by conducting a T-junction DUT test [1]. As shown in Figure 3, the edge A is connected to transmitter, the edge B is connected to receiver, and the edge C is kept open. At the same time, the vector network analyzer was also used to measure the DUT characteristics for reference. The comparison results of channel impulse response is shown in Figure 4. There are two peaks that can be observed. The first peak represent the direct path, and the second peak represent the reflected path from open edge C with a delayed time. There is good agreement between the channel impulse response of DUT measured by VNA and USRP channel sounder that validated the good performance of developed channel sounder.

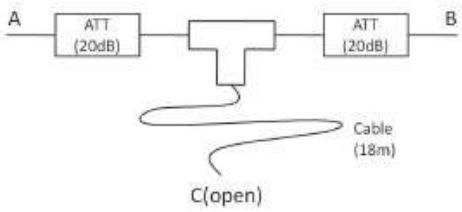

Figure 3: T-junction DUT

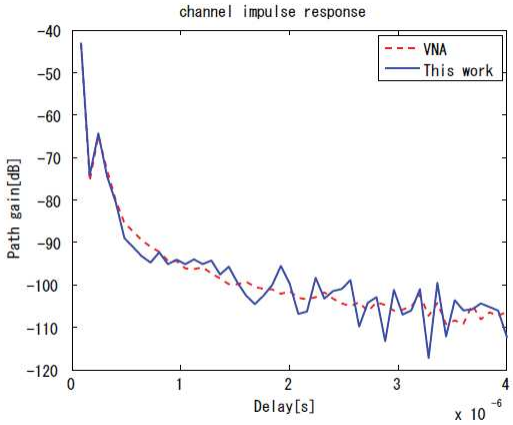

Figure 4: Comparison of impulse response obtained by developed system and vector analyzer (reference)

In order to measure the directional property of propagation channel, array antenna is supposed to be used to detect the angle of departure (AoD) and angle of arrival (AoA) from the multipath. Thus, the phase coherence of the channel sounder is necessarily to be evaluated. A three hours phase coherence test was conducted, the results are shown in Figure 5, the phase changes between -6 and 7 degree, and remains relatively stable at -5 degree.

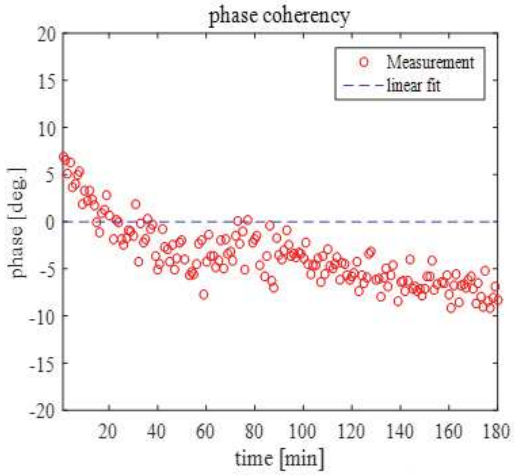

Figure 5: Phase coherence test

2.5 Extension to directional channel sounder

Figure 6 shows the detail structure of directional channel sounder. The Tx/Rx antennas are fixed on the rotators that are controlled by rotation control PC through COM port. The USRP Tx/Rx are controlled by Tx/Rx PC by using TCPIP connection. Also, the Tx/Rx PC are connected with rotation control PC respectively by using TCPIP connection. The Tx PC is set as client, rotation control PC and Rx PC are set as server. Once the Tx PC trigger the Tx USRP to start transmitting signals, the

whole system will start working automatically.

The antenna (shown in Figure 7) of the directional channel sounder is a self-fabricated standard patch antenna that designed by using a commercial electromagnetic simulator (CST). The center frequency of this antenna is 2.4GHz, gain is 5.08dBi and Half power beamwidth is 94.4^0.

We assume the propagation channel characteristics remain unchanged during the whole measurement, and rotate the Tx/Rx antennas over 360^0 degree and acquire the transfer function at each azimuth angle. The antennas that mounted on a tripod are connected to USRP channel sounder. The local oscillator of the USRP sounder is synchronized with a 10MHz output from external rubidium clock. The height of tripod is 1.3 meters that considers almost the same height when mobile phone users using phones. The angle for each rotation is 10^0 that is calculated based on the wavelength of transmit signal. Considering that the beamwidth of the array need to be sharp, the number of virtual array elements is set as 36. The interval distance between two elements is set as half radio wave length. The frequency is 2.4GHz (wave length is $3 \times 10^8/2.4 \times 10^9 = 0.125\text{m}$), so the radius can be calculated as $0.125 \div (10 \div 180 \times \pi) = 0.358\text{m}$.

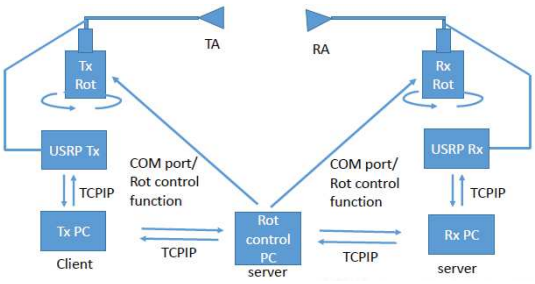

Figure 6: Structure of directional channel sounder

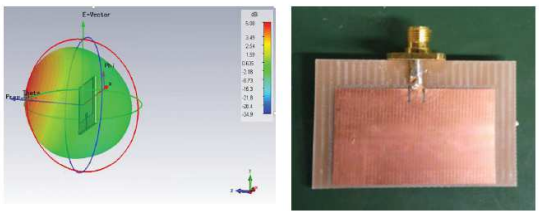

Figure 7: Self-fabricated patch antenna

The virtual array response is obtained based on the simulation results. To get the rotated radiation pattern for each single virtual element, The phase of the single antenna is rotated for each element position. The mode vector of the array response of uniform circular array (UCA) with radius r and element number L is

$$\alpha(\phi, f) = [e^{j\frac{2\pi frcos\phi}{c}}, e^{j\frac{2\pi frcos(\phi-\Delta\eta)}{c}}, ..., e^{j\frac{2\pi frcos(\phi-(L-1)\Delta\eta)}{c}}]^T \quad (2)$$

Then, the rotated single virtual array element is multiplied with the element of mode vector shown as below

$$\mathbf{P}(\phi, f) = [\mathbf{A}(\phi, f) \cdot e^{j\frac{2\pi frcos\phi}{c}}, \mathbf{A}(((\phi - \Delta\eta), f) \cdot e^{j\frac{2\pi frcos(\phi-\Delta\eta)}{c}}, ..., \mathbf{A}((\phi - (L-1)\Delta\eta), f) \cdot e^{j\frac{2\pi frcos(\phi-(L-1)\Delta\eta)}{c}}]^T \quad (3)$$

Here, $\Delta\eta = \frac{2\pi}{L}$. L denotes the number of virtual array elements. $\mathbf{P}(\phi, f)$ denotes the array response of the virtual array, $\mathbf{A}(\phi, f)$ denotes the radiation pattern of single element of virtual array. ϕ is the azimuth rotation angle.

3 Indoor measurement campaign

We conducted an indoor channel sounding measurement by using the developed directional USRP channel sounder. At the same time, we measured the identical measurement environment by using VNA (Rohde Shwartz ZVA 40) to compare and evaluate the performance of directional USRP channel sounder. The configuration of the VNA measurement is the same with the USRP channel sounder.

The measurement was conducted in the laboratory experiment room in Tokyo Institute of Technology South-6 building (Figure 8). There are a lot of fixtures like wooden desks, steel shelves (filled with objects), steel carts, and small objects like measurement equipments. The major scattering objects can be considered as building wall, floor, pillars, and steel shelves.

The Table 1 presents the parameter settings of USRP sounder. For VNA, the sweeping tones number is set as 128, the bandwidth is 12.5MHz, the center frequency is 2.4GHz, and the transmitter power is set as 5 dBm.

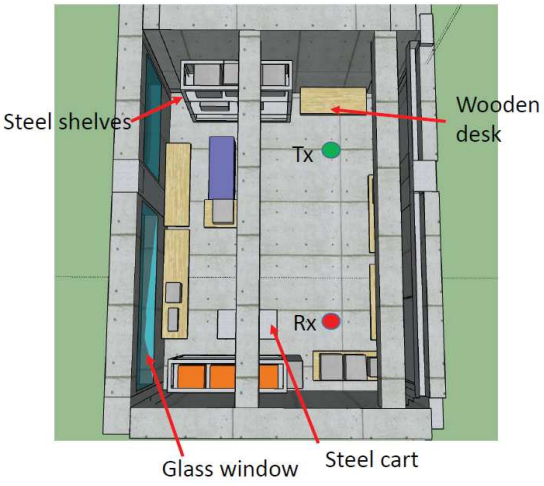

Figure 8: Top view of measurement environment

Table 1: Parameters setting of USRP channel sounder

Carrier frequency	2.4 GHz
Sampling rate	25 MSps
Bandwidth	$12.5MHz$
Transmit signal	Multitone
Number of tones	128
Tone spacing	97.656 kHz
Delay resolution	80 ns
Transmit power	5 dBm

4 Data analysis

A transfer function matrix was defined with the Tx and Rx antenna pointing at i-th and j-th angle, be $\mathbf{H}_{ijk}$. With the inverse fourier transform, the total channel impulse response can be calculated discretely as

$$h_{ij}[n] = \frac{1}{N}\sum_{N}^{k=1} |\xi W[k]\mathbf{H}_{ij}\exp(\frac{\mathrm{j}\mathbf{2}\pi kn}{N}) \qquad (4)$$

where N denotes the total number of tones of multitone signals. $W[k]$ denotes a window function to reduce a side-lobe level, $\xi = \frac{N}{\sum_{N}^{k=1} W[k]}$.

To estimate the angular properties (e.g. AoD, AoA) of the channel, channel estimation algorithm is usually used to perform this estimation. In this work, beamforming algorithm was used to estimate angular parameters. If we define $\mathbf{\Omega}_R = (\phi_R, \theta_R)$, and the $\mathbf{\Omega}_T = (\phi_T, \theta_T)$, then only considering the vertical polarization, the the power spectral density function of AoD and AoA for a subcarrier k is calculated as:

$$Y(\Omega_R, \Omega_T, k) = \frac{\mathbf{a}_R^H(\mathbf{\Omega}_R, k) \cdot \mathbf{H}_{VV}(k) \cdot \mathbf{a}_T^*(\mathbf{\Omega}_T, k)}{\|\mathbf{a}_R(\mathbf{\Omega}_R, k)\|_F^2 \|\mathbf{a}_T(\mathbf{\Omega}_T, k)\|_F^2} \qquad (5)$$

Then, the power spectral density function in delay domain can be obtained by inverse Fourier Transform.

$$y(\Omega_R, \Omega_T, n) = \frac{1}{N}\sum_{k}^{N-1} Y(\mathbf{\Omega}_R, \mathbf{\Omega}_T, k)\exp(\frac{\mathrm{j}2\pi kn}{N}) \qquad (6)$$

5 Measurement results

By integrating the power of this complex amplitude function over delay domain, the double angular power spectrum can be obtained. The comparison of double angular spectrum in azimuth between USRP and VNA is presented in Figure 9 and Figure 10. The clusters detected by VNA and USRP have a good agreement that validates the good performance of developed directional USRP channel sounder. There are four major clusters that are detected. The cluster marked by yellow circle is the LoS cluster which is the direct transmission (yellow line in Figure 11)between transmitter and receiver. The cluster marked by red circles represents the propagation of signal that had one reflection on the door side wall (red line). The clusters marked by green circle represents the propagation of signal that had one reflection on the front side wall (green line). Finally the cluster marked by purple circle represents the propagation of signal that had one reflection on the back side wall (purple line).

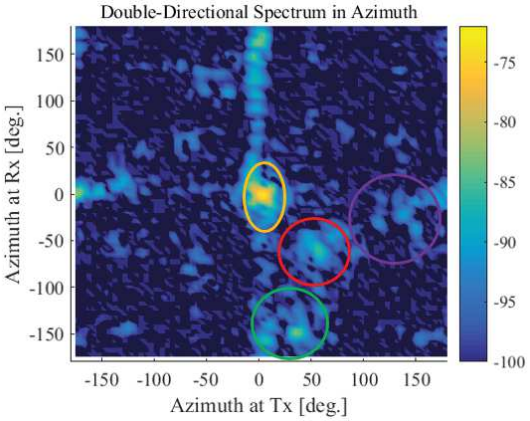

Figure 9: The double angular power spectrum measured by USRP

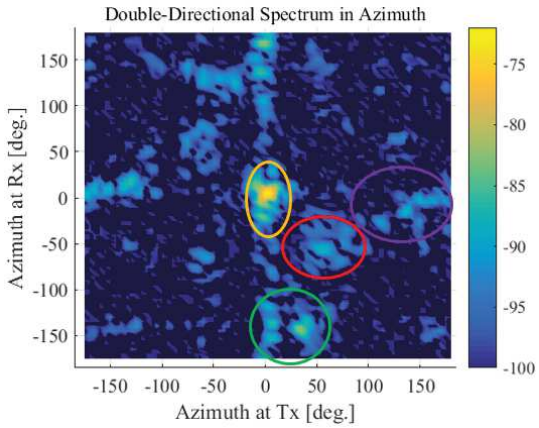

Figure 10: The double angular power spectrum measured by VNA

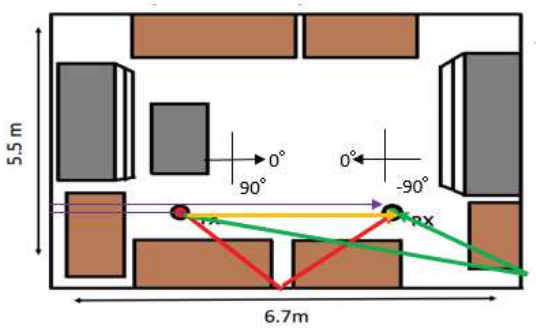

Figure 11: The track of major propagation paths

6 Conclusion

This thesis abstract presents the development of directional channel sounder using USRP and GNU radio. The performance of the developed channel sounder was validated by conducting a comparison indoor channel sounding measurement between USRP and VNA. The results showed that the angular position of the clusters that detected by developed USRP channel sounder and VNA have a good agreement. For future work, this USRP sounder is expected to conduct measurement campaign simultaneously with 60GHz channel sounder in identical environment to clarify the difference of propagation mechanism between UHF radiowave and mili-meter wave.

References

[1] T. Min, M. Kim,J. Takada, "Development of MIMO Channel Sounder using GNU Radio/USRP," *IEICE Technical Report* SR2014-3, pp. 15–21, May. 2014.

[2] M. Kim,J. Takada, Y. Konishi, "Novel Scalable MIMO Channel Sounding Technique and Measurement Accuracy Evaluation With Transceiver Impairments," *IEEE Trans. Instrum.Meas*, vol. 61, no.12, pp. 3185–3197, Dec. 2012.

[3] D. Mass, M. H.Firooz, J. Zhang, N. Patwari and K.Kasera, "Channel sounding for the masses: low complexity GNU 802.11b Channel Impulse Response Estimation," *IEEE Trans. Wireless Commun*, vol. 11, no.1, pp. 1–8, Jan. 2012.

LIFETIME PREDICTION OF REINFORCED SEAWATER CONCRETE MIXED WITH FLY ASH WHICH WERE PRODUCED IN JAPAN OR PHILIPPINES AGAINST CHLORIDE ATTACK

Student Number: 14M18260　Name: Cheng YI　Supervisor: Nobuaki OTSUKI

塩害における日本及びフィリピンで産出されたフライアッシュを用いた海水練り鉄筋コンクリートの寿命予測

易　成

本研究では，淡水の節約と産業副産物の有効利用の観点から，練混ぜ水に海水，混和材に日本及びフィリピンで産出されたフライアッシュ(以下 FA)を使用した鉄筋コンクリートの物質透過性や内部鋼材の腐食挙動を明らかにし，塩害に対する寿命（鉄筋腐食によりコンクリートにひび割れが生じるまでの期間）を定量的に評価した．その結果，海水練りの寿命は淡水練りの 60%程度となるものの，FA を 30%置換すれば海水練りでも約 30 年の寿命となった．また，フィリピン産 FA を使用した方が内部鋼材の腐食抵抗性が高かった．

1. Introduction

While water shortage is concerned, using seawater as concrete material in Japan and Philippines where are surrounded by ocean, is considered. Also, using FA is considered partly because of increasing coal power. However, the usages of seawater and FA as concrete material haven't been investigated enough. Considering this background, following objectives have been set.

1. Clarify the material properties and corrosion behavior of reinforced concrete (RC) mixed with seawater and FA.
2. Predict quantitative lifetime of RC mixed with seawater and FA against chloride attack.

2. Experimental works

2.1 Materials

Freshwater, artificial seawater (ASTMD1141-98(2003), Cl^- 1.98%), and natural seawater (Cl^- 2.06%) were used as mixing water. Land sand and land gravel were used as aggregate. SR235 (φ13mm×10cm) was used as reinforcement. Ordinary Portland cement (OPC) and OPC replaced with FA (replacement ratio is 10%, 30%, 50% and 70 %) were used. Two types of FA include FA produced in Japan (JF) and FA produced in Philippines (PF), were used.

2.2 Specimens

In this study, two types of specimen were used. First one was non-reinforced cylinder concrete specimen shown as Fig.1. This type was used for investigation of Cl^- diffusion coefficient after exposed in seawater for 4 month. Specimens mixed with OPC were exposed in 20°C artificial seawater after cured in 20°C moist air for 5 days. Specimens mixed with JF were exposed in 20°C or 40°C artificial seawater after cured in 20°C or 40°C moist air for 7 days. These specimens were casted in Tokyo. Specimens mixed with PF were exposed in 30°C natural seawater after cured in 30°C moist air for 1 day. These specimens were casted in Manila. Second one was prism shape mortar specimen embedded with streel bar shown as Fig.2. This type was used for investigation of corrosion current density, corrosion threshold Cl^- content, and O_2 permeability through accelerated deterioration test. Specimens were exposed in 50°C, 3 % NaCl condition after 7days cured in 20°C or 40°C water. The same water used for the mixing was used for curing. Totally, 16 patterns of specimen were casted as shown in Tab.1.

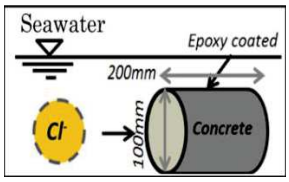

Fig.1. Concrete specimen

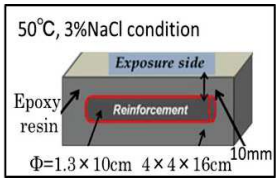

Fig2. Mortar specimen

Tab.1 Mix proportions of specimens

Water binder ratio	Mixing or curing water	FA type	FA replacement ratio, %	Code name	*Note	
					Concrete	Mortal
0.5 (Unit water: 171kg/m^3 to 180kg/m^3)	Fresh water	-	0	OPCW	s/a (Sand aggrigate ratio) is 42~45 % Target slumpe is 8±4 cm Target air content is 3±2 %	S/B (Sand binder ratio) is 2.0
		JF	10	JF10W		
			30	JF30W		
			50	JF50W		
			70	JF70W		
		PF	30	PF30W		
			50	PF50W		
			70	PF70W		
	Seawater (Artificial)	-	0	OPCS		
		JF	10	JF10S		
			30	JF30S		
			50	JF50S		
			70	JF70S		
	Seawater (Natural)	PF	30	PF30S		
			50	PF50S		
			70	PF70S		

2.3 Measurement items and its methods

(1) Cl^- diffusion coefficient

It is calculated from Fick's diffusion equation shown as equation 1. Measurement method is conformed to Japan Society of Civil Engineers (JSCE)-G 572-2010.

$\delta c / \delta t = D\Delta^2 c$ Eq.1

(c: amount of Cl^- content (kg/m^3), t: exposure time (year), D: Cl^- diffusion coefficient (cm^2/year))

(2) Oxygen permeability

It is calculated by substitute limit current density (I_{lim}) obtained from cathodic polarization curve in equation 2. Investigation was conducted when the age of specimen is 140 days.

$\delta Q / \delta t = -I_{lim} / nF$ Eq.2

($\delta Q / \delta t$: Oxygen permeability (mol/cm^2/sec), I_{lim}: limit current density (A/cm^2), n: atomic value (=4), Faraday constant (96500c/mol)).

(3) Corrosion current density

Corrosion current density is evaluated by using equation 3. The polarization resistance of steel embedded in mortar is evaluated based on AC-impedance method using two patterns frequency (10 kHz 10mV, 10 mHz 10mV).

$I_{corr} = K / (Rct \times S)$ Eq.3

(I_{corr}: Corrosion current density (μA/cm^2), Rct: Polarization resistance (Ω), S: Surface area of steel bar (40.82cm^2),

K : Stern-Geary constant (0.0209V))

(4) Corrosion threshold Cl^- content

Investigation was conducted when I_{corr} of specimen has reached 0.2 μA / cm^2 according to CEB Working Party V/4[1]. Measurement method is conformed to JCI-SC45.

2.4 How to predict lifetime of RC against chloride attack

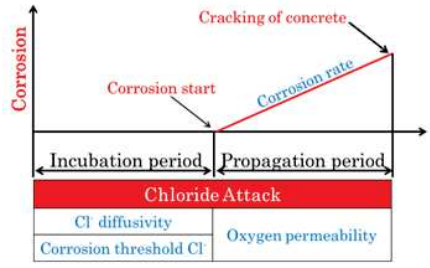

Fig.3 Definition of lifetime

In this study, lifetime of RC against chloride attack is defined as sum of incubation and propagation period which is a performance based design as shown in Fig.3. For the prediction of incubation period, covering depth, initial Cl^- content, surface Cl^- content, Cl^- diffusion coefficient, and corrosion threshold Cl^- content are required. Inputting covering depth, Cl^- diffusion coefficient, initial Cl^- content, and surface Cl^- content to Fick's diffusion law, duration that Cl^- content in covering depth reaches the corrosion threshold Cl^- content is estimated as incubation period. For the prediction of propagation period, the corrosion rate and the critical amount of corrosion for cracking are required. Dividing the critical amount of corrosion for cracking[2] by corrosion rate which is estimated from oxygen permeability[3], the duration that amount of corrosion products reach the amount for cracking is estimated as propagation period.

3 Experimental results

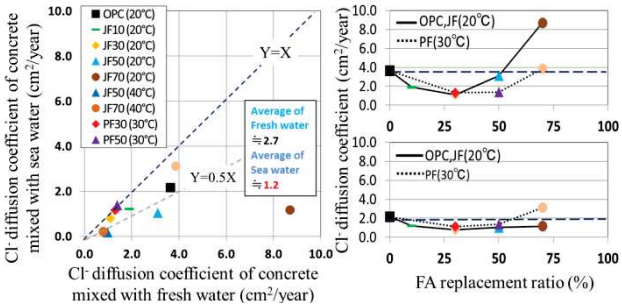

Fig.4 Result of Cl^- diffusion coefficient 1

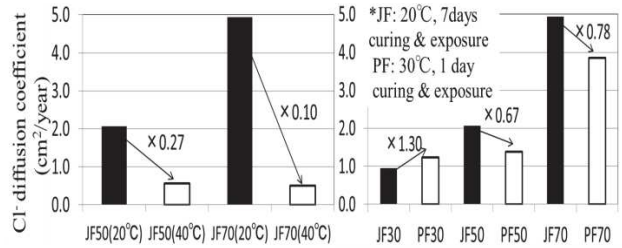

Fig.5 Result of Cl^- diffusion coefficient 2

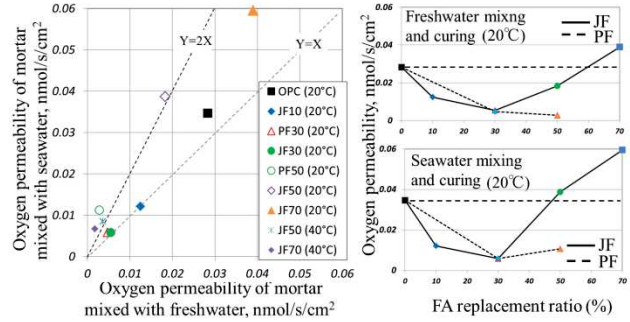

Fig. 6 Result of oxygen permeability 1

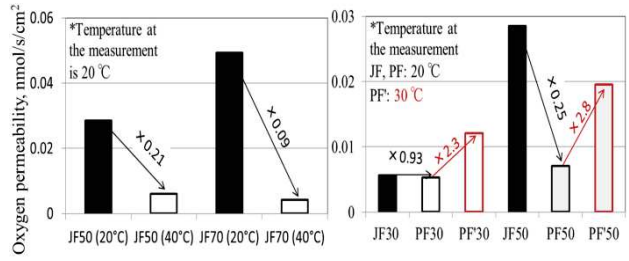

Fig. 7 Result of oxygen permeability 2

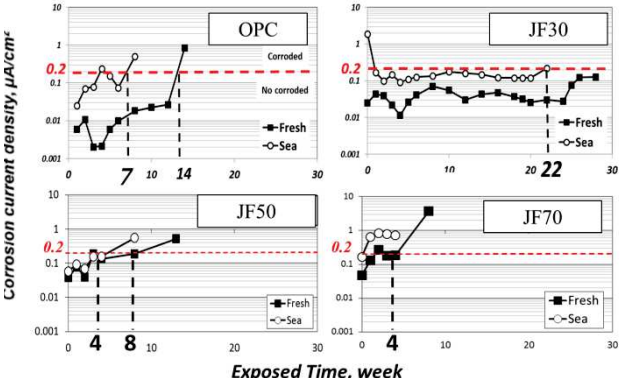

Fig. 8 Result of corrosion current density 1

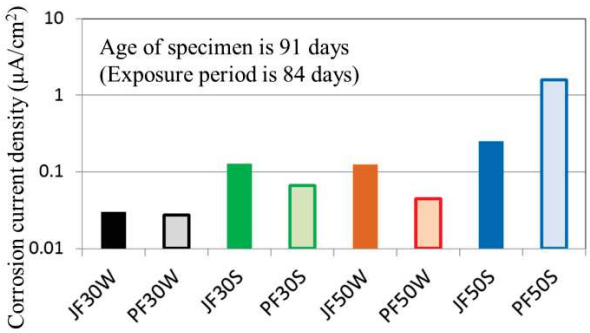

Fig. 9 Result of corrosion current density 2

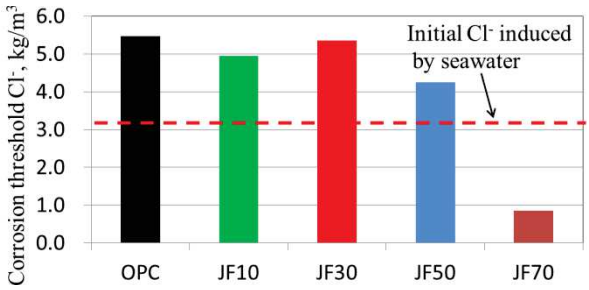

Fig. 10 Result of corrosion threshold Cl^- content

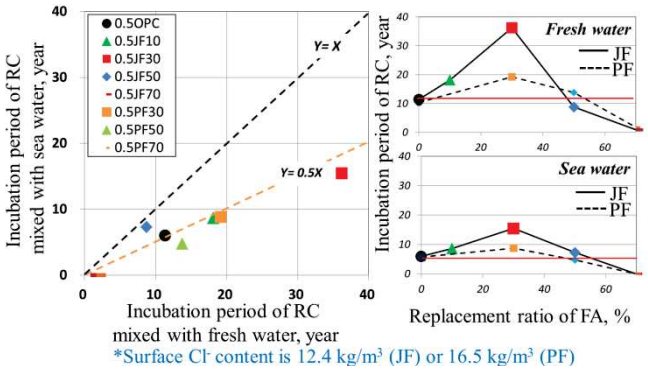

Fig.11 Result of incubation period (Cover depth is 70mm)

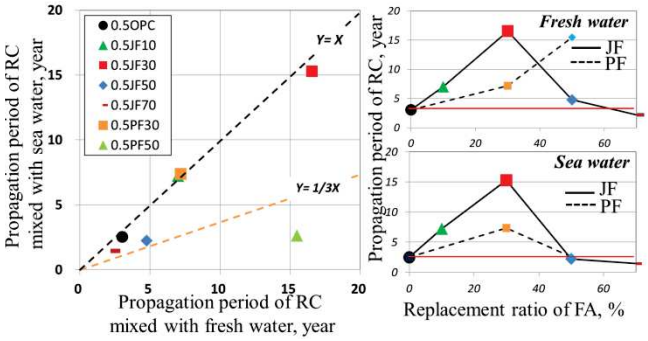

Fig.12 Result of propagation period (Cover depth is 70mm)

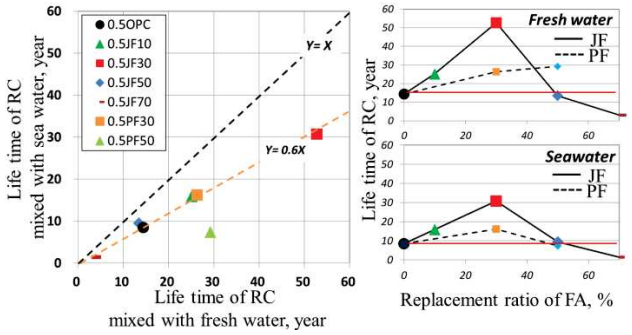

Fig.13 Result of lifetime of RC (Cover depth is 70mm)

3.1 Material properties

(1) Cl^- diffusion coefficient

Fig.4 and Fig.5 show the measured result of Cl^- diffusion coefficient. Focus on mixing water, Cl^- diffusion coefficient of specimens mixed with seawater is smaller than that mixed with freshwater. It might be because initial Cl^- content induced by seawater has reduced concentration gradient of Cl^-.

Focus on FA replacement ratio, Cl^- diffusion coefficient is the smallest when FA replacement ratio is 30%. It might be because concrete is the most tense when FA replacement is 30%. Additionally, the value of FA50 (replace OPC with 50% FA) is almost same or lower than OPC. So in a view point of "not to degrade performance of concrete", the maximum FA replacement ratio is 50%.

Focus on curing and exposure temperature, Cl^- diffusion coefficient of specimens cured and exposed in 40°C are much smaller than that cured and exposed in 20°C. It might be because higher the temperature, faster the reaction of FA.

Focus on FA type, Cl^- diffusion coefficient of specimen mixed with JF is lower than that mixed with PF when FA replacement ratio is 30%. However, it is reversed when FA replacement ratio exceeds 50%. It might be because of the difference of curing period and temperature. It might be that the impact of curing period is dominant when FA replacement ratio is lower than 30% while the impact of temperature is dominant when FA replacement ratio exceeds 50%.

(2) Oxygen permeability

Fig.6 and Fig.7 show the measured result of oxygen permeability. Focus on mixing water, oxygen permeability of specimens mixed with seawater is almost same as that mixed with freshwater when FA replacement ratio is less than 30%. However, the value of specimens mixed with seawater is about twice as that mixed with freshwater when FA replacement ratio exceeds 50%. It might be because of the difference of pore size distribution.

Focus on FA replacement ratio, oxygen permeability decreases up to FA replacement ratio is 30% or 50%. It might be because FA has made the concrete tense.

Focus on curing temperature, oxygen permeability of specimens cured in 40°C is much lower than that cure in 20 °C. It might be because high temperature curing has accelerated the reaction of FA.

Focus on FA type, oxygen permeability of specimens mixed with PF is lower than that mixed with JF especially when FA replacement ratio is 50%. It might be because PF has higher reactivity than JF due to its high content of CaO. CaO produces $Ca(OH)_2$ through hydration which is necessary for the reaction of FA.

Focus on temperature at measurement, oxygen permeability becomes 2 to 3 times when the temperature rises 10°C (from

20°C to 30°C). The results obtained from the measurement conducted in 30°C were used to predict propagation period of RC because air temperature in Philippines is 30°C.

(3) Corrosion current density (I_{corr})

Fig.8 shows the measured result of time-dependent I_{corr} change. The period until I_{corr} reaches the threshold ($0.2\mu A/cm^2$) is compared in this figure. Focus on mixing water, the period of specimens mixed with seawater is shorter than that mixed with freshwater. Focus on FA replacement ratio, the period is the longest when FA replacement ratio is 30%.

Fig.9 shows the measured result of I_{corr} when the ages of specimens are 91 days (84 days exposed in 50°C, 3% NaCl condition). It is for the comparison between specimens mixed with JF and that mixed with PF. It can be said that I_{corr} of specimens mixed with PF tend to be lower than that mixed with JF. Therefore, it can be said that the corrosion resistance of specimens mixed with PF are tend to be higher than that mixed with JF.

(4) Corrosion threshold Cl^- content

Fig.10 shows the measured result of corrosion threshold Cl^- content. It can be said that corrosion threshold Cl^- content decreases significantly when FA replacement ratio is higher than 30%. It might be because of the low pH due to lack of OPC. Since corrosion threshold Cl^- content of specimens mixed with PF has not been investigated, corrosion threshold Cl^- content of specimens mixed with PF is considered the same as that mixed with JF.

3.2 Lifetime prediction of RC against chloride attack

(1) Incubation period

Fig.11 shows the predicted result of incubation period of RC against chloride attack. Focus on mixing water, the incubation period of RC mixed with seawater is about half of that mixed with freshwater. Focus on FA replacement ratio, it shows the longest period when FA replacement ratio is 30%. Focus on type of FA, the period of RC mixed with PF tends to be shorter than that mixed with JF.

(2) Propagation period

Fig.12 shows the predicted result of propagation period of RC against chloride attack. Focus on mixing water, the propagation period of RC mixed with seawater is almost same as that mixed with fresh water up to FA replacement ratio is 30%. However, the period of RC mixed with seawater is much shorter than that mixed with freshwater when FA replacement ratio exceeds 50%. Focus on FA replacement ratio, it shows the longest period when FA replacement ratio is 30% or 50%. Focus on type of FA, the period of RC mixed with PF tends to be shorter than that mixed with JF.

(3) Lifetime

Fig13 shows the predicted result of lifetime of RC against chloride attack. Focus on mixing water, lifetime of RC mixed with seawater is about 60% of that mixed with freshwater. Focus on FA replacement ratio, it shows the longest lifetime when FA replacement ratio is 30% or 50%. The longest lifetime of RC mixed with seawater is about 30 years when FA (JF) replacement ratio is 30%. Focus on type of FA, the lifetime of RC mixed with PF tends to be shorter than that mixed with JF. However, the life time of RC mixed with PF is shortly estimated since the curing period of concrete mixed with PF is one day and mortar mixed with PF is cured in 20°C. If the concrete has been cured in 7 days and mortar has been cured in 30°C, its lifetime would be much longer.

Conclusions

Experimental works were conducted regarding the influences of mixing water (freshwater and seawater), FA replacement ratio to OPC (0%, 10%, 30%, 50% and 70%), type of FA, (JF and PF) and curing or exposure temperature (20°C, 30°C and 40°C) on the material properties and corrosion behavior of RC. Also, the lifetime which is a performance based design includes incubation and propagation periods (duration until crack occurs) of RC against chloride attack were estimated. As results, the following were found:

1) Using seawater as mixing water instead of freshwater can reduce Cl^- diffusion. Replacing FA to OPC from 10% to 50% can reduce Cl^- diffusion and oxygen permeability. Using PF can reduce more Cl^- diffusion coefficient and oxygen permeability than JF. Higher the curing temperature, lower the Cl^- diffusion and oxygen permeability. In case using PF, corrosion current density tends to be lower than in case using JF. It means corrosion resistance of PF tends to be higher than JF.

2) Life time of RC mixed with seawater is about 60% of that mixed with freshwater. Replacing OPC with FA from 10% to 50% can extend the lifetime of RC. Especially, RC mixed with seawater shows the longest lifetime (about 30 years) when FA (JF) replacement ratio is 30%. If there were enough curing period (7days) and temperature (30°C), RC mixed with PF would has shown longer lifetime than that mixed with JF.

References

1) CEB Working Party V/4.1 (1997). Strategies for testing and Assessment of Concrete Structure Affected by Reinforcement Corrosion (draft 4), BBRI-CSTC-WTCB

2) K. Yokozeki et al., (1997). "A Rational Model to Predict Service Life of RC Structures in Marine Environment", Forth CANMET/ACI International Conference on Durability of Concrete 1

3) S. Maruyama, (2004), "Influence of Temperature and Cement on Corrosion Rate of Steel Bar under Carbonation", Master thesis of Tokyo Institute of Technology (in Japanese)

Effect of tangential force on adhesion between an elastic beam and a rigid body

Student number: 14M18075 Name: Shin SHIMAHARA Supervisor: Kunio TAKAHASHI

水平力が弾性梁と剛体平面間に働く凝着力に及ぼす影響

島原森

弾性梁側面が剛体平面に凝着する際に発生する凝着力に水平力が及ぼす影響を議論した。理論解析では線形梁理論を用いて水平力が凝着力に及ぼす影響を計算した。実験ではゲル製の梁とガラス製の基盤が接触する際に発生する力を 6 軸力覚センサを用いて測定した。これにより弾性梁側面凝着モデルにおいても水平力を凝着力の制御に用いることが出来ることが明らかになった。また、凝着力の制御を行う際には梁の引き上げ角度を考慮することが求められることを示唆した。同時に線形梁理論を用いた理論解析が実験結果と一致しないことを示した。これらの結果から梁の凝着モデルを改良する必要性を示した。

1 Introduction

Geckos are well known for its ability to run rapidly on walls and ceilings. This means that geckos realize robust adhesion, easy detachment and compliance with surface roughness. The key to these features is geckos' micro-nano hair structure, which consists of setae and spatulae, on their foot[1]. A single seta is approximately 100μm in length. The tip of setae branches to hundreds of splatulae. A single spatula is approximately 200nm in length[2]. The micro-nano hair structure deforms and absorbs surface roughness to generate robust adhesion. Also they can be detached from the surface in several tens of nanoseconds because of the hairs' structural feature.

Because of these features, gecko-inspired adhesive, which imitate the micro-nano hair structure to realize gecko-like behavior, is expected to be utilized for devices like wall-climbing robots[3, 4, 5, 6].

Regarding adhesion of the micro-nano hair structure, it is known that tangential force affects adhesion[7, 8, 9, 10]. A single seta exhibits a different tribological response depending on direction of parallel drag. When a seta is dragged against setal curvature, repulsive normal force is measured. In contrast, when dragged along setal curvature, adhesive normal force is measured. Gecko-inspired devices utilize this phenomenon for grip-and-release control[4, 6].

In some theoretical studies, a single spatula is assumed to be an elastic tape and the pull-off force is discussed using Kendall peel model[11] for thin adhesive tape[1, 9]. Kendall's theory considers a surface energy term, a potential energy term and an elastic energy term due to extension of the film. However, the effect of bending stiffness on adhesion is also important[12]. In order to consider bending stiffness of a hair, a single spatula is assumed to be an elastic beam in the previous study[13]. Adhesion between side surface of an elastic beam and a rigid body is discussed using linear beam theory. Tangential force is ignored in the discussion in spite of its importance for control of grip-and-release. Therefore the effect of tangential force on adhesion between side surface of the elastic beam and the rigid body has not been clarified.

In the present study, theoretical analysis using linear beam theory and experiment are carried out to clarify the effect of tangential force on adhesion between side surface of an elastic beam and a rigid body.

2 Theoretical analysis

2.1 Model of adhesion between side surface of an elastic beam and a rigid body

The effect of tangential force on adhesion between side surface of an elastic beam and a rigid body is analyzed using linear beam theory. The elastic beam, which has bending stiffness EI and the dimension of length L, thickness H and width W, contacts to the rigid body at angle θ (Fig.1(a)). During the contact, normal force F_n and tangential force F_t are produced. It is assumed that the tangential force F_t contributes only for bending moment within non-adhesion area of the beam. Therefore, shear stress induced by the tangential force is ignored. $\theta < 20°$[14] and $H/L \ll 1$ are assumed. Because of these assumptions, deformation of the beam can be explained by linear beam theory. Of course, the assumption about the tangential force obviously contradicts the reality. However, theoretical analysis including tangential force is important for understanding of adhesion control. Accordingly, this assumption is regard as valid

temporarily. Validity of this assumption is discussed based on experimental result later.

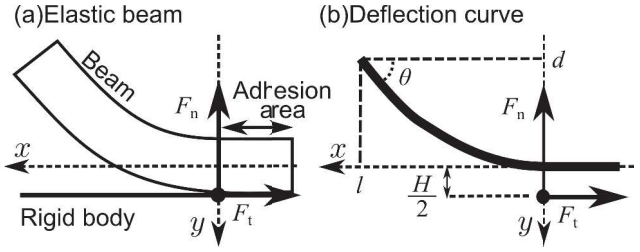

Fig. 1: Contact between side surface of an elastic beam and a rigid body with an angle θ.

2.2 Force between elastic beam and rigid body

As for the calculation, x–y axis is fixed as shown in Fig.1(b). Deformation of the non-adhesion area $0 < x < l$ is obtained using linear beam theory. By considering the relation among the displacement d, the deformation and the force, the normal force is obtained as

$$\tilde{F}_n = \frac{\tilde{F}_t 2\sqrt{3\tilde{F}_t}\sinh\left(2\sqrt{3\tilde{F}_t}\tilde{l}\right)}{2-2\cosh\left(2\sqrt{3\tilde{F}_t}\tilde{l}\right)+2\sqrt{3\tilde{F}_t}\tilde{l}\sinh\left(2\sqrt{3\tilde{F}_t}\tilde{l}\right)} \times\left(\tilde{d}-\frac{1-\cosh\left(2\sqrt{3\tilde{F}_t}\tilde{l}\right)}{2\sqrt{3\tilde{F}_t}\sinh\left(2\sqrt{3\tilde{F}_t}\tilde{l}\right)}\tan\theta\right) \quad (1)$$

where force F, the displacement and the length of the non-adhesion area l are normalized as $\tilde{F}=\frac{F}{12EI/L^2}$, $\tilde{d}=\frac{d}{L}$, $\tilde{l}=\frac{l}{L}$.

The adhesion area is equilibrium at the lowest energy condition. Therefore the length of the non-adhesion area $\tilde{l}$ can be obtained by considering total energy of the system. The total energy of the system consists elastic energy caused by bending U_{elastic}, elastic energy caused by elongation $U_{\text{elongation}}$ and surface energy U_{surface}.

The bending elastic energy is obtained as

$$\tilde{U}_{\text{bend}} = \frac{\tilde{F}_n^2}{4\sqrt{3\tilde{F}_t}\sinh^2\left(2\sqrt{3\tilde{F}_t}\tilde{l}\right)}\left[2\left(1+\frac{\tilde{F}_t}{\tilde{F}_n}\tan\theta\right) \times\left(\cosh\left(2\sqrt{3\tilde{F}_t}\tilde{l}\right)-1\right)\left(\sinh\left(2\sqrt{3\tilde{F}_t}\tilde{l}\right)-2\sqrt{3\tilde{F}_t}\tilde{l}\right) +\left(\sinh\left(2\sqrt{3\tilde{F}_t}\tilde{l}\right)\cosh\left(2\sqrt{3\tilde{F}_t}\tilde{l}\right)+2\sqrt{3\tilde{F}_t}\tilde{l}\right)\frac{\tilde{F}_t^2}{\tilde{F}_n^2}\tan^2\theta\right] \quad (2)$$

where energy U is normalized as $\tilde{U}=\frac{U}{6EI/L}$. Because it is assumed that the tangential force contributes only for the bending moment and doesn't contribute for elongation of the beam, the elongation elastic energy is obtained as

$$\tilde{U}_{\text{elongation}} = 0 \quad (3)$$

Using work of adhesion $\Delta\gamma$, the surface energy is obtained as

$$\tilde{U}_{\text{surface}} = -\Delta\tilde{\gamma}(1-\tilde{l}) \quad (4)$$

where work of adhesion is normalized as $\Delta\tilde{\gamma}=\frac{\Delta\gamma}{6EI/WL^2}$.

From Eq.(1) and the length l obtained by the minimum point of the total energy, the relation between the displacement and the normal force with various tangential force is obtained as shown in Fig.2.

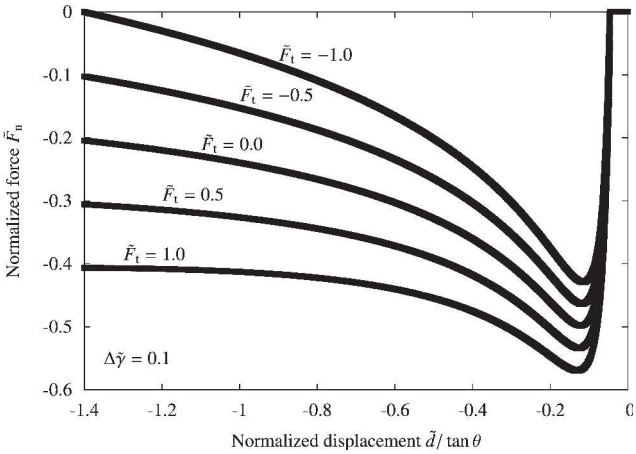

Fig. 2: Relation between the normalized displacement $\tilde{d}/\tan\theta$ and the normalized normal force $\tilde{F}_n$ with various tangential force.

2.3 Effect of tangential force on adhesion

Adhesion force is the minimum value of the normal force. The relation between the tangential force and the adhesion force with various work of adhesion is shown in Fig.3.

3 Experiment

The experimental system is shown in Fig.4. The measurement of the force between an elastic beam and a substrate was carried out by controlling displacement of the elastic beam. In this experiment, the normal force and the tangential force between the beam and the substrate (rigid body) were measured simultaneously by 6-axis force sensor under the quasi-static condition. As for the beam, shock absorbing gel CRG-T2505 (Tanak Co.,Ltd) was used. The beam was 15mm in length, 15mm in width and 5mm in thickness. The Young's module of the beam was measured using tensile

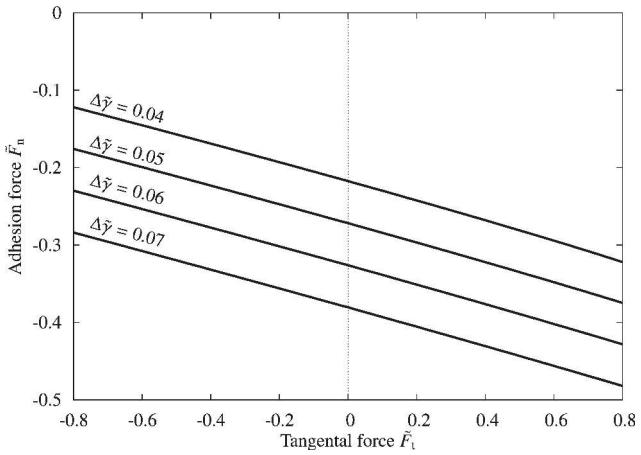

Fig. 3: Relation between the normalized tangential force $\tilde{F}_t$ and the normalized adhesion force$\tilde{F}_{ad}$ with various work of adhesion.

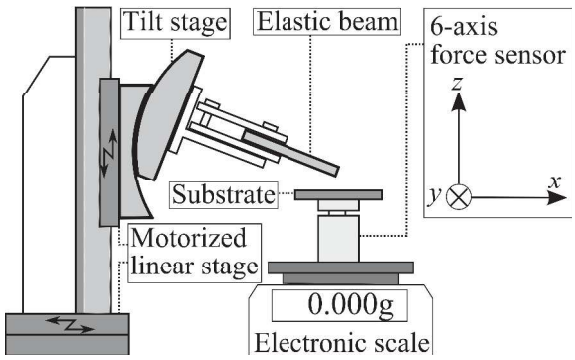

Fig. 4: Experimental system for the measurement of tangential force and normal force between an beam and a glass substrate.

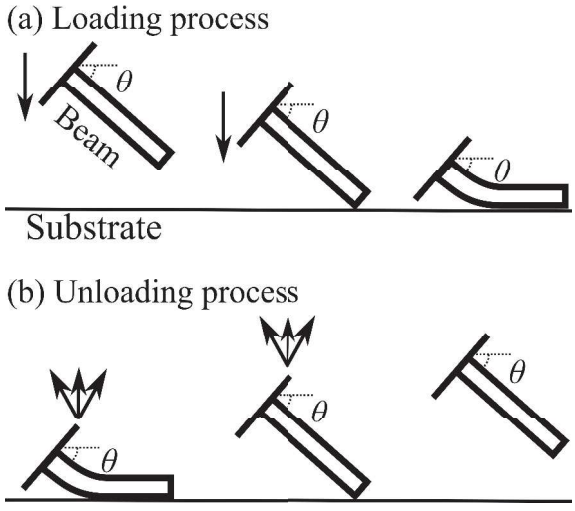

Fig. 5: Schematic illustration of the experimental process.

testing machine for elastic range and obtained 2.3×10^5Pa. As for the substrate, a glass plate was used.

An example of the experimental results is shown in Fig.6. Fig.6 shows transition of the force during the experiment. At the start of the experiment, the edge of the beam contacted to the substrate. Then, the beam was moved down toward the substrate. This phase is called loading process (Fig.5(a)). After the loading process ended at the point A, it was lifted up. This phase is called unloading process (Fig.5(b)). The adhesion force, which is the minimum normal force measured during the unloading process, was measured at the point B. Finally, the separation occurred at the point C.

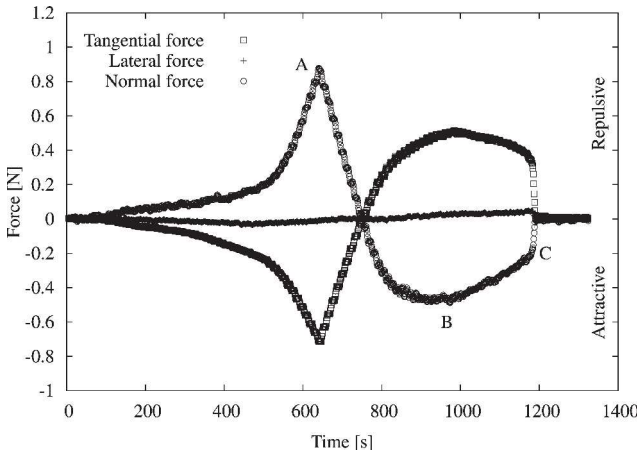

Fig. 6: Transition of the force during the experiment.

4 Discussion

The relation between the adhesion force and the tangential force at the point B is shown in Fig.7. Fig.7 shows that tensile tangential force strengthens the adhesion force and compressing tangential force weakens the adhesion force. This tendency indicates that the tangential force can be utilized for adhesion control. It is remarkable that there are some points where the adhesion force is repulsive. Gecko-inspired adhesive which utilized the model of adhesion between side surface of the elastic beam and the rigid body can realize easy detachment by controlling adhesion applying the tangential force.

Fig.7 also shows that the theoretical analysis using linear beam theory is invalid for estimation of the effect of the tangential force on adhesion. Therefore the adhesion model of the beam has to be modified.

Pull off angle dependence on the tangential force and the adhesion force is shown in Fig.8. Fig.2 shows that there

is the optimal pull off angle to maximize and minimize the tangential force. Because it is important to maximize the variation of the adhesion force for grip-and-release control of gecko-inspired devices, consideration for the optimal pull off angle is important for adhesion control using the tangential force.

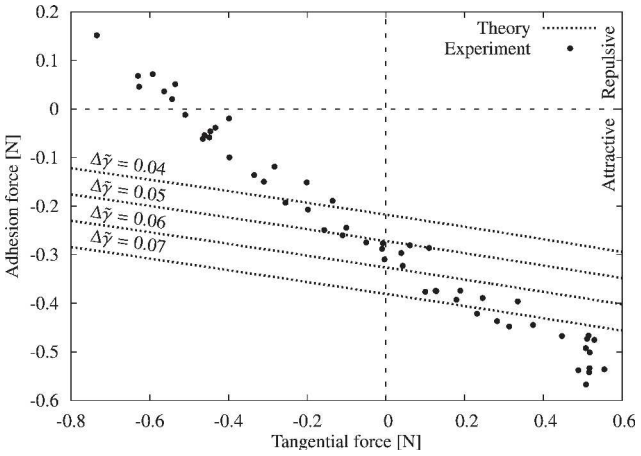

Fig. 7: Relation between the tangential force and the adhesion force.

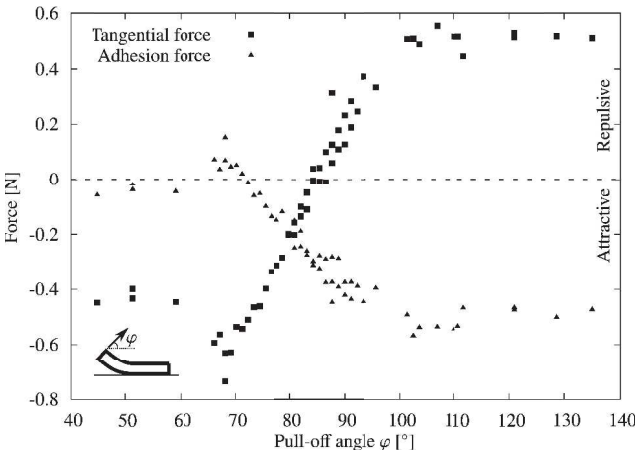

Fig. 8: Pull off angle φ dependence on the tangential force and the adhesion force

5 Conclusion

The effect of the tangential force on adhesion between side surface of the elastic beam and the rigid body is theoretically discussed using linear beam theory. The measurement of the force between the elastic beam and the substrate is carried out by controlling displacement of the elastic beam. In the experiment, the normal force and the tangential force between the beam and the substrate are measured simultaneously by 6-axis force sensor. It is shown by the experimental result that tangential force can be utilized for control of the adhesion force between the elastic beam and the rigid body. In order to maximize the variation of the adhesion force, the optimal pull off angle has to be considered. The experimental result also shows that the theoretical analysis using linear beam theory is invalid for discussion about the effect of the tangential force on adhesion. Therefore the adhesion model of the beam has to be modified.

References

[1] Chen, B., et al., ”Hierarchical modelling of attachment and detachment mechanisms of gecko toe adhesion”, *Proceedings of the Royal Society A*, **464**, pp. 1639-1652, 2008.

[2] Gao, H., et al., ”Mechanics of hierarchical adhesion structures of geckos”, *Mechanics of Materials*, **37**, pp. 275-285, 2005.

[3] Geim A. K., et al., ”Microfabricated adhesive mimicking gecko foot-hair”, *Nature Materials* **2**, 461-463, 2003

[4] Santos, D., et al., ”Directional adhesion for climbing: theoretical and practical considerations”, *Journal of Adhesion Science and Technology*, **21**, pp. 1317-1341, 2007.

[5] Jeonga, H. E., et al., ”A nontransferring dry adhesive with hierarchical polymer nanohairs”, PNAS vol.**106** no.14, 5639-5644, 2009

[6] Kim, S., et al., ”Smooth Vertical Surface Climbing With Directional Adhesion”, *IEEE Transactions on Robotics* vol.**24** no.**1**, pp. 65-74, 2008.

[7] Autumn, K., et al., ”Adhesive force of a single gecko foot-hair”, *Nature* **405**, 681-685, 2000.

[8] Takahashi, K., et al., ”Gecko’s foot hair structure and their ability to hang from rough surfaces and move quickly”, *International Journal of Adhesion and Adhesives* **26**, pp. 639-643, 2006.

[9] Autumn, k., et al., ”Frictional adhesion: a new angle on gecko attachment”, *The Journal of Experimental Biology* **209**, pp. 3569-3579, 2006.

[10] Zhao, B., et al., ”Adhesion and Friction Force Coupling of Gecko Setal Arrays:Implications for Structured Adhesive Surfaces”, *Langmuir*, **24(4)**, pp. 1517-1524, 2008.

[11] Kendall, K., ”Thin-film peeling -the elastic term”, *Journal of Physics D : Applied Physics*, **8**, pp. 1449-1452, 1975.

[12] Sauer, R. A., ”The peeling behavior of thin films with finite bending stiffness and the implications on gecko adhesion”, *The Journal of Adhesion*, **87**, pp. 624-643, 2011.

[13] Y. Sekiguchi, et al., ”Adhesion between side surface of an elastic beam and flat surface of a rigid body”, *Journal of Adhesion Science and Technology*, Vol. **26**, No. 23, pp. 2615-2626, 2012

[14] 奈良泰彦, ”大変形を考慮した弾性梁と剛体間の凝着”, 2014 年精密工学会春季大会講演論文集, No.J13, 735-736, 2014

Development of Simultaneous Measurement System of MIMO Channel Response and Body Motion for Study of Dynamic WBAN Channel

Student Number: 14M18230 Name: Gaochao Chen Supervisor: Jun-ichi Takada

動的無線ボディエリアネットワークチャンネル研究のための MIMO チャンネル応答と人体動作同時測定装置の開発

陳 高超

WBAN のチャンネルは、アンテナ、人体、周囲環境など、様々な要因に影響されて、それらの影響要素が複合的にチャンネル応答だと測定されるから、簡単に分離すことができない。動的な WBAN チャンネルは WBAN のシステムを設計において非常に重要な情報になるから、シミュレーションベースのチャンネル分析が不可欠である。本論文で、MIMO チャンネル応答と人体動作を同時に測定するシステムの開発を通じて、測定結果とシミュレーション結果の比較ができるようになる。研究は将来 WBAN の動的なチャンネルの研究に役立つ。

1 Introduction

Wireless body area network (WBAN) is a network which consists of several sensor/actuator nodes inside, on or around human body [1]. It is expected to be widely utilized in medicine, health-care, sports training and other fields. Dynamic behavior of WBAN channel is important information for design and characterization of WBAN system. However, in measurement, the influences of various factors, such as antenna type, position, orientation, electromagnetic interaction, surrounding environment, human motion as well as scattering from body surface itself are simultaneously measured as channel responses and difficult to separate each other. Furthermore, the disparity of those influential factors leads to difficulty of comparison among those measurement results. Considering the difficulty of body motion repeatability in measurement, simulation is a useful, potential tool for WBAN channel analysis, while the reliability of simulation is still questioned without comparison to measurement.

A comparison between measurement and simulation is presented in [2]. The avatar for simulation is generated in animation software, Poser 6. In order to match the human motion and motion rhythm as same as the avatar in Poser, 60 times of measurements are repeated to find the best the matching. Also video record is utilized to help placing antenna and finding best matching. The average procedure time for one frame is approximately 2 days. The challenges of above comparison system are: firstly, it costs long time to match body motion in measurement and avatar motion in simulation; secondly, the antenna mismatch (including antenna position and orientation) cannot be avoided; thirdly, it is difficult to extend this avatar motion to other body motion. Therefore, a more convenient comparison system is required. In this paper, a simultaneous measurement system of MIMO channel responses and body motion is developed for study of dynamic WBAN channel. The developed system can improve the accuracy and efficiency of comparison between measurement and simulation, and contribute to understand the influential factors such as antenna position and orientation.

The research flowchat is shown in Fig 1. In measurement, a 3x3 MIMO channel sounder is utilized to obtain measured MIMO channel responses of WBAN. During measurement, a motion capture device, Kinect, is utilized to capture body motion. The captured body motion data are utilized to generate body data and antenna data through avatar generation procedure. Then the generated body data and antenna data are imported to a electromagnetic simulator in [3] for channel simulation. Finally the simulated channels are compared to the measured channels.

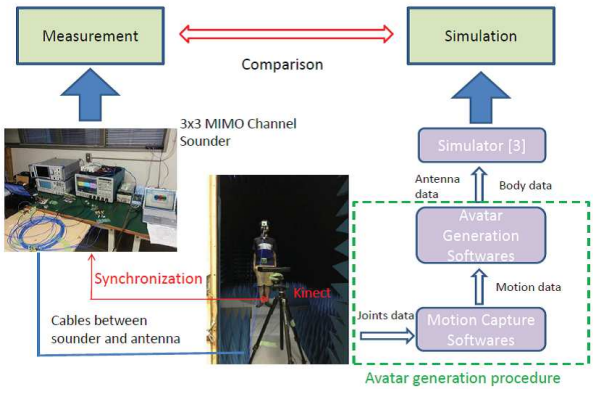

Figure 1: Research flowchat

2 Experiment

2.1 3x3 MIMO channel sounder

A 3x3 MIMO channel sounder is developed for channel measurement. The structure of the sounder is shown in Fig 2. It consists of two dielectric resonator antennas (MIMO DRA) [4, 5] and a multi-port oscilloscope. In transmitter side, a micro controller controlled switch switches 3 ports of MIMO DRA (transmitter) sequentially. This is called time division multiplexing (TDM) scheme. In receiver side, 3 ports of MIMO DRA (receiver) are connected to the multi-port oscilloscope respectively, to receive the signals. Amplifiers are inserted between oscilloscope and receiver to guarantee the measurement range. By applying TDM in transmitter side, a 3x3 MIMO channel is obtained. The performance of the sounder is also evaluated. An attenuator is inserted between port1 in transmitter side and port 1 in receiver side, instead of antennas as a channel simulator, to evaluate the measurement range. The measurement result shows that it can measure the pathgain down to -80 dB with error of less than 2 dB. Also an attenuator of 40 dB is inserted into each port pair (Rx1-Tx1, Rx2-Tx1,...,Rx3-Tx3), to obtain the disparity in different port pairs. The measurement result shows their disparities are less than 1 dB after calibration. More information about the construction as well as performance evaluation of the developed sounder can be found in [6].

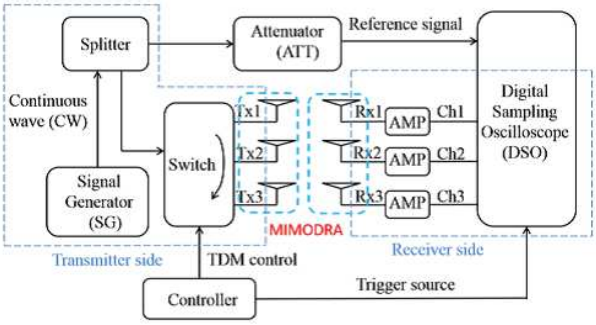

Figure 2: The structure of the MIMO channel sounder

2.2 Measurement

Table 1: Measurement setup

Item	Parameter
Frequency	2.45 GHz
Frame rate	30 fps
Sampling rate	6.25 Giga sample/s
Measurement time	15 s
Sample per frame	20000

The measurement is conducted in an anechoic chamber to alleviate the reflection due to surround environments. The transmitter is placed on navel and receivers are allocated on chest, head, hand and upper leg respectively, which is shown in left part of Fig 3. For each antenna link, the motion of walking and sitting-standing are done. Therefore, totally 8 measurements are conducted. The antenna orientation setup is shown in right part of Fig 3. Transmitter 1 and receiver 1 are perpendicular to body surface, transmitter 2 and receiver 2 are parallel to body surface and oriented horizontally, and transmitter 3 and receiver 3 are parallel to body surface and oriented vertically. Measurement setup for channel sounder is listed on Table 1.

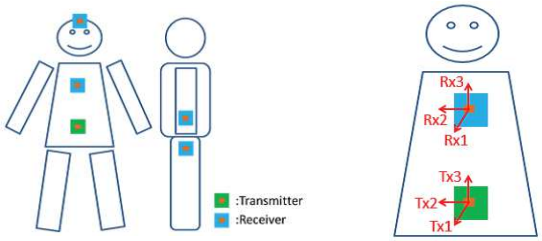

Figure 3: Antenna setup in measurement

3 Simulation

3.1 Avatar generation procedure

The avatar generation procedure is shown in Fig 4. A motion capture device, Kinect, which is shown in upper left part of Fig 4, captures body posture by tracing 20 joints data with frame rate of 30 fps. Then the traced joints data are utilized to create a motion data file, biovision hierarchy file (.bvh). .bvh file is a file which designs body motion with scheme of skeleton. Upper right part of Fig 4 shows one frame of the generated .bvh file. Then the generated .bvh file is imported into animation software, Poser 7, to activate the pre-built avatar. The avatar will do the body motion defined by the .bvh file, as shown in lower left part of Fig 4. The center of gravity of red diamond shows the location of antenna and two diagonals of the red diamond show orientation of the antennas which are parallel to body surface. The cross product of these two diagonals is calculated to obtain the orientation of the antenna which is perpendicular to body surface. Then two types of wavefront.obj (.obj) files (containing diamond and excluding diamond) are exported from Poser 7 in order to obtain antenna data through comparison. Next, the exported .obj file which excludes diamond is voxelized by an application, binvox.exe [7], generating a .binvox file, shown in lower right part of Fig 4. Finally, the generated .binvox file are utilized to convert the voxelized body motion into a digital data file (body data) for numerical simulation.

3.2 Electromagnetic simulator [3]

An electromagnetic simulator in [3] is utilized for channel simulation. In this simulator, finite-difference time domain (FDTD) method is utilized. The simulation setup is listed on Table 2. The simulation domain is 1.5 m$\times$2.3 m $\times$1.5 m, sufficient to cover human motion. And cell size of 0.005 m is much less than wave length of 2.45 GHz (corresponding to 0.1225 m). In the simulation, both

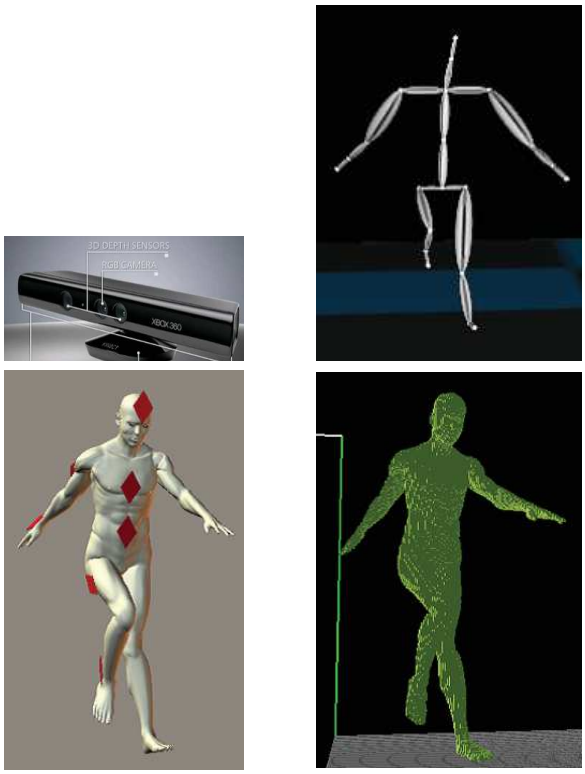

Figure 4: Avatar generation procedure

transmitter and receiver are utilized as infinitesimal small dipole antennas. The concept of simulation domain and procedure can be found in Fig 5. Firstly, the transmitter is oriented to X-orientation, then the generated electromagnetic field in the location of receiver are recorded. Secondly, the same procedure are done by orienting the transmitter to Y-orientation and Z-orientation respectively. Next, the obtained electric fields are converted to received power with antenna data. Finally, the pathgain is obtained with the ratio of received power and transmitted power.

Table 2: Simulation setup

Parameter	Value
Simulation domain	$300 \times 460 \times 300$ (1.5 m×2.3 m×1.5 m)
Cell size	0.005 m
Boundary	10-layer PML
Feed current I	1.0 A
Frequency	CW 2.45 GHz
Dieletric constant of body	53.57
Conductivity of body	1.81 S/m

4 Comparison

4.1 Comparison between measurement and simulation

Comparison between measurement and simulation for antenna link of navel-chest, walking motion is shown in Fig 6. The statistic values of mean and standard deviation are utilized for comparison, and listed on Table 3. In

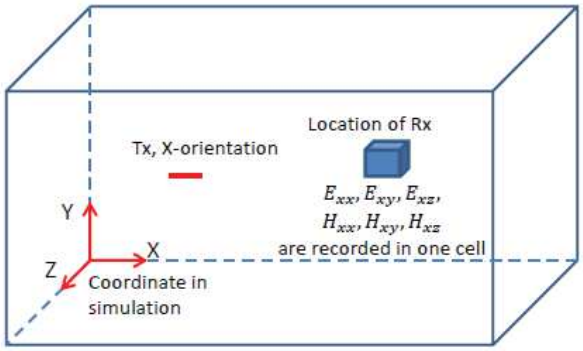

Figure 5: Concept of simulation domain and procedure

different channels, their performance of comparison are different. The gap between strongest channel and weakest channel is larger than 30 dB, which can be confirmed both in measurement and simulation. This phenomenon indicates that polarization combination is an important influential factor to dynamic WBAN channel. Channels of Rx1-Tx1, Rx1-Tx3, Rx3-Tx1 and Rx3-Tx3 have relatively stronger mean values and lower standard deviation. These phenomenons indicate that these channels are less influenced by body motion. While the gap between simulation and measurement in channels of Rx2-Tx1 and Rx2-Tx3 are extremely high. The standard deviations in simulation are much higher than them in measurement. In order to understand the reason, influential factors of antenna in simulation are investigated.

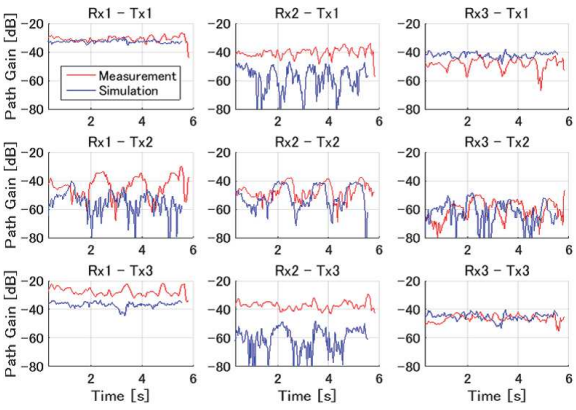

Figure 6: Comparison between measurement and simulation, antenna link of navel-chest, walking motion

4.2 Influential factors discussion in simulation

Due to the mismatch of real human body shape in measurement and avatar shape in simulation, antenna position mismatch and orientation mismatch may happen in comparison. Since the specific antenna orientation in measurement is difficult to obtain, the influences of antenna position mismatch and orientation mismatch to dynamic WBAN channels are investigated through simulation. In order to simplify the analysis of antenna position mismatch, the transmitter is moved along each axis in an-

Table 3: Statistic values of comparison between measurement and simulation, antenna link of navel-chest, walking motion

Channel	Measurement		Simulation	
	Mean [dB]	Std	Mean[dB]	Std
Rx1-Tx1	-30.98	2.04	-32.71	0.95
Rx2-Tx1	-40.68	3.04	-58.25	9.16
Rx3-Tx1	-48.32	3.77	-42.32	1.81
Rx1-Tx2	-44.44	7.46	-55.53	8.06
Rx2-Tx2	-47.61	5.48	-51.87	8.74
Rx3-Tx2	-61.00	6.87	-63.05	8.23
Rx1-Tx3	-27.81	2.90	-36.61	1.84
Rx2-Tx3	-37.55	2.83	-60.89	8.81
Rx3-Tx3	-46.51	2.47	-45.14	2.30

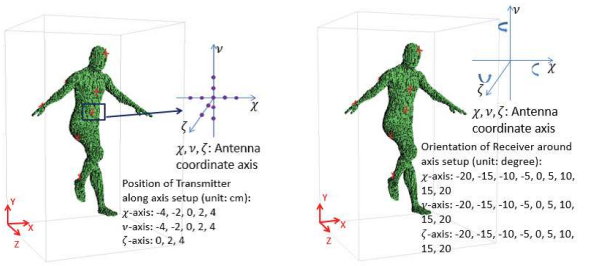

Figure 7: Antenna setup for influential factors investigation

tenna's local coordinate with resolution of 2 cm. For same reason, the receiver is rotated around each axis with resolution of 5 degree. The position setup for transmitter is shown in left part of Fig 7 and the orientation setup for receiver is shown in right part of Fig 7.

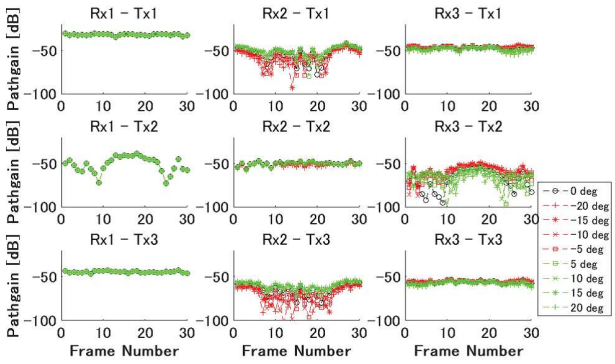

Figure 8: Influence of receiver rotation around ζ-axis

The influence of receiver rotation around ζ-axis is shown in Fig 8. Channels of Rx2-Tx1, Rx3-Tx2 and Rx2-Tx3 are sensitive to orientation mismatch of receiver which is rotated around ζ-axis. For orientation change of 10 degree, their channel strength difference can be greater than 20 dB. Other channels are not sensitive to orientation mismatch of receiver. This phenomenon indicates that in simulation, the orientation of antenna should be prudently designed. Similar results can be found in receiver rotated around χ-axis and υ-axis and transmitter moved along χ-axis, υ-axis and ζ-axis. This is reasonable due to the antenna which is parallel to body surface, its radiation power is more absorbed by body. Also polarization combination is another influential factor to dynamic WBAN channel. In channels of Rx2-Tx2 and Rx3-Tx2, the transmitter and receiver are both parallel to body surface, while due to different polarization combination, their performance are quite different.

5 Conclusion & Future work

5.1 Conclusion

Dynamic WBAN channel is important information for design and characterization of WBAN system. However, the influential factors are integrally measured as channel responses and difficult to separate each other from measurement results. Furthermore, the difficulty of body motion repeatability in measurement leads to difficulty of dynamic WBAN channel analysis. Therefore, simulation based analysis is required. Comparison system of measurement and simulation is necessary to understand the reliability of simulation. There are several drawbacks in motion design and antenna placement in the comparison which is introduced in [2].

Therefore, a simultaneous measurement system of MIMO channel responses and body motion is developed for study of dynamic WBAN channel. The developed system can contribute to investigation of the influential factors such as antenna position and orientation, body motion.

5.2 Future work

In this system, antenna embedding channels are utilized. In order to remove the influential factor of antenna type, antenna de-embedding should be considered. Also investigation of other antenna links and different body motions should be evaluated for this system. Since MIMO channels are utilized in this measurement system, the related research in diversity issue can be discussed.

References

[1] A. Reichman and J. Takada, "Body Communications," in Pervasive Mobile and Ambient Wireless Communications - COST Action 2100, Roberto Verdone and Alberto Zanella, Eds, Springer-Verlag, 2012, ch.15, pp. 609-660.

[2] M. Gallo, P. S. Hall, Q. Bai, Y. I. Nechayev, C. C. Constaninou and M. Bozzetti, "Simulation and Measurement of Dynamic On-Body Communication Channels," *IEEE Trans. Antennas Propag.*, vol. 59, no. 2, pp. 623-630, Feb, 2011.

[3] J. Naganawa, "Antenna De-embedding in Wireless Body Area Network Channel," Doctor Thesis, Tokyo Institute of Technology, Mar, 2015.

[4] K. Ishimiya, J. Langbacka, Z. Ying, and J. Takada, "A Compact MIMO DRA Antenna," 2008 International Workshop on Antenna Technology: Small Antennas and Novel Metamaterials, pp. 286-289, Mar. 2008.

[5] K. Ishimiya, Z. Ying, and J. Takada, "A Compact MIMO DRA for 802.11n Application," 2008 IEEE International Symposium on Antennas and Propagation, July. 2008.

[6] G. Chen, J. Naganawa, M. Kim and J. Takada, "Development of a Tripolarized Dynamic Channel Sounder for Wireless Body Area Network," 9th International Symposium on Medical ICT, Mar. 2015.

[7] URL: http://www.cs.princeton.edu/ min/binvox/